Towards High Energy Density Li and Na Ion Batteries
An Anode Material Study

Xu, Yaolin

Important note
To cite this publication, please use the final published version (if applicable).
Please check the document version above.

Towards High Energy Density Li and Na Ion Batteries

An Anode Material Study

Dissertation

for the purpose of obtaining the degree of doctor

at Delft University of Technology

by the authority of the Rector Magnificus, prof.dr.ir. T.H.J.J. van der Hagen

chair of the Board for Doctorates

to be defended publicly on

Wednesday 23 May 2018 at 15:00 o'clock

by

Yaolin XU

Master of Science in Sustainable Energy Technology,

Delft University of Technology, the Netherlands

born in Henan, China

This dissertation has been approved by the promotor.

Composition of the doctoral committee:

Rector Magnificus	chairperson
Prof. dr. F.M. Mulder	Delft University of Technology, promotor

Independent members:

Prof. dr. B. Dam	Delft University of Technology
Prof. dr. J.J.C. Geerlings	Delft University of Technology
Prof. dr. M.T.M. Koper	Leiden University
Prof. dr. P.H.L. Notten	Eindhoven University of Technology
Dr. ir. M. Wagemaker	Delft University of Technology
Dr. ir. E.M. Kelder	Delft University of Technology

Front Cover: Illustration of Na ion storage in a black phosphorus-carbon nanocomposite

Back Cover: SEM image of silicon nanoparticle deposition

An electronic version of this dissertation is available at http://repository.tudelft.nl/.

To my family

Table of Contents

Chapter 1 Introduction

(Image credit: Sebastian Kotarski/Flickr)

1.1 Rechargeable batteries powering a sustainable future

Sustainable energies need to increasingly power our modern society due to the Paris climate agreements and the depletion of fossil fuels. However, the implementation of sustainable energy technologies requires large-scale energy storage due to the intermittent production of renewable energies such as wind and solar energy [1]. Moreover, the demand for energy storage is also growing due to the rapid development of mobile applications, in particular the development of electric vehicles as an alternative of fossil fuel powered transportation. Intensive research efforts have been made in search of energy storage solutions that could lead to a prosperous and sustainable future, in which rechargeable batteries play a key role [2-4].

A rechargeable battery generally consists of two electrodes in which the active charge carrying element has different chemical potentials, and in between of which there is an electrolyte as an ionic conducting medium. During charge, electrons move from the electrode with a more positive potential (cathode) to the more negative one (anode) via the external electrical circuit, while ionic transport occurs inside the battery through the electrolyte to maintain the charge balance. In this process the anode gets chemically reduced and the cathode is oxidized, turning electrical energy into chemical energy. The reverse process happens during discharge to deliver electrical energy to the working load.

To meet the increasing global demand in batteries for mobile applications and more general energy storage for realizing an economic, sustainable and secure energy future, rechargeable batteries are desired to satisfy the following requirements:

- High energy density
- High power density
- Long cycle life
- Cost effective
- Environmentally friendly
- Safe

Nowadays Li ion batteries dominate the market thanks to the relatively high energy density (Figure 1.1a). In a Li ion battery, Li ions migrate between the anode and cathode across the electrolyte, as illustrated in Figure 1.1b. The commercially available Li ion battery anode material is graphite and $LiCoO_2$ is most widely used as the cathode [5]. Both electrodes

consist of active material, 1-5 wt. % of conductive additives (mostly carbon black) and 3-5 wt. % of binding materials (mostly polyvinylidene fluoride (PVDF)). Cu and Al foils work as the current collector for the anode and cathode, respectively. These two electrodes are physically separated by a polymer separator wetted with a liquid organic electrolyte which is electrically insulating but conductive for Li ion transport.
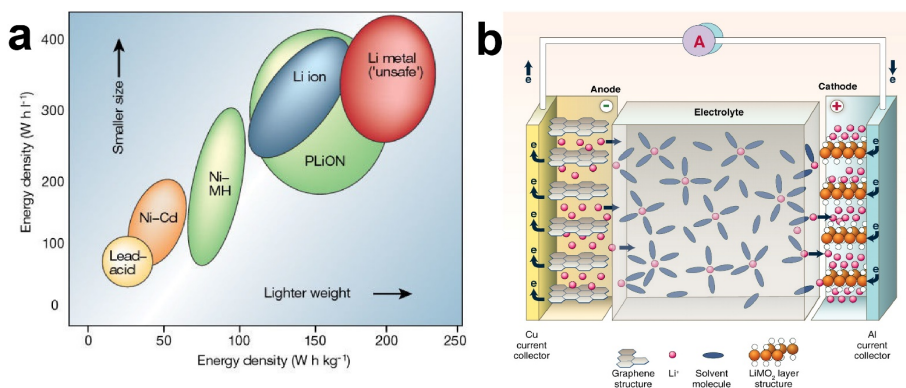
Figure 1.1 (a), Comparison of different categories of rechargeable batteries [5] and (b), Schematic of a Li ion battery [6].

However, the high cost, limited capacity and lack of Li and Co resources in the world may become limiting for reaching the increasing scale of Li ion battery implementation in the future [5, 7, 8]. In recent years, both intensive and extensive research has been performed to find more viable alternatives including advanced Li ion batteries that utilize novel, high capacity and cost-effective electrodes [9, 10] and post Li ion batteries including Li-O_2 [11], Li-S [12], solid-state [13] and Li metal [14] batteries, and beyond Li-based systems such as Na [15], K [16], Mg [17] and Al [18] ion batteries. Despite the progress that has been made, these rechargeable batteries are still in the research stage. Multiple factors have to be addressed before their successful commercialization, among which the high manufacturing cost and the lack of anode materials with high capacity and long cycle life are the major challenges.

1.2 Anode materials for Li ion batteries

Graphite has been the anode material of choice in commercial Li ion batteries for more than 20 years due to its advantages of low cost, high electronic conductivity, relatively high capacity and low lithiation potential *vs* Li/Li$^+$. Li ions are intercalated between the graphene layers of graphite and up to 1 Li atom per 6 C atoms can be stored in this way delivering a

specific capacity of 372 mAh g^{-1}. However, its rather limited capacity has been a major drawback and this is the reason for tremendously intensive research into anode materials with higher capacities.

There are many candidate materials for the anode of Li ion batteries [19], and their capacities are shown in Figure 1.2 [20]. The ongoing research on the pursuit of new anode materials has been focused on advanced carbon materials (e.g. graphene [21] and carbon nanotube [22]), alloy-based [23] and conversion reaction-based anode materials [24], and composite anodes [25]; and recently the research interest in Li metal anodes has been revived and intensified [26].
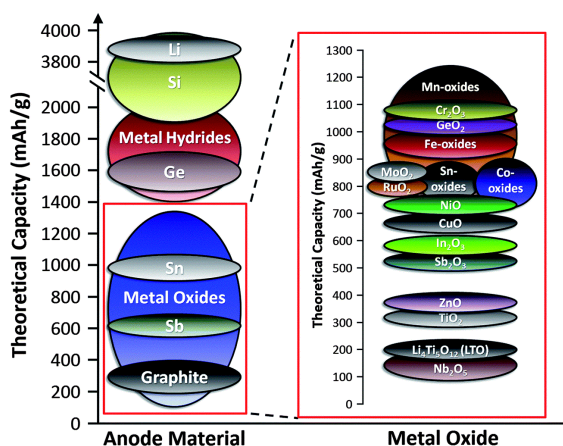
Figure 1.2 Anode material candidate for Li ion batteries [20].

Li metal exhibits a high specific capacity for Li ion storage (3860 mAh g^{-1}, > 10 times higher than graphite) and the lowest redox potential, therefore it has been considered as the "Holy Grail" anode for Li batteries. However, Li deposition occurs in a dendritic form that can result in internal short-circuits (Figure 1.3), eventually, causing thermal runaway and explosion hazards, which imposes immense challenges for its practical application. Various approaches have been researched to suppress the Li dendrite formation and to achieve a stable cycling performance, among which 3D conductive host frameworks have received the most research interest [14, 26-28]. Lu *et al.* [29] fabricated lithiophilic Cu–Ni core–shell nanowire networks as a stable host for Li deposition and improved the lifespan of Li metal anode. Xie *et al.* [30] reported an excellent cycling stability for dendrite-free Li deposition on a 3D graphene@Ni foam scaffold. However, the manufacturing cost involved in these metal anodes are high and great advances are still required towards its realization in practice.
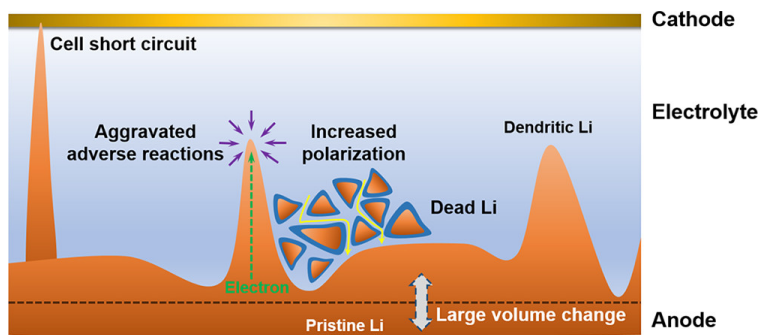
Figure 1.3 Dendrite formation in Li metal anodes [14]**.**

Alloy based materials attract intensive research attention due to their high capacities for Li ion storage (e.g. 4200 mAh g^{-1} for Li$_{4.4}$Si). Conversion reaction-based materials (M$_a$X$_b$, M = metal, X = O, S, F, P, N etc.) have also received considerable research interest in which Li reacts with M$_a$X$_b$ forming Li$_y$X and metallic M while delivering substantial capacities. The definition can be broadened to the cases where M is a Li-alloying element and further improved capacities can be obtained [19]. For instance, the Li ion insertion in MgH$_2$ first follows a conversion reaction: MgH$_2$ + 2 Li $\rightarrow$ Mg + 2 LiH, and further lithiation can takes place with a Li-Mg alloying process: x Li + y Mg $\rightarrow$ Li$_x$Mg$_y$.

However, despite the high specific capacity, these high-capacity alloy and conversion reaction based anode materials suffer from multiple issues as illustrated in Figure 1.4: (1), Severe volume expansion (e.g. > 300 % for Si) happens during lithiation due to the large amount of Li ions inserted into the host. Subsequently the structure collapses upon the extraction of Li ions, which causes the pulverization of active materials upon repetitive de-/lithiation cycles. (2), When liquid electrolytes are used, irreversible solid electrolyte interphase (SEI) formation occurs consuming the active materials. This issue becomes aggravated in the materials undergoing significant volume changes due to the unstable and thus continuous SEI formation over cycling. (3), The electrode also experiences drastic structural and morphological deformation during cycling, leading to the loss of electrical conduction throughout the electrode as well as the loss of active materials, and eventually, the battery failure.
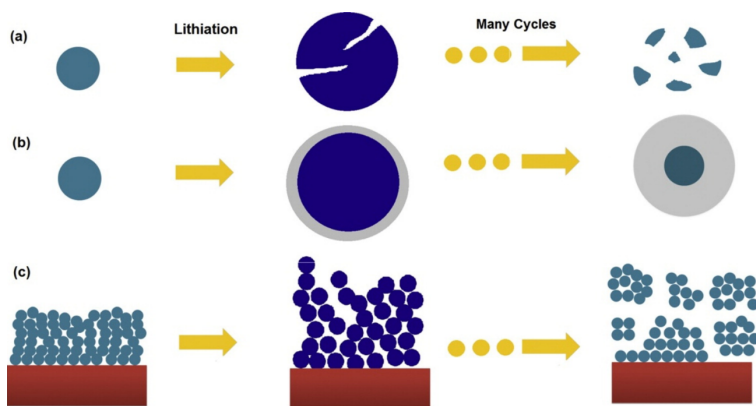
Figure 1.4 Failure mechanisms of high-capacity electrodes. (a) Material pulverization. (b) Continuous SEI growth. (c) Morphology and structure deformation. adopted from [31].

To confine the volume expansion, nanosizing the active materials has been proven to be an effective solution as the particle size has already been small, strains can better be accommodated, and hence the further material pulverization can be avoided [31-34]. Embedding the active materials in advanced carbon nanostructures has also been commonly used to hold the volume change and to integrate the electrical conduction throughout the electrode over cycling [35, 36], especially for the materials with low intrinsic electronic conductivity such as Si and MgH_2 to enable their electrochemical functionality. For example, Magasinski *et al.* [37] showed that Si nanoparticles coated hierarchical carbon black achieved a high capacity of 1950 mA h g^{-1}. Liu *et al.* [38] produced a pomegranate-reminiscent Si-C yolk-shell anode that exhibited a superior cyclability (97 % capacity retention over 1000 cycles). Oumellal *et al.* prepared ultra-small (5.5 nm) MgH_2 nanoparticles embedded within a high surface area graphite host using a bottom-up approach which exhibits a reversible capacity of about 500 mAh g^{-1} for 20 cycles. However, despite the significant progress that has been made, the manufacturing cost of these sophisticated Si electrodes are still too high, and the cycling stability and rate capability of MgH_2 based anodes are still to be improved. Great challenges remain towards commercially viable Si and MgH_2 anodes for Li ion batteries.

1.3 Anode materials for Na ion batteries

Recently Na ion batteries have been intensively researched as an alternative of Li ion batteries due to the limited and uneven distribution of global Li resources and the high natural

abundance and thus low cost of Na compared to Li [39, 40]. Na ion batteries undergo analogous chemistries to Li ion batteries and most of the electrode materials for Li ion batteries have also been researched for Na ion storage [40-42]. However, it remains challenging to find an anode material with an appropriate working potential, a high capacity for Na ion storage and high structural stability. Research on the anode materials has been mainly directed towards carbonaceous materials, alloy-based materials, transitional metal oxides/sulphides and organic composites [40, 43, 44], as demonstrated in Figure 1.5. Analogous to the Li ion counterparts, Na metal, alloy and conversion reaction-based materials show the highest specific capacities for Na ion storage.
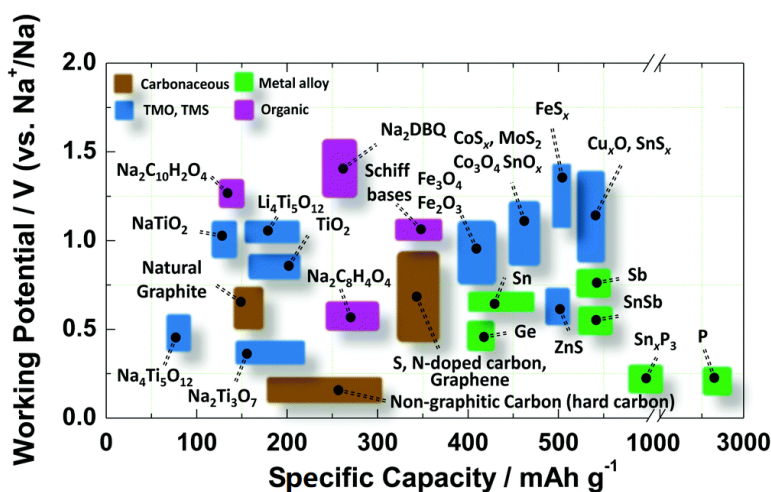
Figure 1.5 Anode material candidates for Na ion batteries [40]**.**

Metallic Na shows a great potential as an anode for Na batteries (such as Na-S [45] and Na-O_2 [46] systems) due to its high theoretical capacity and low redox potential. However, it exhibits a high reactivity with organic electrolyte solvents, and the dendritic Na deposition appears to be more hazardous compared to Li metal anodes. The research on suppressing the Na dendrite formation to achieve a stable Na metal anode has emerged very recently [47-50]. For instance, Zhao *et al.* [50] utilized atomic layer deposition (ALD) of Al_2O_3 to protect the Na metal anode and to suppress the dendritic Na deposition. However, the development of metallic Na anode is still in its infancy and significant challenges still remain.

Among the anode material candidates for Na ion batteries, phosphorus exhibits a particularly high theoretical Na ion storage capacity (2596 mAh g^{-1} for Na_3P) and thus has attracted substantial research attention [51]. Among the phosphorus allotropes, white phosphorus is

flammable and unsafe. Commercially available red phosphorus is electrically insulating, therefore, costly and sophisticated red phosphorus – carbon nanomaterial composites have to be synthesized to enable its electrochemical functionality in Na ion batteries [52-54]. Black phosphorus has recently received increasing research interest thanks to its layered structure similar to graphite, relatively higher electronic conductivity and high chemical stability, however, its synthesis has required high energy and is costly. Moreover, phosphorus undergoes critical volume expansion upon Na ion insertion (490 % from P to Na_3P) that is more significant compared to its lithiation because of the larger size of Na ion compared to Li ion. Therefore, phosphorus based electrodes typically suffer from material pulverization, continuous SEI growth and loss of electrical conduction as described for the alloy-based Li ion battery anode materials in Chapter 1.2, and as a result, the electrochemical cycling stability is poor. Advanced electrodes using nanostructured black phosphorus embedded within carbon matrices are commonly applied to limit the volume change to achieve a stable cycling property. For example, Ramireddy *et al*. [55] synthesized black phosphorus – graphite composites for Na ion batteries which showed a retained capacity of 119 mAh g^{-1} after 50 cycles. Xu *et al*. [56] developed a black phosphorus – Ketjenblack multiwall carbon nanotube composite which showed a high capacity of around 1700 mAh g^{-1} over 100 cycles, but the utilization of costly black phosphorus crystals and carbon nanotubes as well as the complex processing largely compromise its feasibility of commercialization.

Apart from phosphorus, tin is also one of the most promising anode materials for Na ion batteries because of its low cost, high capacity (847 mAh g^{-1} for $Na_{15}Sn_4$) and outstanding electronic conductivity [57]. However, Sn also suffers from similar volume expansion-related problems as explained before. Tin phosphides exhibit the synergistic merits of both P and Sn: metallic Sn networks form an electrical pathway for reducing the P atoms, while the presence of P in the Sn-P compounds improves the Na ion storage capacity compared to a Sn-alone anode. The stepwise sodiation of Sn-P leads to the formation of Na_3P next to Sn that works as an electrical shielding matrix for Sn and prevents its aggregation issues. Therefore, Sn-P compounds can be expected to exhibit improved capacity, cycling stability and rate capability for Na ion batteries and has been intensively researched [58-61]. Among all Sn-P compounds, SnP_3 has the highest content of P and thus the highest theoretical specific capacity for Na ion storage. SnP_3 has been shown to achieve a high capacity (~ 800 mAh g^{-1} at 0.15 A g^{-1}) for Na ion batteries, but the reported cycle life is rather limited (150

cycles) probably due to the gradual structural change during cycling resulting in the loss of electronic conduction [58]. Liu *et al.* [61] showed that a yolk–shell Sn_4P_3@C nanosphere composite based Na ion battery anode obtained a reversible capacity of 360 mA h g^{-1} at 1.5 A g^{-1} after 400 cycles. However, Sn-P compounds based Na ion battery anodes with the improved capacity, rate capability and long-term (> 500 cycles) cycling stability still have to be developed for practical applications.

In addition, it should be noticed that the sodiation chemistries of some materials are different from that in Li ion batteries. The common anode material for Li ion batteries, graphite, has an inferior capability for Na ion intercalation as it is thermodynamically more favourable for Na plating to take place [62]. Non-graphitic carbonaceous materials (highly disordered carbon) allow Na ion insertion and have been comprehensively studied [63, 64] and are regarded as the "first-generation" anodes for Na ion batteries. Moreover, Si, which can store up to 4.4 Li atoms per Si atom, can only take one Na atom per Si atom [65]. Theoretical works have been done suggesting that Na ion uptake in Si can be facilitated with structural modifications and controlled activation barriers [66-69], but successful Na ion storage in Si based materials has previously not been realized in practice. Furthermore, from theoretical studies only the Na ion insertion voltage has been predicted [70, 71], but no reversible Na ion storage in MgH_2 or any other metal hydride has been reported till date probably due to the sluggish Na ion diffusion kinetics.

1.4 This thesis

The aim of this thesis is to search for new methods and materials to realize high energy density anodes for Li and Na ion batteries. Both experimental study and theoretical understanding on the Li/Na ion storage in our developed electrodes are involved.

The scientific challenges and our solutions proposed in this thesis work are outlined as below.

(1), How to effectively suppress the dendrite growth to achieve a stable Li/Na metal anode?

The dendrite formation during Li and Na deposition originates from the inhomogeneous charge distribution on the metal anode [14]. Therefore, to suppress the dendritic growth, in Chapter 2 we introduce a honeycomb-like 3D porous Ni@Cu produced through a facile and rapid electrodeposition of hierarchical nickel branches on a planar Cu foil working as the current collector for both Li and Na metal anodes. Thanks to the presence of numerous conductive nickel tips serving as the nucleation sites and charge centers, the charge

localization at just one or few points on the current collector is avoided and eventually homogeneous Li/Na deposition within the porous nickel host is achieved.

(2), How to enable stable lithiation in a high mass loading, Si-majority anodes?

Considering that the electronic conductivity of Si will be enhanced with several orders of magnitude upon even minimal Li ion insertion [72-74], and that the inactive native SiO_x on the surface of Si particle may induce the formation of a locally protective SEI layer, it can be anticipated that the addition of conductive additives in the Si anode can be reduced or even eliminated, and surface-oxidized Si may behave as non-pulverized after the initial SEI formation. Moreover, interconnected porosities in the electrode provide the liquid electrolyte express pathways to the active materials and therefore facilitate the Li ion diffusion throughout the electrode. Chapter 3.1 presents a thick, carbon/binder-free, interconnected and thin layer surface-oxidized Li ion battery anode synthesized from scalable, high-throughput, Si nanoparticles deposition on a porous current collector. This novel electrode shows unprecedented high areal capacity at high current rates and surprisingly high cycling stability resulting from the one-off, uniform, locally protective SEI formation on the Si nanoparticle clusters throughout the electrode that maintains the structural integrity of the entire electrode.

(3), How to facilitate the Na ion transport kinetics in Si to realize reversible Na ion uptake?

The Na ion diffusion kinetics is known to be facilitated in smaller particles; and amorphous Si has been predicted theoretically to be more favourable for Na ion insertion [68, 69]. In Chapter 3.2 we study ultra-small Si nanoparticles (~ 20 nm) with a high fraction of amorphous Si content as the anode for Na ion batteries. It demonstrates that reversible Na ion uptake in Si nanoparticles is, to the best of our knowledge for the first time, realized in experiments with a considerable capacity, and an electrochemical de-/sodiation mechanism is proposed.

(4), How to accelerate the kinetics of Li/Na ion transport in MgH_2 to improve the reversible lithiation performance of MgH_2 and even to enable reversible Na ion uptake?

The catalysis of TiF_3 and nanosizing have been proven in gas phase experiments to significantly enhance the hydrogen sorption kinetics in MgH_2 [75, 76]. In Chapter 4, we investigate the Li and Na ion insertion behaviours in nanosized MgH_2 catalyzed by TiF_3. The lithiation performance improves remarkably compared to the previous reports on MgH_2 based anodes originating from the catalysis of TiF_3, electrical conduction aided by carbon

nanotubes, stable SEI formation, and improved Li ion transport in the porous electrode. Meanwhile, reversible Na ion storage in MgH_2 is also evidenced for the first time though the reversibility is poor and the reaction mechanism remains to be elucidated.

(5), How to improve the cycling stability of black phosphorus for Na ion storage?

Stable binary bulk compounds of C and P do not exist. Nevertheless the presence of stable C-P bonds in the red phosphorus – nanostructured carbon composites are observed [52, 77, 78]. Such interactions between phosphorus and carbon nanomaterials can thus aid to form a conductive C-P composite. Therefore, in Chapter 5.1 we synthesize nano-crystalline black phosphorus and a black phosphorus – super P carbon black nanocomposite through simple mechanical ball milling. The phosphorus and carbon interact actively with each other and form stable C-P bonds, but cannot form a thermodynamically stable binary compound. The black phosphorus – carbon black composite based Na ion battery anode achieves a high and stable cycling performance, which originates from the sustained electronic conduction throughout the electrode over cycling.

(6), How to improve the specific capacity and cycle life of Sn-P compounds based anodes for Na ion batteries?

Inspired by our work in Chapter 5.1 and the reports [78-80] that stable C-P interactions can be formed in both phosphorus – carbon and metal phosphide – carbon composites upon forming nanocomposites during high energy ball milling, we present in Chapter 5.2 a mixture of SnP_3 and graphene that is mechanically milled for an extended period. The presence of nanostructured carbon next to SnP_3 induces the precipitation of phosphorus from SnP_3 leading to the formation of thermodynamically more stable and electrically more conductive Sn_4P_3 that is bound with the carbon matrix via strong P-C interactions. The precipitated phosphorus turns into black phosphorus that is also electrically connected with the neighbouring carbon network. In this way, without any loss of capacity for Na ion storage, the electronic conduction between the active materials and the conducting carbon network will be maintained even during long-term cycling. The structure integrity of the electrode also remains thanks to the confinement of the mechanically strong graphene scaffold. Ultimately, the novel Sn_4P_3-black@graphene composite Na anode achieves a highly stable cycling performance and an ultra-long cycle life.

References

[1] F.M. Mulder, J. Renewable Sustainable Energy 6 (2014) 033105.

[2] D. Larcher, J.M. Tarascon, Nat. Chem. 7 (2014) 19.

[3] S. Chu, A. Majumdar, Nature 488 (2012) 294.

[4] M. Armand, J.M. Tarascon, Nature 451 (2008) 652.

[5] J.M. Tarascon, M. Armand, Nature 414 (2001) 359.

[6] B. Dunn, H. Kamath, J.-M. Tarascon, Science 334 (2011) 928.

[7] N. Nitta, F. Wu, J.T. Lee, G. Yushin, Mater. Today 18 (2015) 252-264.

[8] D. Deng, Energy Sci. Eng. 3 (2015) 385-418.

[9] A. Manthiram, ACS Cent. Sci. 3 (2017) 1063-1069.

[10] G.E. Blomgren, J. Electrochem. Soc. 164 (2017) A5019-A5025.

[11] J. Lu, L. Li, J.-B. Park, Y.-K. Sun, F. Wu, K. Amine, Chem. Rev. 114 (2014) 5611-5640.

[12] A. Manthiram, Y. Fu, S.-H. Chung, C. Zu, Y.-S. Su, Chem. Rev. 114 (2014) 11751-11787.

[13] A. Manthiram, X. Yu, S. Wang, Nat. Rev. Mater. 2 (2017) 16103.

[14] X.-B. Cheng, R. Zhang, C.-Z. Zhao, Q. Zhang, Chem. Rev. 117 (2017) 10403-10473.

[15] B.L. Ellis, L.F. Nazar, Curr. Opin. Solid State Mater. Sci. 16 (2012) 168-177.

[16] A. Eftekhari, Z. Jian, X. Ji, ACS Appl. Mater. Interfaces 9 (2017) 4404-4419.

[17] R. Mohtadi, F. Mizuno, Beilstein J. Nanotechnol. 5 (2014) 1291-1311.

[18] S.K. Das, S. Mahapatra, H. Lahan, J. Mater. Chem. A 5 (2017) 6347-6367.

[19] N. Nitta, G. Yushin, Part. Part. Syst. Charact. 31 (2014) 317-336.

[20] N. Spinner, L. Zhang, W.E. Mustain, J. Mater. Chem. A 2 (2014) 1627-1630.

[21] X. Cai, L. Lai, Z. Shen, J. Lin, J. Mater. Chem. A 5 (2017) 15423-15446.

[22] P. Sehrawat, C. Julien, S.S. Islam, Mater. Sci. Eng. B 213 (2016) 12-40.

[23] M.N. Obrovac, V.L. Chevrier, Chem. Rev. 114 (2014) 11444-11502.

[24] S.-H. Yu, S.H. Lee, D.J. Lee, Y.-E. Sung, T. Hyeon, Small 12 (2016) 2146-2172.

[25] A. Mauger, H. Xie, C.M. Julien, AIMS Mater. Sci. 3 (2016) 1054-1106.

[26] D. Lin, Y. Liu, Y. Cui, Nat. Nanotechnol. 12 (2017) 194-206.

[27] H. Kim, G. Jeong, Y.-U. Kim, J.-H. Kim, C.-M. Park, H.-J. Sohn, Chem. Soc. Rev. 42 (2013) 9011-9034.

[28] W. Xu, J. Wang, F. Ding, X. Chen, E. Nasybulin, Y. Zhang, J.-G. Zhang, Energy Environ. Sci. 7 (2014) 513-537.

[29] L.-L. Lu, Y. Zhang, Z. Pan, H.-B. Yao, F. Zhou, S.-H. Yu, Energy Storage Mater. 9 (2017) 31-38.

[30] K. Xie, W. Wei, K. Yuan, W. Lu, M. Guo, Z. Li, Q. Song, X. Liu, J.-G. Wang, C. Shen, ACS Appl. Mater. Interfaces 8 (2016) 26091-26097.

[31] H. Wu, Y. Cui, Nano Today 7 (2012) 414-429.

[32] P. Roy, S.K. Srivastava, J. Mater. Chem. A 3 (2015) 2454-2484.

[33] N. Mahmood, T. Tang, Y. Hou, Adv. Energy Mater. 6 (2016) 1600374.

[34] W. Qi, J.G. Shapter, Q. Wu, T. Yin, G. Gao, D. Cui, J. Mater. Chem. A 5 (2017) 19521-19540.

[35] M. Mazar Atabaki, R. Kovacevic, Electron. Mater. Lett. 9 (2013) 133-153.

[36] C. Kang, E. Cha, D.M. Patel, F.H. Wu, W. Choi, J. Carbon Res. 2 (2016) 1-26.

[37] A. Magasinski, P. Dixon, B. Hertzberg, A. Kvit, J. Ayala, G. Yushin, Nat. Mater. 9 (2010) 353-358.

[38] N. Liu, Z. Lu, J. Zhao, M.T. McDowell, H.-W. Lee, W. Zhao, Y. Cui, Nat. Nanotechnol. 9 (2014) 187-192.

[39] K. Kubota, S. Komaba, J. Electrochem. Soc. 162 (2015) A2538-A2550.

[40] J.-Y. Hwang, S.-T. Myung, Y.-K. Sun, Chem. Soc. Rev. 46 (2017) 3529-3614.

[41] L.P. Wang, L. Yu, X. Wang, M. Srinivasan, Z.J. Xu, J. Mater. Chem. A 3 (2015) 9353-9378.

[42] H. Kim, H. Kim, Z. Ding, M.H. Lee, K. Lim, G. Yoon, K. Kang, Adv. Energy Mater. 6 (2016) 1600943.

[43] W. Luo, F. Shen, C. Bommier, H. Zhu, X. Ji, L. Hu, Acc. Chem. Res. 49 (2016) 231-240.

[44] H. Kang, Y. Liu, K. Cao, Y. Zhao, L. Jiao, Y. Wang, H. Yuan, J. Mater. Chem. A 3 (2015) 17899-17913.

[45] D. Kumar, S.K. Rajouria, S.B. Kuhar, D.K. Kanchan, Solid State Ionics 312 (2017) 8-16.

[46] H. Yadegari, Q. Sun, X. Sun, Adv. Mater. 28 (2016) 7065-7093.

[47] Z.W. Seh, J. Sun, Y. Sun, Y. Cui, ACS Cent. Sci. 1 (2015) 449-455.

[48] R. Cao, K. Mishra, X. Li, J. Qian, M.H. Engelhard, M.E. Bowden, K.S. Han, K.T. Mueller, W.A. Henderson, J.-G. Zhang, Nano Energy 30 (2016) 825-830.

[49] A.P. Cohn, N. Muralidharan, R. Carter, K. Share, C.L. Pint, Nano Lett. 17 (2017) 1296-1301.

[50] Y. Zhao, L.V. Goncharova, A. Lushington, Q. Sun, H. Yadegari, B. Wang, W. Xiao, R. Li, X. Sun, Adv. Mater. 29 (2017) 1606663.

[51] F. Yang, H. Gao, J. Chen, Z. Guo, Small Methods 1 (2017) 1700216.

[52] J. Sun, H.-W. Lee, M. Pasta, Y. Sun, W. Liu, Y. Li, H.R. Lee, N. Liu, Y. Cui, Energy Storage Mater. 4 (2016) 130-136.

[53] W. Li, S. Hu, X. Luo, Z. Li, X. Sun, M. Li, F. Liu, Y. Yu, Adv. Mater. (2017) 1605820.

[54] B. Ruan, J. Wang, D. Shi, Y. Xu, S. Chou, H. Liu, J. Wang J. Mater. Chem. A 3 (2015) 19011-19017.

[55] T. Ramireddy, T. Xing, M.M. Rahman, Y. Chen, Q. Dutercq, D. Gunzelmann, A.M. Glushenkov, J. Mater. Chem. A 3 (2015) 5572-5584.

[56] G.L. Xu, Z. Chen, G.M. Zhong, Y. Liu, Y. Yang, T. Ma, Y. Ren, X. Zuo, X.H. Wu, X. Zhang, K. Amine, Nano Lett. 16 (2016) 3955-3965.

[57] Z. Li, J. Ding, D. Mitlin, Acc. Chem. Res. 48 (2015) 1657-1665.

[58] X. Fan, J. Mao, Y. Zhu, C. Luo, L. Suo, T. Gao, F. Han, S.-C. Liou, C. Wang, Adv. Energy Mater. 5 (2015) 1500174.

[59] L. Zheng, R.A. Dunlap, M.N. Obrovac, J. Electrochem. Soc. 163 (2016) A1188-A1191.

[60] J. Qian, Y. Xiong, Y. Cao, X. Ai, H. Yang, Nano Lett. 14 (2014) 1865-1869.

[61] J. Liu, P. Kopold, C. Wu, P.A. van Aken, J. Maier, Y. Yu, Energy Environ. Sci. 8 (2015) 3531-3538.

[62] K. Nobuhara, H. Nakayama, M. Nose, S. Nakanishi, H. Iba, J. Power Sources 243 (2013) 585-587.

[63] H. Hou, X. Qiu, W. Wei, Y. Zhang, X. Ji, Adv. Energy Mater. 7 (2017) 1602898.

[64] E. Irisarri, A. Ponrouch, M.R. Palacin, J. Electrochem. Soc. 162 (2015) A2476-A2482.

[65] H. Morito, T. Yamada, T. Ikeda, H. Yamane, J. Alloys Compd. 480 (2009) 723-726.

[66] V.V. Kulish, O.I. Malyi, M.-F. Ng, Z. Chen, S. Manzhos, P. Wu, Phys. Chem. Chem. Phys. 16 (2014) 4260-4267.

[67] I.M. Oleksandr, L.T. Teck, M. Sergei, Appl. Phys. Express 6 (2013) 027301.

[68] S.C. Jung, D.S. Jung, J.W. Choi, Y.-K. Han, J. Phys. Chem. Lett. 5 (2014) 1283-1288.

[69] F. Legrain, O.I. Malyi, S. Manzhos, Comput. Mater. Sci. 94 (2014) 214-217.

[70] F. Klein, B. Jache, A. Bhide, P. Adelhelm, Phys. Chem. Chem. Phys. 15 (2013) 15876-15887.

[71] M. Ramzan, S. Lebègue, R. Ahuja, Int. J. Hydrogen Energy 35 (2010) 10373-10376.

[72] W. Wenhui, Z. Qianfan, C. Yi, W. Enge, J. Phys. Condens. Matter 22 (2010) 415501.

[73] M.T. McDowell, Y. Cui, Adv. Energy Mater. 1 (2011) 894-900.

[74] E. Pollak, G. Salitra, V. Baranchugov, D. Aurbach, J. Phys. Chem. C 111 (2007) 11437-11444.

[75] A. Grzech, U. Lafont, P.C.M.M. Magusin, F.M. Mulder, J. Phys. Chem. C 116 (2012) 26027-26035.

[76] F.M. Mulder, S. Singh, S. Bolhuis, S.W.H. Eijt, J. Phys. Chem. C 116 (2012) 2001-2012.

[77] J. Song, Z. Yu, M.L. Gordin, X. Li, H. Peng, D. Wang, ACS Nano 9 (2015) 11933-11941.

[78] Z. Yu, J. Song, M.L. Gordin, R. Yi, D. Tang, D. Wang, Adv. Sci. 2 (2015) 1400020.

[79] W. Qi, H. Zhao, Y. Wu, H. Zeng, T. Tao, C. Chen, C. Kuang, S. Zhou, Y. Huang, Sci. Rep. 7 (2017) 43582.

[80] S.-O. Kim, A. Manthiram, Chem. Commun. 52 (2016) 4337-4340.

Chapter 2

Honeycomb-like Porous 3D Nickel Electrodeposition for Stable Li and Na Metal Anodes

This chapter is based on:

Abstract
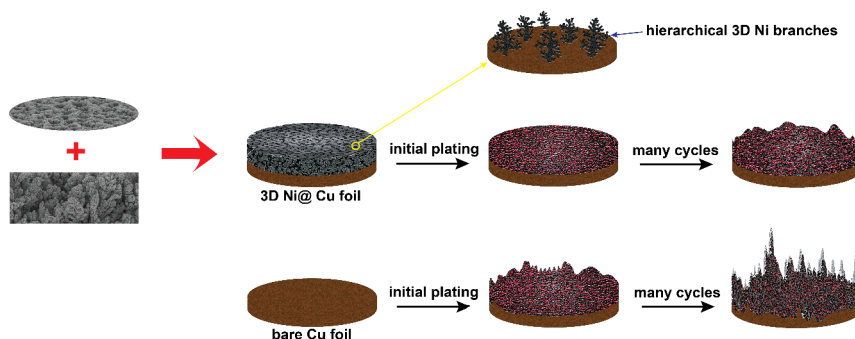
Metallic Li and Na have the highest theoretical anode capacity for Li/Na batteries, but the operational safety hazards stemming from uncontrolled growth of Li/Na dendrites and unstable electrode-electrolyte interfaces hinder their real-world applications. We herein introduce a facile and single-step route to honeycomb-like 3D porous Ni@Cu scaffolds via a hydrogen bubble dynamic template (HBDT) electrodeposition method. This current collector exhibits an outstanding cycling performance for Li/Na plating and stripping by accommodating the volume change in the porous host and suppressing the dendritic Li/Na growth. The beneficial role of $LiNO_3$ as an electrolyte additive in improving the mechanical integrity of solid electrolyte interface (SEI) and mechanistic insights into how the 3D porous structure facilitates Li/Na plating/stripping are comprehensively presented.

2.1 Introduction

Energy storage is one of the key issues of modern society, and the Li metal anode is regarded as the "Holy Grail" of energy storage systems which offers an extremely high theoretical capacity of 3860 mAh g^{-1} and superior electrochemical reduction potential of -3.04 V *vs.* standard hydrogen electrode. Because of these figures-of-merit, Li metal anodes were intensely investigated in the early 1980s but sooner the efforts were largely stymied due to observations where the dendritic growth of Li constituted serious safety hazards. But the ongoing research on high-capacity cathode materials based rechargeable battery systems, such as Li-O$_2$ and Li–S batteries, in order to cope with the increasing energy storage density demand, has recognized the imperative of revisiting this once-abandoned research [1-5]. Meanwhile, driven by the limited and uneven distribution of global lithium resources in addition to the higher abundance and lower cost of Na compared to Li, Na metal batteries have also attracted considerable research interest [6-8].

However, the Li dendrite formation that is fatal to battery operation has largely hindered the practical application of high-energy-density metal anodes. The formation of dendrites is caused by inhomogeneous distribution of current density on the metal anode and generation of charge concentration gradient at the electrolyte/electrode interface [2-4]. Dendrites are tapered branch-like structures that grow out from the anode during cycling [9], which gives rise to several plaguing issues [2-5], such as (1), serious safety concerns which arise when the dendrites penetrate through the separator and come into physical contact with the cathode, which leads to short-circuit of the batteries; (2), the virtually infinite volume expansion owing to its host-less nature that exerts a formidable stress on the solid electrolyte interphase (SEI) layer, leading to the mechanical instability of the SEI layer and low Coulombic efficiency, and when the porous dendritic Li growth occurs this aggravates the problem; (3), the creation of "dead Li" due to the unstable interfacial chemistry, which are basically electrically isolated Li metal generated after repetitive cycling resulting in the loss of active materials and thus the capacity decay. In short, the Li dendrite formation not only jeopardizes the safe operation of Li metal batteries, but also results in a low Coulombic efficiency and limited cycle life. With similar phenomena plaguing Na metal anodes, the progress towards Na metal batteries is also hampered.

In the pursuit of a dendrite-free Li metal anode, different methodologies have been developed to mitigate the above issues. There are many approaches undertaken including Li metal

electrodes with engineered surfaces [10-15] and structures [16-24], structured current collectors [25-38], modified electrolytes [39-47] and separators [48-50]. Among these, 3D conductive host matrices attract the most research interest [21-37] because they hold promise for acting as a scaffold that can accommodate the volume changes whilst ensuring a more homogeneous charge distribution, and thus warranting an improved cycling performance. This can be attributed to the large surface area, which, according to Sand's model, can delay the initial growth of dendrites [2, 5, 51, 52]. Of particular interest are metallic 3D scaffolds which are more promising because of their increased electronic conductivity and mechanical stability. Many 3D structured hosts have been explored including various 3D porous Cu substrates [27-30], free-standing Cu nanowires [31], lithiophilic Cu-Ni core-shell nanowires [24], and 3D graphene@Ni scaffold [32] to name a few. The Cu-Ni core-shell network was prepared through the solution-based synthesis of Cu nanowires onto which Ni was electrodeposited [24]. The 3D porous Cu substrates were prepared from routes e.g. H_2 reduced CuO nanocluster [27] or de-alloying of Cu-Zn alloy [30]. The free-standing Cu nanowires were prepared through a solvent evaporation assisted assembly technique [31]. These 3D porous metallic structures exhibit high mechanical strength and extremely high surface area, ensuring homogeneous charge distribution during Li plating/stripping and pronounced cycling stability of Li metal anode. However, most of these approaches are advanced, complex and costly, which largely limits their commercial viability. Although these efforts have yielded optimistic and encouraging results, with immense scope for further improvement, the commercial realization requires a facile, fast and scalable manufacturing method, which is still to be developed.

On the other hand, sodium metal battery research is still in its infancy but is rapidly evolving since the beginning of this decade. This is mainly motivated by the scarcity of Li and abundancy of Na and therefore the development of Na metal batteries could be a timely substitute to meet the electricity storage challenge.

Similar to the studies on Li metal anodes, research on metallic Na anodes also involve different approaches, including modified electrolytes [53-55], surface coating [56-58], 3D host structures [59] and engineered current collectors [60]. For instance, Luo *et al.* [59] developed carbonized wood with vertical channels as a scaffold for Na metal, which achieves a high cyclability over 500 h at 1.0 mA cm^{-2} but involves a relatively complex fabrication process. Cohn *et al.* [60] developed a nanocarbon nucleation layer on Al current collector

which exhibits a high cycling stability over 1000 plating/stripping cycles, but it was cycled at a low current rate (0.5 mA cm^{-2}) and with a low Na loading (0.25 mAh cm^{-2}).

In this work we introduce a honeycomb-like hierarchical 3D porous nickel electrodeposition on a plain Cu substrate, which is facilely synthesized with a one-step, rapid (~ 30 s) hydrogen bubble dynamic template (HBDT) electrodeposition method [61], fabricating high performance current collectors for both Li and Na metal anodes. The 3D Ni@Cu current collector exhibits excellent electrochemical performance for reversible Li plating/stripping (> 300 cycles at 0.5 mAh cm^{-2} and over 200 cycles at 1.0 mAh cm^{-2} cycling at 1.0 mA cm^{-2}); the effect of LiNO$_3$ additive in the electrolyte has been comprehensively studied and the Li plating mechanism in the porous host has been unveiled. These electrodes also show outstanding cycling performance of Na plating/stripping (stable over 240, 110 and 50 cycles for 0.5, 1.0 and 2.0 mAh cm^{-2} at 1.0 mA cm^{-2}). Thus, our newly-engineered current collectors may serve as an efficient solution to suppress the detrimental dendrite formation, enabling stable Li and Na metal anodes, as illustrated in Figure 2.1.

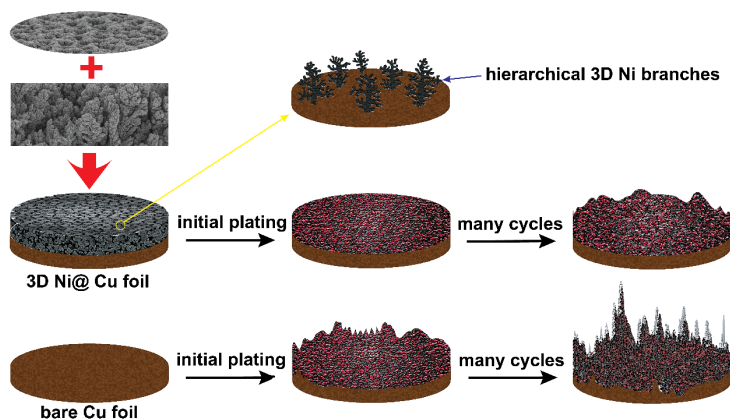**Figure 2.1 A schematic of the Li/Na plating process on a 3D Ni@Cu and a planar Cu foil.**

2.2 Methods

2.2.1 Current collector preparation

The 3D Ni@Cu current collector was prepared by galvanostatic electrochemical deposition using the HBDT method. A simple two-electrode setup (Figure S2.1) was used, in which the working electrode was a polished Cu foil and the counter electrode was a Ni foil. The base

electrolyte was prepared with 0.12 M $NiSO_4 \cdot 6/7H_2O$ and 1.5 M NH_4Cl dissolved in deionized water. The electrodeposition was carried out at room temperature and the size of the 3D Ni@Cu is 1 cm x 1 cm. The experimental setup and details of the electrodeposition process are provided in the Supporting Information (SI).

The 3D Ni@Cu is prepared by electrodepositing nickel at 3.0 A cm^{-2} for 30 s using polyethylene glycol (PEG) 4000 as a surfactant additive in the base electrolyte, and the concentration of PEG was fixed at 100 mg per 300 mL electrolyte solution. The as-synthesized 3D Ni@Cu samples were dried in a vacuum oven (60 ^{o}C) overnight before the electrochemical measurement.

To control the characteristics of the 3D nickel deposition layer, various deposition parameters can be adjusted including the concentration of PEG additive (Figure S2.2), electrodeposition duration (Figure S2.3) and current density (Figure S2.4) and protective post-deposition (Figure S2.5). We noted that a number of possibilities in other applications can be envisioned when appropriate modifications to the nickel electrodeposition have been made [61]. Detailed discussions are included in the SI.

2.2.2 Electrochemistry measurement

Li/Na ion symmetrical cells were assembled inside an Ar-filled glove box (O_2 and H_2O: < 0.1 ppm). The 3D Ni@Cu (or reference bare Cu foil) was used as the working electrode and a Li/Na metal foil worked as the counter electrode, and one piece of celgard® 2400 separator wetted with liquid electrolyte was inserted in between.

In the Li cells, 1 M bis(trifluoromethylsulfonyl)amine lithium salt (LiTFSI) dissolved in 1,2-dimethoxyethane (DME) and 1,3-Dioxolane (DOL) (DME : DOL = 1:1 in volume) with or without 1 wt. % $LiNO_3$ was utilized as the electrolyte. For Na cells, the working electrolyte was 1 M Sodium hexafluorophosphate ($NaPF_6$) in diethylene glycol dimethyl ether (DEGDME).

The galvanostatic electrochemical performance were evaluated using a Maccor 4600 battery cycler at room temperature. The cells were firstly cycled within 0.01 and 1.0 V at 50 µA cm^{-2} for five cycles to remove surface contaminations and to stabilize the interface, after which the electrochemical Li/Na plating and stripping was carried out. The plating process was terminated when a targeted capacity was reached; and a cut-off voltage of 0.5 V was applied

for Li/Na stripping process. Electrochemical impedance spectroscopy (EIS) was performed using a PGSTAT302N Autolab within a frequency range between 100 kHz and 0.1 Hz.

2.2.3 Characterization

X-ray diffraction (XRD) was carried out with a PANalytical X'Pert Pro PW3040/60 diffractometer with Cu K$_\alpha$ radiation and the working voltage and current were 45 kV and 40 mA, respectively. Micro-morphological images were taken with a JEOL JSM 6010F scanning electron microscope (SEM) working at 10 kV.

2.3 Results and discussions

2.3.1 Characterization on the current collector

XRD patterns of the 3D Ni@Cu (Figure 2.2a) demonstrate that, apart from the peaks from the underlying Cu foil, all the other diffraction peaks can be assigned to crystalline nickel, which is in line with the SEM based EDX (Energy-dispersive X-ray spectroscopy) analysis (Figure S2.6). Rietveld refinement on the XRD patterns (Figure S2.7 and Table S2.1) suggests that the average crystalline domain size of nickel is around 19.1 nm calculated based on Scherrer equation using a Lorentzian broadening.

Figure 2.2b – e shows that the as-synthesized 3D Ni@Cu appears as a honeycomb-like porous nickel layer on a Cu substrate. The walls of the honeycombs are made up of vertically-grown hierarchical nickel branches, of which the nickel particles are arrayed into a cauliflower-like nanosized spherical morphology. The thickness of the nickel deposition is about 30 μm, and it reaches ~ 50 μm when the nickel electrodeposition duration is doubled to 60 s (Figure S2.3).
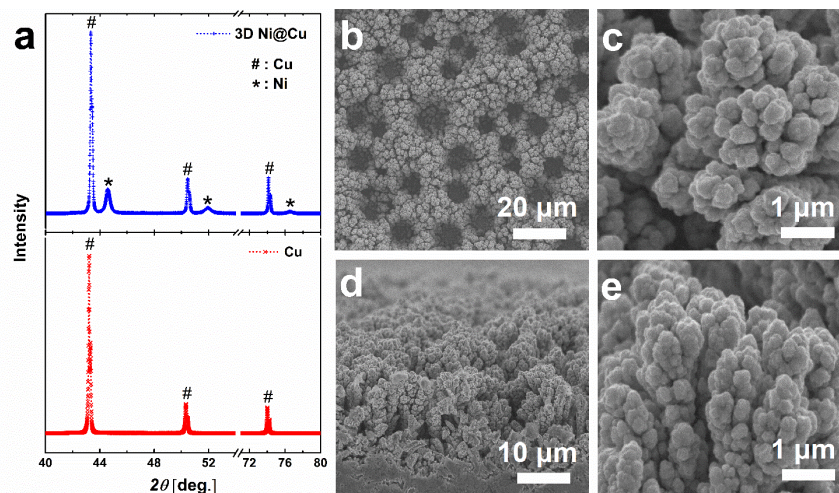
Figure 2.2 Characterization on the as-synthesized 3D Ni@Cu. (a), XRD patterns. (b) – (c), top view and (d) - (e), cross-sectional SEM images.

Polyethylene glycol (PEG) is a common additive in the electrodeposition process [62], which works as a surfactant to reduce the surface tension between the gas-liquid (H_2 - electrolyte) interface in order to inhibit the coalescence of the bubble resulting in reduced bubble sizes and thus smaller pore sizes in the electrodeposition layer. The overall porosity of the 3D nickel layer, calculated based on the Faradaic efficiency, amounts to 81.7 % (details in the SI). Such a high porosity is more favorable to accommodate the substantial volume expansion upon Li deposition. Moreover, the estimated volumetric and gravimetric capacities of a Li metal anode with such nickel scaffold is significantly higher than a commercial graphite anode (Table S2.2 & S2.3).

2.3.2 Li deposition

2.3.2.1 Electrochemical performance & effects of LiNO₃

Li-ion cells were assembled using either a planar Cu foil or 3D Ni@Cu as the working electrode and Li metal foil as the counter electrode; and the Coulombic efficiency and voltage hysteresis are measured as the benchmark to evaluate the reversible Li plating/stripping performance.

As shown in Figure 2.3a – b, cycling at 1.0 mA cm^{-2} in a LiTFSI (without LiNO₃) based electrolyte, the cycling performance is found to be stable with a Coulombic efficiency of > 96 % over 300 cycles for an areal capacity of 0.5 mAh cm^{-2}; and a high performance can be

retained for ~140 cycles when the capacity increases to 1.0 mAh cm^{-2}. When the Li deposition increases to 3.0 mAh cm^{-2}, the 3D Ni@Cu can still achieve a stable Coulombic efficiency above 97 % for ~ 60 cycles (Figure S2.8a – b).

It should be noted that the initial Coulombic efficiency (without LiNO$_3$ addition) is low (43.8 % and 45.4 % for a capacity of 0.5 and 1.0 mAh cm^{-2}, respectively), which may originate from the substantial irreversible SEI formation due to the porous nature of the nickel layer that presents a large surface area; and the limited intrinsic kinetics of Li-ion diffusion may also play a role. Figure S2.8c shows that the Coulombic efficiency improves when Li is stripped at a much lower current rate (0.1 mA cm^{-2}), indicating that the limited Li-ion diffusion kinetics accounts for the low Coulombic Efficiency during initial cycles. Nevertheless, the improvement in Coulombic efficiency is rather limited compared to the large amount of accumulated irreversible capacity during the previous cycles, suggesting that the unstable and thus continuous irreversible SEI formation plays a major role in the efficiency loss in the initial cycles. Figure S2.8c also shows that, after about 140 cycles, the Coulombic efficiency drops drastically but a short-circuit (i.e. infinite plating process) does not happen. When the current density of Li stripping is set at 0.1 mA cm^{-2} (at the 168th cycle) a large amount of Li can be stripped leading to an apparent high Coulombic efficiency of 159.3 %. It indicates that a substantial amount of lithium suffers from limited Li-ion transport over cycling possibly by the accumulated SEI layer on the electrode, but it is possible to recover partially.

To suppress the SEI formation and to enhance the mechanical stability of the SEI layer, LiNO$_3$ has been commonly applied as an additive in the electrolyte, which has been previously employed in Li-S systems to produce a stable interface layer on the Li metal in order to inhibit the problematic polysulfide shuttle [63, 64]. The positive effects of LiNO$_3$ as well as other nitrates such as KNO$_3$ in suppressing the dendritic Li deposition have also been reported [65]. In the initial cycle, LiNO$_3$ decomposes and reacts with Li to form a uniform and stable SEI film on the Li metal surface and prevents further SEI growth. From Figure 2.3c it can be observed that, when 1 wt. % LiNO$_3$ is added into the electrolyte, the initial Coulombic efficiency increases to 92.9 % and remains above 96 % over 200 cycles. Figure S2.8d shows that, when cycling at a high current density of 5.0 mA cm^{-2}, the Coulombic efficiency is practically stable over 90 cycles. Compared with the performance in an electrolyte without LiNO$_3$, the remarkable improvement in both Coulombic efficiency and cycling stability points to the formation of a more stable SEI layer upon LiNO$_3$ addition.

The positive effects of $LiNO_3$ addition in the electrolyte is also supported by the galvanostatic voltage profiles (Figure 2.3d – f) and EIS spectra (Figure 2.3g – i). It is observed that the charge transfer resistance of the bare Cu electrode grows gradually over cycling and so does the voltage hysteresis between charge and discharge. In comparison, the 3D Ni@Cu electrode exhibits a much lower charge transfer resistance but with an increasing voltage hysteresis (without $LiNO_3$ addition). The gradual increase of resistance for both cases roots in the continuously growing SEI layer. However, when $LiNO_3$ is added, the initial resistance during Li plating is higher than that using a $LiNO_3$-free electrolyte due to the presence a compact, non-conductive SEI layer and therefore a higher nucleation energy barrier, but the resistance remains stable over cycling. The voltage hysteresis halts at ~ 120 mV after 100 cycles (compared with 179 mV after 100 cycles in a $LiNO_3$-absent electrolyte) illustrating that the SEI stabilizes after the first cycle and further growth is negligible. Moreover, when the cycling rate increases from 1.0 to 5.0 mA cm^{-2}, the voltage hysteresis between charge and discharge merely increases by ~ 50 mV (Figure S2.8e) indicating that the DC resistance of the $LiNO_3$ based SEI layer is basically low, which is also consistent with the previous report [65].

To further understand the role of the $LiNO_3$ during cycling, the evolution of the morphology and chemical composition of the SEI layer is studied with SEM, XRD and X-ray photoelectron spectroscopy (XPS) techniques. SEM images of the 3D nickel electrodes (Figure 2.3j – p) reveal that, cycling in an electrolyte without $LiNO_3$, the surface of the nickel layer has been covered by a distinct SEI stratum after merely 5 cycles which thickens over cycling, and consequently, the resistance and overpotential increases. In comparison, the SEI layer on the electrode cycled in a 1 wt.% $LiNO_3$-LiTFSI based electrolyte is hardly noticeable after 5 cycles and only a thin and fluffy interphase layer is formed after 50 cycles suggesting the significant suppression of SEI growth and hence a stabilized low resistance due to the presence of a stable SEI layer. This is in good agreement with the voltage and EIS analysis. XRD patterns (Figure S2.9) show that no peaks belonging to the SEI layer can be observed, indicating that it is amorphous; meanwhile, the peak intensity of the nickel phase reduces after cycling owing to the coverage of the SEI layer, and the reduction is more pronounced using a $LiNO_3$-free electrolyte. It reveals that the $LiNO_3$ has effectively controlled the SEI formation resulting in a much thinner SEI layer, which is consistent with the micrographs. XPS spectra (Figure S2.10) indicate that the SEI layer formed in a pure LiTFSI based

electrolyte consists of Li_2CO_3, Li_2O, $R_3COLi–(CH_2)–$, $R_3CO–R$, Li_xSO_y, LiF and Li_2S_x, etc. [66-69] originating from the decomposition of LiTFSI salt and DME/DOL solvents. In comparison, the SEI grown in a 1 wt.% $LiNO_3$-LiTFSI based electrolyte contains $R_3CO–R$, Li_xNO_y, Li_xSO_y and LiF, etc. [66-69], and remarkably no Li_2CO_3, Li_2O, $R_3COLi–(CH_2)–$ and Li_2S_x is observed. It also verifies the suppressed SEI formation due to the presence of $LiNO_3$ which first decomposes and forms a stable and compact Li_xNO_y based layer and ultimately inhibits the continuous progression of SEI growth.

Based on the observations in Figure 2.3 and Figure S2.8 – S2.10, we can conclude that the failure mechanism of the 3D Ni@Cu current collector for Li plating/stripping roots in the following aspects: (i), when a $LiNO_3$-free electrolyte is used, the unstable and thus continuous SEI growth results in a low Coulombic efficiency and the accumulation of non-conductive interphase that increases the internal resistance and overpotential. (ii), using a $LiNO_3$-containing electrolyte, the Coulombic efficiency has been significantly promoted (> 96% over 200 cycles) but still indicates that a minor fraction of the deposited Li is not recovered during stripping. For both (i) and (ii), the limited Coulombic efficiency may originate from the long Li diffusion pathway in the nanopores of the nickel host, apart from the finite intrinsic Li diffusion kinetics. This problem will be aggravated when a higher cycling current density and/or a higher Li deposition capacity is applied. (iii), the mechanical strength of the nickel structure appears to be limited over repetitive Li plating and stripping (Figure 2.3p), which needs to be improved to maintain the structural integrity of the electrode to prolong its cycle life.
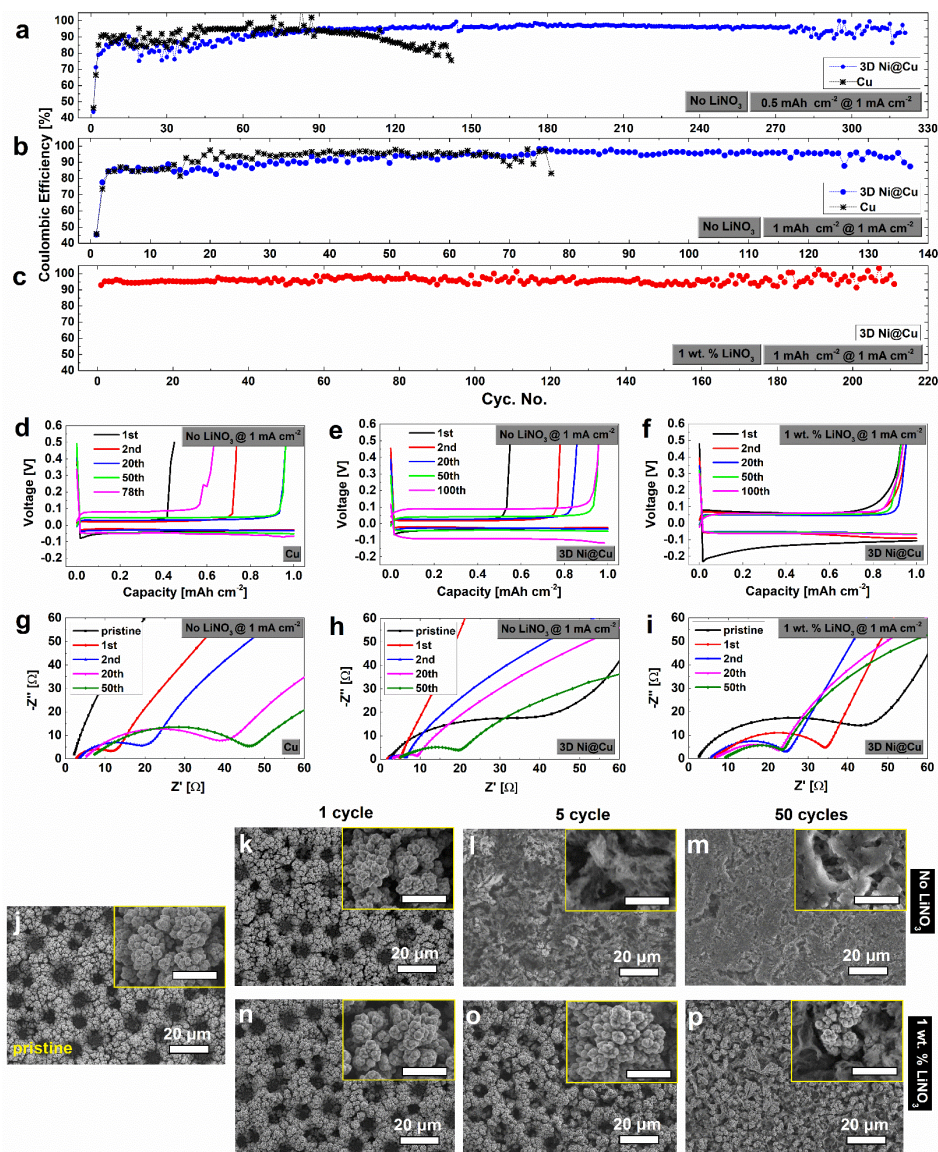
Figure 2.3 Performance of the planar Cu and 3D Ni@Cu for reversible Li deposition and the morphological evolution of 3D Ni@Cu during cycling. (a) – (c), Cycling performance, (d) – (f), Cycling voltage profiles and (g) – (i), EIS spectra of bare Cu and 3D Ni@Cu electrode for Li plating and stripping cycling at 1 mA cm^{-2}. Here the capacity of Li deposition is fixed at 0.5 mAh cm^{-2} in Figure (a) and 1.0 mAh cm^{-2} in all the other figures. (j) – (p), SEM images of the 3D Ni@Cu electrodes: (j), pristine; (k) – (m), after 1, 5 and 50 cycles in the LiNO$_3$-free electrolyte; (n) – (p), after 1, 5 and 50 cycles in the LiNO$_3$-containing electrolyte. In Figure (k) – (p), the capacity is fixed at 1.0 mAh cm^{-2} and the applied current density is fixed at 1.0 mA cm^{-2}. Length of the scale bars in the insets: 500 nm.

2.3.2.2 Li plating mechanism

To elucidate the mechanism of Li plating in the 3D nickel structure, micro-morphologies of the Li deposits under varying current densities and with different capacities were *ex-situ* imaged, as shown in Figure 2.4 and Figure S2.11.

Depositing a fixed amount of Li (0.5 mAh cm^{-2}) at various current rates, the increasing current density results in reduced Li nuclei sizes together with an increased areal nuclei number density (Figure 2.4b – f). At a low current rate of 0.05 mAh cm^{-2}, the Li deposits appear as irregular-shaped clusters with a size in the range of tens of microns, likely due to the fusing of multiple Li nuclei at such low current density. When the current rate increases from 0.2 to 1.0 mA cm^{-2}, the size of Li nuclei reduces (average nuclei size of ~10, ~ 8 and ~ 6 μm at 0.2, 0.5 and 1.0 mA cm^{-2}, respectively) but the areal number density of the nuclei grows gradually; meanwhile, the nuclei size distribution becomes increasingly more homogeneous and the nuclei shape appears increasingly more spherical. These observations are supported by the inverse relationship between the critical nuclei radius and the overpotential of Li deposition [70] and are also in agreement with the Li nuclei growth mechanism reported in ref. [71]. When the current density further increases to 2.0 mA cm^{-2}, no further reduction in the Li nuclei size is observed; whereas most of the Li nuclei turn into open hollow spheres, and as a result, the nuclei number density grows and the mass density drops, which may imply that the growth of the Li nuclei initiates with a thin toroid and progresses inward. It should also be noted that the Li deposits grow homogeneously on the nickel honeycomb skeleton within the 3D porous host which can be attributed to the homogeneous ionic charge distribution and low current density on the porous nickel current collector. This uniform Li nucleation benefits from the presence of numerous conductive nickel tips on the honeycomb-like skeleton, all of which function as nucleation sites and charge centres for Li deposition and thus the charge localization in just one or few points has been avoided. As a result, Li nucleates and grows evenly on the nickel host and fills the pores of the 3D porous current collector, and can be expected to form a relatively even Li surface.

To further investigate the Li nucleation and growth mechanism in the 3D nickel host, various amounts of Li were deposited at a current density of 1.0 mA cm^{-2}, as shown in Figure 2.4e & g – k. From 0.2 to 0.5 mAh cm^{-2}, the Li nuclei appear as spheres with a size of around 5 μm, and the areal number density of Li nuclei rises when the capacity increases. It is also observed that the initial Li nucleation mostly takes place in the pores of the 3D nickel structure rather

than on the top surface of the nickel layer. This may be attributed to: (i), the fact that the initial nucleation is not limited by any Li^+ ion depletion of the electrolyte, and (ii), the nickel walls of the honeycomb are multi-branched exhibiting numerous nickel tips in the pores of the 3D nickel host and limited amount of nickel tips on the top surface of the nickel layer, therefore, there are many more sites for Li nucleation in the pores than on top of the nickel layer. After nucleation the subsequent Li plating continues predominantly at all these nuclei in the pores. When the capacity of Li deposition grows to ≥ 1.0 mAh cm^{-2}, the size of Li nuclei grows, because after the initial Li nucleation, it is more energetically favourable for the following Li plating to take place on the initial Li nuclei rather than on the nickel skeleton. It is also observed that the Li nuclei become at larger sizes surface-cracked, possibly induced by the rising internal stress with the increasing capacity. With further Li deposition above 3.0 mAh cm^{-2}, the nuclei fill up the honeycomb pores and may even grow out of the nickel structure and fuse with their neighbouring nuclei. The entire nickel layer is homogeneously covered by Li deposits when the areal capacity reaches about 5.0 mAh cm^{-2}.

Based on the analysis above, an outline of the Li deposition progression mechanism is illustrated by Figure 2.4l. In comparison, the Li grown on a planar Cu foil (Figure S2.12) shows discrete island-like deposits, which is highly inhomogeneous, establishing the significantly positive effects of the 3D nickel structure for the suppression of Li dendrites. The dendritic Li growth on a planar Cu current collector occurs because the initial Li deposition nuclei function as the charge centres for additional Li nucleation and thus the subsequent Li deposition takes place on these sharp edges and induces the dendritic Li growth.
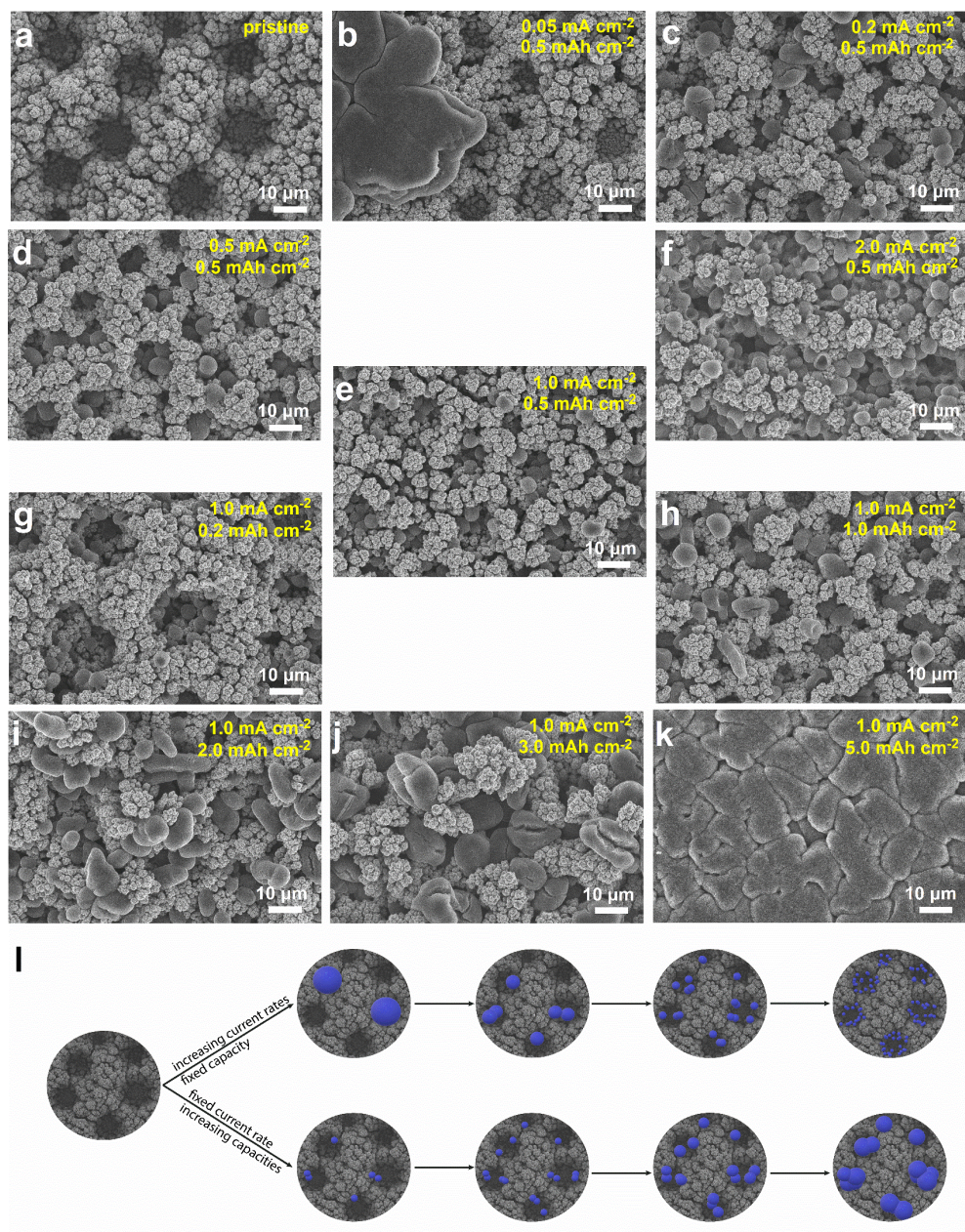
Figure 2.4 Mechanisms of Li plating in the 3D Ni@Cu structure in a LiTFSI based electrolyte with 1 wt. % LiNO₃. (a) – (f), SEM images of the 3D Ni@Cu with 0.5 mAh cm^{-2} Li deposited under varying current densities from 0.05 to 2.0 mA cm^{-2}; (e) and (g) – (k), micrographs of the 3D Ni@Cu with different amounts of Li deposits cycling at 1.0 mA cm^{-2}. (l), a schematic illustrating the Li deposit growing mechanism in the 3D Ni@Cu based on the micrographs in Figure (a) – (k).

2.3.3 Na plating performance

The promising cycling performance of 3D Ni@Cu on Li deposition/dissolution encouraged us to explore its potential for the reversible Na plating and stripping, which was characterized using 3D Ni@Cu as the working electrode and Na metal as the counter electrode.

Figure 2.5a shows that, generally, compared to bare Cu foil, 3D Ni@Cu exhibits a much improved cycling stability and lifespan for Na plating/stripping. The porous conductive current collector achieves an exceptional cycling stability with a Coulombic efficiency of > 99.5 % for over 220 cycles cycling at a current density of 1.0 mA cm^{-2} for a capacity of 0.5 mAh cm^{-2}; when the Na deposition capacity increases to 1.0 and 2.0 mAh cm^{-2}, 3D Ni@Cu can still obtain a stable cycling performance for ~ 110 and 50 cycles, respectively.

Figure 2.5b – c shows the galvanostatic voltage profiles of the bare Cu and 3D Ni@Cu for Na deposition and dissolution. It shows that the voltage hysteresis between charge and discharge grows continuously over cycling with a planar Cu current collector (~ 11 and 23 mV at 1st and 100th cycle, respectively); whereas 3D Ni@Cu exhibits stable overpotential (~ 17 mV) after the initial cycle. The initial voltage hysteresis of the 3D Ni@Cu is relatively higher, which is probably associated with a higher activation energy barrier of the porous nickel skeleton for Na nucleation owing to higher thermodynamic costs of forming a critical cluster of Na atoms on the nanosized nickel tips compared to a smooth Cu foil.

Morphological evolution of initial Na deposition on the 3D nickel current collector (Figure 2.5d – f) reveals the Na plating mechanism in the porous nickel host. It illustrates that the Na deposits initially grow in some of the vertical pores of the honeycomb structure and gradually progress horizontally when the capacity increases; vertical growth (thickening) of the Na deposition layer is evidenced as well. Fusing of Na deposits takes place when the Na deposits evolve and meet the neighbouring ones, and, eventually, a flat-surface Na anode (i.e. dendrite-free deposition) is obtained. The Na plating occurs uniformly throughout the current collector area and is superior to the inhomogeneous Na growth on a planar Cu foil (Figure S2.13), thanks to the beneficial nano/micro-morphological features of these 3D conductive structures enabling non-dendritic Li deposition as explained above. It is interesting that the sodium deposition appears to be even more uniform than Li deposits at a current density of 1.0 mA cm^{-2}, which can be attributed to the advantageous NaPF$_6$/DEGDME electrolyte that has been reported to help to suppress the dendritic Na growth [53].
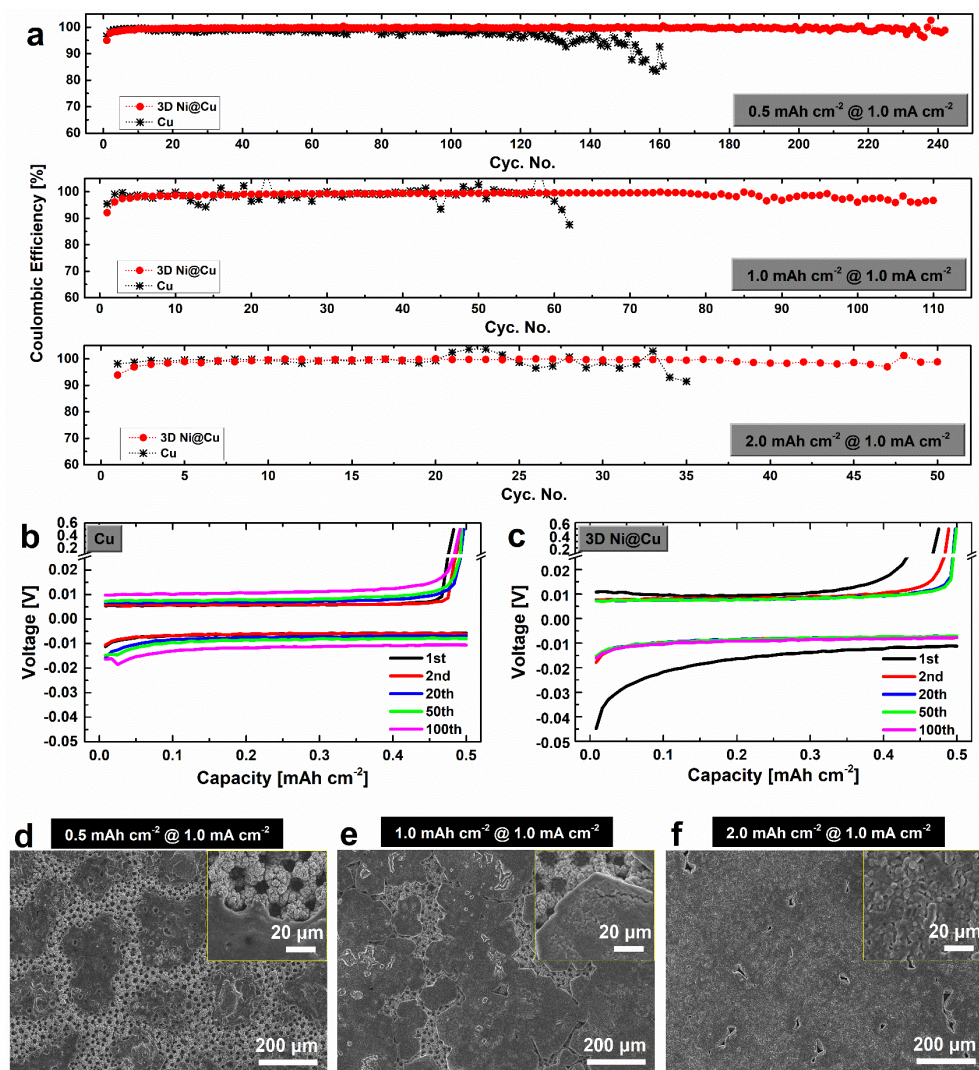
Figure 2.5 Performance of the 3D Ni@Cu for Na plating/stripping at 1.0 mA cm⁻². (a), cycling performance with different areal capacities; (b), voltage profiles of the planar Cu electrode; (c), voltage response of 3D Ni@Cu electrode. (d) – (f), Morphologies of various amounts of Na deposited on 3D Ni@Cu.

2.4 Conclusions

We presented a facile one-step and low-cost synthesis of 3D porous current collectors for stable Li/Na metal anodes. The 3D scaffolds developed here are reminiscent of a honeycomb, with hierarchically electrodeposited nickel nanoparticles building micro walls on a copper

substrate. Although the presence of nickel in the 3D Ni@Cu current collector replaces some volume, it will not reduce the volumetric energy density of the electrode when compared to a dendritic porous Li deposition layer. This is because it facilitates remarkably homogeneous Li deposition fully filling its well defined porous structure that acts as a scaffold, leading to a highly stable cycling performance. Addition of $LiNO_3$ to the electrolyte can effectively suppress the SEI formation and improve the Coulombic efficiency, and thus prolongs the lifespan of battery cycling. These current collectors also offer excellent cycling performance of Na plating/stripping with higher Columbic efficiently and stability. Moreover, this straight-forward process of 3D porous Ni@Cu scaffolds can in principle be extended to other application domains by adjusting the electrodeposition parameters. Therefore, considering the ease of our method for fabricating 3D current collectors, new insights into Li/Na plating-stripping and role of electrolyte additive promoting a robust solid electrolyte interface, our results provide promising solutions to expedite the implementation of Li/Na metal based high energy density batteries.

References

[1] H. Kim, G. Jeong, Y.-U. Kim, J.-H. Kim, C.-M. Park, H.-J. Sohn, Chem. Soc. Rev. 42 (2013) 9011-9034.

[2] X.-B. Cheng, R. Zhang, C.-Z. Zhao, Q. Zhang, Chem. Rev. 117 (2017) 10403–10473 .

[3] D. Lin, Y. Liu, Y. Cui, Nat. Nanotechnol. 12 (2017) 194-206.

[4] J. Lang, L. Qi, Y. Luo, H. Wu, Energy Storage Mater. 7 (2017) 115-129.

[5] W. Xu, J. Wang, F. Ding, X. Chen, E. Nasybulin, Y. Zhang, J.-G. Zhang, Energy Environ. Sci. 7 (2014) 513-537.

[6] B.L. Ellis, L.F. Nazar, Curr. Opin. Solid State Mater. Sci. 16 (2012) 168-177.

[7] W. Luo, L. Hu, ACS Cent. Sci. 1 (2015) 420-422.

[8] J.-Y. Hwang, S.-T. Myung, Y.-K. Sun, Chem. Soc. Rev. 46 (2017) 3529-3614.

[9] K.N. Wood, M. Noked, N.P. Dasgupta, ACS Energy Lett. 2 (2017) 664-672.

[10] K. Liu, A. Pei, H.R. Lee, B. Kong, N. Liu, D. Lin, Y. Liu, C. Liu, P.-c. Hsu, Z. Bao, Y. Cui, J. Am. Chem. Soc. 139 (2017) 4815-4820.

[11] G. Zheng, S.W. Lee, Z. Liang, H.-W. Lee, K. Yan, H. Yao, H. Wang, W. Li, S. Chu, Y. Cui, Nat. Nanotechnol. 9 (2014) 618-623.

[12] A.C. Kozen, C.-F. Lin, O. Zhao, S.B. Lee, G.W. Rubloff, M. Noked, Chem. Mater. 29 (2017) 6298-6307.

[13] J.-S. Kim, D.W. Kim, H.T. Jung, J.W. Choi, Chem. Mater. 27 (2015) 2780-2787.

[14] X. Liang, Q. Pang, I.R. Kochetkov, M.S. Sempere, H. Huang, X. Sun, L.F. Nazar, Nat. Energy 6 (2017) 17119.

[15] L. Wang, L. Zhang, Q. Wang, W. Li, B. Wu, W. Jia, Y. Wang, J. Li, H. Li, Energy Storage Mater. (2017).

[16] Y. Zhang, J. Qian, W. Xu, S.M. Russell, X. Chen, E. Nasybulin, P. Bhattacharya, M.H. Engelhard, D. Mei, R. Cao, F. Ding, A.V. Cresce, K. Xu, J.-G. Zhang, Nano Lett. 14 (2014) 6889-6896.

[17] J. Park, J. Jeong, Y. Lee, M. Oh, M.-H. Ryou, Y.M. Lee, Adv. Mater. Interfaces 3 (2016) 1600140.

[18] D. Lin, Y. Liu, Z. Liang, H.-W. Lee, J. Sun, H. Wang, K. Yan, J. Xie, Y. Cui, Nat. Nanotechnol. 11 (2016) 626-632.

[19] B. Li, D. Zhang, Y. Liu, Y. Yu, S. Li, S. Yang, Nano Energy 39 (2017) 654-661.

[20] X.-B. Cheng, C. Yan, H.-J. Peng, J.-Q. Huang, S.-T. Yang, Q. Zhang, Energy Storage Mater. (2017).

[21] Y. Liu, D. Lin, Z. Liang, J. Zhao, K. Yan, Y. Cui, Nat. Commun. 7 (2016) 10992.

[22] C. Jin, O. Sheng, J. Luo, H. Yuan, C. Fang, W. Zhang, H. Huang, Y. Gan, Y. Xia, C. Liang, J. Zhang, X. Tao, Nano Energy 37 (2017) 177-186.

[23] Z. Liang, D. Lin, J. Zhao, Z. Lu, Y. Liu, C. Liu, Y. Lu, H. Wang, K. Yan, X. Tao, Y. Cui, Proc. Natl. Acad. Sci. 113 (2016) 2862-2867.

[24] L.-L. Lu, Y. Zhang, Z. Pan, H.-B. Yao, F. Zhou, S.-H. Yu, Energy Storage Mater. 9 (2017) 31-38.

[25] A. Zhang, X. Fang, C. Shen, Y. Liu, C. Zhou, Nano Res. 9 (2016) 3428-3436.

[26] Y. Zhang, B. Liu, E. Hitz, W. Luo, Y. Yao, Y. Li, J. Dai, C. Chen, Y. Wang, C. Yang, H. Li, L. Hu, Nano Res. 10 (2017) 1356-1365.

[27] Z. Zhang, X. Xu, S. Wang, Z. Peng, M. Liu, J. Zhou, C. Shen, D. Wang, ACS Appl. Mater. Interfaces 8 (2016) 26801-26808.

[28] Q. Li, S. Zhu, Y. Lu, Adv. Funct. Mater. 27 (2017) 1606422.

[29] C.-P. Yang, Y.-X. Yin, S.-F. Zhang, N.-W. Li, Y.-G. Guo, Nat. Commun. 6 (2015) 8058.

[30] Q. Yun, Y.-B. He, W. Lv, Y. Zhao, B. Li, F. Kang, Q.-H. Yang, Adv. Mater. 28 (2016) 6932-6939.

[31] L.-L. Lu, J. Ge, J.-N. Yang, S.-M. Chen, H.-B. Yao, F. Zhou, S.-H. Yu, Nano Lett. 16 (2016) 4431-4437.

[32] K. Xie, W. Wei, K. Yuan, W. Lu, M. Guo, Z. Li, Q. Song, X. Liu, J.-G. Wang, C. Shen, ACS Appl. Mater. Interfaces 8 (2016) 26091-26097.

[33] H.-K. Kang, S.-G. Woo, J.-H. Kim, J.-S. Yu, S.-R. Lee, Y.-J. Kim, ACS Appl. Mater. Interfaces 8 (2016) 26895-26901.

[34] X.-B. Cheng, T.-Z. Hou, R. Zhang, H.-J. Peng, C.-Z. Zhao, J.-Q. Huang, Q. Zhang, Adv. Mater. 28 (2016) 2888-2895.

[35] W. Liu, D. Lin, A. Pei, Y. Cui, J. Am. Chem. Soc. 138 (2016) 15443-15450.

[36] S.-S. Chi, Y. Liu, W.-L. Song, L.-Z. Fan, Q. Zhang, Adv. Funct. Mater. 27 (2017) 1700348.

[37] R. Zhang, X.-R. Chen, X. Chen, X.-B. Cheng, X.-Q. Zhang, C. Yan, Q. Zhang, Angew. Chem. Int. Ed. 56 (2017) 7764-7768.

[38] S. Matsuda, Y. Kubo, K. Uosaki, S. Nakanishi, ACS Energy Lett. 2 (2017) 924-929.

[39] M.D. Tikekar, S. Choudhury, Z. Tu, L.A. Archer, Nat. Energy 1 (2016) 16114.

[40] R. Miao, J. Yang, X. Feng, H. Jia, J. Wang, Y. Nuli, J. Power Sources 271 (2014) 291-297.

[41] J. Guo, Z. Wen, M. Wu, J. Jin, Y. Liu, Electrochem. Commun. 51 (2015) 59-63.

[42] E. Markevich, G. Salitra, F. Chesneau, M. Schmidt, D. Aurbach, ACS Energy Lett. 2 (2017) 1321-1326.

[43] W. Li, H. Yao, K. Yan, G. Zheng, Z. Liang, Y.-M. Chiang, Y. Cui, Nat. Commun. 6 (2015) 7436.

[44] J. Qian, W.A. Henderson, W. Xu, P. Bhattacharya, M. Engelhard, O. Borodin, J.-G. Zhang, Nat. Commun. 6 (2015) 6362.

[45] J. Shim, H.J. Kim, B.G. Kim, Y.S. Kim, D.-G. Kim, J.-C. Lee, Energy Environ. Sci. 10 (2017), 1911-1916.

[46] X.-Q. Zhang, X.-B. Cheng, X. Chen, C. Yan, Q. Zhang, Adv. Funct. Mater. 27 (2017) 1605989.

[47] C.-Z. Zhao, X.-B. Cheng, R. Zhang, H.-J. Peng, J.-Q. Huang, R. Ran, Z.-H. Huang, Energy Storage Mater. 3 (2016) 77-84.

[48] K. Liu, D. Zhuo, H.-W. Lee, W. Liu, D. Lin, Y. Lu, Y. Cui, Adv. Mater. 29 (2017) 1603987.

[49] W.-K. Shin, A.G. Kannan, D.-W. Kim, ACS Appl. Mater. Interfaces 7 (2015) 23700-23707.

[50] Y. Liu, Q. Liu, L. Xin, Y. Liu, F. Yang, E.A. Stach, J. Xie, Nat. Energy 2 (2017) 17083.

[51] J.-N. Chazalviel, Phys. Rev. A 42 (1990) 7355-7367.

[52] C. Brissot, M. Rosso, J.-N. Chazalviel, S. Lascaud, J. Power Sources 81 (1999) 925-929.

[53] Z.W. Seh, J. Sun, Y. Sun, Y. Cui, ACS Cent. Sci. 1 (2015) 449-455.

[54] R. Cao, K. Mishra, X. Li, J. Qian, M.H. Engelhard, M.E. Bowden, K.S. Han, K.T. Mueller, W.A. Henderson, J.-G. Zhang, Nano Energy 30 (2016) 825-830.

[55] J. Song, G. Jeong, A.-J. Lee, J.H. Park, H. Kim, Y.-J. Kim, ACS Appl. Mater. Interfaces 7 (2015) 27206-27214.

[56] W. Luo, C.-F. Lin, O. Zhao, M. Noked, Y. Zhang, G.W. Rubloff, L. Hu, Adv. Energy Mater. 7 (2017) 1601526.

[57] Y. Zhao, L.V. Goncharova, A. Lushington, Q. Sun, H. Yadegari, B. Wang, W. Xiao, R. Li, X. Sun, Adv. Mater. 29 (2017) 1606663.

[58] Y.-J. Kim, H. Lee, H. Noh, J. Lee, S. Kim, M.-H. Ryou, Y.M. Lee, H.-T. Kim, ACS Appl. Mater. Interfaces 9 (2017) 6000-6006.

[59] W. Luo, Y. Zhang, S. Xu, J. Dai, E. Hitz, Y. Li, C. Yang, C. Chen, B. Liu, L. Hu, Nano Lett. 17 (2017) 3792-3797.

[60] A.P. Cohn, N. Muralidharan, R. Carter, K. Share, C.L. Pint, Nano Lett. 17 (2017) 1296-1301.

[61] B.J. Plowman, L.A. Jones, S.K. Bhargava, Chem. Commun. 51 (2015) 4331-4346.

[62] J.-H. Kim, R.-H. Kim, H.-S. Kwon, Electrochem. Commun. 10 (2008) 1148-1151.

[63] S.S. Zhang, Electrochim. Acta 70 (2012) 344-348.

[64] S.S. Zhang, J. Power Sources 322 (2016) 99-105.

[65] W. Jia, C. Fan, L. Wang, Q. Wang, M. Zhao, A. Zhou, J. Li, ACS Appl. Mater. Interfaces 8 (2016) 15399–15405.

[66] X.-B. Cheng, R. Zhang, C.-Z. Zhao, F. Wei, J.-G. Zhang, Q. Zhang, Adv. Sci. 3 (2016) 1500213.

[67] M.R. Busche, T. Drossel, T. Leichtweiss, D.A. Weber, M. Falk, M. Schneider, M.-L. Reich, H. Sommer, P. Adelhelm, J. Janek, Nat. Chem. 8 (2016) 426-434.

[68] R. Dedryvère, S. Leroy, H. Martinez, F. Blanchard, D. Lemordant, D. Gonbeau, J. Phys. Chem. B 110 (2006) 12986-12992.

[69] D. Aurbach, E. Pollak, R. Elazari, G. Salitra, C.S. Kelley, J. Affinito, J. Electrochem. Soc. 156 (2009) A694-A702.

[70] D.R. Ely, R.E. García, J. Electrochem. Soc. 160 (2013) A662-A668.

[71] A. Pei, G. Zheng, F. Shi, Y. Li, Y. Cui, Nano Lett. 17 (2017) 1132-1139.

Supporting Information for Chapter 2

S2.1 Fabrication of 3D Ni@Cu

Figure S2.1 shows the two-electrode setup used in this work, in which the working electrode was a polished Cu foil of 5 cm^2, of which an area of 1 cm x 1 cm was exposed to the electrolyte. The remaining part of the foil was insulated with tape. The counter electrode was a Ni foil of larger area (10 cm^2). The electrodes were supported by sticking it to a glass plate and were kept at a fixed distance of 2 cm. The base electrolyte was prepared with 0.12 M NiSO$_4 \cdot$6/7H$_2$O and 1.5 M NH$_4$Cl dissolved in deionized water. Polyethylene glycol (PEG) 4000 was added in the base electrolyte as a surfactant additive, and the concentration of PEG varied from 0 to 500 mg per 300 mL electrolyte solution. Both electrodes were thoroughly washed with ethanol and deionized water before the electrodeposition.
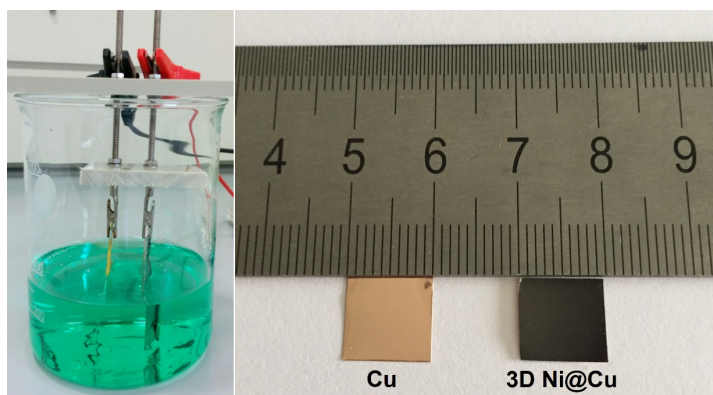
Figure S2.1 Photos of the experimental setup of electrodeposition (left) and electrodeposited 3D Ni@Cu sample (right).

S2.2 Further investigations on the nickel electrodeposition

HBDT produced 3D nickel are prepared on the conductive Cu substrate through galvanostatic electrodeposition of nickel at a high current density. This method is a fast, simple method to produce three dimensional monometallic and bimetallic structures. Apart from the obvious advantage of being particularly simple and fast, this method also offers numerous possibilities to modify the different characteristics of the electrodeposited nickel. We have investigated various aspects of the 3D Ni fabrication method in order to optimize its performance for Li/Na metal deposition and to aid the development of such substrates for more possible applications.

General effects of the varying deposition parameters are listed below,

(1), A higher concentration of PEG leads to (i), smaller nickel aggregates and larger surface area and (ii), a larger pore sizes and thus a higher porosity in the structure but a lower mechanical strength.

(2), A higher current density for electrodeposition results in a higher number density of pores and thus a higher porosity.

(3), Deposition with a prolonged electrodeposition duration produces a nickel layer with higher thickness.

S2.2.1 PEG concentration
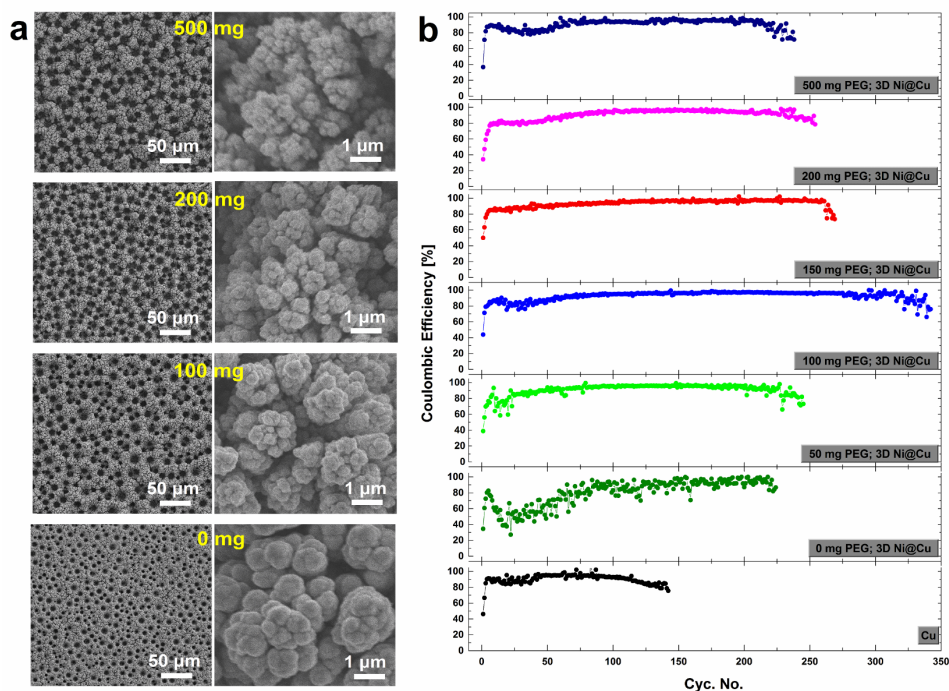
Figure S2.2 Morphologies and electrochemical performance on the bare Cu foil and various 3D Ni@Cu for Li deposition in an electrolyte without $LiNO_3$. (a), SEM images of the various 3D Ni@Cu current collectors synthesized with different concentrations of PEG from 0 to 500 mg per 300 mL of electrolyte solution. The current density for nickel electrodeposition was fixed at 3.0 A cm^{-2} and the deposition duration was fixed at 30 s. (b), Electrochemical cycling performance of various current collectors. Here the capacity of Li deposition is fixed at 0.5 mAh cm^{-2} and the applied current density was fixed at 1.0 mA cm^{-2}.

S2.2.2 Deposition duration
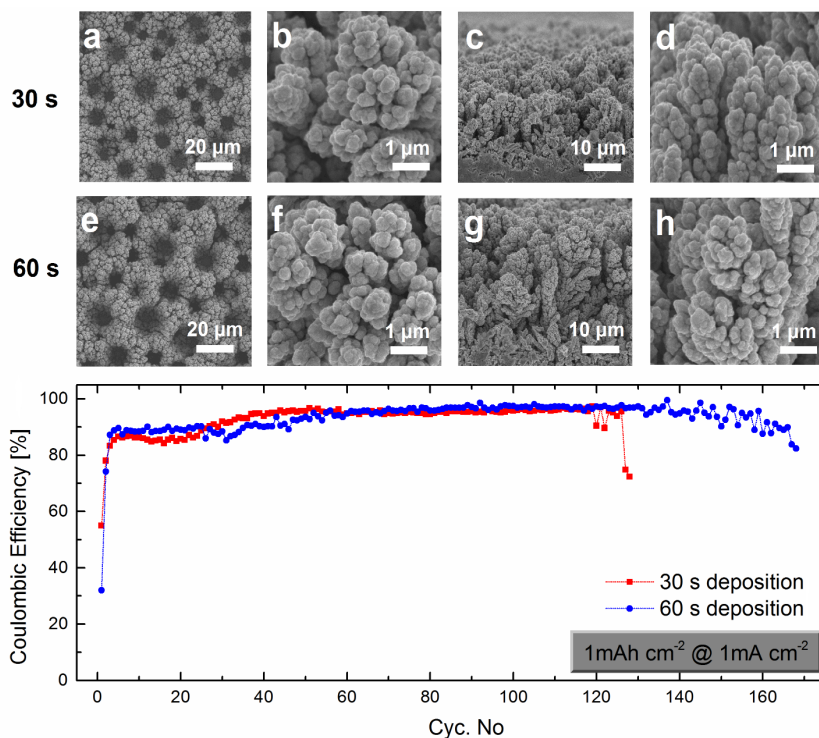
Figure S2.3 Morphologies and cycling performance of nickel depositions with different deposition durations in a LiNO$_3$-free electrolyte. (a) – (b), top and (c) – (d), cross-sectional view of the 30 s' nickel deposition. (e) – (f), top and (g) – (h), cross-sectional view of the 60 s' nickel deposition. (i), Electrochemical cycling performance for Li plating and stripping. Here the current density applied for electrodeposition was fixed at 3.0 A cm^{-2} and the amount of PEG addition in the electrolyte bath was fixed at 100 mg. It should be noted that the improvement of 60 s' nickel electrodeposition compared to 30 s is rather limited considering that both the required energy of production and the mass of nickel would be doubled.

S2.2.3 Current density
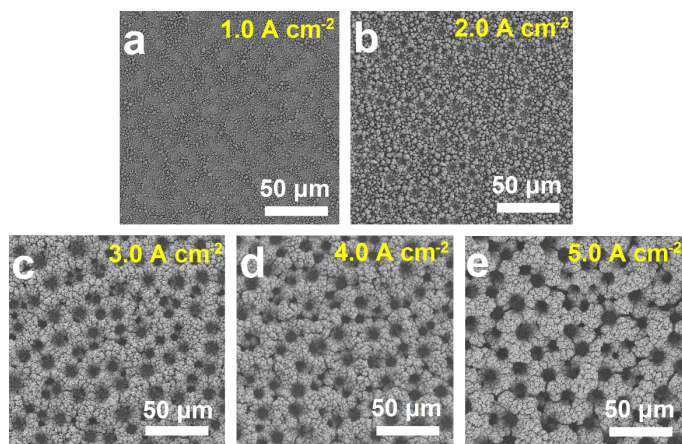
Figure S2.4 Nickel deposition at various current densities. (a), 1.0 A cm^{-2}; (b), 2.0 A cm^{-2}; (c), 3.0 A cm^{-2}; (d), 4.0 A cm^{-2}; (e), 5.0 A cm^{-2}. The PEG addition was fixed at 100 mg per 300 mL electrolyte solution.

S2.2.4 Post-deposition

It can be expected that the nickel structure produced with a high concentration of PEG and/or a high electrodeposition current density exhibits a higher porosity and thus a relatively lower mechanical strength. To improve the mechanical strength of the 3D porous nickel structure, post-deposition with an extremely low current density, which produces a protective, dense and compact nickel layer, appears to be an effective solution. (Post-deposition was not applied for the 3D Ni@Cu substrates in the main text.)
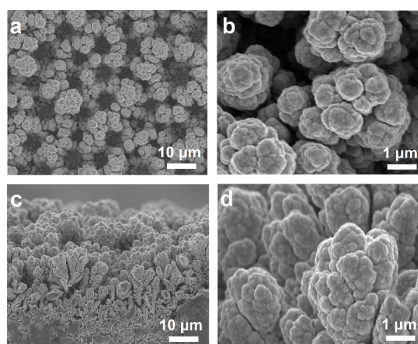
Figure S2.5 3D Ni@Cu (deposition @ 3.0 A cm^{-2} for 30 s; 100 mg PEG) with post-deposition at a low current density of 0.1 A cm^{-2} for 30 s.

S2.3 SEM-EDX analysis of 3D Ni@Cu
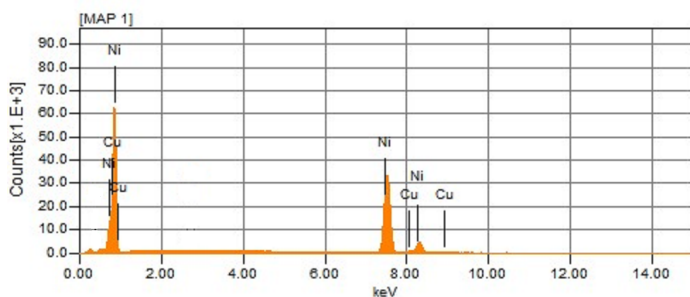
Figure S2.6 SEM-EDX spectra of the 3D Ni@Cu.

S2.4 Rietveld refinement of the XRD pattern

Rietveld refinement on the XRD patterns was carried out using the General Structure Analysis System (GSAS) software suite [S1].
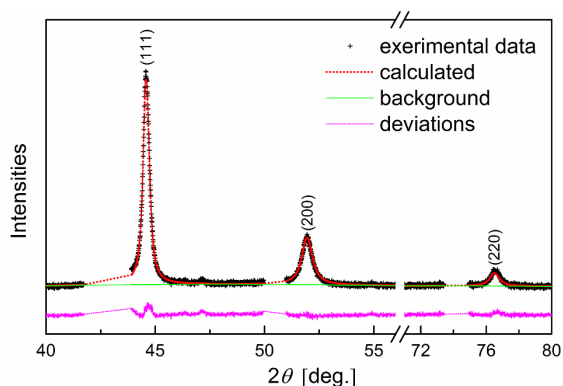
Figure S2.7 XRD patterns of the 3D Ni@Cu with Rietveld refinement of the nickel phase (space group: *Fm-3m*). The reflections of the Cu substrate are removed for clarity.

phase	Space group	Lattice parameters [Å]	Atom coordinates	U_{iso}	Avg. domain size [nm]
Ni	*Fm-3m*	$a = b = c = 3.523$	(0, 0, 0)	0.031	19.1

Table S2.1 Results of the Rietveld refinement on the prisinte Ni.

S2.5 Discussions on the 3D nickel structure

S2.5.1 Estimation on the porosity

The HBDT method is an effective way to produce highly porous structures and the efficiency loss during deposition can be directly translated to the porosity of the deposited structure.

The amount of Ni deposited was calculated by weighing the sample before and after the deposition. The mass loading was found out to be m_{actual} = ~5.0 mg cm^{-2}. The current efficiency (Faradaic efficiency) of this process thus can be defined as the ratio of the actual mass of a substance deposited from an electrolyte by the electrodeposition to the theoretical mass deposited as predicted by the the Faraday's law of electrolysis.

According to the law, the theoretical weight of the metal deposited in grams is,

$$m_{theoretical} = ItM \: / \: nF \tag{S2.1}$$

where m_t = mass loading of deposited metal in [g cm^{-2}], I = electrodeposition current density in [A cm^{-2}], t = time in [s], M = atomic weight of the metal in [g mol^{-1}], n = number of electrons invloved in the electrodeposition and Faraday's constant F = 96485.309 C mol^{-1}. The theoretically predicted weight of metal plated using this equation with I = 3.0 A cm^{-2} and t = 30 s gives $m_{theoretical}$ = 27.3 mg cm^{-2}. The current efficiency (η) then maybe calculated as,

$$\eta = m_{actual} \: / \: m_{theoretical} = 5 \: / \: 27.3 = 0.183 = 18.3\% \tag{S2.2}$$

This low efficiency is attributed to the fact that a significant amount of current is used in reducing the H$^+$ in the electrolyte to the H$_2$ gas which can be translated into a high porosity of the 3D nickel structure. The efficiency loss can be translated to the porosity of the nickel structure (Φ), which can be calculated as,

$$\Phi = V_{porosity} \: / \: V_{overall} = 1 - V_{nickel} \: / \: V_{overall} = 1 - (\: m_{nickel} \: / \: \rho_{nickel} \:) \: / \: (m_{nickel} \: / \: \rho_{overall}) = 1 - \rho_{overall} \: /$$
$$\rho_{nickel} = 1 - (\rho_{overall} \: V_{overall}) \: / \: (\rho_{nickel} \: V_{overall}) \: = 1 - m_{actual} \: / \: m_{theoretical} = 1 - \eta = \: 81.7 \: \% \tag{S2.3}$$

where, $V_{porosity}$ is the free volume, $V_{overall}$ is the total volume of the nickel layer, V_{nickel} is the volume of the deposited nickel, m_{nickel} is the mass of the nickel deposit.

S2.5.2 Estimations on the practical capacities

The practical capacities of the 3D Ni@Cu based Li metal anode and the commercial graphite anode have been estimated with the following approach.

The Li@3D Ni electrode consists of Li, Ni and pores + electrolyte, and the commercial graphite electrode is made up of graphite, binder and pores + electrolyte. For the Li@3D Ni electrode, the volume ratio of Ni (0.18) is set based on the above porosity estimations, and that of the pores + electrolyte is estimated to be 0.1. The volume ratios of all components of the commercial graphite electrode and the LiFePO$_4$ (LFP) cathode are adopted from the Argonne database [S2].

Therefore, the weight ratio of component x: $M_x = (\rho_x * \rho_x) / \sum(\rho_x * V_x)$

where ρ_x is the density of component x, V_x is the volume ratio of component x.

Finally, the volumetric and gravimetric capacities of the electrodes can be calculated as

volumetric capacity: $C_V = C_0 * \rho_{Li/C} * V_{Li/C}$

gravimetric capacity: $C_M = C_0 * M_{Li/C}$

where C_0 is the theoretical capacity in mAh g^{-1}.

The results of the estimation are summarized in the tables below:

Li anode with 3D porous nickel scaffold (*excl.* Cu substrate)			
theoretical capacity (C_0) [mAh g^{-1}]	3860		
components of the electrode	Ni	Li	pores + electrolyte
densities of components (ρ) [g cm^{-3}]	8.90	0.53	~ 1.0
volume ratio (V) [-]	0.18	0.72	0.10 (estimated)
weight ratio (M) [-]	0.77	0.18	0.05
volumetric capacity (C_V) [mAh cm^{-3}]	1478		
gravimetric capacity (C_M) [mAh g^{-1}]	695		
Full-cell capacity with a LFP cathode [mAh g^{-1}] (LFP : C : binder = 0.89 : 0.06 : 0.05, porosity: 50 % ; [S2]) (theoretically capacity of LFP: 170 mAh g^{-1}) (assuming $C_{anode} = C_{cathode}$ in [mAh])	197		

Table S2.2. Estimations on the capacities of a Li@3D Ni anode.

Graphite anode (*excl.* Cu substrate)			
theoretical capacity (C_0) [mAh g^{-1}]	374		
components of the electrode	binder	graphite	pores + electrolyte
densities of components (ρ) [g cm^{-3}]	1.78	2.10	~ 1.0
volume ratio (V) [-] (ref. [2])	0.10	0.56	0.34
weight ratio (M) [-]	0.11	0.69	0.20
volumetric capacity (C_V) [mAh cm^{-3}]	440		
gravimetric capacity (C_M) [mAh g^{-1}]	258		
Full-cell capacity with a LFP cathode [mAh g^{-1}] (LFP : C : binder = 0.89 : 0.06 : 0.05, porosity: 50 % ; [S2]) (theoretically capacity of LFP: 170 mAh g^{-1}) (assuming $C_{anode} = C_{cathode}$ in [mAh])	159		

Table S2.3. Estimations on the capacities of a graphite anode.

S2.6 Electrochemical performance at a high current rate and with a high capacity
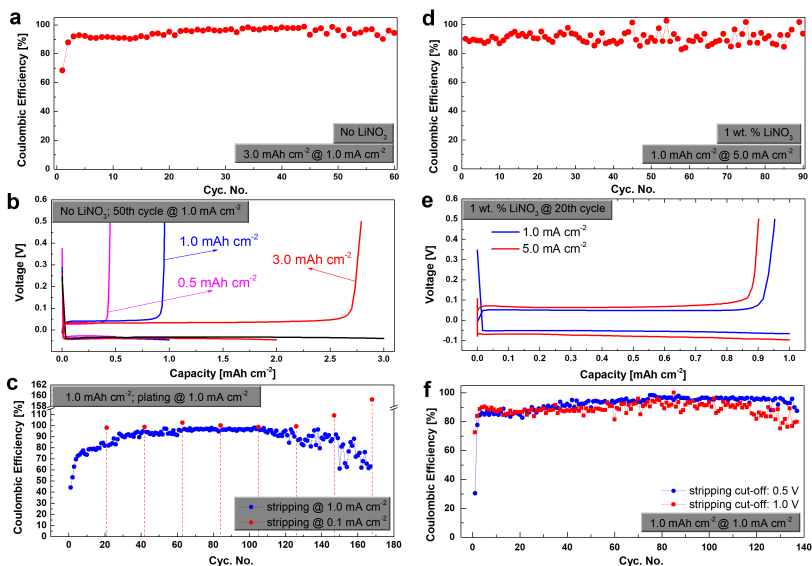
Figure S2.8 Electrochemical cycling performance for reversible Li deposition on 3D Ni@Cu. (a) – (b), cycling performance for 3 mAh cm^{-2} Li depostion at 1.0 mA cm^{-2} in a LiNO$_3$-free electrolyte. (c), study on the Li-ion diffusion kinetics: the current rate for Li plating was fixed at 1.0 mA cm^{-2} and stripping of Li occurred at two current rates: 1.0 mA cm^{-2} for every first 20 cycles, and 0.1 mA cm^{-2} for every 21th cycle. (d) – (e), cycling performance for 1 mAh cm^{-2} Li depostion at 5.0 mA cm^{-2} in a LiNO$_3$-containing electrolyte. (f), Cycling performance with different stripping cut-off voltages (0.5 and 1.0 V) using an electrolyte without LiNO$_3$.

S2.7 XRD patterns
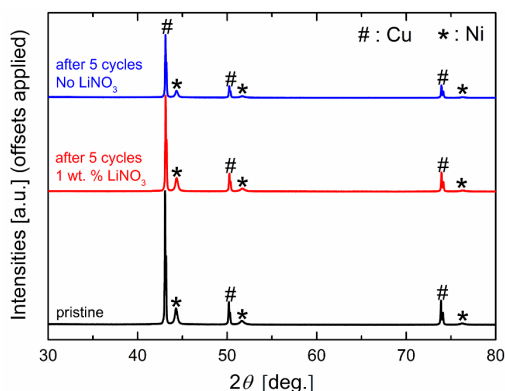
Figure S2.9 XRD patterns of the 3D Ni@Cu electrode at different states: pristine and after five cycles in LiNO$_3$-free and LiNO$_3$-containing electrolytes.

S2.8 XPS analysis
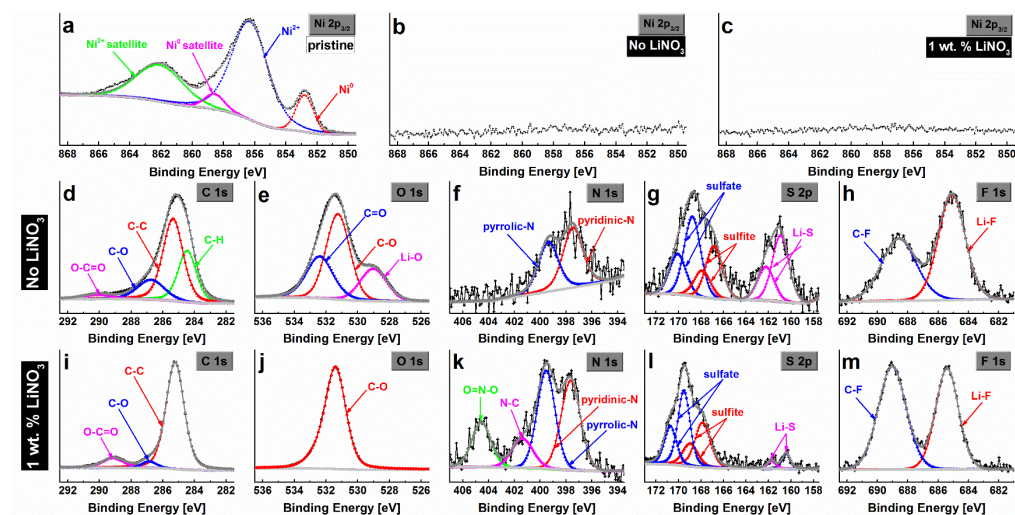
Figure S2.10 XPS specctra of the 3D Ni@Cu electrode at different stages: pristine and after 5 cycles in LiNO$_3$-free and LiNO$_3$-containing electrolytes. (a) – (c), Ni 2p$_{3/2}$ XPS spectra. (d) – (h), XPS spectra of the electrode after five cycles using a LiTFSI based electrolyte. (i) – (m), XPS spectra of the electrode cycled in a 1 wt.% LiNO$_3$-LiTFSI based electrolyte.

S2.9 Micro morphology Li plating on 3D Ni@Cu and planar Cu
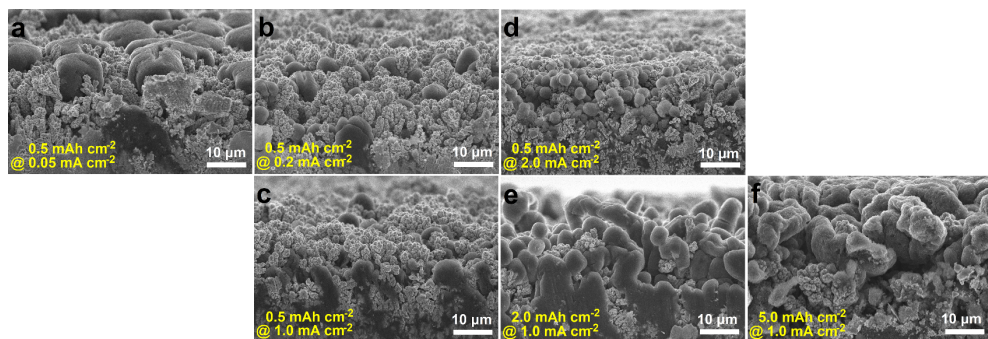
Figure S2.11 Cross-sectional micrographs of the Li deposit in the 3D Ni@Cu host. The areal capacity of Li in Figure (a) – (d) is 0.5 mAh cm^{-2} deposited at various current rates; and Figure (c), (e) and (f) show different amounts of Li deposits deposited at 1.0 mA cm^{-2}.
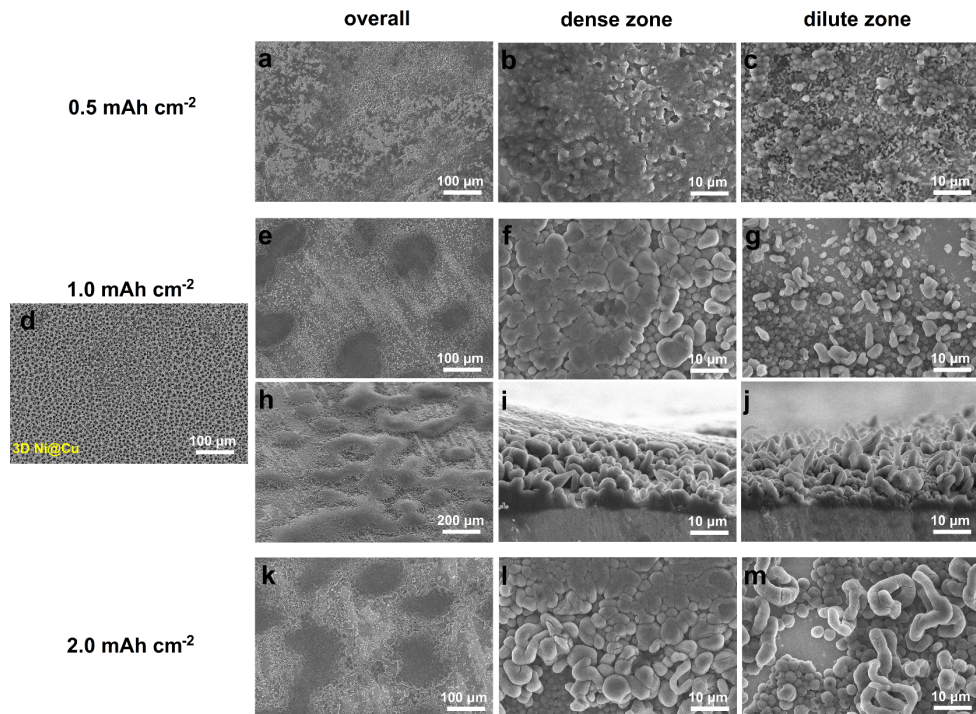
Figure S2.12 Micrographs of the initial dendritic Li growth on bare Cu at 1.0 mA cm^{-2}. (a) – (c), Li deposits of 0.5 mAh cm^{-2}; (e) – (j), Li deposits of 1.0 mAh cm^{-2}; (k) – (m), Li deposits of 2.0 mAh cm^{-2}. Figure (d) shows 1 mAh cm^{-2} Li deposites on 3D Ni@Cu as a comparison with that on bare Cu foil in Figure (e). Figure (h) is an oblique image of the inhomogeneous Li deposits and Figure (i) – (j) are the cross-sectional views of the Li deposits in different zones.

S2.10 Micro-morphological evolution of Na plating on planar Cu
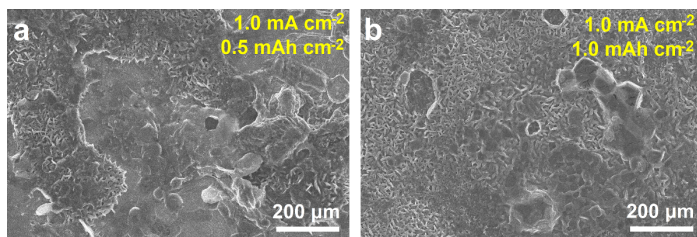
Figure S2.13 SEM images of Na deposits on a planar Cu foil with different capacities.

References

[S1] A.C. Larson, R.B. Von Dreele, Los Alamos National Laboratory Report LAUR (2000) 86-748.

[S2] P.A. Nelson, K.G. Gallagher, I. Bloom, D.W. Dees, Modeling the Performance and Cost of Lithium-Ion Batteries for Electric-Drive Vehicles, second edition, Argonne National Laboratory, 2012.

Chapter 3

Li and Na Ion Batteries Based on Si Nanoparticles

In this chapter, we investigate Si nanoparticles produced from scalable and high-throughtput plasma enhanced chemical vapor deposition (PECVD) for both Li and Na ion storage. The thick, carbon/binder-free Si nanoparticle deposition avhieves excellent cycling stability and high areal capacities working as the anode for Li ion batteries. Reversible Na ion uptake in the Si nanoparticles is realized experimentally for the first time.

Chapter 3.1

A High-Performance Li Ion Anode from Direct Deposition of Si Nanoparticles

This chapter is based on:

Abstract
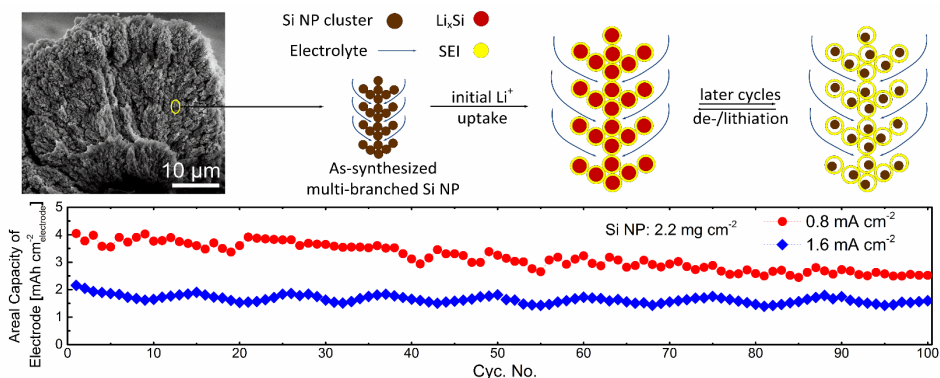
Nanostructured silicon has been intensively investigated for its electrochemical performance as a high capacity Li-ion battery anode. However, the commercial introduction still requires advances in the scalable synthesis of sophisticated Si nanomaterials and electrodes. Moreover, the electrode degradation due to volume changes upon de-/lithiation, low areal electrode capacity, and application of large amounts of advanced conductive additives are some of the challenging aspects. Here we report a Si electrode, prepared from direct deposition of Si nanoparticles on a current collector without any binder or conducting additives, that addresses all of the above issues. It exhibits an excellent cycling stability and a high capacity retention taking advantages of what appears to be a locally protective, yolk-shell reminiscent, solid electrolyte interphase (SEI) formation. Cycling an electrode with a Si nanoparticle loading of 2 mg cm^{-2} achieved an unrivalled areal capacity retention, specifically, up to 4 mAh cm^{-2} and ~ 1.5 mAh cm^{-2} at 0.8 mA cm^{-2} and 1.6 mA cm^{-2}, respectively.

3.1.1 Introduction

Energy storage is one of the key issues of modern society. The development of Li-ion battery based energy storage devices is flourishing, in an effort to meet the increasing power demand of a diverse range of applications, such as electrical vehicles and widely used portable electronics [1-5]. Si based anode materials have been extensively studied for Li ion batteries mostly due to the unparalleled theoretical capacity of Si (4200 mAh g^{-1} for $Li_{4.4}Si$). However, the huge volume change and its resulting electrode pulverization upon Li uptake leads to electrical conduction loss and rapid capacity degradation, which have severely reduced its promise for practical applications [6-9]. Research has been focusing on various kinds of nanostructured Si materials to resolve the different aspects leading to capacity loss, and to achieve stable cycling performance [10-12]. Current studies mostly synthesize sophisticated nanostructured Si, including nanowires [13, 14], nanotubes [15, 16], nanospheres in a flexible matrix or 3D architecture [17, 18], etc., or apply protective coatings [19, 20] to prevent electrode pulverization and to provide continuous electronic and ionic conduction pathways during cycling. However, these synthetic approaches on a lab scale appear to have poor scalability and therefore until now limited large scale commercial viability. Moreover, methods that do use potentially more scalable methods involve large amounts of additional relatively costly nanoscale carbonaceous conducting networks (graphene [21], nanotube [22], nanofiber [23], etc.) and advanced binder materials [24, 25], which lowers the cost-effectiveness and overall capacity that is realised.

Another major challenge for Si based anodes is to enhance the areal capacity, which is generally poor owing to the low mass loading of active materials [14-17, 26-28]. Progress has been made to increase the mass loading of Si and/or electrode packing density to improve the performance [29-36], but these electrode manufacturing approaches are still hardly industrially viable as they introduce either high cost materials or complicated production processes.

Thus the main challenge for the practical implementation of Si anodes is to develop cost-effective and commercial viable techniques to prepare Si anodes. The technique should be capable of producing Si particles that are nanosized to accommodate volume changes, and that are electronically connected throughout the structure. In addition the technique should have a high production rate and be scalable. When possible advanced carbons and binders in the process should be minimized and further processing for electrode manufacturing should

also be eliminated. Progress has been made to realize the scalable synthesis of nanostructured Si anodes [37-40] as well as to produce binder-free Si electrodes [41-46].

In this study, a novel but simple and industrially scalable process was developed to synthesize Si anodes. (Figure 3.1.1) In this process silicon nanoparticles (Si NP) are directly deposited on a porous carbon current collector by plasma enhanced chemical vapour deposition (PECVD). The obtained additive- and binder-free electrode can be used as an anode in a Li-ion battery without further processing.
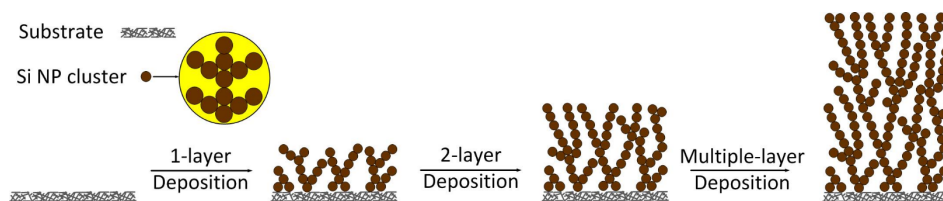
Figure 3.1.1 A schematic of electrode preparation process via direction deposition of Si nanoparticles.

Previous studies on the Si deposition based Li ion anodes consider nanowires, nanoscale Si films on 3D substrates, or thin structured Si films [13-16, 28, 42, 47-51]. The novel approach in this work introduces a facile one-step synthesis by direct deposition of Si nanoparticles with at least an order of magnitude higher mass loading of Si compared to the previous studies (max. 5 μm Si layer in previous reports), and without the need for catalysts or other additional 3D nanostructures. The Si electrode in this work exhibits several advantages: (1), CVD based Si deposition is industrially well-developed and scalable due to its present widespread applications in solar cells and electronics. The thickness and porosity of Si NP deposition layers can be monitored and controlled. (2), The plasma aided self-assembly of nanoparticle layers produces hierarchical nano and micro structured Si NP branched structures, which results into sufficient porosity to accommodate the volume expansion during Li ion uptake. (3), The Si nanoparticles appear naturally interconnected, which eliminates the need for binders and conductive additives and thus improves the overall capacity of the electrode and reduces processing cost. (4), Controlled oxidation on the surface of Si NP is achieved through low pressure O_2 exposure between the plasma deposition cycles. The inactive and solid SiO_x scaffold appears to reinforce structural integrity of the electrode during cycling. (5), The inter-particle porosities are connected in nanoscale, which provides an express way for electrolyte infiltration and thus good Li ion transport throughout the electrode. Hence high

performance can be reached for electrodes with increased thicknesses, enabling high areal capacities with increased Si mass loading. (6), A templating effect [51, 52] is introduced by the open porosity of the used carbon substrate. This results in interconnected micron scale porosities allowing electrolyte to enter the Si NP layer, which shortens the diffusion pathway of Li ion towards active materials and thus enables fast Li ion transport within the electrode. (7), The density of this Si NP electrode (~ 0.5 g cm^{-3}) may not appear high but this is about 20 % of the density of bulk silicon, significantly higher than in other reports where a much smaller fraction of the bulk Si density is reached [15,16,28,47]. The density is however sufficiently low to allow space for the large volume expansion of Si; up to 400 % expansion would just fill the total available volume, let alone the space required for the SEI growth.

3.1.2   Methods

3.1.2.1 Electrode preparation

The Si NP electrodes were prepared via Plasma Enhanced Chemical Vapour Deposition (PECVD) from silane using an Expanding Thermal Plasma (ETP) source [53, 54]. Si NP depositions were performed on a porous carbon sheet (Caplinq) layer by layer and each layer includes 30 s' deposition of Si NP. The specific process and conditions for the Si NP deposition are stated in the Supporting Information (SI). The as-synthesized Si NP-C sample was directly applied as the electrode after drying in a vacuum oven for 12 hours. For comparison, Si NP deposition was also carried out on a non-porous planar Cu foil (Goodfellow) and its morphology before and after de-/lithiation is shown in SI.

3.1.2.2 Sample characterization

For the pristine Si NP electrode, SEM images were taken using a JEOL JSM 6010F scanning electron microscope at an accelerating voltage of 5 kV; The high resolution SEM images (Figure 3.1.2d & g) were acquired using Hitachi S4800 working at 2 kV. For TEM measurement Si particles were carefully scraped off from the electrode. Bright field TEM images were acquired using FEI-Tecnai operating at 200 kV. XRD patterns were measured with a PANalytical X'Pert Pro PW3040/60 diffractometer with Cu K$_\alpha$ radiation operating at 45 kV and 40 mA. Raman mapping spectra on Si NP particles were obtained from a Renishaw InVia Raman spectrophotometer. The wavelength of the laser applied is 785 nm and the laser power is set at 0.2 mW. TGA is carried out with a Perkin Elmer TGA 7 thermogravimetric analysis analyser. The Si NP sample were scraped from the carbon substrate and heated in a

20 % O_2/Ar mixture from room temperature to 1000 °C followed by a full oxidation at 1000 °C for 200 min. XPS was performed with a K-Alpha X-ray Photoelectron Spectrometer (XPS) System.

All cycled electrodes were washed with diethyl carbonate (DEC) for 3 times to remove soluble electrolyte residuals in the electrode, and were dried in a glove box before the measurement. The SEM images were acquired using Hitachi S4800 with an accelerating voltage of 15 kV. STEM-EDX mapping was done at FEI-Titan operating at 300 kV with Oxford instrument EDX system. TEM, XRD and XPS measurement were performed using the same equipment and working conditions as were utilized for pristine samples.

3.1.2.3 Electrochemistry

The half-cell employed for the electrochemical measurement were a lab-designed prototype (Figure S3.1.1) which consists of two stainless steel flanges, an O-ring in between the flanges, and a plastic vacuum clamp to hold them together. There is a separate stainless steel plate supported by a metal spring to provide the necessary pressure and mechanical compaction inside the battery. Half-cell Li ion batteries for test were assembled inside an Ar environment glovebox with the O_2 and H_2O levels < 0.1 ppm. A Li metal foil (Aldrich) worked as the counter electrode. A borosilicate glass micro fibre (Whatman) was applied as the separator, and 1 M $LiPF_6$ dissolved in DEC, ethylene carbonate (EC) and fluoroethylene carbonate (FEC) (1:1:1 in volume) was utilized as the electrolyte.

The galvanostatic electrochemical performance were measured with a MACCOR 4600 battery cycler at room temperature. The cut-off voltages for discharge and charge are 0.005 V and 2 V versus Li/Li^+ , respectively. Cyclic voltammetry was perform with a PGSTAT302N Autolab potentiostat within the same voltage range. EIS measurements were carried out with a PGSTAT302N Autolab within the frequency range of 1 MHz and 0.01 Hz.

3.1.2.4   Subtraction of the carbon capacity

Specific capacities of the Si NP reported in this paper were calculated based on the mass of the Si NP layer (*excl.* the carbon substrate). The capacity of the carbon substrate was determined by measuring the capacity retentions of the carbon paper at a series of current rates and then fitting the capacity data with a logistic function; (Figure S3.1.3) using this function, the capacities of the carbon substrate could be calculated regarding the corresponding current rates applied on carbon. The specific capacities of the Si NP were

determined by subtracting the capacity of carbon from that of the Si NP-C electrode. (More details about the subtraction of the capacity contribution from carbon substrate are described in SI**.**)

3.1.3   Results and discussions

3.1.3.1 Electrode manufacturing and characterization

Si NP anodes were synthesized via expanding thermal plasma chemical vapour deposition from silane. Si NP depositions were performed on a planar but porous carbon substrate layer by layer; cooling and air exposure were applied in between. In this study 1 to 4 layers of Si NP depositions were carried out on the carbon substrates. The as-prepared Si NP-C electrodes are tested in a half cell with a Li metal counter electrode, separator and liquid electrolyte.

Figure 3.1.2 shows the morphology of a 4-layer Si NP deposition on the carbon sheet. The thickness of the Si NP layer is around 40 μm (Si NP: ~ 2 mg cm^{-2}). Scanning Electron Microscopy (SEM) (Figure 3.1.2a – g) shows that small silicon nanoparticles (< 20 nm) form clusters with typical sizes of approximately100 nm scale, and a hierarchically multi-branched porous nanostructure appears throughout the Si NP layers. Transmission Electron Microscopy (TEM) (Figure 3.1.2h – j) demonstrates that the particles reside as clusters of ~ 100 nm scale; while individual particles (~ 20 nm) are spherical with a very thin native SiO$_x$ layer on the surface. The oxidation layers are amorphous as only X-ray diffraction peaks (XRD) of crystalline Si are observed (Figure 3.1.2k). While the presence of both amorphous and crystalline Si phases is evidenced by Raman spectroscopy (Figure 3.1.2l). Energy Dispersive X-ray spectroscopy (EDX) elemental mapping performed on the Si NP layer (Figure S3.1.5) shows that the oxygen distribution is uniform throughout the Si NP layers. Individual Si nanoparticles are thus homogeneously oxidized on the surface, which is also consistent with the TEM results. To determine the amount of oxygen present in the sample, Thermal Gravimetric Analysis (TGA) (Figure S3.1.6) was applied by heating the Si NP under 20% O$_2$/Ar gas and fully oxidizing Si into SiO$_2$. The result indicates the fraction of Si inside the sample amounts to 46.3 wt. % (i.e. Si : SiO$_2$ = 0.65 : 0.35 in mole). Such an amount of SiO$_2$ is consistent with the observation of a very thin layer (1.6 nm) on a 15 nm diameter Si particle in the high resolution TEM images.
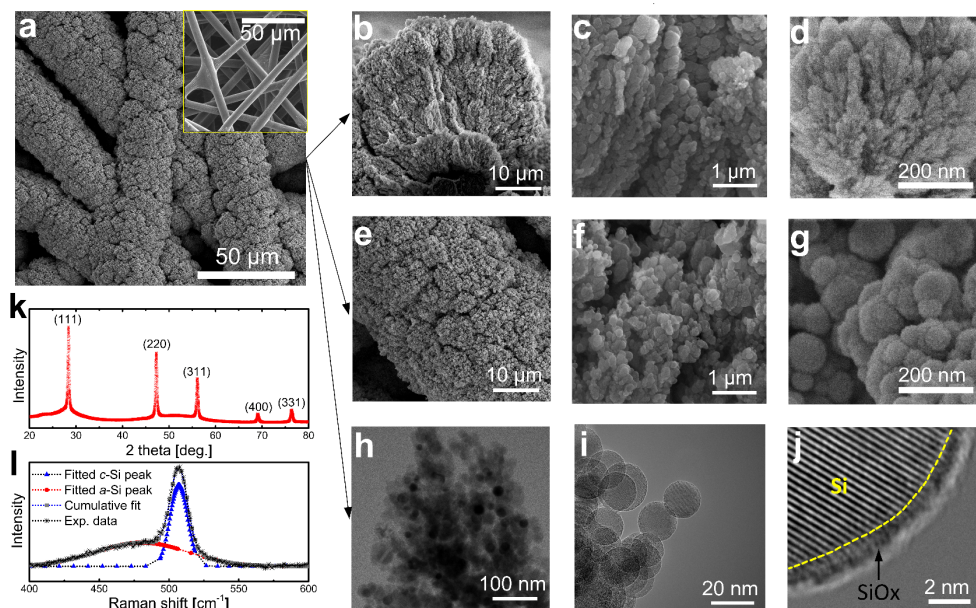
Figure 3.1.2 Morphology of as-synthesized Si NP on a porous C substrate. (a). A SEM image of the Si NP electrode; inset of (a): SEM micrograph of the porous C fibre sheet applied as a substrate for Si deposition. (b) - (d), cross-sectional and (e) - (g), top view SEM micrographs of the nanostructured Si layer imaged at different magnifications; (h) - (j) TEM image of a Si nanoparticle cluster and individual particles as-synthesized from PECVD. (k) XRD patterns of Si nanoparticles as synthesized (the specimen for X-ray diffraction was loose Si nanoparticles scraped from the substrate). (l) Raman spectra of the Si nanoparticles indicating the co-existence of crystalline and amorphous Si.

3.1.3.2 Electrochemical performance

The electrochemical performance of Si NP-C electrode was verified by cycling the electrode against a Li metal counter electrode. The electrochemical performance of Si NP-C electrodes has contributions from both Si NP and the carbon substrate. The capacity contribution from the carbon substrate was determined and subtracted from that of the Si NP-C electrode. Details about the capacity subtraction are described in Experimental details and SI. In this paper, all the reported specific capacities are calculated based on the mass of the Si NP layer, including the mass of SiO_2.

Cycling a Si NP (mass loading of 0.5 mg cm^{-2}) electrode on the carbon substrate at 0.1 A g^{-1} shows a highly stable reversible capacity (Figure 3.1.3a). A delithiation capacity retention of 1825 mAh g^{-1} is obtained after 30 cycles; Given that the amount of SiO_x accounts for about

half of the sample, the specific capacity of Si (*excl.* SiO_x) would be doubled and therefore be remarkably close to the theoretical capacity assuming SiO_x does not contribute to the reversible capacity.

Figure 3.1.3b demonstrates a remarkable cycling stability over 100 cycles for Si NP-C electrodes with various mass loadings cycling at 0.8 A g^{-1}. The small and periodic capacity fluctuations stem from ambient temperature variations. At this charge rate the achieved capacity of Si NP-C declines with growing Si NP loadings; the capacity varies around 1600 mAh g^{-1}, 1200 mAh g^{-1} and 800 mAh g^{-1} for electrodes with 0.7 mg cm^{-2}, 1.3 mg cm^{-2} and 2.0 mg cm^{-2} Si NP, respectively. The slight capacity fading along cycling originates from the gradual structural deformation along repetitive dis-/charges.

Cycling at 0.8 mA cm^{-2} the areal capacity for the Si NP-C electrode (Figure 3.1.3c) drops gradually, regardless of the slight swings, from the initial reversible capacity of 4.2 mAh cm^{-2} to 2.5 mAh cm^{-2} after 100 cycles. A greatly promoted cycling stability is observed when the current density is increased to 1.6 mA cm^{-2} which demonstrates an areal capacity retention of about 1.5 mAh cm^{-2} and no apparent capacity degradation after 100 cycles. The improvement of cycleability, when the current rate increases from 0.8 mA cm^{-2} to 1.6 mA cm^{-2}, results from the rapid and incomplete lithiation of Si NP at high current rate and therefore less structural deformation along cycling. The achieved areal capacity is high compared to the recent literature reports on advanced Si based electrodes (Table S3.1.2).

Galvanostatic dis-/charge of the Si NP-C electrodes also shows an excellent rate capability. (Figure 3.1.3d) A remarkable rate performance is observed for the Si NP-C electrode with a relative lower mass loading (1.0 mg cm^{-2}). The capacity achieved at 0.1 A g^{-1} reaches > 1600 mAh g^{-1}; and no apparent capacity degradation occurs when the current rate is increased to higher currents up to 1 A g^{-1}. Increasing the mass loading of Si on carbon sheet slightly reduces capacities. ~ 1400 mAh g^{-1} for 1.7 mg cm^{-2} and above 1300 mAh g^{-1} for 2.4 mg cm^{-2}, respectively, were realized for deep lithiation (i.e. low current densities); The capacity fades with either rising current rates or increases in mass loadings.

Measuring the electrochemical performance of the electrode at different constant temperatures between 10 °C and 40 °C (Figure S3.1.7), it is observed that a higher temperature leads to a higher initial capacity and a relatively faster degradation. A lower temperature results into a lower capacity retention but a much more stable cycling stability.

Moreover, regardless of the capacity retention disparity at different temperatures, no obvious capacity swings can be observed. This reveals that the phenomenon of apparent capacity fluctuations observed in Figure 3.1.3 resulted from the temperature variations between day and night in the laboratory. It is more pronounced for the electrode with a higher mass loading because the absolute value of the applied current (0.8 A g^{-1}) is higher for a larger mass.

The main de-/lithiation of Si NP occurs at a lower voltage range (< 0.8 V), which is evidenced by the voltage profiles (Figure 3.1.3e – h) and the cyclic voltammograms (Figure 3.1.3i). A solid electrolyte interphase (SEI) layer is formed, due to the decomposition of the organic electrolyte solvent and reaction with the electrode materials, at a higher voltage plateau (0.7 V, Figure 3.1.3e) during the initial Li ion uptake. Nevertheless, this phenomenon is not observed in the following cycles; instead, later cycles show highly reversible capacities and rather symmetrical voltage profiles for charge and discharge indicating a low overpotential between charge and discharge. Figure 3.1.3f & g demonstrate that the overpotential grows when the mass loading of Si NP is higher and at elevated current rates, which is due to the limited Li ion diffusivity in the Si NP electrode and intrinsic electronic conductivity. However, regardless of the increasing overpotentials, considerable reversible capacity retentions are still achieved.

To study the equilibrium potential the galvanostatic intermittent titration technique (GITT) was applied by pulsing a current of 0.1 A g^{-1} for 1 h and a relaxation period of 4 hours after each pulse. Figure 3.1.3h reports that overpotentials during both Li uptake and release decrease with higher lithiation levels.
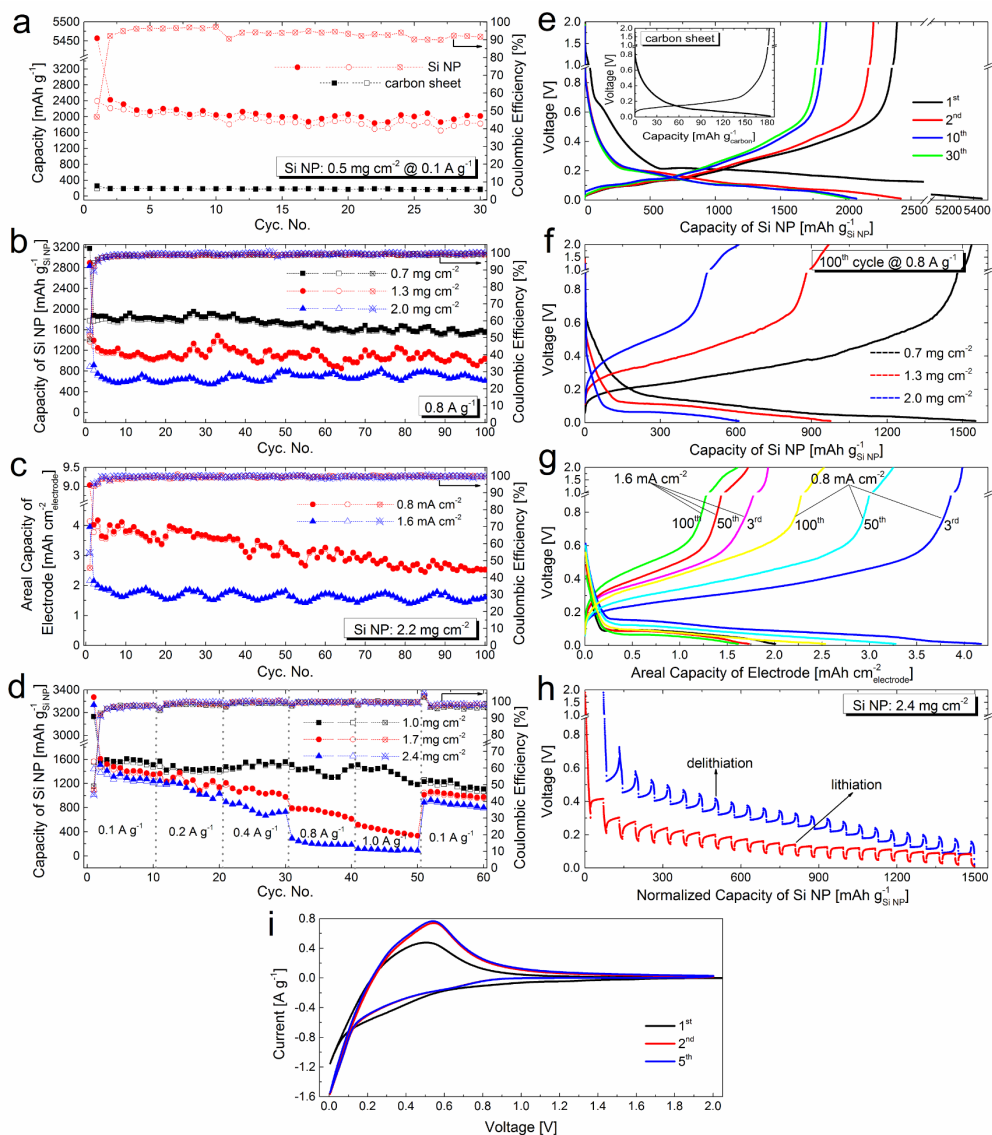
Figure 3.1.3 Electrochemical performance of the Si NP-C electrode for de-/lithiation at room temperature. (a), Capacity retentions and Coulombic efficiencies of the Si NP (0.5 mg cm^{-2}) at 0.1 A g^{-1} and the capacity retentions of the carbon substrate cycling with the same measurement program. (b), Electrochemical performance of the Si NP-C electrodes with different mass loadings cycling at 0.8 A g^{-1}. (c), Areal capacity retentions and Coulombic efficiencies of the Si NP-C (2.2 mg cm^{-2}) electrodes cycling at 0.8 and 1.6 mA cm^{-2}. (d), Rate capabilities of the Si NP electrode with different mass loadings. (In Figure (a) – (d), solid symbols: lithiation capacities; open symbols: delithiation capacities; cross-centered open symbols: Coulombic efficiencies.) (e), Voltage profiles of Si NP (0.5 mg cm^{-2}) at 0.1 A

g^{-1}. Inset of Figure (e): voltage profiles of the carbon substrate. (f), Voltage responses of the Si NP-C electrodes with different mass loadings cycling at 0.8 A g^{-1}. (g), Voltage profiles of the Si NP-C (2.2 mg cm^{-2}) electrodes cycling at 0.8 and 1.6 mA cm^{-2}. (h), GITT de-/lithiation of Si NP-C electrode. GITT was carried out on the thickest Si NP-C electrode (2.4 mg cm^{-2}) following the rate performance test in Figure (g). Current pulses: 0.1 A g^{-1} for 0.5 h during charge/discharge; Relaxation for 2 h. (i), Cyclic voltammograms of the Si NP-C electrode. (scan rate: 0.5 mV s^{-1}).

3.1.3.3 Electronic / ionic conductivity

The electronic conductivity of Si can be expected to be greatly enhanced upon trace amounts of Li insertion, leading to even metallically conducting Si [55-57]. This could be an explanation of why an initially poorly conducting electrode that merely consists of Si nanoparticles is capable of fast Li ion uptake and release. For the as-prepared nanostructured electrode, with its packed structure of individual insulating SiO_2 coated particles, the electrical conduction enhancement induced by Li insertion/doping will be of paramount importance. A simple *in-situ* resistance measurement was performed during chemical lithiation by pressing a Li foil against the Si NP layers; purely in the solid state, without any electrolyte addition. Figure 3.1.4a demonstrates that the DC electrical resistance of the pristine Si NP layer (1.5 mg cm^{-2}) is as high as ~ 500 kΩ. Most remarkably the electrical resistance reduces by one order of magnitude within as little as 2 minutes of all solid chemical lithiation; it further decreases rapidly to < 50 Ω in 2.5 hours. The electronic conductivity of the Si NP layer thus increases by about 4 orders of magnitude during solid state lithiation at room temperature, which is comparable to the published results on electrochemical lithiation of a single Si nanowire / thin solid film (100 nm) [56, 57]. This finding may illustrate how the Si NP electrode, even without addition of any conducting additives, achieves sufficient electronic conductivity for Li ion insertion and extraction. The presence of SiO_2 apparently has no large detrimental effect on the DC conductivity.

Furthermore, electrochemical impedance spectroscopy (EIS) is performed to investigate ionic conductivity of the Si NP anode in a half cell with a Li counter electrode and liquid electrolyte. Nyquist plots (Figure 3.1.4b) of the Si NP anode demonstrate semicircles in the high frequency region corresponding to the interface resistance of the Si NP anode related to the SEI layer and charge transfer resistance of Li ions. Linear tails in the low frequency range are related to the long range Li-ion diffusion in the electrode [58, 59]. It is observed that before cycling, the charge transfer resistance is large (> 300 Ω) as no electrochemical reaction

has happened and a large barrier for Li ion diffusion exists. After the first cycle it decreased significantly to around 70 Ω. After dis-/charge for 100 cycles at 0.8 A g^{-1}, the interface resistance increases only slightly, indicating that there is no apparent change in the transfer resistance of Li-ions from and into the Si NP electrode. This indicates that the composition as well as structure of the electrode was retained after the first cycle and essentially stay intact during cycling.
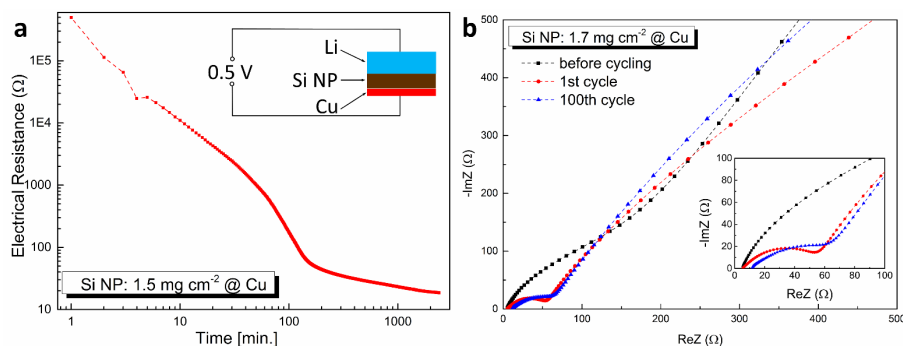
Figure 3.1.4 Impedance measurements. (a), The electronic DC resistance of the Si NP layer during chemical lithiation; inset: experimental set-up of in-situ impedance measurement during chemical lithiation of Si NP. The influence of the Cu substrate, Li foil and cell tester has been subtracted by carrying out a parallel experiment with the same set-up and test conditions but replacing the Si NP-Cu electrode with a blank Cu foil without Si NP. (b), Nyquist plots of the Si NP anode in a half cell with Li metal counter electrode and liquid electrolyte, before cycling and after 1, and after 100 cycles.

3.1.3.4 One-off in-situ uniform SEI formation

SEI formation is commonly believed to be a crucial disadvantage for nanostructured Si anode materials since repetitive cracking of SEI layers due to the large volume expansion and contraction of the electrode and continuous formation of new SEI ceaselessly reduces available active material, leading to a rapid capacity degradation [4, 6, 11, 60]. However, in this article the SEI layer turns out to behave differently and is even beneficial for the cycling stability.

Fluoroethylene carbonate (FEC) addition into the electrolyte has proved to be advantageous as it creates a compact and stable LiF-dominant SEI layer that limits the further formation of SEI [61-63]. Moreover, it is anticipated that a SEI layer will form on the exposed surface of the nano-porous electrode layer of individual particles during the 1st Li ion uptake. Electron microscopy in Figure 3.1.5a – f shows that, regardless of the initial growth of cluster size,

the SEI covered Si NP clusters after 100 cycles appear to remain the same typical size as after the 1st cycle. The same is true for the micro-structure of the electrode. Apparently, after the rigid protective SEI is formed, it largely stays intact during later cycles without apparent loss of coherence. There may be a little additional growth, which is consistent with the EIS analysis in Figure 3.1.4b. The rationale for the cycling stability may be that now the volume change of individual particles is accommodated by the space available between individual particles and their SEI. In this way the contact throughout the electrode is not destroyed during cycling, as illustrated in Figure 3.1.5g. This one-off SEI formation with the remaining coherence throughout the nanoparticle strands is of remarkable advantage. Specifically the local SEI surrounding the particles apparently has outstanding elasticity and mechanical strength, which protects the electrode. It therefore prevents further SEI formation while it also provides ionic conduction.

Furthermore, the SEI layer growth is also investigated by EDX element mapping of F and O (mostly from LiF, Li_2CO_3, and Li-Si-O (see below) in the SEI layer). Figure 3.1.5k shows that F and O appear more concentrated in the shell of the Si NP cluster, which may be indicative of its yolk-shell configuration on the scale of the clusters (~ 100 nm). The SEI thus surrounds the clusters of NP, rather than the individual NP. On the larger scale of the entire electrode (10 μm scale) Figure S3.1.9 shows that F and O distribute evenly throughout the electrode indicating a uniform SEI growth throughout the Si NP layer. The resulting morphology of a spontaneous SEI layer around the Si-NP clusters, extending throughout the electrode without breaking the electronic contacts between the clusters apparently exhibits high resistance against stresses caused by the Si volume expansion and contraction of individual particles, therefore it ensures the structural integrity of the Si NP layer and hence supports the cycling stability. In addition it may be deduced from the electrochemical performance that the entire SEI formation takes place only in the first cycles and thus provides a stabilised electrode morphology afterwards.

Figure 3.1.5 Morphology of the Si NP electrode at three different stages: pristine, after the 1st cycle and after 100 cycles at 0.8 A g^{-1}. (a) - (f), SEM images showing the morphology of Si NP clusters at different stages: (a) - (b), pristine; (c) - (d), SEI shell after the 1st cycle; (e) - (f), SEI shell after the 100th cycle; (g), A schematic of the morphology change of the hierarchically nanostructured Si NP during de-/lithiation process. (h) - (k), STEM-EDX result: layered image and element mapping of Si, O and F, respectively. The measurements were performed on electrode after 100 de-/lithiation cycles at 0.8 A g^{-1}.

XRD patterns (Figure 3.1.6a) indicate that crystalline Si is observed in pristine Si NP, and that it has been totally amorphized after the first cycle. Li$_x$SiO$_y$ compounds can be identified from the XRD spectra after dis-/charge for 100 cycles. Irreversible formation of Li$_x$SiO$_y$ (mostly Li$_4$SiO$_4$, Reaction (3.1.1)) is commonly recognized for Si/SiO$_x$ based materials; whereas reversible Li$_2$Si$_2$O$_5$ formation (Reaction (3.1.2)) may also be present [64-66].

irreversible reaction: $2 \text{ SiO}_2 + 4 \text{ Li}^+ + 4 \text{ e}^- \rightarrow \text{Li}_4\text{SiO}_4 + \text{Si}$ (3.1.1)

reversible reaction: $5 \text{ SiO}_2 + 4 \text{ Li}^+ + 4 \text{ e}^- \leftrightarrow 2 \text{ Li}_2\text{Si}_2\text{O}_5 + \text{Si}$ (3.1.2)

The Si 2p XPS spectrum (Figure 3.1.6b) of the electrode demonstrates that pristine Si NP consists of Si (99.4 eV) and SiO_2 (103.3 eV). The peak from SiO_2 dominates since XPS is surface sensitive (~ few nm). Upon initial dis-/charge SiO_2 has been partially reduced to SiO_x (~ 102.4 eV); the production of Li_xSiO_y (~ 100.5 eV) is also evident according to reactions (1) and (2); The peak of Si is almost invisible under XPS due to the coverage of the SEI. After 100 cycles, the Si 2p spectrum is dominated by Li_xSiO_y due to the further consumption of SiO_x and formation of Li_xSiO_y (mainly in SEI).

The XPS spectra after the 1st cycle indicate that the SEI layer is composed of a series of substances, such as LiF, Li_2CO_3, Li_xSiO_y, and ROCOOLi, etc., which are produced upon the decomposition of organic electrolyte and the following reactions with Si NP. The commonly recognized LiF is evidenced from the dominating peak at 684.8 eV in the F 1s spectrum and the one at 55.5 eV in the Li 1s spectrum. Meanwhile, Li_xPF_y and $Li_xPO_yF_z$ are also observed, which originate from the decomposition of $LiPF_6$ in the electrolyte.

Comparing the XPS spectra after 100 cycles and after the 1st cycle, it shows that the composition of the SEI varies slightly. The amounts of Li_xSiO_y, ROCOOLi, ionic C-F and $Li_xPO_yF_z$ appear to increase, and LiF and Li_xPF_y turn out to be less. This phenomenon can be ascribed to a couple of reasons: (1) Different reactions may take place over time due to the presence of the initial SEI stratum; (2) The SEI layer thickens slightly with fresh layers along cycling. Since XPS is surface sensitive, the SEI formed in later cycles is more visible.
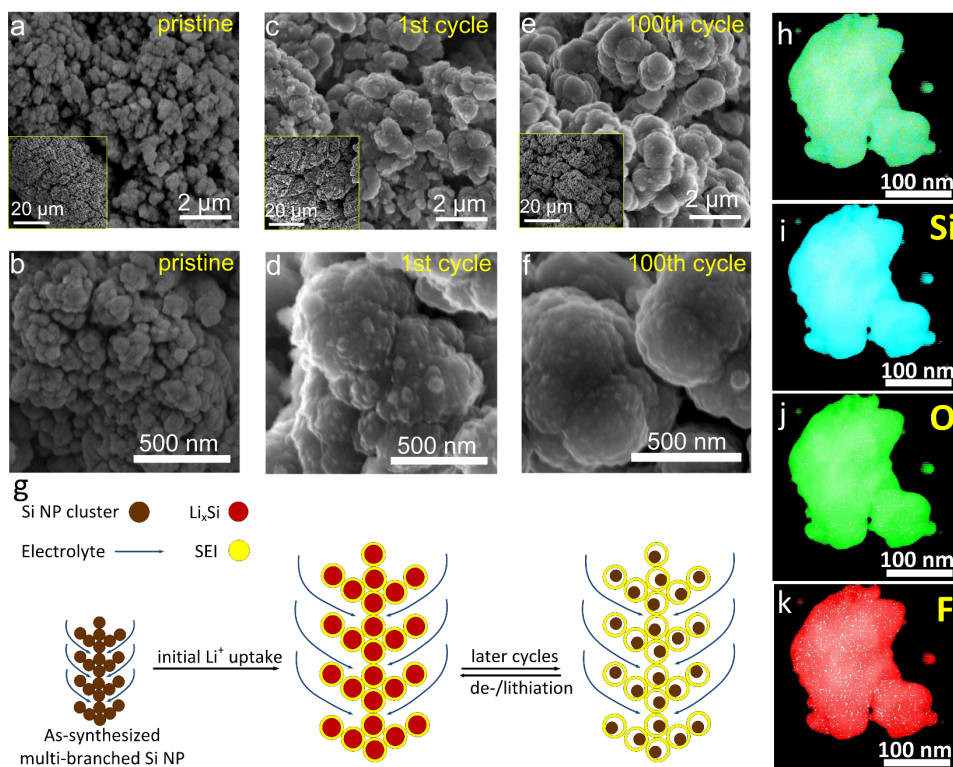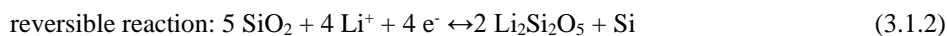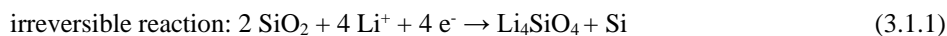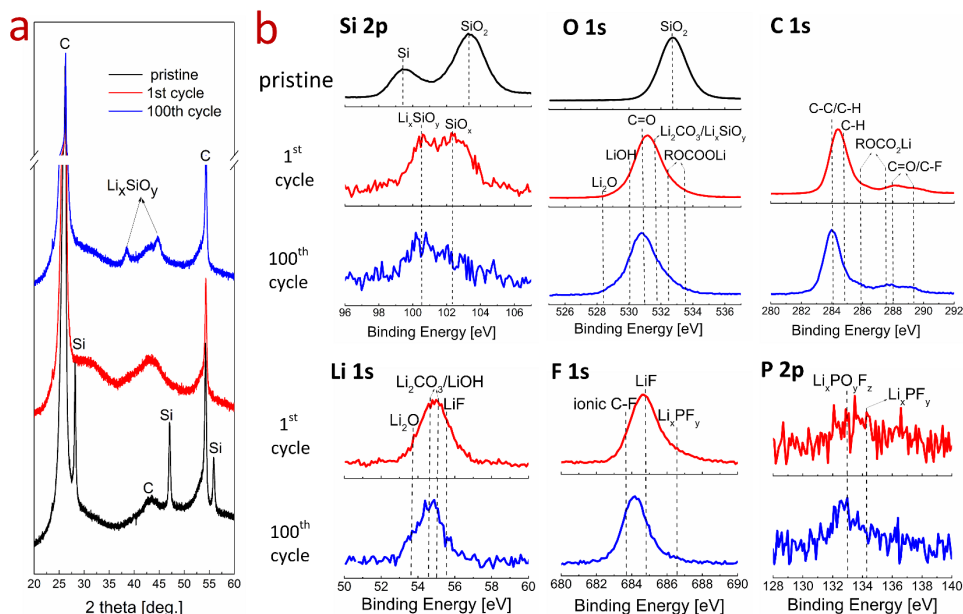
Figure 3.1.6 Characterization on the Si NP electrode at three different stages: pristine, after the 1st cycle and after 100 cycles at 0.8 A g^{-1}. (a), XRD patterns of Si NP electrode. (b), XPS spectra of Si NP electrode. The electrodes were washed with DEC for 3 times to remove any chemical residuals (mainly LiPF$_6$) on the electrode and were then dried in glove box to evaporate any organic volatile compounds (mostly DEC) before XPS and XRD measurement.

3.1.4   Conclusions

In conclusion, the binder/carbon-free Si NP anode synthesized via direct PECVD promises a particularly rapid and scalable synthesis method for Si anodes of Li ion batteries. The electrodes show high specific and areal capacity as well as cycling stability. The Si NP anode shows sufficient electronic conductivity facilitated by the lithiation of Si throughout the solid. Excellent cycling stability results from the *in-situ* formation of locally protective SEI on the clusters of the individual nanoparticles throughout the electrode; it apparently reinforces the cohesion of the clusters the single particles as well as the entire electrode, while the electronic conduction throughout the electrode is maintained. Overall, this novel and binder/C-free Si anode exhibits unprecedented high areal capacity at high current rates and surprising resistance to electrode degradation. Using modified but large throughput solar photovoltaic production equipment the method also may provide a significant promise for the commercial large scale production of Si anodes for Li ion batteries.

References

[1] S. Chu, A. Majumdar, Nature 488 (2012) 294-303.

[2] B. Dunn, H. Kamath, J.-M. Tarascon, Science 334 (2011) 928-935.

[3] M. Armand, J.M. Tarascon, Nature 451 (2008) 652-657.

[4] Y. Sun, N. Liu, Y. Cui, Nat. Energy (2016) 16071.

[5] J.M. Tarascon, M. Armand, Nature 414 (2001) 359-367.

[6] M.N. Obrovac, L. Christensen, Electrochem. Solid-State Lett. 7 (2004) A93-A96.

[7] D. Ma, Z. Cao, A. Hu, Nano-Micro Lett. 6 (2014) 347-358.

[8] M. Ashuri, Q. He, L.L. Shaw, Nanoscale 8 (2016) 74-103.

[9] X. Zuo, J. Zhu, P. Müller-Buschbaum, Y.-J. Cheng, Nano Energy 31 (2017) 113–143.

[10] A.S. Arico, P. Bruce, B. Scrosati, J.-M. Tarascon, W. van Schalkwijk, Nat. Mater. 4 (2005) 366-377.

[11] H. Wu, Y. Cui, Nano Today 7 (2012) 414-429.

[12] X. Su, Q. Wu, J. Li, X. Xiao, A. Lott, W. Lu, B.W. Sheldon, J. Wu, Adv. Energy Mater. 4 (2014) 1300882.

[13] C.K. Chan, H. Peng, G. Liu, K. McIlwrath, X.F. Zhang, R.A. Huggins, Y. Cui, Nat. Nanotechnol. 3 (2008) 31-35.

[14] L.-F. Cui, R. Ruffo, C.K. Chan, H. Peng, Y. Cui, Nano Lett. 9 (2009) 491-495.

[15] T. Song, J. Xia, J.-H. Lee, D.H. Lee, M.-S. Kwon, J.-M. Choi, J. Wu, S.K. Doo, H. Chang, W.I. Park, D.S. Zang, H. Kim, Y. Huang, K.-C. Hwang, J.A. Rogers, U. Paik, Nano Lett.10 (2010) 1710-1716.

[16] H. Wu, G. Chan, J.W. Choi, I. Ryu, Y. Yao, M.T. McDowell, S.W. Lee, A. Jackson, Y. Yang, L. Hu, Y. Cui, Nat. Nanotechnol. 7 (2012) 310-315.

[17] H. Ma, F. Cheng, J.Y. Chen, J.Z. Zhao, C.S. Li, Z.L. Tao, J. Liang, Adv. Mater. 19 (2007) 4067-4070.

[18] B. Liu, P. Soares, C. Checkles, Y. Zhao, G. Yu, Nano Lett. 13 (2013) 3414-3419.

[19] B. Zhu, N. Liu, M. McDowell, Y. Jin, Y. Cui, J. Zhu, Nano Energy 13 (2015) 620-625.

[20] X. Zhou, Y.-X. Yin, L.-J. Wan, Y.-G. Guo, Adv. Energy Mater. 2 (2012) 1086-1090.

[21] K. Evanoff, A. Magasinski, J. Yang, G. Yushin, Adv. Energy Mater. 1 (2011) 495-498.

[22] L. Xue, G. Xu, Y. Li, S. Li, K. Fu, Q. Shi, X. Zhang, ACS Appl. Mater. Interfaces 5 (2013) 21-25.

[23] S.-M. Jang, J. Miyawaki, M. Tsuji, I. Mochida, S.-H. Yoon, Carbon 47 (2009) 3383-3391.

[24] G. Liu, S. Xun, N. Vukmirovic, X. Song, P. Olalde-Velasco, H. Zheng, V.S. Battaglia, L. Wang, W. Yang, Adv. Mater. 23 (2011) 4679-4683.

[25] C. Wang, H. Wu, Z. Chen, M.T. McDowell, Y. Cui, Z. Bao, Nat. Chem. 5 (2013) 1042-1048.

[26] Q. Xiao, Y. Fan, X. Wang, R.A. Susantyoko, Q. Zhang, Energy Environ. Sci. 7 (2014) 655-661.

[27] H. Wu, G. Yu, L. Pan, N. Liu, M.T. McDowell, Z. Bao, Y. Cui, Nat. Commun. 4 (2013) 1943.

[28] Y. Yao, M.T. McDowell, I. Ryu, H. Wu, N. Liu, L. Hu, W.D. Nix, Y. Cui, Nano Lett. 11 (2011) 2949-2954.

[29] Z. Chen, C. Wang, J. Lopez, Z. Lu, Y. Cui, Z. Bao, Adv. Energy Mater. 5 (2015) 1614-6840.

[30] I.H. Son, J. Hwan Park, S. Kwon, S. Park, M.H. Rummeli, A. Bachmatiuk, H.J. Song, J. Ku, J.W. Choi, J.-m. Choi, S.-G. Doo, H. Chang, Nat. Commun. 6 (2015) 7393.

[31] D. Lin, Z. Lu, P.-C. Hsu, H.R. Lee, N. Liu, J. Zhao, H. Wang, C. Liu, Y. Cui, Energy Environ. Sci. 8 (2015) 2371-2376.

[32] X. Li, M. Gu, S. Hu, R. Kennard, P. Yan, X. Chen, C. Wang, M.J. Sailor, J.-G. Zhang, J. Liu, Nat. Commun. 5 (2014) 4105.

[33] N. Liu, Z. Lu, J. Zhao, M.T. McDowell, H.-W. Lee, W. Zhao, Y. Cui, Nat. Nanotechnol. 9 (2014) 187-192.

[34] Y. Li, K. Yan, H.-W. Lee, Z. Lu, N. Liu, Y. Cui, Nat. Energy 1 (2016) 15029.

[35] Q. Xu, J.Y. Li, J.K. Sun, Y.X. Yin, L.J. Wan, Y.G. Guo, Adv. Energy Mater. 6 (2016) 1601481.

[36] M. Ko, S. Chae, J. Ma, N. Kim, H.-W. Lee, Y. Cui, J. Cho, Nat. Energy 1 (2016) 16113.

[37] Y. Jin, S. Zhang, B. Zhu, Y. Tan, X. Hu, L. Zong, J. Zhu, Nano Lett. 15 (2015) 7742-7747.

[38] L. Zong, B. Zhu, Z. Lu, Y. Tan, Y. Jin, N. Liu, Y. Hu, S. Gu, J. Zhu, Y. Cui, Proc. Natl. Acad. Sci. U. S. A. 112 (2015) 13473-13477.

[39] L. Zong, Y. Jin, C. Liu, B. Zhu, X. Hu, Z. Lu, J. Zhu, Nano Lett. 16 (2016) 7210-7215.

[40] G. Shoorideh, Y.S. Kim, and Y.L. Joo, Electrochim. Acta 222 (2016) 946-955.

[41] X. Hu, Y. Jin, B. Zhu, Y. Tan, S. Zhang, L. Zong, Z. Lu, J. Zhu, ChemNanoMat 2 (2016) 671-674.

[42] L.-F. Cui, L. Hu, J.W. Choi, Y. Cui, ACS Nano 4 (2010) 3671-3678.

[43] D.P. Wong, R. Suriyaprabha, R. Yuvakumar, V. Rajendran, Y.-T. Chen, B.-J. Hwang, L.-C. Chen, K.-H. Chen, J. Mater. Chem. A 2 (2014) 13437-13441.

[44] D. Nan, Z.-H. Huang, R. Lv, Y. Lin, L. Yang, X. Yu, L. Ye, W. Shen, H. Sun, F. Kang, J. Nanomater. 2014 (2014) 10.

[45] C. Li, C. Liu, W. Wang, J. Bell, Z. Mutlu, K. Ahmed, R. Ye, M. Ozkan, C.S. Ozkan, Chem. Commun. 52 (2016) 11398-11401.

[46] L. Fei, S.H. Yoo, R.A.R. Villamayor, B.P. Williams, S.Y. Gong, S. Park, K. Shin, Y.L. Joo, ACS Appl. Mater. Interfaces 9 (2017) 9738-9746.

[47] J. Graetz, C.C. Ahn, R. Yazami, B. Fultz, Electrochem. Solid-State Lett. 6 (2003) A194-A197.

[48] H. Wolf, Z. Pajkic, T. Gerdes, M. Willert-Porada, J. Power Sources 190 (2009) 157-161.

[49] H. Liu, L. Hu, Y.S. Meng, Q. Li, Nanoscale 5 (2013) 10376-10383.

[50] T. Le Duc, M. Eric, Z. Mihai Robert, J. Jemee, K. Young Woo, P. Didier, Mater. Res. Express 3 (2016) 015003.

[51] B. Erika, S. Alice, B. Andrea Li, B. Paola, Z. Yun, X. Ming, Nanotechnology 27 (2016) 245401.

[51] F. Cheng, Z. Tao, J. Liang, J. Chen, Chem. Mater. 20 (2008) 667-681.

[52] D.P. Singh, F.M. Mulder, A.M. Abdelkader, M. Wagemaker, Adv. Energy Mater. 3 (2013) 572-578.

[53] B. Hoex, A.J.M. van Erven, R.C.M. Bosch, W.T.M. Stals, M.D. Bijker, P.J. van den Oever, W.M.M. Kessels, M.C.M. van de Sanden, Prog. Photovolt: Res. Appl. 13 (2005) 705-712.

[54] I. Dogan, N.J. Kramer, R.H.J. Westermann, K. Dohnalova, A.H.M. Smets, M.A. Verheijen, T. Gregorkiewicz, M.C.M.v.d. Sanden, J. Appl. Phys. 113 (2013) 134306.

[55] W. Wan, Q. Zhang, Y. Cui, E. Wang, J. Phys. Condens. Matter 22 (2010) 415501.

[56] M.T. McDowell, Y. Cui, Adv. Energy Mater. 1 (2011) 894-900.

[57] E. Pollak, G. Salitra, V. Baranchugov, D. Aurbach, J. Phys. Chem. C 111 (2007) 11437-11444.

[58] R. Ruffo, S.S. Hong, C.K. Chan, R.A. Huggins, Y. Cui, J. Phys. Chem. C 113 (2009) 11390-11398.

[59] J. Guo, A. Sun, X. Chen, C. Wang, A. Manivannan, Electrochim. Acta 56 (2011) 3981-3987.

[60] M.B. Pinson, M.Z. Bazant, J. Electrochem. Soc. 160 (2013) A243-A250.

[61] V. Etacheri, O. Haik, Y. Goffer, G.A. Roberts, I.C. Stefan, R. Fasching, D. Aurbach, Langmuir 28 (2012) 965-976.

[62] Y.-M. Lin, K.C. Klavetter, P.R. Abel, N.C. Davy, J.L. Snider, A. Heller, C.B. Mullins, Chem. Commun. 48 (2012) 7268-7270.

[63] K. Schroder, J. Alvarado, T.A. Yersak, J. Li, N. Dudney, L.J. Webb, Y.S. Meng, K.J. Stevenson, Chem. Mater. 27 (2015) 5531-5542.

[64] W.-S. Chang, C.-M. Park, J.-H. Kim, Y.-U. Kim, G. Jeong, H.-J. Sohn, Energy Environ. Sci. 5 (2012) 6895-6899.

[65] N. Yan, F. Wang, H. Zhong, Y. Li, Y. Wang, L. Hu, Q. Chen, Sci. Rep. 3 (2013) 1568.

[66] X. Hu, K. Zhang, L. Cong, F. Cheng, J. Chen, Chem. Commun. 51 (2015) 15827-15830.

Supporting Information for Chapter 3.1

S3.1.1 Set-up of the electrochemical cell

The configuration design and photos of the lab-made electrochemical cell utilized in this work are shown in Figure S3.1.1. During the fabrication of a half-cell Li ion battery, a Li foil, a separator wetted with electrolyte, and the Si NP electrode were placed onto a blank stainless steel flange in sequence; Subsequently the cell was closed by placing an O-ring and a flange with a spring on top and finally closing it with a vacuum clamp.
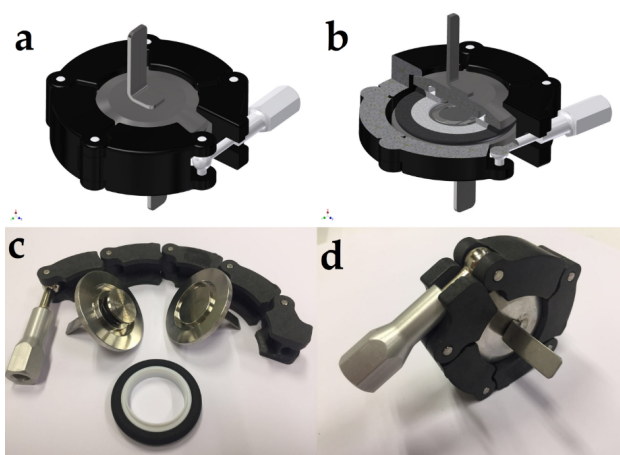

Figure S3.1.1 The electrochemical cell utilized in this work. (a) - (b), design of the prototype cell; and photos of (c), all the cell components and (d) a closed cell.

S3.1.2 Process for Si NP production

Silicon nanoparticles used for electrode preparations were made in a Plasma enhanced chemical vapour deposition (PECVD) process. It starts with generation of an Argon plasma at sub-atmospheric pressure in a cascaded arc, followed by the supersonic expansion of the plasma in a low pressure chamber in which silane is injected. Silicon nanoparticles were deposited on the carbon substrate for multiple layers before it was taken out for further processing. The substrate was transported through the plasma for a fixed exposure time of 30 seconds resulting in the deposition of one layer. Between each deposition, the sample was allowed to cool down below 35 °C in a load lock followed by exposure to air for a few seconds.
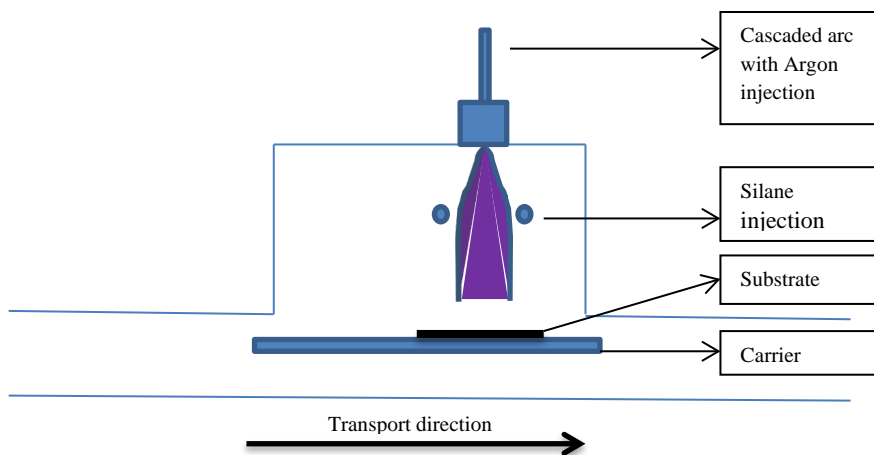
Figure S3.1.2 Schematic representation of the deposition process

Parameter	Power	Argon	Silane	Pressure
Setting	1665 W	4 slm	0.4 slm	1-1.5 mbar

Table S3.1.1 Experimental settings of the PECVD process (slm: Standard Liter per Minute)

Si nanoparticles are deposited onto two types of current collectors: porous carbon sheet (Spectracarb™ 2050A, 127 μm, Caplinq) and non-porous Cu foil (Goodfellow, 12.5 μm). The morphology of the carbon sheet was imaged with SEM (inset of Figure 3.1.2a), it shows that it is made up of thin carbon fibres (~ 6 μm in diameter) and large porosity can be observed.

S3.1.3 Subtraction of the capacity of carbon sheet substrate

The capacity of the carbon sheet itself is determined by cycling the blank carbon sheet electrode at different current rates and then fitting the capacity data with a logistic equation as is indicated in the graph. (Figure S3.1.3) Using this equation, the capacities of the carbon sheet substrate is calculated with respect to the corresponding current rates applied on carbon; and in this way the specific capacity of Si NP can be determined by subtracting the capacity of carbon from that of the Si NP-C electrode.
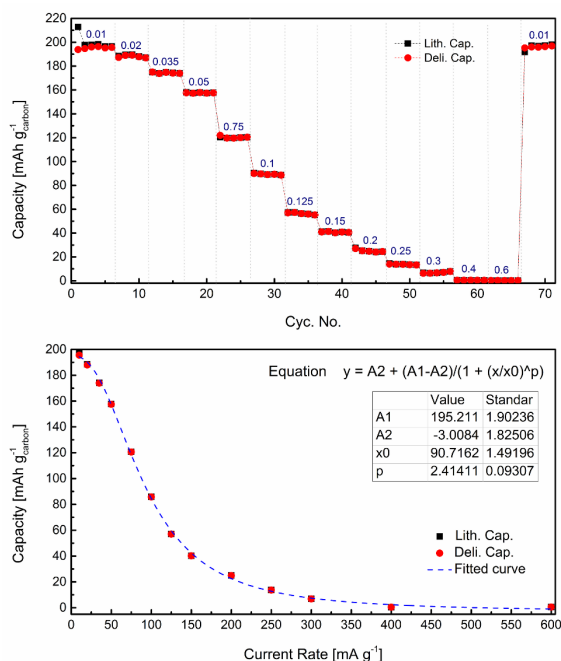
Figure S3.1.3 Top: capacity retention of the carbon sheet cycled at different current rates. The current rates applied are the numbers above the plot in blue font, and the unit is A g^{-1}. Bottom: average capacity retentions of carbon paper under different cycling rates and the fitted plot of capacity retention *vs.* current rate.

Meanwhile, cycling Si NP-C/Cu electrodes with a low mass loading at a low current rate achieves the maximum capacity of the Si NP; as is shown in Figure S3.1.4, the capacity of Si NP with a C substrate, utilizing the above way to subtract the carbon capacity, is numerically in agreement with the achieved capacity of Si NP with a plain Cu substrate.
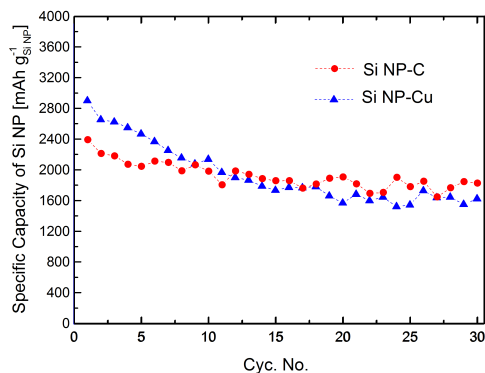
Figure S3.1.4 Electrochemical performance of the Si NP-C/Cu electrode (mass loading: 0.5 mg cm^{-2}) cycled at 0.1 A g^{-1}.

Furthermore, this capacity of carbon was also achieved by, along with each measurement of Si NP-C electrode, measuring a blank carbon sheets using the same test program as that for the Si NP-C electrode. (e.g. in Figure 3.1.3a) The capacity of carbon achieved from these two approaches are comparable. (189 mAh g^{-1} and 184 mA g^{-1} for these two approaches respectively for the measurement in Figure 3.1.3a.) Thus the approach applied to subtract the carbon capacity in the paper is reproducible.

S3.1.4 Morphology of Si NP on Cu as synthesized

Figure S3.1.5 demonstrates the morphology of the Si NP layer on a Cu foil. It shows a branched porous Si NP layer, which is very similar to that on a carbon sheet but much denser since it has no porosity caused by the open structure of the carbon sheet.
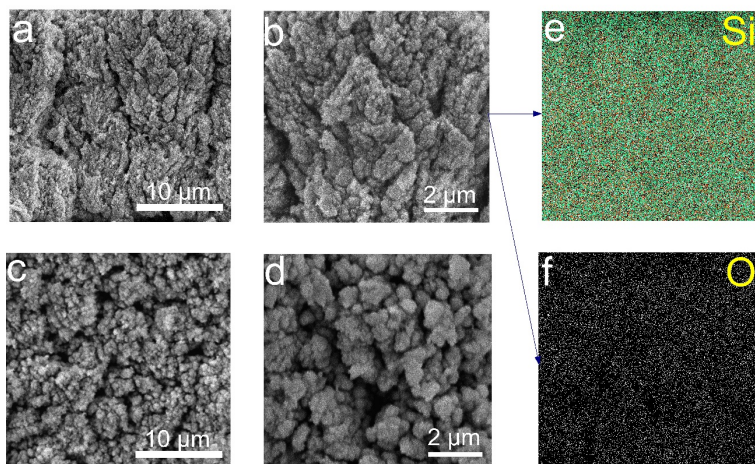
Figure S3.1.5 Morphology of as-synthesized Si NP on a planar Cu substrate. (a) - (b), cross-sectional and (c) – (d), top-view SEM micrographs of the nanostructured Si layer imaged at different magnifications. (e) & (f), EDX element mapping results of Si and O elements, respectively, for the electrode region shown in (b).

S3.1.5 TGA of as-synthesized Si NP

TGA tests show a slight mass decrease during the first half hour due to the evaporation of moisture that is absorbed from air due to its large surface area. After holding the temperature at 1000 °C for 200 min, all Si will be oxidized to SiO_2 and the weight of the sample stops increasing, as can be seen in Figure S3.1.6. It was found that the oxidation level of Si NP on the carbon sheet was higher than that on Cu, which may result from the higher porosity of Si NP layer on carbon leading to a larger surface exposed to air. The details are indicated below.

Assuming the composition of the initial sample is *x* Si + *(1-x)* SiO_2; and after heating under O_2/Ar, all Si is oxidized to SiO_2.

x Si + *(1-x)* SiO_2 + *x* O_2 = *x* SiO_2 + *(1-x)* SiO_2
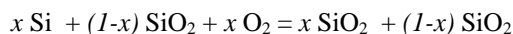
from this equation we get:

x = 0.65 for Si NP on C and *x* = 0.68 for Si NP on Cu

Thus the weight fraction of Si inside the Si NP sample:

Si fraction in Si NP on C: 46.3 wt. % (Si : SiO_2 = 0.65 : 0.35 in mole)

Si fraction in Si NP on Cu: 50.0 wt. % (Si : SiO_2 = 0.68 : 0.32 in mole)

Figure S3.1.6 TGA result of the Si nanoparticles deposited on C/Cu. (The TGA samples are Si nanoparticles scraped from the substrate.)

S3.1.6 Comparison between the Si NP-C electrode and the Si anodes cited in the text

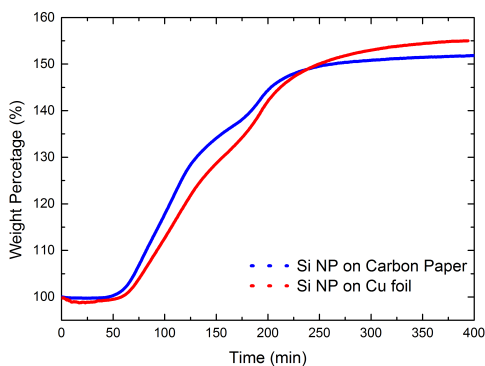| electrode	Type and amount of conducting additives	Type and amount of binder	wt. % of Si	SiO_x treatment	Si loading (mg cm^{-2})	Areal capacity	Ref. # in the text
Si NP layer	**N.A.**	**N.A.**	**100%**	**N.A.**	**2.2**	**2.5 – 4.2 mAh cm^{-2} at 0.8 mA cm^{-2}**	**This work**
Si nanowire	N.A.	N.A.	100%	HF etching	--	--	13
Crystalline-amorphous Si nanowire	N.A.	N.A.	100%	--	0.2	< 0.5 mAh cm^{-2} at 0.2C	14
Arrays of Si nanotube	N.A.	N.A.	100%	--	0.27	0.8 mAh cm^{-2} at 0.05C	15
Double wall Si nanotube	N.A.	N.A.	100%	N.A.	0.02 - 0.1	< 0.13 mAh cm^{-2} at 1C	16
Nest-like Si nanosphere	Carbon black, 12%	PTFE, 3%	85%	--	--	--	17
3D Si NP/PPy/CNT	SWCNT, conductive PPy framework, 30%		~ 70%	--	0.3 – 0.5	--	18
ZnO coated Si NP	carbon black, 10 %	CMC, 10%	80%	--	1.4	> 1.1 mAh cm^{-2} at 0.5 C	19
Graphene encapsulated Si NP	Graphene, 15.9% carbon black, 10%	PVDF, 10%	64.1%	HF etching	--	--	20
Si NP coated graphene	Graphene, 34%	PAA, 15%	51%	--	--	--	21
Si@C–CNTs	C coating, 6.6% CNT, 36.8%	PAI, 20%	36.6%	--	--	--	22
Si–PC–CNF–RC–PC composite	pyrolytic C, 8.5% CNF, 41.3%	CMC, 5% SBR, 10%	35.2%	--	--	--	23
Si NP-PFFOMB	Conductive polymer PFFOMB, 33.3%		66.6%	--	--	--	24
Si MP-SHP/CB	Carbon black, 7%	Self-healing polymer, 46.5%	46.5%	--	0.5 – 0.7	1.5 – 2.1 mAh cm^{-2} at 0.2C	25
Si-CNT coaxial nanofiber	CNT, 40%	N.A.	60%	--	0.42	1.25 mAh cm^{-2} at 0.2C	26
polymerized PANi-Si NP	in situ polymerized conductive framework, 25%		75%	--	0.2-0.3	< 0.5 mAh cm^{-2} at 0.2-0.3 mA cm^{-2}	27

Interconnected Si hollow spheres	N.A.	N.A.	100%	HF etching	0.1 – 0.2	< 0.5 mAh cm^{-2} at 0.5C	28
Si-SHP/CB	Carbon black, 7.7%	Self-healing polymer, 29.0%	63.3%	--	> 1.0	~2.4 mAh cm^{-2} at 0.3 mA cm^{-2}	29
Non-defective Graphene-Si	4.75% graphene	PAA, 20%	75.25 %	--	1.2	2.5 - 3 mAh cm^{-2} at 0.5C	30
Nano-Si @ void @ Carbon cluster	C coating, 3.9 – 21.6 % MWCNT, 5.2% carbon black, 20 %	PVDF, 15%	38.2 – 55.9%	HF etching	2.02	~ 2.5 mAh cm^{-2} at 0.5 mA cm^{-2}	31
Mesoporous sponge with thin Si walls	CVD carbon, 27.2 %	NaCMC, 20%	52.8%	etching in HF/EtOH	~ 2	~1.5 mAh cm^{-2} at 0.5 mA cm^{-2}	32
Si pomegranate @ void @ Carbon	C coating, 19.6 % CNT, 5%	PVDF, 10%	65.4%	HF etching	1.49	~ 2 mAh cm^{-2} at 0.5 mA cm^{-2}	33
Conformal graphene encapsulated Si MP	Graphene, 8.1%	PVDF, 10%	81.9%	HF etching	~2	~ 2 mAh cm^{-2} at 1.4 mA cm^{-2}	34
Si/C Microspheres with hierarchical buffer	C pyrolysis and deposition, 78.75% carbon black, 5 %	NaCMC, 2.5% SBR, 2.5%	11.25 %	--	0.5125	2.54 - 1.91 mAh cm^{-2} at 0.246 mA cm^{-2}	35
Si nanolayer /graphite/carbon hybrids	Graphite & C coating, 87.2% carbon black, 1%	NaCMC, 1.7% SBR, 1.5%	8.62%	--	0.585	3.3 mAh cm^{-2} at 0.5C	36

Table S3.1.2 Comparison of the electrode presented here with Si based electrodes in literature.

Note: 1,"--": no available data can be found in the references.; "N.A.": "not applicable".

2, Some of the data shown in this table were recalculated based on the results from the references when they are not directly specified in the references.

S3.1.7 Temperature effects

The electrochemical performance of the Si NP-C electrode was measured different constant temperatures between 10 °C and 40 °C by placing the batteries inside constant temperature chambers during the measurement. It is observed that, regardless of the capacity retention disparity at different temperatures, no obvious capacity swings was observed.
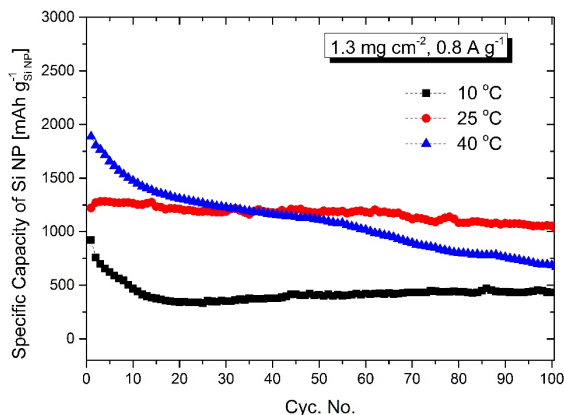
Figure S3.1.7 Capacity retentions of the Si NP-C electrode (Si NP: 1.3 mg cm^{-2}) cycling at 0.8 A g^{-1} for 100 cycles under different constant temperatures. (Temperature accuracy: ± 1 °C)

S3.1.8 Morphologies of Si NP on C/Cu after de-/lithiation

The thickness of the 4-layer Si NP electrode on Cu increased by ~ 150 % after dis-/charged at 0.4 A g^{-1} for 100 cycles; in comparison, the thickness of a 4-layer Si NP electrode on C increased by ~ 150 % and ~ 50 % cycling at 0.4 A g^{-1} and 0.8 A g^{-1}, respectively, due to its higher porosity present in the Si NP layers. EDX element mapping of Si, O and F on the electrode reveals that SEI grows homogeneously throughout the Si NP layers.
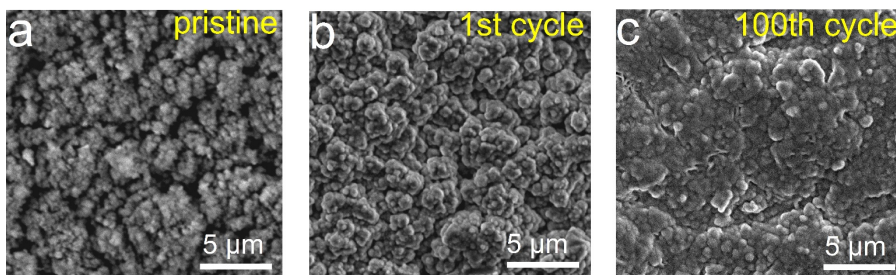
Figure S3.1.8 Morphology of Si NP on a planar Cu substrate cycled at 0.4 A g^{-1}.
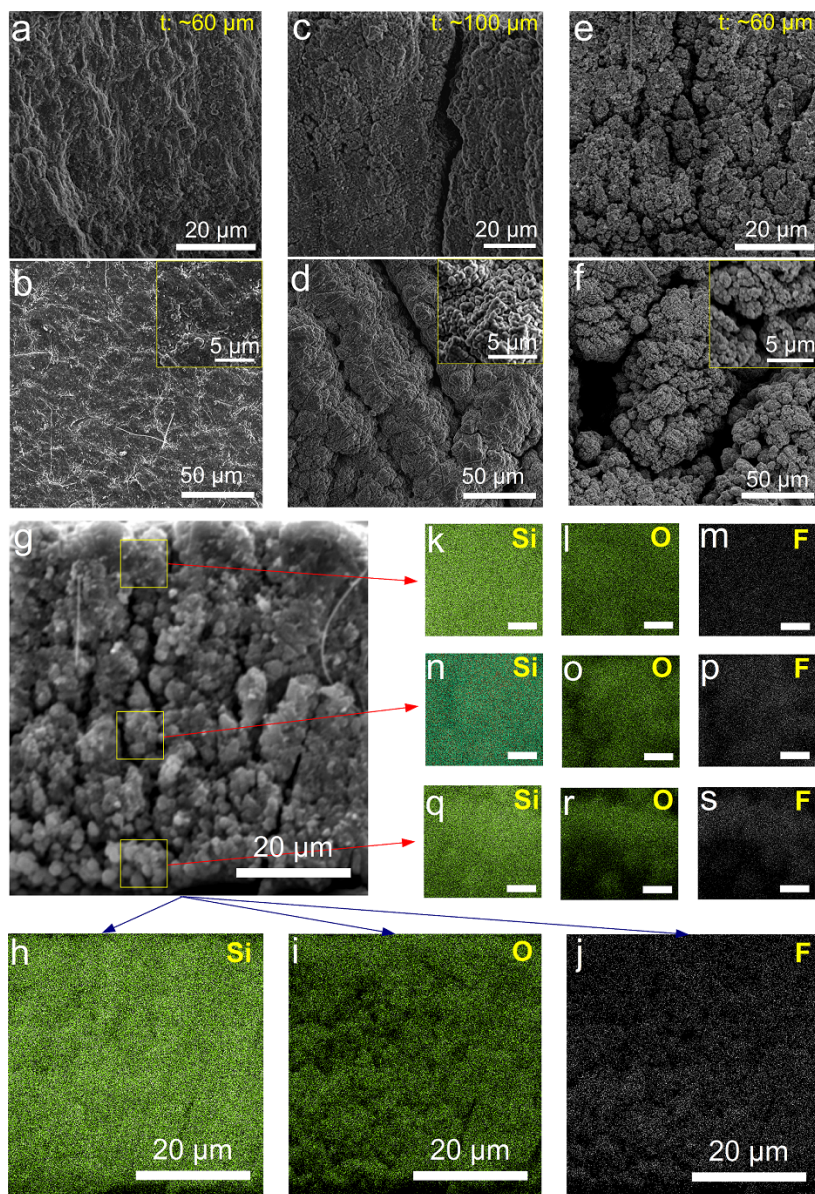
Figure S3.1.9 Morphology of Si NP electrodes after cycling for 100 cycles. (a), cross-sectional and (b), top view of the Si NP layer on Cu after cycling at 0.4 A g^{-1}. (c), cross-sectional and (d), top view of the Si NP layer on C after cycling at 0.4 A g^{-1}. (e), cross-sectional and (f), top view of the Si NP layer on C after cycling at 0.8 A g^{-1}. (g) Si NP layer in (e) and selected areas for EDX element mapping of Si, O and F elements, respectively. EDX element mapping results on the entire Si NP layer: (h) – (j) as well as top: (k) – (m), middle: (n) – (p) and bottom: (q) – (s) part of the electrode. (The length of the scale bars in Figure S3.1.9k – s is 1 μm.)

S3.1.9 Electrochemical performance Si NP on C and Cu

Along with the Si NP-C electrodes, the electrochemical performance of Si NP-Cu based electrodes was measured and compared with the properties of a carbon substrate. The results are demonstrated in Figure S3.1.10 – S3.1.11.
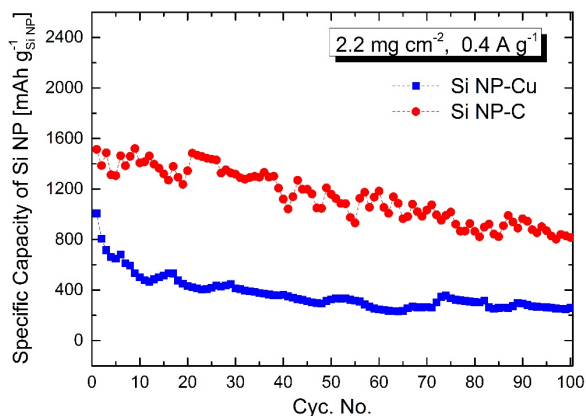
Figure S3.1.10 Capacity retentions of Si NP-C/Cu (Si NP: 2.2 mg cm^{-2}) cycled at 0.4 A g^{-1}. (To be accurate, the current rate for the Si NP-C electrode is 0.36 A g^{-1}, which is recalculated based on the electrochemical measurement at 0.8 mA cm^{-2} in Figure 3.1.3c.)
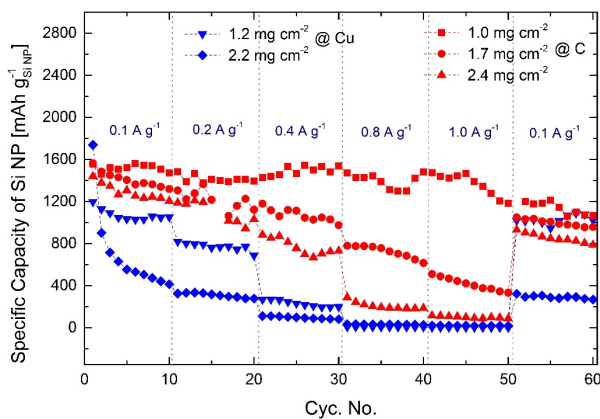
Figure S3.1.11 Specific capacity retentions of Si NP on C and Cu with different mass loadings cycled at different current rates. The planar Cu substrate exhibits inferior rate capabilities since it does not provide the required micron scale porosity as in ref. [52].

S3.1.10 XRD patterns of the Si NP-C electrode at different stages
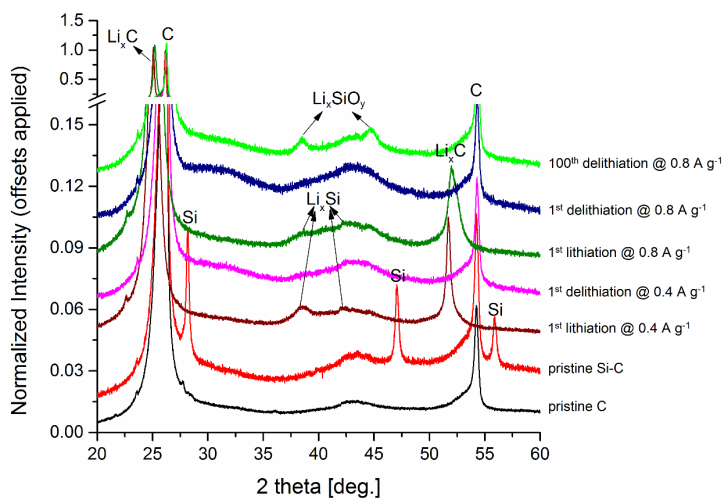
Figure S3.1.12 XRD patterns of the Si NP-C electrode at different stages (offsets applied).

Chapter 3.2

Reversible Na Ion Uptake in Si Nanoparticles

This chapter is based on:

Y. Xu, E. Swaans, S. Basak, H.W. Zandbergen, D.M. Borsa, F.M. Mulder, *Reversible Na-Ion Uptake in Si Nanoparticles*, **Adv. Energy Mater. 6 (2016) 1501436.**

Abstract
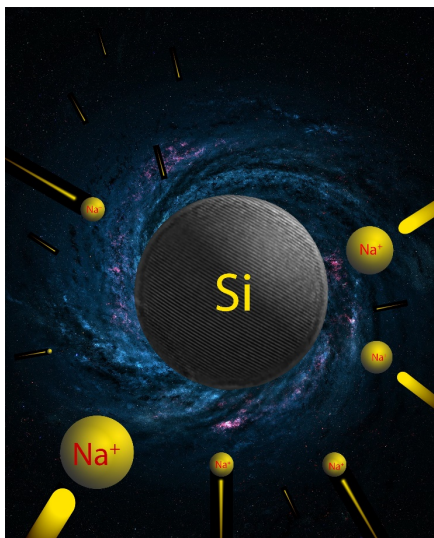
Theoretical studies have predicted that Si can store up to one Na atom per Si atom, but no successful Na ion storage in Si has been reported till date. In this work, Si nanoparticles produced by expanding thermal plasma chemical vapor deposition (ETPCVD) show reversible electrochemical Na ion uptake at room temperature. Sodiation of Si occurs in a two-phase equilibrium reaction; whereas the desodiation involves a solid solution of $Na_{1-x}Si$ ($0 < x < 1$). Si nanomaterials appear as promising anode materials for Na ion batteries for the first time.

3.2.1   Introduction

Na ion batteries attract significant research interest since they provide potentially high energy density while using low cost and abundant sodium as the active ion [1-5]. Due to the analogy between Li and Na ions, different types of materials that have been applied in Li-ion batteries are also studied for application in Na ion batteries and vice versa [6-9]. Si has been extensively investigated since it has high theoretical lithiation capacity up to $Li_{4.4}Si$ [10-12]. In general the sodiation of Si is anticipated to be different with respect to phase behaviour, insertion voltages and kinetic barriers when compared to Li ion, for instance because of the difference in ionic radius of Na^+ (0.97 Å) and Li^+ (0.68 Å) [13, 14]. From thermal synthesis of Na-Si materials it is known that NaSi is the most Na rich phase for Na-Si binary compounds [15], which would enable a sizeable capacity of 954 mAh g^{-1} and be promising for Na-ion battery anodes.

Electrochemical sodiation of Si has been studied theoretically [14, 16-20]; micron-sized Si [21] and nanosized Si (100 nm) [22] also have been studied in experiments but until now reversible sodium insertion has remained unsuccessful. Anticipating that nanoscaling is of advantage for the kinetics of ion insertion and extraction [23, 24], and considering the fact that amorphous Si is more favourable for Na insertion [17, 20], we studied Si nanoparticles (NP) with much reduced size (~ 20 nm) containing a large fraction of amorphous Si obtained from Expanding Thermal Plasma Chemical Vapour Deposition (ETPCVD) of silane. The work presented here reports that, to our knowledge for the first time, reversible electrochemical Na ion uptake in Si is experimentally achieved for a significant capacity.

3.2.2   Experimental details

Characterization: Scanning electron microscopy (SEM) images were taken on Si NP with Au coating on the surface with a JEOL JSM 6010LA scanning electron microscopes at an accelerating voltage of 5 kV; Bright field high resolution transmission electron microscopy (HRTEM) images were captured using a monochromated FEI-Tecnai with a field emission gun (FEG) source operating at 200 kV; X-ray diffraction (XRD) patterns were measured with a PANalytical X'Pert Pro PW3040/60 diffractometer with Cu $K_α$ radiation operating at 45 kV and 40 mA; Raman mapping spectra on Si NP particles were obtained from a Renishaw InVia Raman spectrophotometer with an exposure time of 5 s. The wavelength of the laser applied is 785 nm and the laser power is set at 0.2 mW; Thermogravimetric analysis (TGA)

is carried out with a Perkin Elmer TGA 7 thermogravimetric analyser, Si NP were heated in 20 % O_2/Ar mixture from room temperature to 1000 °C followed by a full oxidation at 1000 °C for 5 h.

Electrode preparation: Electrodes were prepared by a conventional emulsion based process: a well-mixed slurry was prepared by mixing Si nanoparticles as obtained from ETPCVD, sodium carboxymethyl cellulose (NaCMC) (Aldrich) binder and Super P® conductive carbon black in a weight ratio of 5:3:2 in deionized water; then the well-mixed slurry was cast onto Cu foil (Goodfellow) by doctor blading, followed by drying in a vacuum oven and pressing with a roller compressor for good electrical contact.

Electrochemistry: Half-cell Na ion batteries were tested with a counter electrode of Na metal foil, a borosilicate glass micro fibre separator (Whatman), and 1 M $NaClO_4$ dissolved in ethylene carbonate (EC) and propylene carbonate (PC) (1:1 in volume) working electrolyte. Electrochemical performance were measured with a MACCOR 4600 battery cycler. Cyclic voltammetry (CV) tests were conducted using a PGSTAT302N Autolab potentiostat.

3.2.3   Results and discussions

The morphology of Si NP produced by ETPCVD are characterized with SEM and TEM. Figure 3.2.1a shows that bundles of Si nanoparticle clusters are observed in a fibrous, tree like, morphology with micron sized fibre branches consisting of small nanoparticles. Figure 3.2.1b demonstrates that individual crystalline Si particles appear to be nicely spherical, whereas the surface layer has been oxidized. A native oxidation layer grows on the surface of individual Si nanoparticles when they are exposed to traces of air after synthesis. The presence of such limited pacifying oxide layer appeared of advantage for the further processing in air. The average thickness of the oxidation layer is around 1.2 nm, and it is amorphous when observed by XRD (Figure 3.2.1c) i.e. only peaks corresponding to crystalline Si are visible. For a particle with a size of 20 nm Si in diameter and 1.2 nm outer layer of SiO_2, the volume percentage of SiO_2 is 28.8 %. Raman spectra (Figure 3.2.1d) on the sample report that both crystalline and amorphous Si exist and the amount of amorphous Si is significant (*c*-Si : *a*-Si = 0.39 : 0.61; quantitative analysis in the Supporting Information (SI)). To determine the amount of oxygen in the sample, TGA is carried out by heating the Si NP sample under a mixture of O_2/Ar gas and fully oxidizing Si into SiO_2. The result indicates that the amount of Si accounts for 69.0 wt. % of the sample (Figure S3.2.2), i.e. Si :

SiO_2 = 0.83 : 0.17 in mole. Meanwhile, the volume fraction from the estimated mass ratio above is 28.2 % and is in good quantitative agreement with the one estimated from TEM.
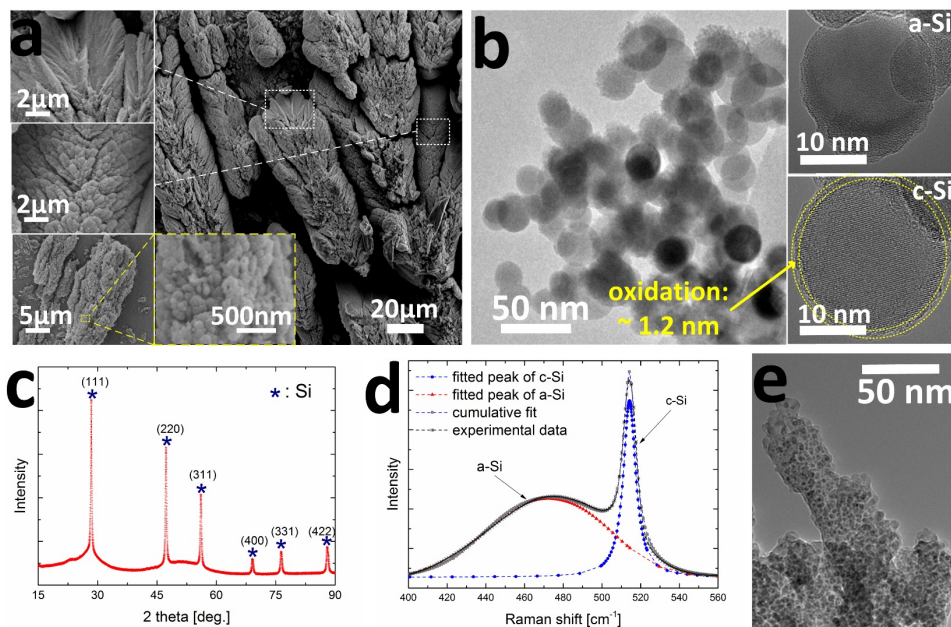
Figure 3.2.1 Characterization on the as-synthesized Si NP and cycled electrode. (a) SEM of Si nanoparticle clusters; (b) TEM of Si nanoparticles; (c) X-ray diffraction patterns on as-synthesized Si nanoparticles; (d) Raman spectroscopy of Si nanoparticles showing the coexistence of a-Si & c-Si; (e) morphology of sodiated Si NP electrode after charge/discharge for 100 cycles at 20 mA g^{-1}.

Galvanostatic tests on the Si NP electrode are performed using different dis-/charge currents between applied potentials of 0.01 V and 2.8 V. In this paper all specific currents applied are calculated with respect to the mass of Si. De-/sodiation capacities of Si stated in this paper are the capacities after subtracting the capacity of the super P carbon black (Figure S3.2.3), and excluding inactive SiO_x inside the sample.

Figure 3.2.2a demonstrates an initial sodiation capacity of 1027 mAh g^{-1} for Si at 20 mA g^{-1}, which is higher than the theoretical capacity (954 mAh g^{-1} for NaSi). A large part of this initial capacity is attributed to the irreversible formation of a solid electrolyte interface (SEI) layer on the surface of Si in combination with some decomposition of electrolyte, and possibly also the irreversible formation of sodium silicate from reaction with SiO_2. The subsequent Na ion extraction process achieves a capacity up to 270 mAh g^{-1}, indicating that

a significant Na fraction is stored reversibly, next to the large irreversible part. For the subsequent few cycles the sodiation capacity decreases from above 410 mAh g^{-1} to around 300 mAh g^{-1} but the desodiation capacity is relatively stable around 260 mAh g^{-1}. The Coulombic efficiency grows gradually to > 90 %, after which the de-/sodiation capacity becomes relatively stable. After 100 cycles the reversible capacity retention reaches 248 mAh g^{-1}, which is 92 % of the first desodiation capacity; and the Coulombic efficiency declines slowly to 87 % in this cycle test. Additionally, Figure 3.2.1e shows that after charge/discharge for 100 cycles Si particles in this electrode got fractured into small grains and no crystalline phase is observed.

The galvanostatic sodiation voltage profile (Figure 3.2.2b) demonstrates a higher voltage plateau at ~ 1.1 V for the 1st Na insertion process, attributed to the SEI formation and side reactions with SiO$_x$; while this is not visible for the following cycles. A long sloping lower voltage plateau is observed during which most sodium is inserted into Si. In comparison, during desodiation the voltage pattern shows a more continuous increase from 0.1 V to the cut-off voltage. In terms of the energy efficiency the higher voltages during desodiation are not favourable.

The Si NP electrode is also cycled at a varying current range from 10 mA g^{-1} to 500 mA g^{-1}. Figure 3.2.2c shows that an initial reversible desodiation capacity of 279 mAh g^{-1}, corresponding to Na$_{0.29}$Si, is achieved at 10 mA g^{-1}. At the higher cycling rates the capacity appears to be reaching lower values, but at the highest dis-/charge rate there is still a capacity retention of 90 mAh g^{-1}. Meanwhile the Coulombic efficiency appears to grow with increasing current rates, and an efficiency of > 98 % is achieved at 500 mA g^{-1}. Higher current rate probably mainly leads to a surface layer reaction of Si avoiding deeper Na ion diffusion into the particles. This reduces the ionic transport time and accelerates the desodiation kinetics, hence a higher Coulombic efficiency can be achieved at relatively high rates.

Figure 3.2.2d shows that the overpotentials resulting from higher current rates are rather symmetrical for both Na insertion and extraction. The electronic and ionic resistances in the system make that the cut-off voltage are reached more rapidly at higher rates, hence the achieved capacity reduces. Still in Figure 3.2.2c it is visible that increasing dis-/charge rates is possible with lower capacity but with improved Coulombic efficiency. Apart from sufficient ionic conductivity this also indicates sufficient electronic conductivity, likely because the inserted Na ions and associated doping lead to a better electronic conductivity of

the electrode. Similar effects have been reported on lithiation of Si [25, 26], and theoretical studies on Na ion insertion in Si based materials [14, 16].

To obtain insight in the equilibrium potentials during sodiation and desodiation the galvanostatic intermittent titration technique (GITT) is utilized. Current pulses of 20 mA g^{-1} for a 5 min duration are applied, with a relaxation period of 25 min in between in which the potential has time to relax in the direction of equilibrium. GITT (Figure 3.2.2e) shows a capacity of 771 mAh g^{-1} (i.e. Na$_{0.81}$Si) for Si during sodium insertion and a capacity of 360 mAh g^{-1} (i.e. Na$_{0.38}$Si) upon sodium extraction.

Figure 3.2.2e gives an indication of the overpotentials during cycling as well. Lower overpotentials are observed at lower voltage; whereas a relatively large overpotential up to ~ 0.3 V can be observed when the voltage is above 1.0 V. A higher Na concentration apparently results in a better internal ionic and/or electronic conductivity.

The sloping lower voltage plateau (< 0.5 V) for GITT sodiation, which is also observed in Figure 3.2.2b & d, may result from the coexistence of Si and NaSi. The proposal is thus that sodiation occurs in a two phase equilibrium Reaction (3.2.1):

x Na + Si = x NaSi + *(1-x)* Si   (3.2.1)

CV measurements were performed between 0.01 V and 2.8 V at different scan rates. Figure 3.2.2f shows, at a scan rate of 0.2 mV s^{-1}, a distinct cathodic peak at 0.04 V attributed to the Na ion insertion into crystalline Si, which is extracted at 0.08 V during the anodic scan; whereas Na uptake in amorphous Si occurs at a higher and broader voltage range (< 0.8 V). At increasing scan rates the potential peaks shift gradually to lower voltages for sodiation and higher potentials for desodiation, respectively, caused by the increasingly significant overpotentials. (More CV measurements on Si NP electrode and super P carbon electrode can be found in Figure S3.2.6.)
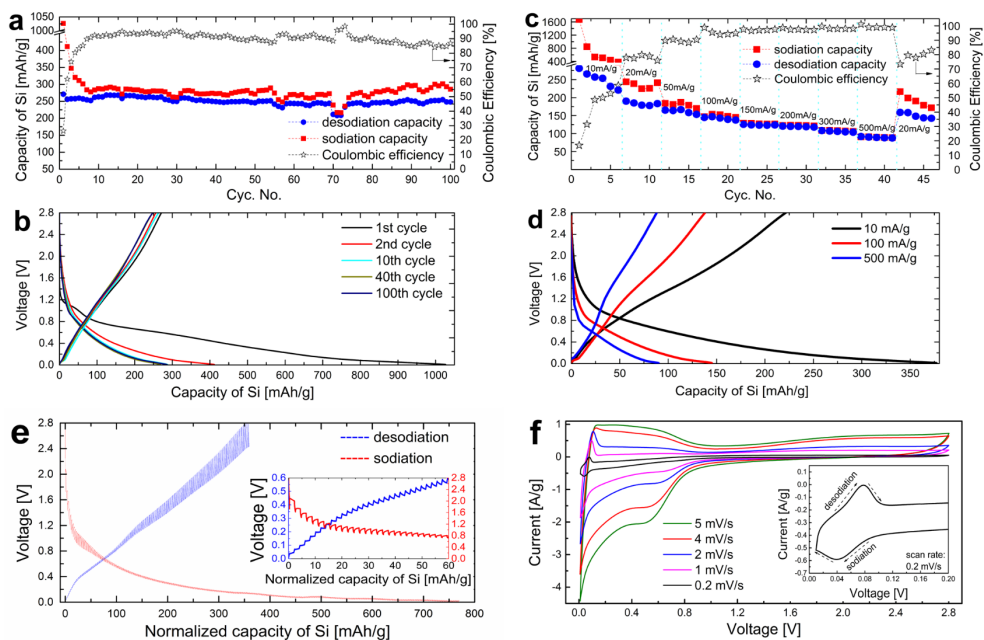
Figure 3.2.2 Electrochemical tests of Si NP electrodes. (a) capacity retention and Coulombic efficiency & (b) charge/discharge voltage profiles at 20 mA g^{-1}; (c) rate capability; (d) voltage response of 5th cycle dis-/charge at different current rates; (e) GITT de-/sodiation test (current pulses: 20 mA g^{-1} for 5 min during charge/discharge; relaxation for 25 min). GITT was carried out on a battery cell after cycling at 20 mA g^{-1} for 5 cycles. (f) Cyclic voltammograms of Si NP electrode at different scan rates. (inset: cyclic voltammogram in the voltage range < 0.2 V at a scan rate of 0.2 mV s^{-1}.)

To obtain more information about the sodiation mechanism of Si, XRD is conducted on an electrochemically cycled thicker ($\sim$ 300 μm) pressed pellet electrode with the same composition as a slurry based electrode. The thicker electrode results in a better signal to noise ratio and avoids strong diffraction peaks from a Cu substrate. The pellet electrode is sodiated at 10 mA g^{-1} and a capacity of 736 mAh g^{-1} is achieved from this process. For the as-prepared and sodiated electrode a reflection mode XRD pattern was obtained under Ar atmosphere from the side of the electrode that has been in contact with the electrolyte, as is shown in Figure 3.2.3a and 3.2.3b. The peaks of crystalline Si are strongly reduced in the initially sodiated electrode, demonstrating the Na ion uptake and alloying process with crystalline Si. No distinct sharp extra peaks can be identified from the sodiated electrode. A broad bump at lower 2θ (20 - 30°) emerges when comparing with the pristine electrode. Since various Na-Si alloys with larger unit cells exist, a contribution of such type of material can

be present, however, in view of the large integrated intensity and the relatively smaller loss of Si diffraction intensity most of this additional broad diffraction intensity has to be attributed to the formation of an SEI layer on top of the Si electrode.
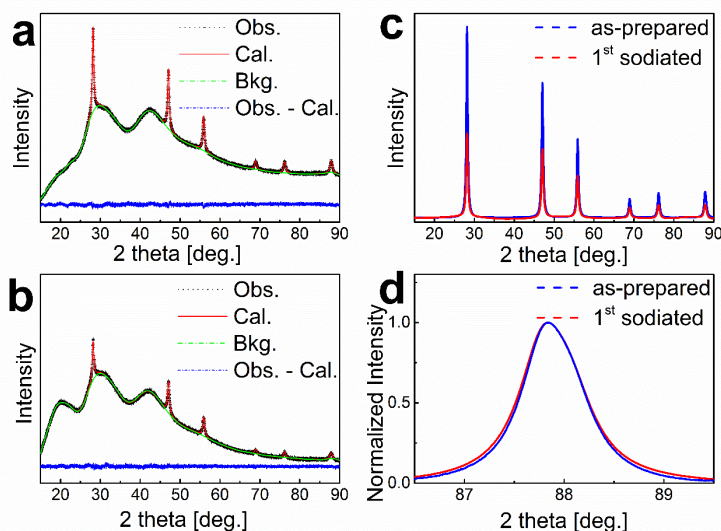

Figure 3.2.3 XRD patterns. (a) the as-prepared and (b) first cycle sodiated thick pellet electrode including Rietveld refinement; (c) refined XRD patterns of a Si NP pressed pellet electrode before and after initial sodiation, after subtraction of background; (d) Lorentzian broadening (L_x) as observed at $2\theta = 87.9°$ before and after sodiation.

The Rietveld refinement of the thick electrode before and after 1st sodiation is performed via General Structure Analysis System (GSAS) program by including crystalline Si (space group: *Fd-3m*). There is a negligible lattice parameter increase (0.0014 Å) of the Si after sodiation which may indicate that at most a negligible amount of Na will be inserted in the crystalline Si phase. The difference before and after sodiation is a small but distinct domain size reduction of the crystalline Si. The size decreases from avg. 20.9 nm to 18.7 nm calculated by the Scherrer equation using a Lorentzian broadening (L_x) as observed in Figure 3.2.3d. Such size reduction corresponds to a reduction of 28.4 % in volume, and therefore in mass. The amount of crystalline Si visible also decreased, but to an extend of 62 % in the Rietveld refinement. This larger peak intensity drop will be resulting from the absorption and scattering by the SEI layer on top of the electrode that weakens the X-ray diffraction intensity from the crystalline Si. We assume that the capacity for Na insertion may reach the composition Na_1Si in both amorphized Si on the surface of the crystalline particles and in the

amorphous Si particles in the sample. Considering that the crystalline volume part reduces by 28.4 % in the first cycle, the capacity contribution of crystalline and amorphous Si could be 954 * 28.4 % = 271 mAh g^{-1}, which fairly matches the reversible capacity observed for the whole sample, including the amorphous fraction. The Na storage in the amorphous Si therefore can consistently have a similar magnitude as in the crystalline fraction, which rapidly becomes amorphous upon sodiation. The further capacity loss during the first cycle must be due to the SEI formation. Also in view of the stable capacity retention for subsequent cycles in which crystalline Si is further converted to amorphous Si (Figure 3.2.1e & Figure S3.2.9) there is no reason to assume a difference between Na insertion in amorphous or crystalline silicon.

The Na ion extraction occurs at different more strongly sloping voltages which may be indicating a desodiation reaction involving a solid solution of $Na_{1-x}Si$ with a Na content varying between 1 and 0, as is in Reaction (3.2.2):

$$NaSi = Na_{1-x}Si + x\,Na \tag{3.2.2}$$

Such phases are also observed in high temperature synthesized NaSi and in $Na_{1-x}Si$ alloys and clathrate structures that are produced during high temperature extraction of Na ion from NaSi [27, 28], In view of the higher potentials during Na extraction desodiation from NaSi proves to be more difficult than sodiation of Si.

3.2.4   Conclusions

In conclusion, nanoparticles containing both amorphous and crystalline Si, produced by ETPCVD, demonstrate an excellent reversible capacity of 279 mAh g^{-1} for Si at 10 mA g^{-1} and a capacity retention of 248 mA g^{-1} after 100 cycles at 20 mA g^{-1}. Significant reversible capacities can be achieved at high dis-/charge rates as well. We conclude that reversible electrochemical Na ion uptake in Si can be realized at room temperature. Nanoscaling benefits the Na insertion and extraction kinetics in Si although reversible Na uptake and release for the full theoretical capacity has not been reached. Initial amorphous and crystalline Si are performing an equally active role in the electrochemical sodiation. Coexistence of Si and NaSi may occur during Na insertion into amorphous Si and on the surface of the Si crystallites; while a solid solution desodiation reaction is evidenced when Na is being extracted. The observed first sizeable activity for reversible Na uptake may be applicable in a Na ion battery.

References

[1] X. Fan, J. Mao, Y. Zhu, C. Luo, L. Suo, T. Gao, F. Han, S.-C. Liou, C. Wang, Adv. Energy Mater. 5 (2015) 1500174.

[2] H. Pan, X. Lu, X. Yu, Y.-S. Hu, H. Li, X.-Q. Yang, L. Chen, Adv. Energy Mater. 3 (2013) 1186-1194.

[3] V. L. Chevrier, G. Ceder, J. Electrochem. Soc. 158 (2011) A1011-A1014.

[4] B. L. Ellis, L. F. Nazar, Curr. Opin. Solid State Mater. Sci. 16 (2012) 168-177.

[5] V. Palomares, P. Serras, I. Villaluenga, K. B. Hueso, J. Carretero-Gonzalez, T. Rojo, Energy Environ. Sci. 5 (2012) 5884-5901.

[6] J. Ding, H. Wang, Z. Li, A. Kohandehghan, K. Cui, Z. Xu, B. Zahiri, X. Tan, E. M. Lotfabad, B. C. Olsen, D. Mitlin, ACS Nano 7 (2013)11004-11015.

[7] Y. Kim, Y. Kim, Y. Park, Y. N. Jo, Y.-J. Kim, N.-S. Choi and K. T. Lee, Chem. Commun. 51 (2015) 50-53.

[8] Y. Zhu, X. Han, Y. Xu, Y. Liu, S. Zheng, K. Xu, L. Hu, C. Wang, ACS Nano 7 (2013) 6378-6386.

[9] D. Wu, X. Li, B. Xu, N. Twu, L. Liu, G. Ceder, Energy Environ. Sci. 8 (2015) 195-202.

[10] C. K. Chan, H. Peng, G. Liu, K. McIlwrath, X. F. Zhang, R. A. Huggins, Y. Cui, Nat. Nanotechnol. 3 (2008) 31-35.

[11] M.-H. Park, M. G. Kim, J. Joo, K. Kim, J. Kim, S. Ahn, Y. Cui, J. Cho, J. Cho, Nano Lett. 9 (2009) 3844-3847.

[12] H. Wu, Y. Cui, Nano Today 7 (2012) 414-429.

[13] S. P. Ong, V. L. Chevrier, G. Hautier, A. Jain, C. Moore, S. Kim, X. Ma, G. Ceder, Energy Environ. Sci. 4 (2011) 3680-3688.

[14] V. V. Kulish, O. I. Malyi, M.-F. Ng, Z. Chen, S. Manzhos, P. Wu, Phys. Chem. Chem. Phys. 16 (2014) 4260-4267.

[15] H. Morito, T. Yamada, T. Ikeda, H. Yamane, J. Alloys Compd. 480 (2009) 723-726.

[16] I. M. Oleksandr, L. T. Teck, M. Sergei, Appl. Phys. Express 6 (2013) 027301.

[17] S. C. Jung, D. S. Jung, J. W. Choi, Y.-K. Han, J. Phys. Chem. Lett. 5 (2014) 1283-1288.

[18] O. Malyi, V. V. Kulish, T. L. Tan, S. Manzhos, Nano Energy 2 (2013) 1149-1157.

[19] F. Legrain, S. Manzhos, J. Power Sources 274 (2015) 65-70.

[20] F. Legrain, O. I. Malyi, S. Manzhos, Comput. Mater. Sci. 94 (2014) 214-217.

[21] L. D. Ellis, B. N. Wilkes, T. D. Hatchard, M. N. Obrovac, J. Electrochem. Soc. 161 (2014) A416-A421.

[22] S. Komaba, Y. Matsuura, T. Ishikawa, N. Yabuuchi, W. Murata, S. Kuze, Electrochem. Commun. 21 (2012) 65-68.

[23] Y. Wang, H. Li, P. He, E. Hosono, H. Zhou, Nanoscale 2 (2010) 1294-1305.

[24] P. G. Bruce, B. Scrosati, J. M. Tarascon, Angew. Chem. Int. Ed. 47 (2008) 2930-2946.

[25] M. T. McDowell, Y. Cui, Adv. Energy Mater. 1 (2011) 894-900.

[26] E. Pollak, G. Salitra, V. Baranchugov, D. Aurbach, J. Phys. Chem. C 111 (2007) 11437-11444.

[27] M. Pouchard, C. Cros, P. Hagenmuller, E. Reny, A. Ammar, M. Ménétrier, J.-M. Bassat, Solid State Sci. 4 (2002) 723-729.

[28] G. K. Ramachandran, J. Dong, J. Diefenbacher, J. Gryko, R. F. Marzke, O. F. Sankey, P. F. McMillan, J. Solid State Chem. 145 (1999) 716-730.

Supporting Information for Chapter 3.2

S3.2.1 Supplementary TEM characterization on the as-synthesized Si NP sample:

As is observed in Figure S3.2.1, some small volume fraction of amorphous particles (< 5 nm) stay on the surface of the 10-20 nm particles; and amorphous and crystalline 10-20 nm Si particles distribute quite evenly in the sample.
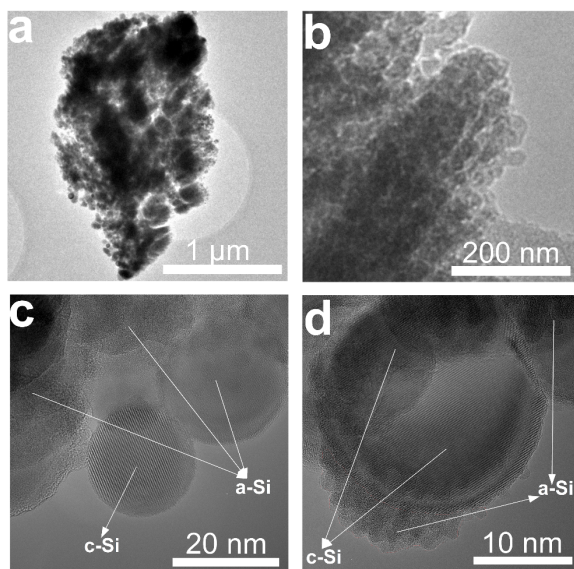

Figure S3.2.1 (a) – (b), low-resolution and (c) - (d), high-resolution TEM images showing the morphology of as-prepared Si nanoparticles.

S3.2.2 Raman Spectra for Quantitative Crystallinity analysis

A Raman spectral mapping on a pressed Si NP pellet was carried out on an area of 33 * 34 μm using a laser with a wavelength of 785 nm. The Raman spectra were taken with a step size of 1 μm for both height and width, therefore in total 33 * 34 = 1122 spectra were taken, from which a spectrum with average intensity at each wavenumber was obtained.

The main peaks of c-Si and a-Si in the average spectrum are clearly observed. A deconvolution was done to obtain the individual spectra of c-Si and a-Si, as well as the integrated Raman signals I_c and I_a, from c-Si and a-Si respectively. In our experiments, $I_c : I_a$ = 0.26 : 0.74.

The fraction of crystalline phase X_c can be calculated from a simple formula (S3.2.1), [Ref. S1-S4]

$$X_c = I_c / (I_{c + y} * I_a) \qquad\qquad (S3.2.1)$$

where y is the ratio of Raman diffusion cross-section for c-Si over a-Si.

The value of y can be calculated from the equation (S3.2.2) proposed by Bustarret $et\ al.$, [Ref. S4]

$$y = 0.1 + exp^{-(d/25)} \qquad\qquad (S3.2.2)$$

where d is the mean crystallite size in nm.

From Rietveld Refinement of XRD patterns and TEM images we have acquired a value for the mean size of Si crystallite of ~ 20 nm, and therefore by substituting this value in the above equations, the value of y is determined, $y = 0.55$.

So the fraction of crystalline phase is $X_c = 0.26 / (0.26 + 0.55 * 0.74) = 39$ %.

S3.2.3 TGA

TGA tests report a slight mass decrease (from 100% to 99.6%) during the first half hour due to the evaporation of moisture that is absorbed from air due to its large surface area.

After holding the temperature at 1000 ℃ for a sufficiently long enough duration (5 hours), all Si will be oxidized to SiO_2 and the weight of the sample stops increasing, as is in Figure S3.2.2.

X-ray Diffraction has been carried out on the sample after TGA heating, and Figure S3.2.2 shows that after heating no Si peaks can be observed, indicating that it has been fully oxidized to SiO_2. Compared with the XRD patterns of sample holder, it is clear that a broad bump at around 21.5 ° can be observed, which is attributed to the main peak broadening of amorphous SiO_2.

Assuming the composition of the initial sample is x Si + $(1-x)$ SiO_2; and after heating under O_2/Ar, all Si is oxidized to SiO_2.

x Si + $(1-x)$ SiO_2 + x O_2 = x SiO_2 + $(1-x)$ SiO_2
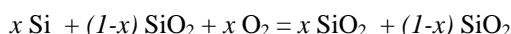
thus $60.08 / (28.09 * x + 60.08 * (1-x)) = 177.93 / 99.6$

from this equation we get: $x = 0.83$

Weight fraction of Si inside the sample:

$28.09 * 0.82 / (28.09 * 0.83 + 60.08 * 0.17) * 100 \% = 69.0 \%$

So the weight fraction of pure Si inside the Si NP sample accounts for 69.0 %.
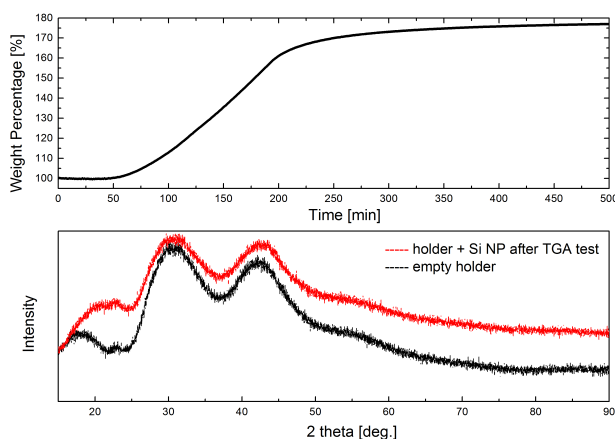
Figure S3.2.2 Top: result of TGA in O_2/Ar; Bottom: X-ray diffraction on the reacted sample after TGA measurement in O_2/Ar.

S3.2.4 Performance of super P carbon black (CB) for Na ion batteries at different current rates
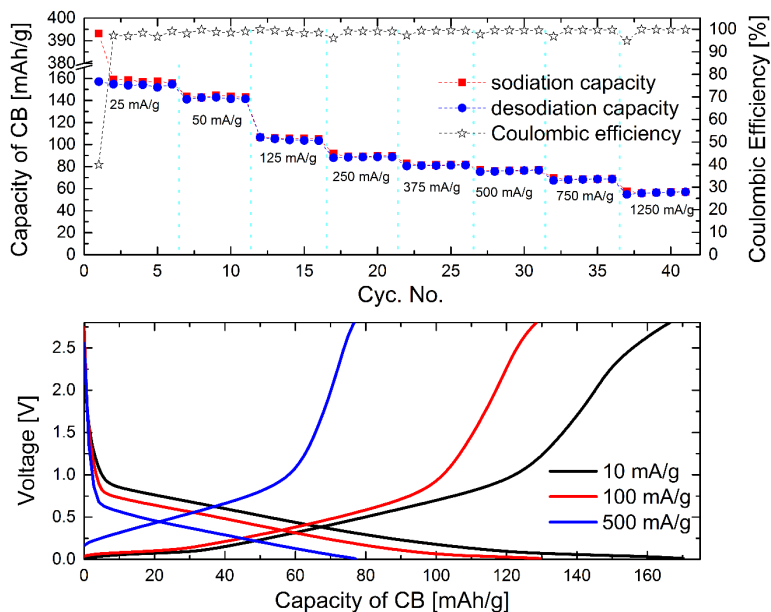
Figure S3.2.3 Top: electrochemical performance of CB electrode for Na ion uptake at different current rates; Bottom: voltage profiles of CB electrode for Na ion insertion / extraction at different current rates.

S3.2.5 Galvanostatic current (20 mA g^{-1}) performance of the Si nanoparticle sample for a Na ion battery without subtracting the influence of SiO$_2$
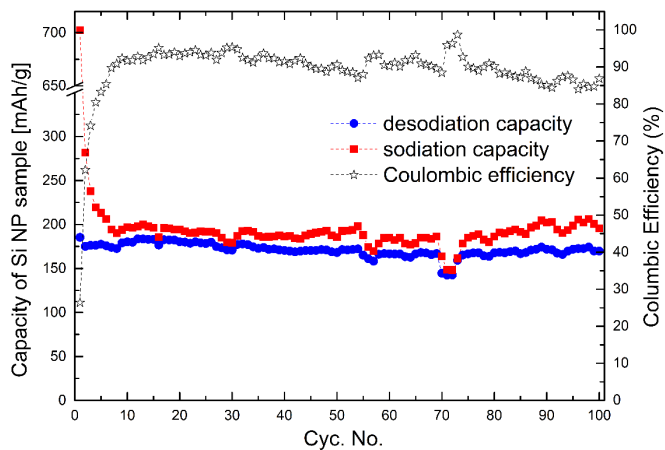
Figure S3.2.4 Electrochemical performance of Si NP for Na ion uptake at 20 mA g^{-1} without subtracting the impact of SiO$_2$.

S3.2.6 Rate capability of the Si nanoparticle sample for a Na ion battery without subtracting the impact of SiO$_2$
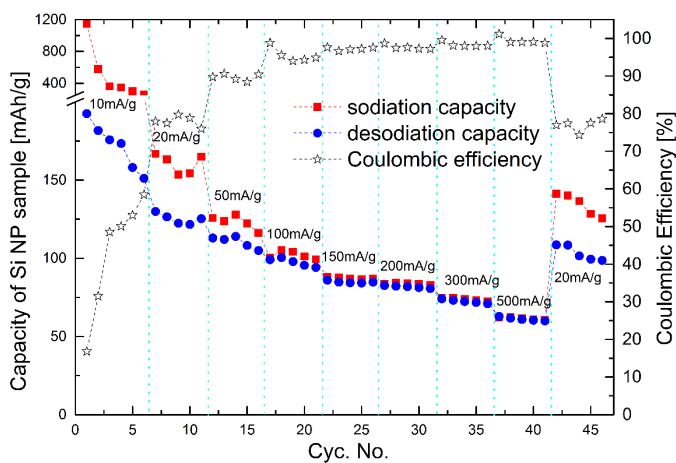
Figure S3.2.5 Rate performance of Si NP for Na ion uptake without subtracting the impact of SiO$_2$.

S3.2.7 CV tests on Si NP electrode and super P carbon black (CB) electrode

CV measurements were carried out between 0.01 V and 2.8 V. For the CB electrode at a scan rate of 0.2 mV s^{-1}, the reduction peak at around 0 V is commonly recognized as the sodium ion insertion into carbon black; (Ref. [S5-S7]) and the anodic scan peak at 0.12 V is caused by the extraction of Na ion from carbon.
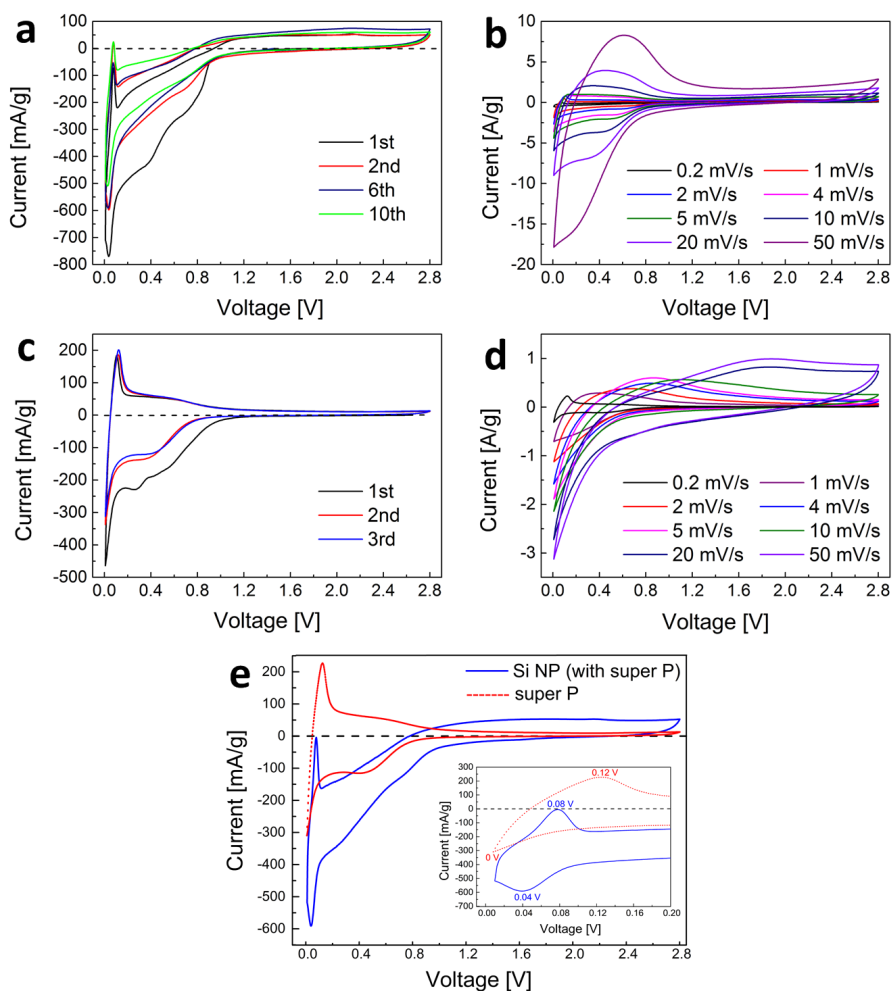
Figure S3.2.6 (a) CV test on Si NP electrode (Si NP : NaCMC : CB = 5 : 3 : 2 in weight) at a scan rate 0.2 mV s^{-1}. (b) Cyclic voltammograms of Si NP electrode at different scan rates. (c) CV measurement on Super P carbon black electrode (CB: NaCMC = 3 : 2 in weight) at a scan rate 0.2 mV s^{-1}. (d) Cyclic voltammograms of CB electrode at different scan rates. (e) Comparison of cyclic voltammograms of the Si NP electrode and the CB electrode; the inset shows the voltage range < 0.2 V.

S3.2.8 Electrochemical performance of the thick pellet Si NP electrode for the first sodiation
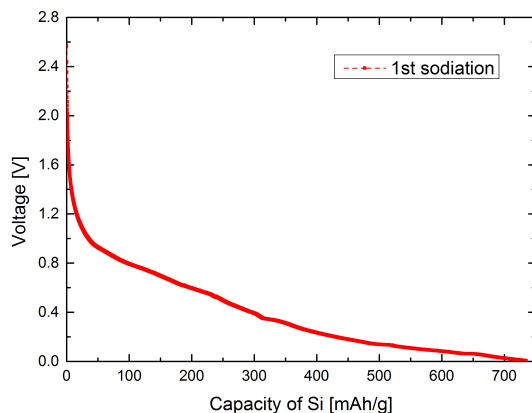
Figure S3.2.7 Electrochemical voltage profile of the thick pellet Si NP electrode during the 1st sodiation.

S3.2.9 XRD patterns of as-prepared, de-/sodiated super P carbon black (CB) electrode

The contribution from super P carbon black to the diffraction peaks of the Si NP electrode can be excluded according to the XRD patterns of an electrode, without Si NP, consisting of super P carbon black and NaCMC. The diffraction pattern of sodiated carbon electrode does not show additional diffraction peaks as in the Si NP electrode, and in fact is the same as that of the desodiated carbon electrode. This indicates that the amorphous carbon black does not contribute to the XRD peaks of the Si NP electrode.
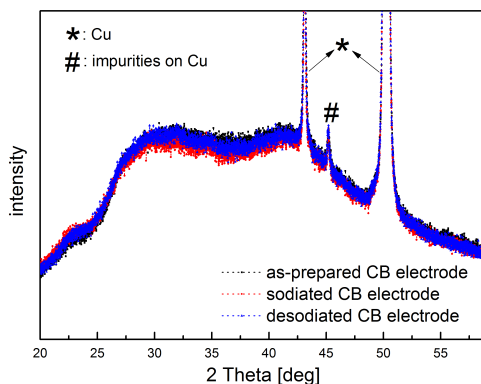
Figure S3.2.8 XRD patterns of as-prepared, de-/sodiated super P carbon black (CB) electrode.

S3.2.10 Selected Area Electron Diffraction (SAED) ring pattern of cycled Si NP electrode

Figure S3.2.9 indicates that only diffraction rings belonging to the TEM grid are observed; whereas no peaks corresponding to crystalline Si can be seen.
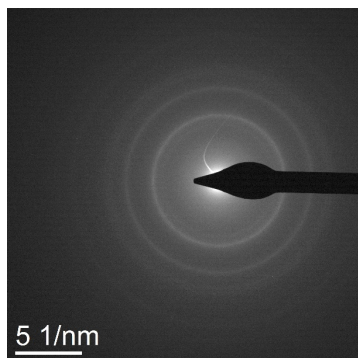
Figure S3.2.9 Selected Area Electron Diffraction (SAED) ring pattern taken on the Si NP electrode after de-/sodiation for 100 cycles. All the bright diffraction rings correspond to the TEM grid.

References

[S1] C. Droz, E. Vallat-Sauvain, J. Bailat, L. Feitknecht, J. Meier, A. Shah, Sol. Energy Mater. Sol. Cells 81 (2004) 61-71.

[S2] M. Ledinský, A. Vetushka, J. Stuchlík, T. Mates, A. Fejfar, J. Kočka, J. Štěpánek, J. Non-Cryst. Solids 354 (2008) 2253-2257.

[S3] R. Tsu, J. Gonzalez-Hernandez, S. S. Chao, S. C. Lee, K. Tanaka, Appl. Phys. Lett. 40 (1982) 534-535.

[S4] E. Bustarret, M. A. Hachicha, M. Brunel, Appl. Phys. Lett. 52 (1988) 1675-1677.

[S5] Y. Cao, L. Xiao, M. L. Sushko, W. Wang, B. Schwenzer, J. Xiao, Z. Nie, L. V. Saraf, Z. Yang and J. Liu, Nano Lett. 12 (2012) 3783-3787.

[S6] H.-G. Wang, Z. Wu, F.-L. Meng, D.-L. Ma, X.-L. Huang, L.-B. Wang and X.-B. Zhang, ChemSusChem 6 (2013) 56-60.

[S7] L. Fu, K. Tang, K. Song, P. A. Van Aken, Y. Yu and J. Maier, Nanoscale 6 (2014) 1384-1389.

Chapter 4

TiF$_3$ Catalyzed MgH$_2$ as a Li/Na Ion Anode

This chapter is based on:

Abstract
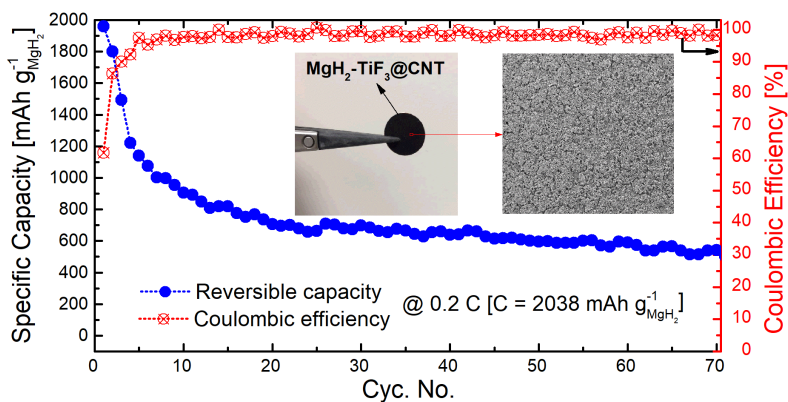
MgH_2 has been considered as a potential anode material for Li ion batteries due to its low cost and high theoretical capacity. However, it suffers from low electronic conductivity and slow kinetics for hydrogen sorption at room temperature that result in poor reversibility, cycling stability and rate capability for Li ion storage. This work presents a MgH_2-TiF_3@CNT based Li ion battery anode manufactured via a conventional slurry based method. Working with a liquid electrolyte at room temperature, it achieves a high capacity retention of 543 mAh g^{-1} in 70 cycles at 0.2 C and an improved rate capability, thanks to the improved hydrogen sorption kinetics with the presence of catalytic TiF_3. Meanwhile, the first realization of Na ion uptake in MgH_2 has been evidenced in experiments.

4.1 Introduction

MgH$_2$ has been intensively researched as an active material for hydrogen storage due to its high capacity (7.6 wt. %) and low cost [1, 2]. It was introduced as a conversion anode material for reversible electrochemical Li ion uptake in 2008 [3], and has attracted growing research interest since then due to its high theoretical capacity for Li ion storage and cost-effectiveness [4-7]. Its lithiation undergoes dehydrogenation of MgH$_2$ with the formation of LiH (Reaction 4.1) resulting in a Li ion storage capacity of 2038 mAh g^{-1}, which is defined as the theoretical capacity; Li-Mg alloying (Reaction 4.2) takes place when further lithiation proceeds and the achieved capacity can be even higher.

$$2 \text{ Li} + \text{MgH}_2 \rightarrow \text{Mg} + 2 \text{ LiH} \tag{4.1}$$

$$x \text{ Li} + y \text{ Mg} \rightarrow \text{Li}_x\text{Mg}_y \tag{4.2}$$

Despite its high theoretical capacity, the reversible Li ion uptake in MgH$_2$ faces tremendous challenges in its realization, including: (1), the electrically insulating property of MgH$_2$; (2), limited H mobility in MgH$_2$ at room temperature; (3), adverse volume change (up to 85 %) leading to the material pulverization and electrical contact loss over cycling; (4), the continuous growth of solid electrolyte interphase (SEI) in liquid electrolytes resulting in the loss of active materials and capacity decay.

To address these issues, many approaches have been investigated and progress has been made [3, 8-18]. The advances to accelerate the crucial hydrogen sorption kinetics in MgH$_2$ includes size reduction of MgH$_2$ [3, 8, 9], producing more cyclable β-MgH$_2$ through gas phase hydrogenation of Mg [10-12], utilizing Mg-M-H (M = Fe, Co, Ni, etc.) compounds [13, 14] and incorporating secondary hydride phases (TiH$_2$ or LiBH$_4$) [10, 11, 15, 16] and catalysts (Nb$_2$O$_5$ [15-17] or Al$_2$O$_3$ [18]). Advanced carbon nanomaterials and binders may also be applied to maintain the electronic conduction and structural integrity to promote the cycling stability. For instance, a MgH$_2$ electrode with 33 % of carboxymethyl cellulose formate binder and 33 % preground carbon achieved a reversible capacity retention of 542 mAh g^{-1} after 40 cycles at 0.05 C (C = 2038 mA g^{-1}) [12].

However, it should be noted that, for the MgH$_2$ anodes that work with liquid electrolytes at room temperature [3, 8-14], the cycling current rates are rather low, and the cycling stability as well as rate capability still needs much improvement. MgH$_2$ has also been studied as the anode in solid state Li ion batteries [4, 7, 15-18] to avoid the problematic SEI formation, but

the sluggish kinetics of Li ion diffusion and hydrogen sorption in solids appears to be a major issue. Therefore, the solid state batteries worked at elevated temperatures (above 100 ℃) and involved catalysts (e.g. Nb_2O_5 [15-17]) to bring the kinetic properties to the reaction, and a substantial amount of costly $LiBH_4$ [15, 16] was also often required. A (MgH_2-Nb_2O_5)-$LiBH_4$-acetylene black (4:3:3 in mass) composite achieved a capacity retention of 700 mAh g^{-1} in 100 cycles at 120 ℃ thanks to the synergistically improved hydrogen mobility [7]. However, the high operating temperature and cost-ineffectiveness have largely reduced its potential for practical applications. Moreover, in experimental studies mechanically pressed disc-like electrodes were universally prepared for the electrochemistry measurement. In such electrodes the kinetics is limited because the pellet should remain intact, which is a further handicap for a sustained cycling stability and high rate capabilities. A slurry-based method is conventional and standard to produce porous, thin film electrodes in Li ion batteries but has not been introduced in metal hydrides based electrodes.

To overcome the above challenges, in this work, we present a MgH_2 based Li ion battery anode fabricated through a slurry-based approach using anhydrous tetrahydrofuran (THF) as the solvent. To enhance the kinetics for Li ion uptake and release in MgH_2, 5 mol. % TiF_3 was added as a catalyst, which has been previously shown by some of us that, in gas phase experiments, the hydrogen absorption/release is possible at reduced temperatures with the catalysis of TiF_3 [19]. Furthermore, carbon nanotubes (CNT) were added to enable sufficient electronic charge transport throughout the electrode. In addition, to suppress the SEI growth, 10 wt. % fluoroethylene carbonate (FEC) was utilized as an electrolyte additive. The MgH_2-TiF_3@CNT electrode in this work exhibits a high capacity retention of 543 mAh g^{-1} in 70 cycles at 0.2 C and outstanding rate capability at room temperature, which is superior than the previous reports on MgH_2 anodes that work with liquid electrolytes (Table S4.1). Meanwhile, this work has, for the first time, experimentally achieved Na ion uptake in a MgH_2 based electrode.

4.2 Experimental details

Sample preparation: MgH_2 (hydrogen-storage grade, Aldrich) was mixed with 5 mol. % TiF_3 (Alfa Aesar) and CNT (industrial standard, $150 - 210$ m^2 g^{-1}) (MgH_2-TiF_3 : CNT = 3 : 1 in mass), and subsequently was ball milled with a Fritsch Planetary Mono Mill PULVERISETTE 6 for 50 hours at 400 rpm under Ar atmosphere using a Tungsten Carbide grinding bowl and a ball-to-powder mass ratio of 50 : 1. To eliminate the excess heat

generated during mechanical milling that may dehydrogenate the sample, the milling period was divided into 100 repetitions of a 30 min milling followed with a 10 min rest allowing the grind bowl to cool down.

Characterization: The micro-morphology of the ball-milled MgH_2-TiF_3@CNT and the as-prepared electrode were imaged with a JEOL JSM 6010F scanning electron microscope (SEM) working at 5 kV. X-ray Diffraction (XRD) measurements were performed with a PANalytical X'Pert Pro PW3040/60 diffractometer (Cu K_α radiation) operating at 45 kV and 40 mA. The lithiated electrode for XRD measurement was washed 3 times with diethyl carbonate (DEC) to remove soluble electrolyte residuals in the electrode, and were dried in a glovebox before the measurements.

Electrode preparation: The MgH_2 based Li ion battery anodes were prepared inside an Ar-filled glovebox using a conventional slurry based method. Specifically, a binder, polyvinylidene difluoride (PVDF, Kynar flex), was first dissolved in anhydrous Tetrahydrofuran (THF; ≥ 99.9 %, Sigma-Aldrich) under magnetic stirring. Next, super P carbon black (TIMCAL) and the ball-milled MgH_2-TiF_3@CNT were added into the colloidal solution (MgH_2-TiF_3@CNT: super P carbon black : PVDF = 70 : 15: 15 in mass) and kept stirring overnight until a homogeneous suspension was obtained. Subsequently, the slurry was casted onto a planar Cu foil (12.5 μm, Goodfellow) with a doctor blade. After drying, they were cut into circular electrodes, and then mechanically compacted before the cell assembly. The thickness of active materials was ~ 20 μm and the mass loading was ~ 0.5 mg cm^{-2}.

The composition/preparation of the MgH_2 based Na ion battery anodes was similar to that of the Li ion batteries except that super P carbon black instead of CNT was utilized as the conducting additive in the ball milled composite.

Electrochemistry: Half-cell Li/Na ion batteries were assembled inside an Ar-atmosphere glovebox with the O_2 and H_2O levels < 0.1 ppm. A Li/Na foil (Aldrich) was applied as the counter electrode. The working electrolyte for Li ion batteries was 1 M $LiPF_6$ dissolved in DEC, ethylene carbonate (EC) and fluoroethylene carbonate (FEC) (EC : DEC = 1:1 in volume with 10 % FEC); and 1 M $NaPF_6$ dissolved in EC and dimethyl carbonate (DMC) and (EC : DMC = 1:1) was applied as the electrolyte in Na ion batteries. A borosilicate glass micro fibre (Whatman) was used as the separator.

The galvanostatic electrochemical properties were tested with a MACCOR 4600 battery cycler. The cut-off voltages for Li ion batteries were 0.005 V and 3.0 V *versus* Li/Li$^+$ for discharge and charge, respectively; and the working voltage range for Na ion batteries was 0.005 – 2.8 V *versus* Na/Na$^+$.

Subtraction of the carbon capacity: The specific capacities reported in this paper were calculated based on the mass of MgH$_2$ (*excl.* carbon additives). The capacity of CNT was determined by measuring its electrochemical performance (Figure S4.1) in Li ion batteries; and the capacity of super P carbon black has been determined by us in previous work [20]. The capacity contributions from these carbon additives were then subtracted to obtain the specific capacity of MgH$_2$.

4.3 Results and discussions

The MgH$_2$-TiF$_3$@CNT composite was synthesized via high energy ball milling (details in the Supporting Information (SI)). XRD patterns of the composite (Figure 4.1a) show the characteristic diffraction peaks of MgH$_2$ (110), (101), (200) and (211) lattice planes at 27.7°, 35.6°, 39.6°and 54.4°, respectively. Weak but distinguishable peaks of TiF$_3$ are present at 23.1°, 31.4°, 41.0° and 48.3°. The peaks at 25.6°, 42.7° and 78.2° can be allocated to the Bragg reflections on CNT [21, 22]. The average crystalline domain size of MgH$_2$ is ~ 10 nm calculated based on the line shape of MgH$_2$ in the Rietveld refinement (Figure S4.2). The SEM images of the sample (Figure 4.1b – d) show aggregates of sub-micro grains induced by the high energy ball milling. Energy-dispersive X-ray spectroscopy (EDX) (Figure S4.3) demonstrates that the distribution of TiF$_3$ next to MgH$_2$ is homogeneous on the basis of the superposition of Mg and F element distribution at the submicro-/nanoscale. The nature of the small grains is thus the agglomeration of nanosized MgH$_2$ and TiF$_3$ which warrants an optimal catalytic activity of TiF$_3$.

The electrode was fabricated with a slurry based electrode preparation method utilizing 15 % PVDF as a binder and 15 % super P carbon black to integrate the conducting network throughout the electrode. Morphological images of the as-prepared electrode (Figure 4.1e – f & S4.4) show that the active material loading is uniform with micro-/nanoscale porosities all over the electrode, and the active material grains are integrated by the binder and carbon matrix. The porous nature of the electrode allows the access of liquid electrolyte throughout the electrode and reduces the Li ion diffusion pathway through the solid phase fractions.
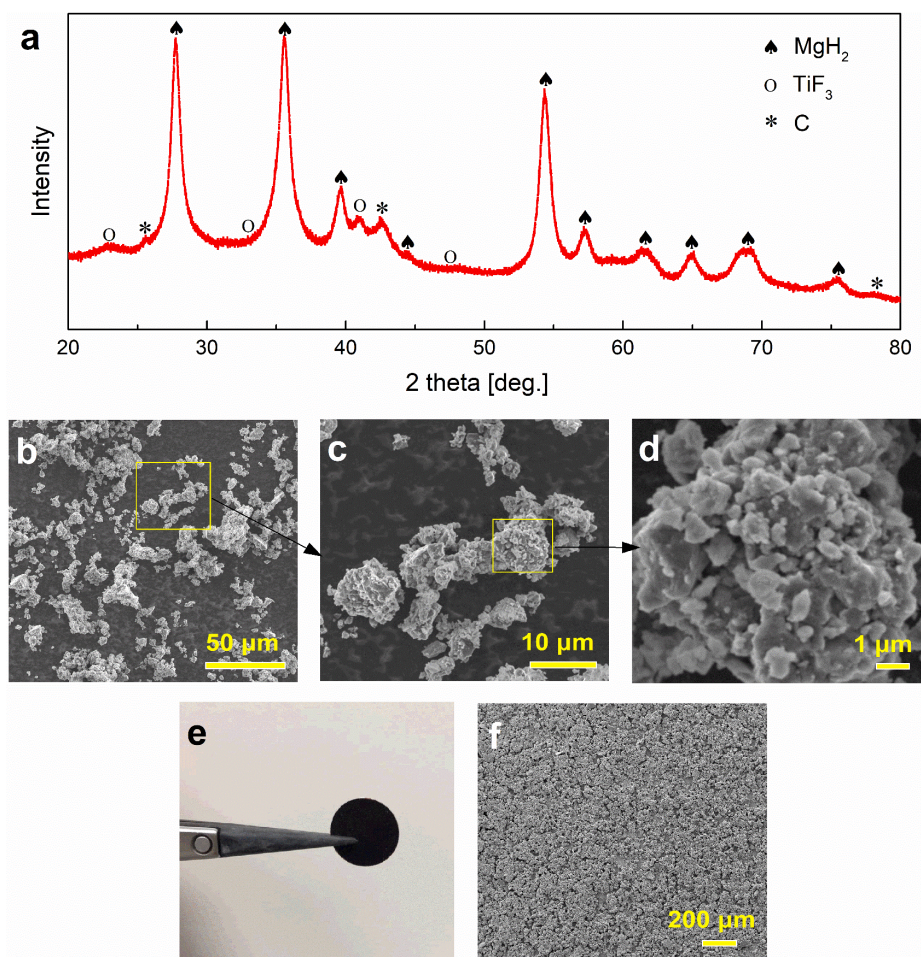
Figure 4.1 (a), XRD patterns of the ball-milled MgH₂-TiF₃@CNT sample. (b) – (d), SEM images of the sample at different magnifications. (e), a photo and (f), a SEM image of the as-prepared electrode (12.7 mm in diameter).

The electrochemical performance of the MgH₂ based electrodes was measured within half-cell Li ion batteries. The specific capacities reported in this paper are calculated based on the mass of MgH₂ (*excl.* carbon additives). The capacity contributions from the carbon additives in the electrode have been subtracted to obtain the capacity of MgH₂ (details in the SI).

Figure 4.2a shows that, cycling at 0.2 C, a capacity of 3254 mAh g⁻¹ was achieved for the first lithiation, and the following delithiation reaches a capacity of 1959 mAh g⁻¹. This relatively low Coulombic efficiency (61.7 %) mainly originates from the irreversible SEI formation. The reversible capacity declines during the first few cycles and 1139 mAh g⁻¹ is

retained after 5 cycles. The Coulombic efficiency increases to 86.3 % and 97.4 % at the 2nd and 5th cycle, respectively. The capacity retention slips to 707 mAh g^{-1} after 20 cycles, and reaches 543 mAh g^{-1} in 70 cycles. Figure 4.2b shows that the initial reversible capacity for Li ion storage amounts to 2293, 2291 and 824 mAh g^{-1} at 0.05, 0.1 and 0.5 C, respectively. Compared with the published results on MgH₂ based anode cycling in liquid electrolytes [5-7, 10], the MgH₂-TiF₃@CNT electrode in this work exhibits improved rate capability. Such improved kinetics supports that TiF₃ is an effective catalyst for hydrogen absorption and release in Mg/MgH₂.

The initial Li ion uptake (Figure 4.2c) shows a voltage plateau at ~ 1.2 V corresponding to the SEI formation, which is not observed in the following cycles, and a lithiation capacity of around 200 mAh g^{-1} is reached during this process. The main lithiation of MgH₂ takes place at a lower voltage range including two stages: (i), a voltage plateau at ~ 0.2 V related to the hydrogen extraction from MgH₂ with the formation of LiH (Reaction 4.1); and (ii), a low voltage plateau ~ 0.05 V associated with the alloying process between Mg and Li (Reaction 4.2). At the beginning of the first stage, the voltage undergoes a dip to 0.13 V, which is consistent with the other studies [3, 8-10] possibly originating from the large energy barrier of initial LiH nucleation on the surface of Mg, before it rises to the main voltage plateau at ~ 0.2 V due to the co-existence of Mg and MgH₂. Upon the complete depletion of MgH₂, the presence of a single MgH₂ phase results in a declining voltage slope. When the voltage goes down to 0.08 V the cumulative lithiation capacity reaches above 2150 mAh g^{-1} indicating that the Li ion uptake in MgH₂ achieves a capacity of ~ 1950 mAh g^{-1}, which is close to the theoretical capacity. In the second stage, the voltage also exhibits a plateau originating from the co-existence of Li and Mg solid solutions and a following sloped voltage attributed to one single phase (Li solid solution) [3, 8]. The cumulative lithiation capacity reaches ~ 3250 mAh g^{-1} when the cut-off voltage is reached revealing a Li ion storage capacity of ~ 1100 mAh g^{-1} (i.e. Li : Mg ≈ 1 : 1) in the alloying reaction. In the following delithiation, the voltage exhibits a reverse course of lithiation. It begins with a de-alloying process from Li$_x$Mg$_y$ that occurs at a voltage range < 0.25 V achieving a capacity of about 600 mAh g^{-1}. Subsequently, it undergoes a plateau at ~ 0.6 V associated with the delithiation from LiH and the hydrogenation of Mg, which obtains a capacity of ~ 1400 mAh g^{-1}. The Coulombic efficiency (72 %) of the delithiation from LiH is higher than that of the de-alloying process

(55 %), indicating that the Li ion extraction from the Li-Mg alloys is less reversible and may cause the active material loss and capacity deterioration over cycling.

The overpotential between the Li-Mg de-alloying and alloying is less than 0.2 V; while it rises up to 0.5 V between the lithiation of MgH_2 (forming Mg) and the reverse reaction. This overpotential increase stems from the significant conductivity reduction from conductive metallic Mg to electrically insulating MgH_2. Over cycling, the voltage plateaus become increasingly sloped with growing overpotentials, which results from the build-up of internal resistance due to the gradual structural deformation over repetitive volume expansion and contraction. As a result, the voltage reaches the cut-off earlier and the achieved capacity within the working voltage range drops. Therefore, we can conclude that the drastic capacity drop within the first 20 cycles mainly originates from the vanishing Li-Mg alloying over cycling as the overpotential grows gradually, since the lower voltage plateau near 0 V disappears in 20 cycles in Figure 4.2c.

The voltage profiles at different current rates (Figure 4.2d) show growing overpotentials when the current rate increases. It leads to a more rapid voltage collapse to the cut-off voltage and thus a lower capacity when it is lithiated at a higher current rate; and hence in the following Li ion extraction step, the achieved capacity is lower. It is also observed that the Li-Mg alloying reaction (near 0 V) reduces significantly as the overpotential grows.
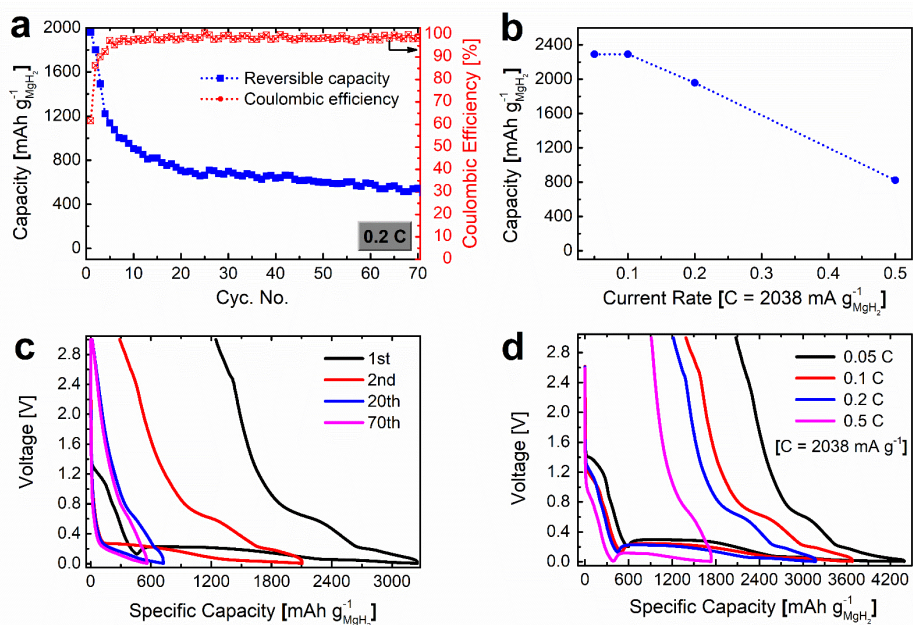
Figure 4.2 Electrochemical performance of MgH₂ anode based Li ion batteries. (a), The capacity retention and Coulombic efficiency at 0.2 C (C = 2038 mA g⁻¹). (b), The initial reversible capacity of the MgH₂-TiF₃ anode at different C-rates. (c), Voltage profiles of the 1st, 2nd, 20th and 70th cycles of the MgH₂-TiF₃ anode at 0.2 C. (d), Voltage profiles of the MgH₂-TiF₃ anode for the 1st cycle at different C-rates.

The high performance of the MgH₂-TiF₃@CNT electrode may benefit from the synergistic effects of several factors. Firstly, the slurry-casting manufactured electrode, compared with a pellet electrode, is more porous and allows a facile access for the liquid electrolyte to the active materials and may enable faster Li ion transport throughout the electrode. Therefore, a lower internal ionic resistance is expected resulting in a lower overpotential, and the rate capability could be promoted as well. Moreover, the voids in the electrode can accommodate the volume change upon Li ion insertion. Secondly, the active material grains are embedded within the CNT matrix warranting intimate electronic conduction between the active materials and the carbon network induced by high energy ball milling, and enabling sustained electrical conduction between the grains over cycling. Thirdly, The FEC additive in the electrolyte induces a thin, stable and compact LiF-dominant SEI layer that prevents further SEI growth, and therefore an enhanced Coulombic efficiency and cycling stability can be achieved [23-25]. This is also evidenced by comparing with the results with a FEC-free

electrolyte (Figure S4.5c). Last but not least, the catalytic TiF_3 accelerates the hydrogen sorption kinetics in MgH_2 and leads to facilitated lithium ion uptake. Specifically, during the initial lithiation, apart from the dehydrogenation of MgH_2 (Reaction 4.1), the presence of TiF_3 next to MgH_2 leads to the formation of MgF_2 and TiH_2 (Reaction 4.3). Subsequently, MgF_2 acts as a grain refiner for MgH_2/Mg and keeps their crystallites small [19, 26]. This grain refinement mechanism results in a destabilized system, which lowers the enthalpy of hydride formation and thus leads to an accelerated hydrogen sorption and, ultimately, ameliorated Li ion uptake. Meanwhile, TiH_2 may also be lithiated (Reaction 4.4) and vanishes, but it is much more difficult since the enthalpy of formation of TiH_2 ($-$ 136 kJ mol^{-1}) is more negative than MgH_2 ($-$ 74 kJ mol^{-1}) and there is no alloying between Li and Ti [27].

$$2\ Li + 3\ MgH_2 + 2\ TiF_3 \rightarrow 3\ MgF_2 + 2\ TiH_2 + 2\ LiH \tag{4.3}$$

$$2\ Li + TiH_2 \rightarrow Ti + 2\ LiH \tag{4.4}$$

The advantageous catalytic effect is also evidenced by measuring the performance of a TiF_3-free electrode at the same conditions as the MgH_2-TiF_3 electrode (Figure S4.5c).

To further investigate the behaviours of TiF_3 and MgH_2 during cycling, XRD patterns of a MgH_2-TiF_3@CNT electrode (Figure 4.3) were acquired at different stages: pristine, lithiated to 0.05 V and 0.005 V, respectively, at 0.1 C. In the pristine electrode, apart from the peaks from MgH_2, the main diffraction peaks of TiF_3 are weak but distinctively recognizable. Bragg diffractions on the CNT are visible as well. When it is lithiated to 0.05 V, MgH_2 disappears while Mg and LiH show up, and the Li-Mg alloy emerges as well. It indicates that the dehydrogenation of MgH_2 (Reaction 4.1) is accomplished and the lithiation has proceeded to the Mg-Li alloying (Reaction 4.2). It is also observed that TiF_3 vanishes due to Reaction 4.3, but the peaks of MgF_2 and TiH_2 are hardly visible due to their much lower presence together with much smaller grain sizes ($\sim$ 3 nm) compared with MgH_2/Mg ($\sim$ 10 nm) based on the Rietveld refinement (Figure S4.6 & Table S4.2 – S4.3), and the peak broadening is significant in the XRD signals. These findings are in good agreement with the previous studies [19, 26]. During the further lithiation till 0.005 V, LiH remains unaffected while Mg alloys with Li forming Li_xMg_y; the stoichiometry is x : y $\approx$ 1 : 1, and the average alloy grain size amounts to 18.3 nm based on the Rietveld refinement (Table S4.4).
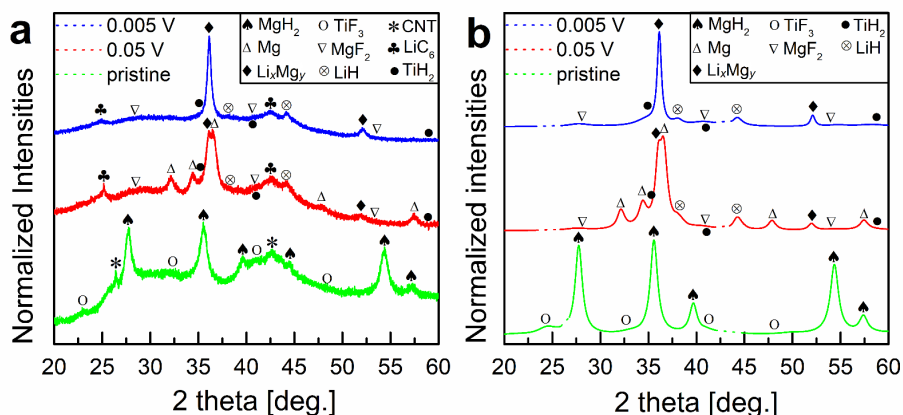
Figure 4.3 XRD patterns of the MgH₂ electrode at different stages: pristine, lithiated to 0.05 V and 0.005 V, respectively. (a), experimental data; (b), Refined XRD patterns after subtraction of background; (The 2 theta ranges of carbon and Li-C alloy has been subtracted since it is out of the scope of this work. Details on the refinement are displayed in Figure S4.6.) Here the electrode is a pressed pellet (~ 70 μm in thickness), instead of a slurry based electrode, in order to avoid the strong Bragg reflections from the Cu current collector and to produce XRD patterns with a higher signal-to-noise ratio.

The promising results of the TiF₃ catalyzed MgH₂ anode in Li ion batteries encourage us to investigate its potential for Na ion batteries. Though a sodiation voltage has been predicted theoretically [28, 29], MgH₂, or any other metal hydride, has not been reported to have a capability of Na ion storage probably due to the poor kinetics of Na ion transport. The improved kinetics of Li ion uptake in the TiF₃ catalyzed MgH₂ suggests that the Na ion diffusion may be facilitated with the catalytic TiF₃ and thus enable the realization of Na ion uptake in MgH₂.

In this work, the possibility of Na ion insertion in MgH₂ was studied by testing MgH₂ based anodes within Na ion half-cells. The experimental result illustrates that, judging from the comparison of voltage profiles between the MgH₂ based electrode (Figure 4.4a) and the carbon additive based electrode (Figure S4.7a), the voltage plateau at 0.15 V and part of the sloping voltage between 0.15 V and the sodiation cut-off voltage originate from the sodiation of MgH₂, and the achieved capacity in this process is only ~ 350 mAh g^{-1}; during desodiation, the sloping voltage range of 0.4 – 0.9 V may be partially related to the Na ion extraction from the product of sodiated MgH₂ achieving a capacity of merely ~ 80 mAh g^{-1} (*excl.* the capacity contribution from the carbon additive [20]). Although the achieved capacity is low, the

realization of Na ion insertion in MgH$_2$ is evident. It is also evidenced by the cyclic voltammograms (Figure 4.4b & S4.7b) and the XRD patterns of the sodiated MgH$_2$ electrode (Figure S4.8).
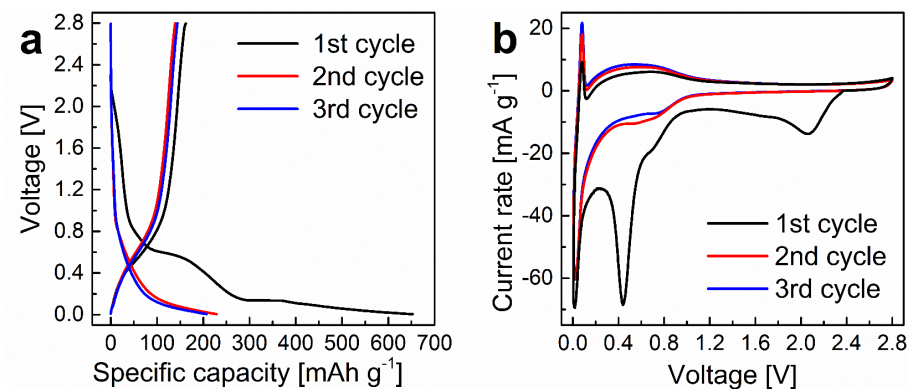

Figure 4.4 Electrochemical sodiation performance in MgH₂. (a), Voltage profiles at 0.05 C and (b), Cyclic voltammograms (scan rate: 0.02 mV s^{-1}) of the MgH$_2$-TiF$_3$ electrode tested in a Na ion half-cell.

4.4 Conclusions

This work presents a novel MgH$_2$-TiF$_3$@CNT composite based anode which achieves promising electrochemical performance in liquid electrolyte based Li ion batteries. The improved the kinetics of electrochemical hydrogen sorption and Li ion uptake in MgH$_2$,with the catalysis of TiF$_3$, originates from the grain refinement effect of MgF$_2$ formed during the initial lithiation. We also find out that the dealloying of intermetallic Li-Mg is less reversible than the delithiation of LiH due to its larger grain size. Moreover, Na ion uptake in the MgH$_2$-TiF$_3$ electrode has been, for the first time, witnessed in experiments even though the cycling performance is poor and the reaction mechanism is still to be elucidated. It may stimulate considerable follow-up research on metal hydrides for reversible Li/Na ion uptake.

References

[1] L. Schlapbach, A. Zuttel, Nature 414 (2001) 353-358.

[2] A. Züttel, Mater. Today 6 (2003) 24-33.

[3] Y. Oumellal, A. Rougier, G. A. Nazri, J. M. Tarascon, L. Aymard, Nat. Mater. 7 (2008) 916-921.

[4] S. Brutti, D. Meggiolaro, A. Paolone, P. Reale, Mater. Today Energy 3 (2017) 53-59.

[5] S. Sartori, F. Cuevas, M. Latroche, Appl. Phys. A: Mater. Sci. Process. 122 (2016) 1-7.

[6] L. Aymard, Y. Oumellal, J.-P. Bonnet, Beilstein J. Nanotechnol. 6 (2015) 1821-1839.

[7] L. Zeng, K. Kawahito, T. Ichikawa, Alkali-ion Batteries, InTech Ch. 4 (2016).

[8] S. Brutti, G. Mulas, E. Piciollo, S. Panero, P. Reale, J. Mater. Chem. 22 (2012) 14531-14537.

[9] Y. Oumellal, C. Zlotea, S. Bastide, C. Cachet-Vivier, E. Leonel, S. Sengmany, E. Leroy, L. Aymard, J.-P. Bonnet, M. Latroche, Nanoscale 6 (2014) 14459-14466.

[10] L. Huang, L. Aymard, J.-P. Bonnet, J. Mater. Chem. A 3 (2015) 15091-15096.

[11] N. Berti, F. Cuevas, J. Zhang, M. Latroche, Int. J. Hydrogen Energy 42 (2017) 22615-22621.

[12] W. Zaïdi, Y. Oumellal, J. P. Bonnet, J. Zhang, F. Cuevas, M. Latroche, J. L. Bobet, L. Aymard, J. Power Sources 196 (2011) 2854-2857.

[13] W. Zaïdi, J. P. Bonnet, J. Zhang, F. Cuevas, M. Latroche, S. Couillaud, J. L. Bobet, M. T. Sougrati, J. C. Jumas, L. Aymard, Int. J. Hydrogen Energy 38 (2013) 4798-4808.

[14] J. Zhang, W. Zaidi, V. Paul-Boncour, K. Provost, A. Michalowicz, F. Cuevas, M. Latroche, S. Belin, J.-P. Bonnet, L. Aymard, J. Mater. Chem. A 1 (2013) 4706-4717.

[15] L. Zeng, K. Kawahito, S. Ikeda, T. Ichikawa, H. Miyaoka, Y. Kojima, Chem. Commun. 51 (2015) 9773-9776.

[16] L. Zeng, T. Ichikawa, K. Kawahito, H. Miyaoka, Y. Kojima, ACS Appl. Mater. Interfaces 9 (2017) 2261–2266.

[17] S. Ikeda, T. Ichikawa, K. Kawahito, K. Hirabayashi, H. Miyaoka, Y. Kojima, Chem. Commun. 49 (2013) 7174-7176.

[18] S. Ikeda, T. Ichikawa, K. Goshome, S. Yamaguchi, H. Miyaoka, Y. Kojima, J. Solid State Electrochem. 19 (2015) 3639-3644.

[19] F. M. Mulder, S. Singh, S. Bolhuis, S. W. H. Eijt, J. Phys. Chem. C116 (2012) 2001-2012.

[20] B. Peng, Y. Xu, X. Wang, X. Shi, F. M. Mulder, Sci. China Phys. Mech. Astron. , 2017, 60, 064611.

[21] M.-L. Chen, W.-C. Oh, Nanoscale Res. Lett. 6 (2011) 398-398.

[22] V. Gupta, T. A. Saleh, in Carbon Nanotubes - From Research to Applications, InTech, Ch. 17 (2011).

[23] A. M. Haregewoin, A. S. Wotango, B.-J. Hwang, Energy Environ Sci. 9 (2016) 1955-1988.

[24] K. Schroder, J. Alvarado, T. A. Yersak, J. Li, N. Dudney, L. J. Webb, Y. S. Meng, K. J. Stevenson, Chem. Mater. 27 (2015) 5531-5542.

[25] M. Nie, J. Demeaux, B. T. Young, D. R. Heskett, Y. Chen, A. Bose, J. C. Woicik, B. L. Lucht, J. Electrochem. Soc. 162 (2015) A7008-A7014.

[26] A. Grzech, U. Lafont, P. C. M. M. Magusin, F. M. Mulder, J. Phys. Chem. C 116 (2012) 26027-26035.

[27] Phase diagram of Li-Ti, FACT light metal alloy databases, http://www.crct.polymtl.ca/fact/documentation/FTlite/Li-Ti.jpg, (accessed October 2017)

[28] F. Klein, B. Jache, A. Bhide, P. Adelhelm, Phys. Chem. Chem. Phys. 15 (2013) 15876-15887.

[29] M. Ramzan, S. Lebègue, R. Ahuja, Int. J. Hydrogen Energy 35 (2010) 10373-10376.

Supporting Information for Chapter 4
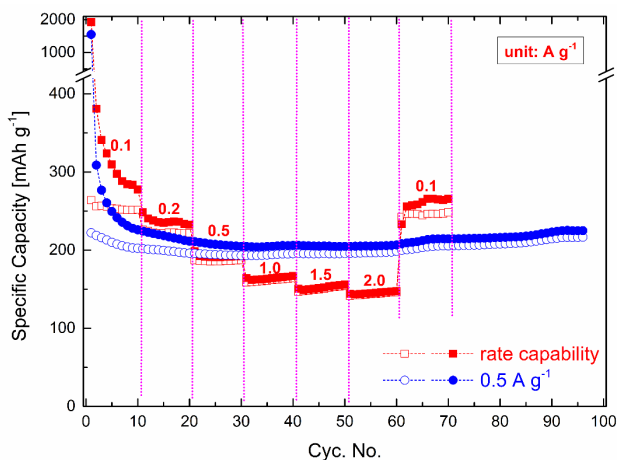
S4.1 The capacity of CNT for Li ion storage

Figure S4.1 The capacity retentions at 0.5 A g^{-1} and the rate capability of CNT based negative electrode for Li ion batteries. Here the CNT based anode is composed of CNT and PVDF with a mass ratio of 0.85 : 0.15, and the electrochemical performance was measured under the same conditions applied for the MgH₂ anode based Li ion batteries.

S4.2 A comparison of the electrochemical performance of the MgH$_2$ based Li ion battery anodes that operate in organic liquid electrolytes at room temperature

electrodes	Electrode composition & configuration	Initial reversible capacity (mAh g^{-1})	Current rate (C)	Cycling performance	Ref. # in the article
MgH$_2$ + 0.05 TiF$_3$	**MgH$_2$-TiF$_3$@CNT: PVDF: super P carbon black = 70 : 15: 15 on planar Cu foil (by slurry casting method)**	**2293**	**0.05**		**this work**
		1959	**0.2**	**543 mAh g^{-1} in 70 cycles**	
MgH$_2$	MgH$_2$ with 10% carbon SP pressed in Cu foam	1480	0.05	520 mAh g^{-1} in 50 cycles	[3]
MgH$_2$	MgH$_2$: PVDF: super P carbon = 7 : 1 : 2, pressed pellet	1000	0.05	< 50 mAh g^{-1} in 10 cycles	[8]
MgH$_2$	50MgH$_2$@HSAG-500: SP carbon = 8 : 2, pressed pellet	950	0.05	500 mAh g^{-1} in 20 cycles	[9]
0.7 MgH$_2$ + 0.3 TiH$_2$	MgH$_2$-TiH$_2$: with 10 % C$_{t, x}$, pressed pellet	1540	0.05	530 mAh g^{-1} in 7 cycles	[10]
MgH$_2$	MgH$_2$: CMC-f : C$_{7, 460}$ = 1 : 1 : 1, pressed pellet	1900	0.05	542 mAh g^{-1} in 40 cycles	[12]
Mg$_2$NiH$_4$	Mg-M-H (M = Ni, Co, Fe) with 10 % C$_{7, 460}$, pressed pellet	--	0.025	N.A.	[13]
Mg$_2$CoH$_5$			0.02		
Mg$_2$FeH$_6$			0.017		

Table S4.1 Electrochemical performance of the MgH$_2$ based Li ion battery anodes tested with the conventional LiPF$_6$ containing liquid electrolytes at room temperature. (Some results in the table are adopted from ref. [7] in the article.)

S4.3 Rietveld refinement with GSAS

Rietveld refinement was performed using a General Structure Analysis System (GSAS) program [S1] by including crystalline MgH_2 (space group: *P42/mnm*). The main 2-theta ranges of TiF_3 and CNT were excluded from the spectrum to achieve a more accurate refinement.

The mean crystalline domain size of MgH_2 was calculated with Scherrer equation (Equation (S4.1)).

$$D = 1800\, k\, \lambda\, /(\pi\, Lx) \tag{S4.1}$$

Where D is the average domain size; λ is the X-ray wavelength; k is a dimensionless shape factor and it has a typical value of about 0.9. L_x is the Lorentzian broadening obtained from the Rietveld refinement.

The average crystalline domain size of MgH_2 from the ball-milled sample is 10.1 nm calculated with the above equation.
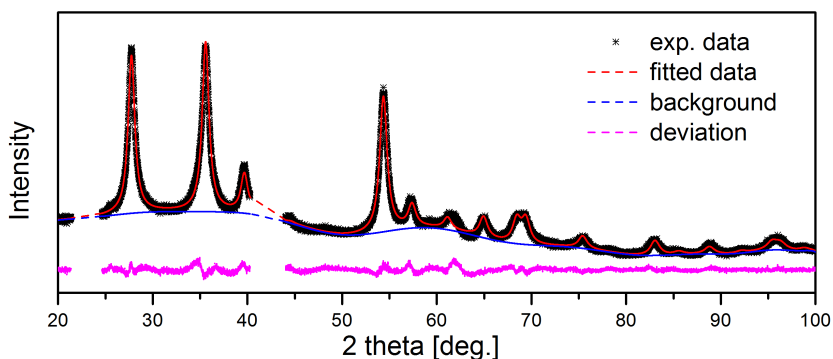

Figure S4.2 Rietveld refinement on the XRD patterns of the ball-milled sample. (The main peaks of TiF_3 and C has been subtracted to obtain an accurate refinement.)

S4.4 SEM-EDX on the ball-milled MgH₂-TiF₃@CNT sample
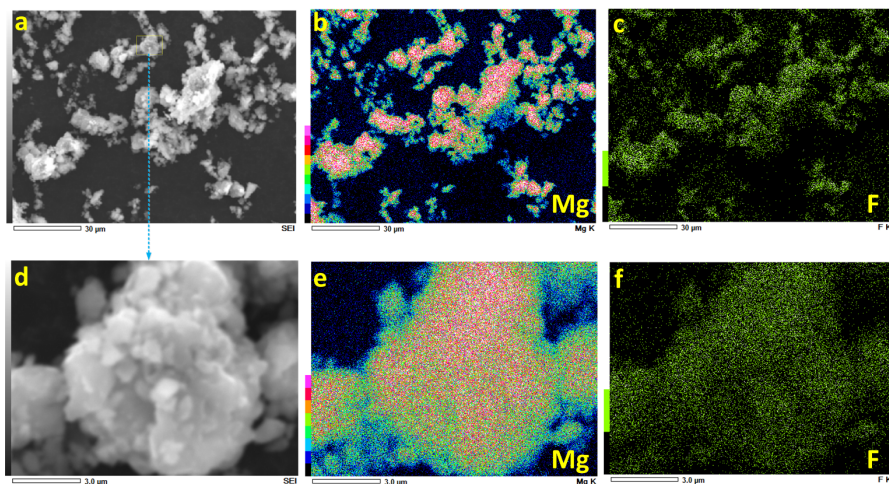
Figure S4.3 SEM-EDX on the ball-milled MgH₂-TiF₃@CNT sample. (a) – (c), a low magnification and (d) – (e), a high magnification SEM-EDX on the ball-milled MgH₂-TiF₃@CNT sample: layered image and element mapping of Mg and F, respectively.

S4.5 Morphology of the MgH₂ electrode
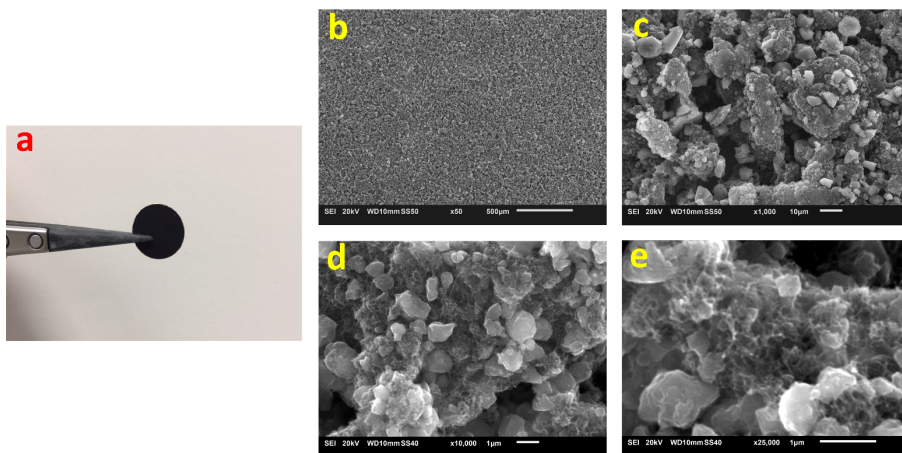
Figure S4.4 Morphology of the MgH₂ electrode. (a), A photo of an electrode (12.7 mm in diameter). (b) – (e), Micro images of the electrode with magnifications of 50x, 1000x, 10000x and 25000x, respectively. The SEM were obtained with a JEOL JSM 6010F scanning electron microscope with an accelerating voltage of 20 kV.

S4.6 Electrochemical performance of the MgH₂ based Li ion anodes
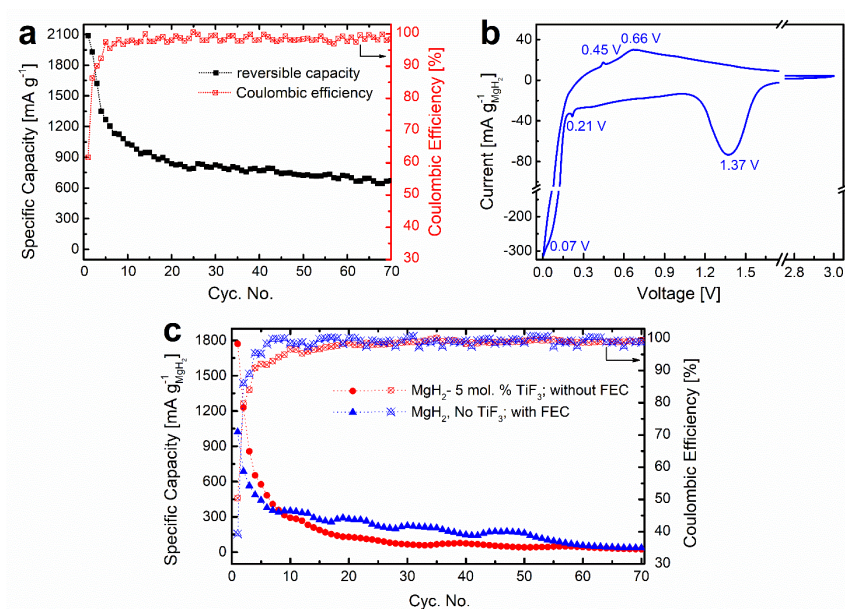
Figure S4.5 Electrochemical performance. (a), The specific capacity and Coulombic efficiency of the MgH₂-TiF₃ based anode including the capacity contribution from the carbon additives (i.e. without subtracting the capacity of the carbon additives). (b), Cyclic voltammogram of the MgH₂ electrode at the first cycle. (scan rate: 0.02 mV s⁻¹.) (c), The electrochemical performance of the MgH₂ anode without TiF₃ addition and the MgH₂-TiF₃ based electrode cycling in an electrolyte without FEC.

S4.7 Rietveld refinement on the XRD patterns of Li ion anode based on MgH₂.

Figure S4.6 Rietveld refinement on the XRD patterns of electrode at different stages: pristine, lithiated to 0.05 and 0.005 V, respectively. (The 2 theta ranges of carbon and Li-C alloy has been subtracted since it is out of the scope of this work.)

Details of the Rietveld refinement are list in the tables below.

phase	Space group	Lattice parameters	Avg. domain size [nm]
MgH$_2$	*P42/mnm*	$a = b = 4.54$, $c = 3.03$	10.1
TiF$_3$	*R-3c h*	$a = b = 4.95$, $c = 13.99$	3.0

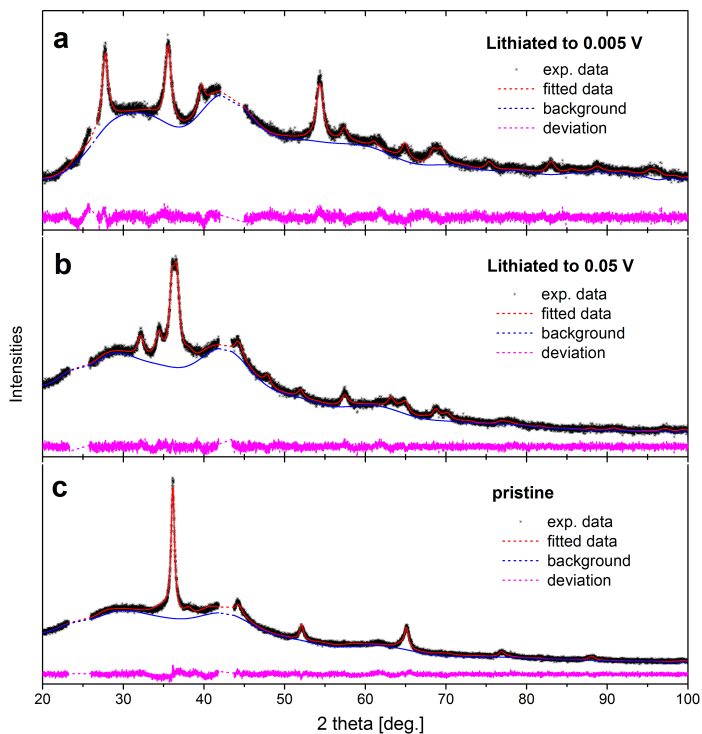Table S4.2 Results of Rietveld refinement on the pristine electrode.

phase	Space group	Lattice parameters	Avg. domain size [nm]
Mg	*P63/mmc*	$a = b = 3.20$, $c = 5.18$	10.1
Li$_{\sim 0.5}$Mg$_{\sim 0.5}$	*Im-3m*	$a = b = c = 3.50$	12.4
LiH	*Fm-3m*	$a = b = c = 4.08$	7.5
MgF$_2$	*P42/mnm*	$a = b = 4.54$, $c = 2.96$	2.8
TiH$_2$	*Fm-3m*	$a = b = c = 4.46$	2.9

Table S4.3 Results of Rietveld refinement on the electrode lithiated to 0.05 V.

phase	Space group	Lattice parameters	Avg. domain size [nm]
Li$_{\sim 0.5}$Mg$_{\sim 0.5}$	*Im-3m*	$a = b = c = 3.50$	18.3
LiH	*Fm-3m*	$a = b = c = 4.08$	7.8
MgF$_2$	*P42/mnm*	$a = b = 4.53$, $c = 2.97$	3.0
TiH$_2$	*Fm-3m*	$a = b = c = 4.44$	2.7

Table S4.4 Results of Rietveld refinement on the electrode lithiated to 0.005 V.

S4.8 MgH₂ based anode for Na ion batteries

The composition of the MgH₂ based Na ion anode is similar to that of MgH₂-TiF₃ based Li ion anode in the main text but a more cost-effective super P carbon black was utilized instead of the carbon nanotubes. The electrochemical sodiation properties of the MgH₂ electrode were tested in half-cell Na ion batteries by testing it against a Na metal counter electrode within 0.005 – 2.8 V *versus* Na/Na⁺ at 0.01 C (C = 2038 mA g⁻¹). 1 M NaPF₆ dissolved in ethylene carbonate (EC) and dimethyl carbonate (DMC) and (EC : DMC = 1:1) was applied as the electrolyte. The cut-off voltage for charge was limited to 2.8 V instead of 3.0 V as it underwent some decomposition of electrolyte at ~ 2.9 V in the electrochemical tests; more electrolyte solvents, such as diethyl carbonate (DEC) and propylene carbonate (PC), were studied as an alternative for DMC, however, the electrolyte decomposition still took place as observed from the voltage profile (an infinite voltage plateau appeared at about 2.9 – 3.0 V).

For comparison, the electrochemical sodiation properties of super P carbon black were tested under the same conditions as that for the MgH₂ electrode and the results are displayed in Figure S4.7.
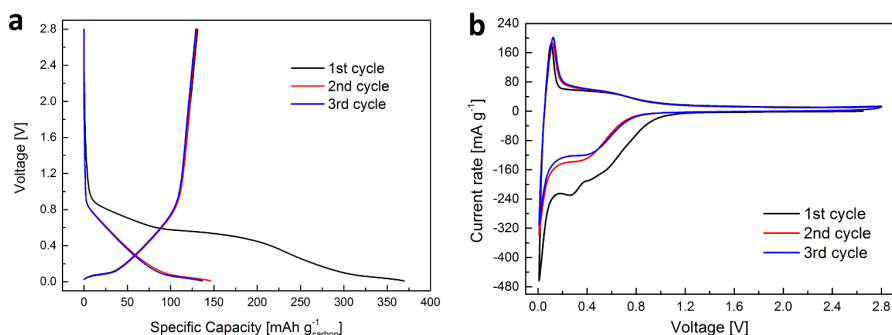
Figure S4.7 (a), Voltage profile and (b), CV curve (scan rate: 0.1 mV s⁻¹) of the super P carbon black electrode tested within a Na ion half-cell.

To investigate the mechanism of the sodiation in the MgH₂ electrode, the crystalline structure of a pellet-like electrode was characterized at different stages: pristine and sodiated to 0.1 V at 0.01 C, respectively. XRD patterns of the pristine electrode showed the spectral contributions of MgH₂, TiF₃ and carbon. When the electrode was electrochemically sodiated to 0.1 V, the relative intensity of MgH₂ dropped and several new sharp diffraction peaks appeared. However, we have not been able to identify them successfully, although the

absence of a Mg phase may indicate that a Na-Mg alloy is formed; the reaction mechanism is not clear yet.
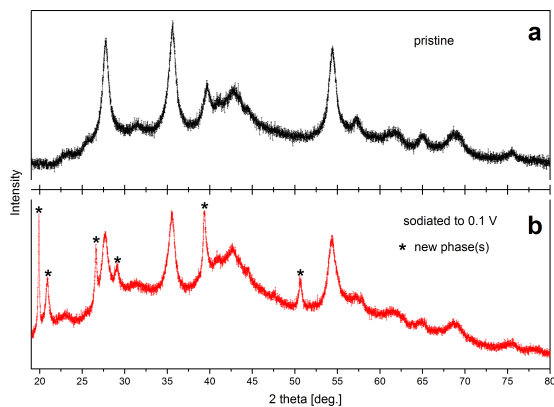
Figure S4.8 XRD patterns of MgH$_2$-TiF$_3$ pellet electrode at two different stages: pristine and sodiated to 0.1 V, respectively.

References

[S1] A.C. Larson, R.B. Von Dreele, Los Alamos National Laboratory Report LAUR (2000) 86-748.

Chapter 5

Phosphorus Based Anode Materials for Na Ion Batteries

In this chapter, we utilize facile mechanochemical method to synthesize black phosphorus – carbon and Sn_4P_3-black phosphorus@graphene nanocomposites. Both materials exhibit outstanding electrochemical cycling performance working as the anode for Na ion batteries.

Chapter 5.1

High-Performance and Low-Cost Na Ion Anode Based on a Facile Black Phosphorus – Carbon Nanocomposite

This chapter is based on:

Abstract
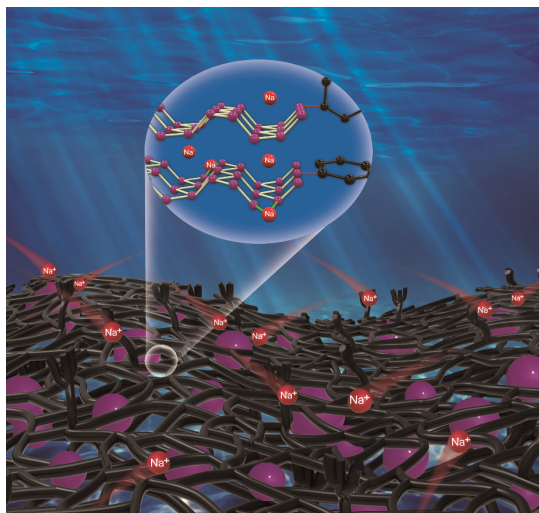
Black phosphorus (BP) has received increasing research attention as an anode material in Na ion batteries due to its high capacity, electronic conductivity and chemical stability. However, it is still challenging for BP based Na ion battery anodes to achieve a high electrochemical performance utilizing cost-effective materials and synthetic methods. This work presents a Na ion anode based on a facile BP – carbon nanocomposite synthesized from commercial red phosphorus and low-cost super P carbon black. Intimate interactions between BP and carbon are present which help to maintain the electrical conduction during cycling and therefore a high cycling stability is achieved. It exhibits a high capacity retention of 1381 mAh g^{-1} for Na ion storage after 100 cycles, maintaining 90.5 % of the initial reversible capacity. Such high performance / materials cost ratio may provide direction for future phosphorus based anodes in high energy density Na ion batteries.

5.1.1 Introduction

Cost-effective and high energy density batteries and battery materials are required to meet the demand of electricity storage. Na ion batteries attract increasing research attention because of the high abundance of sodium compared to lithium, and significant progress has been made in recent years [1-3]. Among the high-capacity anode materials (Sb, Sn, etc.) for sodium ion storage, phosphorus exhibits the highest theoretical capacity of 2596 mAh g^{-1} (Na$_3$P). Significant research interest has been triggered by the prospects of high energy density Na ion batteries based on phosphorus anodes [4, 5].

Phosphorus exists in several allotropes that exhibit strikingly different properties. White phosphorus is chemically unstable, volatile, toxic and non-conducting, and therefore not suitable for battery applications. The most common allotrope, red phosphorus, is widely available and chemically stable, and has been studied intensively for sodium ion batteries [6-13]. However, its low electrical conductivity appears to be a major drawback. To address this issue, these electrodes included a large amount of costly carbon nanomaterials (graphene, carbon nanotube (CNT), carbon nanofiber (CNF), etc.). For large scale applications the use of CNT's needs orders of magnitude reduced cost levels [14], while also graphene and its processing are considered costly [15]. With respect to energy density and manufacturing cost these material factors [16] form a barrier for the commercial introduction of phosphorus as the anode materials for Na ion batteries. Cost-effective super P carbon black are also investigated [17], but the cycle life of the electrode (only 30 de-/sodiation cycles were reported) is still to be improved.

The use of carbon should be noted because carbon and phosphorus do not form binary inorganic or molecular compounds; they can, however, form composites of phosphorus and carbon nanostructures held together by what will likely be weak van der Waals forces. The fact that no P-C compounds are stable implies that upon Na insertion and extraction there are no strong P-C bonds to break or there need not be P or C interdiffusion and/or (de-)mixing during the reactions.

It also should be noticed, during the manufacturing of these red phosphorus based Na ion batteries, mechanical ball milling was frequently applied to promote the integration of the conductive carbon matrix as well as to reduce the particle size of the active materials [11, 12]. The presence of black phosphorus was not reported, however, though It can be

speculated that red phosphorus might have been partially converted into black phosphorus during ball milling.

Black phosphorus, which appears with a layered structure similar to graphite, is thermodynamically the most stable among the allotropes. Meanwhile, it has a relatively high bulk electronic conductivity (~100 S m^{-1}) and low band gap (0.34 eV). Therefore, it has recently drawn much research attention in various energy storage applications including Na ion batteries [18-20]. The first black phosphorus–carbon composite was prepared by Ramireddy *et al.* through a ball milling approach from red phosphorus, and the as-synthesized phosphorus-graphite composite achieved a considerable initial capacity (1427 mAh g^{-1}) for Na ion batteries but poor cycling stability (119 mAh g^{-1} for the 50th cycle) [21]. Since then progress has been made to improve the cycling stability of black phosphorus in Na ion batteries. Cui's group presented a phosphorene (single layer black phosphorus) - graphene hybrid electrode with a reversible sodiation capacity of 2080 mAh g^{-1} in 100 cycles with respect to the mass of phosphorene present [22]. Amine's group developed a black phosphorus – Ketjenblack multiwall carbon nanotube composite that exhibits a high specific capacity with excellent cyclability (~1700 mAh g^{-1} in 100 cycles) [23]. However, these electrodes utilized highly expensive black phosphorus crystals (synthesized under extremely high pressure and temperature [24]) as the starting materials together with a large amount of costly carbon nanomaterials, including CNT and graphene, as well as sophisticated sample processing. Such costly processing and nanomaterials use will limit the commercial viability of phosphorus based anodes in Na ion batteries as described above.

In this work, black phosphorus and a nanocomposite of the black phosphorus and super P carbon black are facilely synthesized through mechanical ball milling. Such technique can in principle be made continuous and scalable [25]. Evidence of bonds between phosphorus and carbon can be found, indicating the intimate contacts between black phosphorus and carbon, which may help to maintain the electronic conduction during cycling and thus to achieve a high cycling stability in Na ion batteries. The black phosphorus exhibits an initial reversible capacity of 1525 mAh g^{-1} for sodium ion storage and 90.5 % of that can still be retained after 100 cycles, which indicates a significant improvement compared to ref. [21] and a superior performance/cost ratio than previous reports on black phosphorus based Na ion battery anodes.

5.1.2 Experimental details

Sample synthesis: To synthesize black phosphorus (BP), commercial red phosphorus (Alfa Aesar, 99 %) was mechanically milled for 70 hours at a rotation speed of 400 rpm with a 100:1 ball-to-material mass ratio under 1 bar argon using a Fritsch Planetary Mono Mill PULVERISETTE 6. The BP - carbon composite (BP-C) was prepared by mechanically milling the as-synthesized BP and super P carbon black (TIMCAL) with a mass ratio 7 : 3 for 20 hours at the same milling conditions as used for the BP synthesis.

Characterization: Scanning electron microscope (SEM) images and the SEM based Energy-dispersive X-ray Spectroscopy (EDX) analysis of the ball-milled samples were taken with a JEOL JSM 6010F scanning electron microscope that operates at an accelerating voltage of 5 kV. Transmission electron microscope (TEM) images and the STEM-EDX analysis were obtained using a monochromated FEI-Tecnai with a field emission gun (FEG) source at an accelerating voltage of 200 kV. X-ray diffraction (XRD) patterns were obtained with a PANalytical X'Pert Pro PW3040/60 diffractometer using a Cu K_α source. The operating voltage and current were 45 kV and 40 mA, respectively. Raman spectroscopy was conducted with a Thermo Scientific Nicolet Almega XR Dispersive Raman Spectrometer. X-ray photoelectron spectroscopy (XPS) measurement was performed with a K-alpha Thermo Fisher Scientific spectrometer using a monochromatic Al K_α source, and the spectra were analyzed with a Thermo Avantage software.

Electrode preparation: The working electrodes were prepared with a conventional slurry based method using the BP-C composite, super P carbon black and sodium carboxymethyl cellulose (NaCMC) with a mass ratio of 8 : 1 : 1 and deionized water as the solvent. Firstly, the slurry was casted on a Cu foil current collector (12.5 μm, Goodfellow) by doctor blading, followed by drying in a vacuum oven at 70 °C and mechanical compaction with a roller compressor for a good electrical contact. Then it was cut into circular test electrodes with a diameter of 12.7 mm. The mass loading of active materials amounts to ~ 1 mg cm^{-2}.

Electrochemistry: The electrochemical performance of the BP-C composite based electrodes was evaluated within half-cell Na ion batteries in which sodium metal was used as the counter electrode. A borosilicate glass micro fiber (Whatman) was employed as the separator. 1 M sodium perchlorate (NaClO$_4$) dissolved in ethylene carbonate (EC) and propylene carbonate (PC) (EC : PC = 1 : 1 in volume) with 10 % fluoroethylene carbonate (FEC) was employed

as the electrolyte. Galvanostatic electrochemical performance of the BP-C anode was studied at room temperature using a MACCOR 4600 battery cycler. Cyclic voltammetry (CV) tests were carried out with a PGSTAT302N Autolab potentiostat. The cut-off voltages were 0.005 V and 1.5 V vs. Na/Na$^+$ for discharge and charge, respectively.

5.1.3   Results and discussions

SEM images (Figure 5.1.1a) show that the as-synthesized BP appears as agglomerates of micron and sub-micron scale due to the high energy ball milling. Upon milling with carbon, the BP-C composite appears more refined (Figure 5.1.1b). TEM images (Figure 5.1.1c & d and Figure S5.1.1 in the Supporting Information (SI)) of the BP-C composite shows that the sample is poorly crystalline with, judging from the lattice spacing, nano-domains of crystalline phosphorus embedded in the amorphous carbon matrix. Meanwhile, EDX analysis based on SEM and STEM element mapping (Figure S5.1.2) shows that both phosphorus and carbon distribute homogeneously throughout the composite; and oxygen appears on the surface of phosphorus and in the carbon network.

XRD patterns (Figure 5.1.1e) reveal that, unlike red phosphorus which is amorphous, black phosphorus shows characteristic crystalline peaks indicating the lattice planes of (020) at 16.8°, (021) at 26.6° and (111) at 35.0°. The grain size of black phosphorus is also gradually reduced for longer durations of ball milling. The average crystalline domain size of black phosphorus reached 8.5 nm using Scherrer's equation and the Rietveld refinement (Figure 5.1.1f and Figure S5.1.4a).

Poorly crystalline Super P carbon black shows two extremely broad characteristic peaks at $2\theta = 25.3°$ and 42.8° corresponding to the Bragg reflection on the (002) and (100) lattice planes. After milling with carbon the BP still shows the characteristic crystalline peaks but they are broader due to the further reduced average crystalline domain size (4.0 nm from the Rietveld refinement in Figure S5.1.4b) and thus poor crystallinity, which is also in line with the TEM analysis. We interpret that as a further refinement of BP domain sizes enabled by a separation or refinement due to the presence of carbon that interferes with the aggregation of BP into larger domains. Moreover, apart from the diffraction peaks of BP, a distinct peak at 22.7° appears, which can be attributed to the reflection of the (002) planes of carbon with an increased lattice spacing. Such expansion may be explained by a concentration of phosphorus

introduced in the carbon when comparing with XRD patterns of phosphorus doped carbon in literature [26, 27].

Raman spectra (Figure 5.1.1g) show the fingerprint Raman bands of black phosphorus corresponding to the A1g, B2g and A2g modes appear at about 354, 428, and 454 cm^{-1}, respectively, which vanished after the milling with carbon. This probably results from the encapsulation of carbon on BP and the high optical absorption of the laser in carbon. The Raman spectrum of super P carbon exhibits both the characteristic carbon D (1360 cm^{-1}) and G band (1579 cm^{-1}) of carbon. The G band is related to the first-order scattering of the E2g mode for sp^2 carbon; and the D band is related to structural defects. After ball milling with black phosphorus, a red-shift of the G band by 13 cm^{-1} from 1579 to 1592 cm^{-1} was accrued, which could be attributed to the Van der Waals interactions between BP and carbon and the formation of P−C bond.
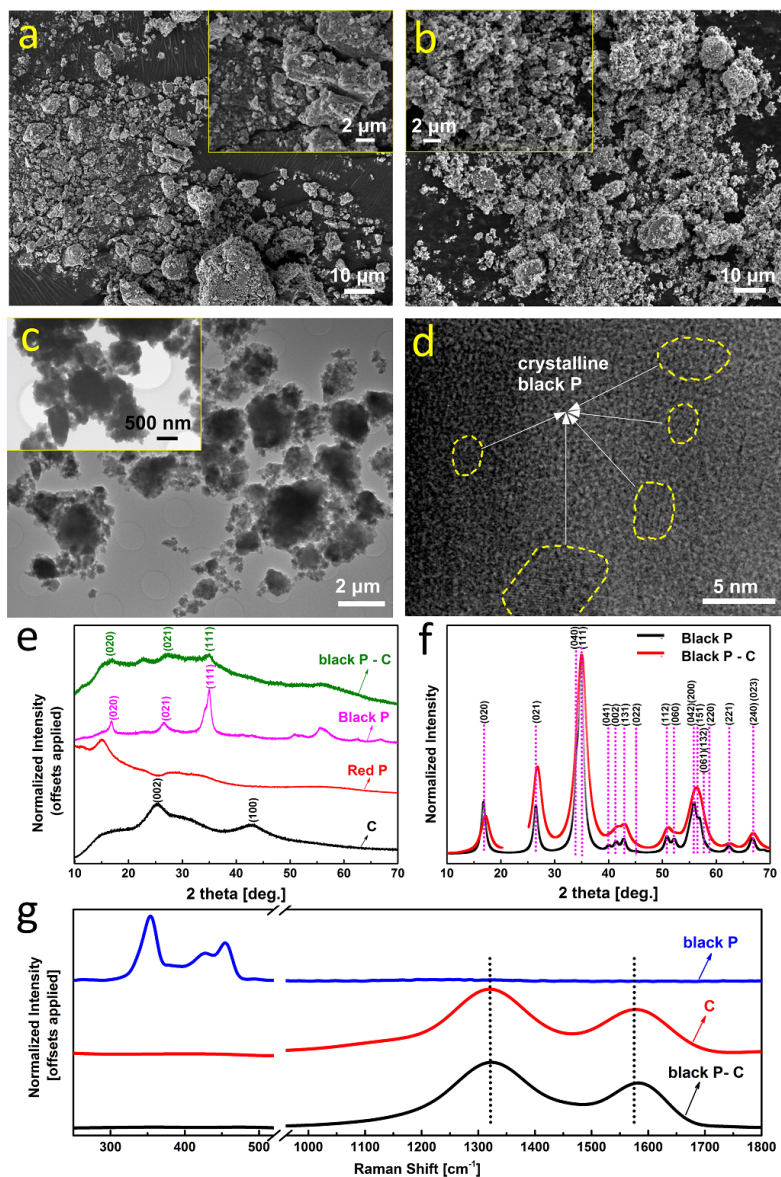
Figure 5.1.1 Characterization on the BP-C related samples. (a), SEM images of ball-milled black phosphorus; (b), SEM images of the BP-C composite. (c) – (d), TEM images of the BP-C composite at different magnifications. (e), XRD patterns of super P carbon black, pristine red phosphorus, black phosphorus and the BP-C composite, respectively. (f), Refined XRD patterns of the black phosphorus and the BP-C composite after subtraction of background; (space group: cmce, $a = 3.364$, $b = 10.472$, $c = 4.326$; detailed refinement in Figure S5.1.4) (g), Raman spectra of super P carbon black, black phosphorus and the as-synthesized BP-C composite.

In order to further investigate the interaction between BP and carbon, XPS was applied to analyse the surface chemical compositions of the samples (Figure 5.1.2). Since the samples are treated in air and water when producing the electrodes the materials studied by XPS were also exposed to air before the measurement. In Figure 5.1.2a, distinct P $2p_{1/2}$ and P $2p_{3/2}$ peaks are identified at 130.1 eV and 131.0 eV, respectively. Broad peaks at a higher energy range are also observed, which corresponds to the surface chemisorption of oxygen (131.9 eV) and oxidation of phosphorus (135.4 eV). The C 1s spectrum (Figure 5.1.2b) illustrates a dominant sp^2 C=C/C-C (284.4 eV) peak indicating a high graphitization level in the sample; a sp^3 carbon peak at 285.4 eV and a low C=O peak at 289.9 eV also appear.

Comparing the XPS spectra of high-energy ball milled BP and the BP-C composite, the characteristic P 2p peak appears to be much more resolved in the latter (Figure 5.1.2c). It indicates that less oxygen/oxidation exists in black phosphorus which is indicative of encapsulation and thus protection by the carbon network when exposed to air. Meanwhile, indistinctive but observable peaks are attributed to P-C (133.1 eV) [28-30], P-O-C (134.1 eV) [30-32] and P-O (135.1 eV) [29, 31]. The presence of chemical bonds between BP and carbon are also evidenced in the C 1s spectrum (Figure 5.1.2d). Specifically, a C-P bond attributed to phosphorus which is located as doping in the carbon (consistent with the increased carbon lattice spacing from XRD) is located at 284.1 eV; the peak from C-O-P/C-O-C lies at 286.7 eV; and a distinct peak appears at 289.7 eV that can be assigned to P-C=O/O-C=O [13, 32, 33]. The bonds with oxygen originate from the oxidation of ball milled carbon upon exposure to air. The BP in the composite shows a marked reduction of the P-O signal. In addition, a more evident appearance C−O/C=O than P-O in the BP-C composite, as well as the higher intensity of the phosphorus - carbon interactions in the C 1s spectrum than in the P 2p range are present. These findings suggest a morphology of black phosphorus encapsulated by carbon rather than an independent uniform distribution of carbon next to phosphorus; oxygen is now seized by the carbon outer layer. This is consistent with the TEM observations that nanosized crystalline phosphorus particles are embedded in the amorphous carbon matrix and the more concentrated oxygen presence in the carbon network and on the surface of phosphorus particles. Such result indicates a reduced oxidation sensitivity of BP in air in the composite, thus facilitating the low-cost, environmentally-friendly, water based slurry method for electrode production.

With respect to the peaks of carbon, super P carbon black is dominated by sp^2 carbon. The BP-C composite still contains both sp^2 and sp^3 carbon, but the intensity of the sp^2 carbon signal is lower, possibly due to a lower level of graphitization in the sample due to the high-energy ball milling.
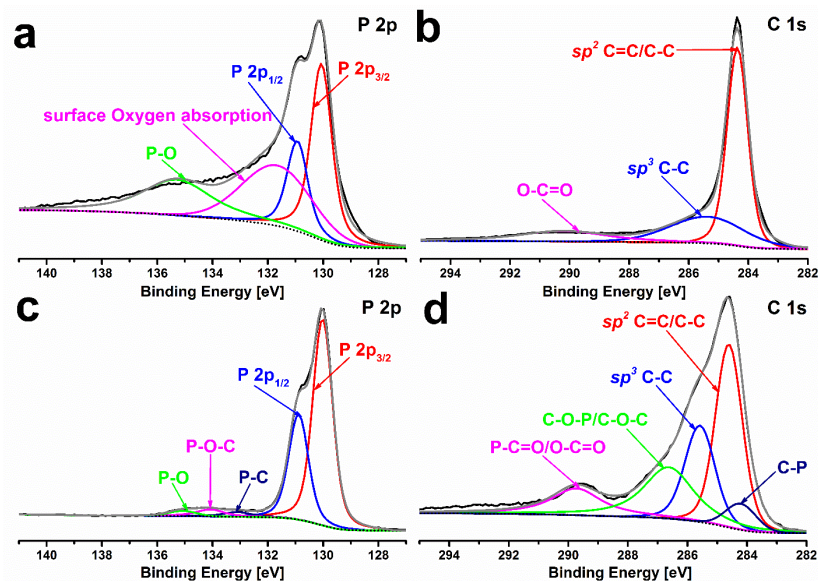

Figure 5.1.2 XPS spectra of the samples. (a), P 2p spectrum of black phosphorus; (b), C 1s spectrum of super P carbon black; (c), P 2p, and (d), C 1s of the BP-C composite.

The electrochemical performance of the BP-C composite anode (Figure 5.1.3) was evaluated within half-cell Na ion batteries. The working electrodes were prepared with a conventional slurry based method using the BP-C composite, super P carbon black and NaCMC with a mass ratio of 8 : 1 : 1 and deionized water as the solvent. The capacity contribution from super P carbon black has been determined in past work [34] and then subtracted from the BP-C electrode. The specific capacities reported in this paper were the capacity calculated based on the mass of black phosphorus (subtracting of the capacity stored in carbon; the capacity based on the mass of the full BP-C composite is displayed Figure S5.1.5). Figure 5.1.3a shows that, cycling at 0.1 A g^{-1}, the BP-C anode achieved a reversible capacity of 1525 mAh g^{-1} for sodium ion insertion in the 1st cycle; and the Coulombic efficiency amounts to 62.4 %. The capacity loss in the 1st cycle can be ascribed to irreversible decomposition of electrolyte and solid electrolyte interphase (SEI) formation. The Coulombic efficiency increased to 97.2 % for the 2nd cycle and remained stable close to 100% after that, indicating that the

SEI layer is mostly formed during the 1st cycle. Further SEI formation in the following cycles was limited, possibly aided by the use of FEC in the electrolyte [35, 36]. A high capacity of 1381 mAh g^{-1} was retained after 100 cycles which accounts for 90.5 % of the capacity from the first cycle.

The Rate capability of the electrode (Figure 5.1.3b) has been studied at various current rates from 0.1 to 2.0 A g^{-1}. The capacities reached 1460, 975, 700 and 465 mAh g^{-1} at 0.2, 0.5, 1.0 and 2.0 A g^{-1}, respectively. Afterwards a capacity of about 1490 mAh g^{-1} was obtained when the rate was reset to 0.1 A g^{-1}.These high rate capabilities indicate that the electrical conductivity has been greatly enhanced throughout the electrode by the conducting carbon network that enables good electronic charge transport.

A sloped voltage plateau at ~ 0.6 V originating from the irreversible SEI formation is observed in the 1st sodium ion insertion of the BP-C electrode (Figure 5.1.3c); it disappears in the following cycles. This is consistent with the anodic cyclic voltammetry (CV) profiles (Figure 5.1.3d). The major sodium ion uptake and formation of Na$_x$P occurs between 0.5 – 0.2 V *vs.* Na/Na$^+$; while the release of sodium ion mostly takes place between 0.4 – 0.9 V. This is also in accordance with the CV profile. The cathodic peaks at around 0.59 V, 0.69 V and 0.93 V are related to the stepwise release of sodium ion from the fully sodiated phases (Na$_x$P).

The improved cycling stability in the BP-C electrode when compared to a black phosphorus electrode without carbon addition (rapid capacity degradation over cycling, Figure S5.1.6), may thus result from the following: (1) As described in the XRD analysis black phosphorus has been downsized to only a few nm through the apparent refinement induced by the presence of carbon. Such further nanoscaling will enable a more rapid kinetics for sodium ion uptake. Moreover, the small grain size may also allow for a higher stress tolerance upon the volume changes that occur during dis-/charge and minimize further particle pulverization as the particles are already small. (2) Interactions between black phosphorus and carbon are present in the sample as deduced from the XRD, Raman and XPS spectra. These interactions help to maintain electrical contact between BP and the carbon network and also preserve the structural integrity of the electrode during cycling.

The improvement in cycling performance compared to ref. [21] will be the beneficial effects of several factors: (1), reduced size of carbon materials which enables better electrical

conduction in the composite and more interactions with phosphorus; (2), higher energy applied in the ball milling procedure, which reduces the particle size allowing for faster kinetics and stronger interactions between phosphorus and carbon;(3), increased FEC concentration in the electrolyte which creates a more stable SEI layer and (4), limited voltage window for cycling resulting in ameliorated structural deformation along cycling [21, 37, 38].
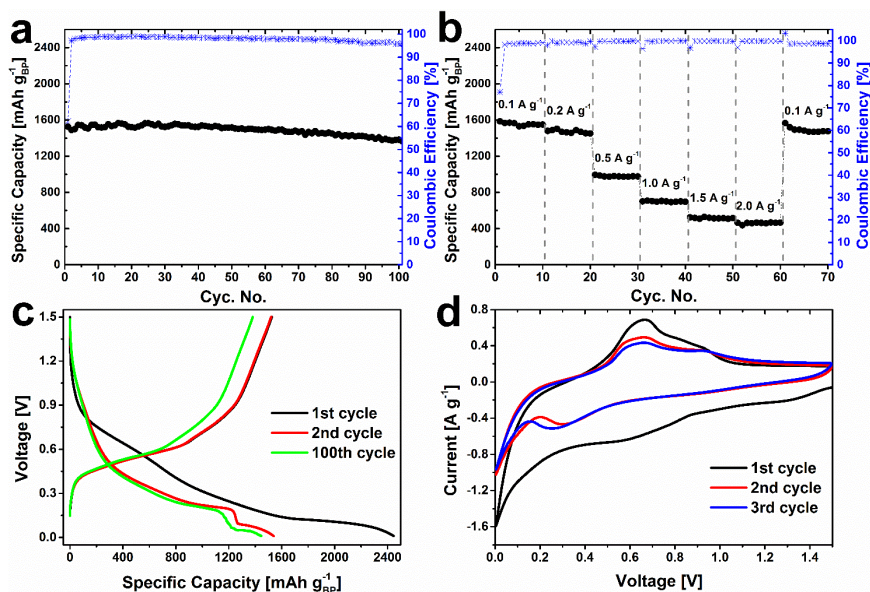

Figure 5.1.3 Electrochemical performance of the BP-C composite anode for sodium ion batteries. (a), Capacity retention and Coulombic efficiency cycling at 0.1 A g^{-1}; (b), Rate capability; (c), Voltage profile of the electrode cycling at 0.1 A g^{-1}; (d), Cyclic voltammetry of the electrode for the first 3 cycles. (scan rate: 0.2 mV s^{-1})

5.1.4   Conclusions

In summary, we developed a cost-effective, high-performance anode for Na ion batteries based on a facilely synthesized black phosphorus – carbon composite. The active material for the electrode was synthesized via a scalable ball-milling approach utilizing low-cost commercial red phosphorus and super P carbon black starting materials. The synthetic black phosphorus becomes intimately bound within the protective and conducting carbon matrix and a high capacity retention and cycling stability for sodium ion storage has been achieved (1381 mAh g^{-1} in 100 cycles accounting for 90.5 % of the initial reversible capacity). Taking into account the low cost materials together with the industrially scalable synthesizing

approach and compared to the previous studies on black phosphorus based Na ion battery anodes, the facile black phosphorus – carbon composite reported in this work may be considered to exhibits a remarkable performance/cost ratio and may have considerable potential for its commercial introduction in high energy density Na ion batteries.

References

[1] B. L. Ellis, L. F. Nazar, Curr. Opin. Solid State Mater. Sci. 16 (2012) 168-177.

[2] W. Luo, F. Shen, C. Bommier, H. Zhu, X. Ji, L. Hu, Acc. Chem. Res. 49 (2016) 231-240.

[3] H. Kim, H. Kim, Z. Ding, M.H. Lee, K. Lim, G. Yoon, K. Kang, Adv. Energy Mater. 6 (2016) 1600943.

[4] M. Dahbi, N. Yabuuchi, K. Kubota, K. Tokiwa, S. Komaba, Phys. Chem. Chem. Phys. 16 (2014) 15007-15028.

[5] M. Shimizu, H. Usui, K. Yamane, T. Sakata, T. Nokami, T. Itoh, H. Sakaguchi, Int. J. Electrochem. Sci. 10 (2015) 10132-10144.

[6] W. Li, S. H. Hu, X. Luo, Z. Li, X. Sun, M. Li, F. Liu, Y. Yu, Adv. Mater. 29 (2017) 1605820.

[7] C. Zhang, X. Wang, Q. Liang, X. Liu, Q. Weng, J. Liu, Y. Yang, Z. Dai, K. Ding, Y. Bando, J. Tang, D. Golberg, Nano Lett. 16 (2016) 2054-2060.

[8] W. Li, Z. Yang, M. Li, Y. Jiang, X. Wei, X. Zhong, L. Gu, Y. Yu, Nano Lett. 16 (2016) 1546-1553.

[9] W. J. Li, S. L. Chou, J. Z. Wang, H. K. Liu, S. X. Dou, Nano Lett. 13 (2013) 5480-5484.

[10] L. Pei, Q. Zhao, C. Chen, J. Liang, J. Chen, ChemElectroChem 2 (2015) 1652-1655.

[11] J. Song, Z. Yu, M. L. Gordin, S. Hu, R. Yi, D. Tang, T. Walter, M. Regula, D. Choi, X. Li, A. Manivannan, D. Wang, Nano Lett. 14 (2014) 6329-6335.

[12] J. Song, Z. Yu, M. L. Gordin, X. Li, H. Peng, D. Wang, ACS Nano 9 (2015) 11933-11941.

[13] B. Ruan, J. Wang, D. Shi, Y. Xu, S. Chou, H. Liu, J. Wang, J. Mater. Chem. A 3 (2015) 19011-19017.

[14] M.F.L. De Volder, S.H. Tawfick, R.H. Baughman, A.J. Hart, Science 339 (2013) 535-539.

[15] K. S. Novoselov, V.I. Falko, L. Colombo, P.R. Gellert, M.G. Schwab, K. Kim, Nature 490 (2012) 192-200.

[16] Y. Gogotsi, P. Simon, Science 334 (2011) 917-918.

[17] Y. Kim, Y. Park, A. Choi, N.-S. Choi, J. Kim, J. Lee, J. H. Ryu, S. M. Oh, K. T. Lee, Adv. Mater. 25 (2013) 3045-3049.

[18] K. P. S. S. Hembram, H. Jung, B. C. Yeo, S. J. Pai, S. Kim, K. R. Lee, S. S. Han, J. Phys. Chem. C 119 (2015) 15041-15046.

[19] V. V. Kulish, O. I. Malyi, C. Persson, P. Wu, Phys. Chem. Chem. Phys. 17 (2015) 13921-13928.

[20] L. Q. Sun, M. J. Li, K. Sun, S. H. Yu, R. S. Wang, H. M. Xie, J. Phys. Chem. C 116 (2012) 14772-14779.

[21] T. Ramireddy, T. Xing, M. M. Rahman, Y. Chen, Q. Dutercq, D. Gunzelmann, A. M. Glushenkov, J. Mater. Chem. A 3 (2015) 5572-5584.

[22] J. Sun, H.-W. Lee, M. Pasta, H. Yuan, G. Zheng, Y. Sun, Y. Li, Y. Cui, Nat. Nanotechnol. 10 (2015) 980-985.

[23] G. L. Xu, Z. Chen, G. M. Zhong, Y. Liu, Y. Yang, T. Ma, Y. Ren, X. Zuo, X. H. Wu, X. Zhang, K. Amine, Nano Lett. 16 (2016) 3955-3965.

[24] P. W. Bridgman, J. Am. Chem. Soc. 36 (1914) 1344-1363.

[25] P. Baláž, in Mechanochemistry in Nanoscience and Minerals Engineering, Springer Berlin Heidelberg, 2008, pp. 103-132.

[26] J. Wu, Z. Yang, Q. Sun, X. Li, P. Strasser, R. Yang., Electrochim. Acta 127 (2014) 53-60.

[27] J. Wu, C. Jin, Z. Yang, J. Tian, R. Yang, Carbon 82 (2015) 562–571.

[28] J. Zhu, S.P. Jiang, R. Wang, K. Shi, P.K. Shen, J. Mater. Chem. A 2 (2014) 15448-15453.

[29] J.-S. Li, Y. Wang, C.-H. Liu, S.-L. Li, Y.-G. Wang, L.-Z. Dong, Z.-H. Dai, Y.-F. Li, Y.-Q. Lan, Nat. Commun. 7 (2016) 11204.

[30] J.M. Rosas, R. Berenguer, M.J. Valero-Romero, J. Rodríguez-Mirasol, T. Cordero, Front. Mater. 1 (2014) 29.

[31] W. Qi, H. Zhao, Y. Wu, H. Zeng, T. Tao, C. Chen, C. Kuang, S. Zhou, Y. Huang, Sci. Rep. 7 (2017) 43582.

[32] J. Sun, H.-W. Lee, M. Pasta, Y. Sun, W. Liu, Y. Li, H. R. Lee, N. Liu, Y. Cui, Energy Storage Mater. 4 (2016) 130–136.

[33] J. Sun, G. Zheng, H.-W. Lee, N. Liu, H. Wang, H. Yao, W. Yang, Y. Cui, Nano Lett. 14 (2014) 4573-4580;

[34] Y. Xu, E. Swaans, S. Basak, H. W. Zandbergen, D. M. Borsa, F. M. Mulder, Adv. Energy Mater. 6 (2016) 1501436.

[35] M. Dahbi, N. Yabuuchi, M. Fukunishi, K. Kubota, K. Chihara, K. Tokiwa, X.-f. Yu, H. Ushiyama, K. Yamashita, J.-Y. Son, Y.-T. Cui, H. Oji, S. Komaba, Chem. Mater. 28 (2016) 1625-1635.

[36] N. Yabuuchi, Y. Matsuura, T. Ishikawa, S. Kuze, J.-Y. Son, Y.-T. Cui, H. Oji, S. Komaba, ChemElectroChem 1 (2014) 580-589.

[37] C.-M. Park, H.-J. Sohn, Adv. Mater. 19 (2007) 2465–2468.

[38] B. Mortemard De Boisse, D. Carlier, M. Guignard, L. Bourgeois, C. Delmas, Inorg. Chem. 53 (2014) 11197–11205.

Supporting Information for Chapter 5.1

S5.1.1 TEM image of the BP-C composite

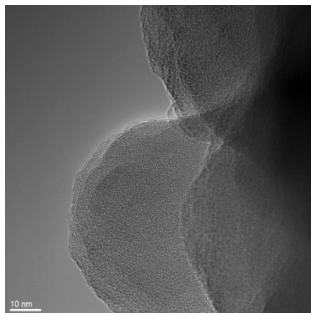Figure S5.1.1 TEM image of the BP-C composite.

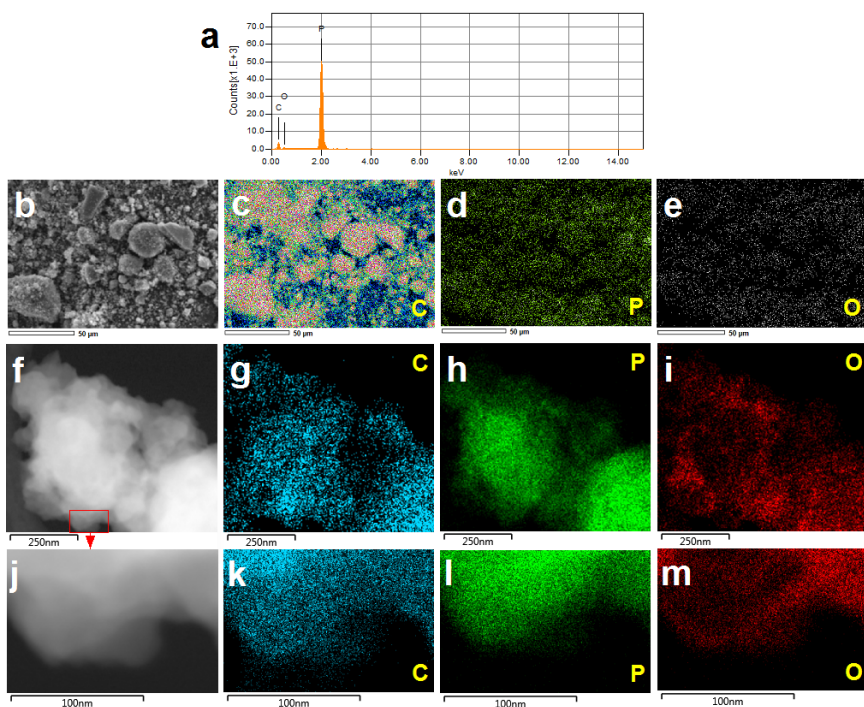### S5.1.2 SEM-EDX characterization on the BP-C composite

Figure S5.1.2 (a), SEM-EDX spectrum and (b) – (e), SEM based EDX element mapping results (scale bar: 50 μm): the layered SEM image and the element mapping of C, P and O in the BP-C composite, respectively. (f) - (m), STEM based EDX mapping results (scale bars: 250 nm and 100 nm, respectively).

5.1.3 XRD analysis on the samples
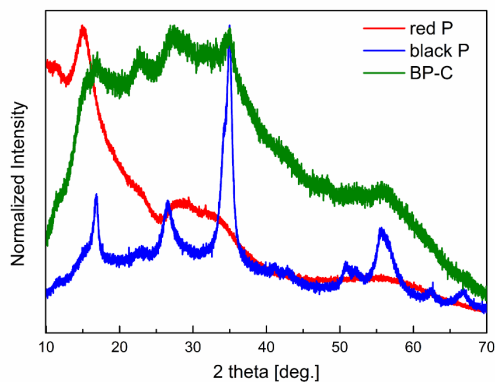
Figure S5.1.3 Normalized XRD patterns of the pristine red P, as-synthesized black P and the BP-C composite.

Rietveld refinement on the XRD patterns of black phosphors and the BP-C composite was carried out within the General Structure Analysis System (GSAS) software suite [S1].

Figure S5.1.4 Rietveld Refinement on the black phosphorus (space group: *Cmce*) phase in the XRD patterns of (a), the ball-milled BP and (b), the BP-C composite. (In Figure (b), the 2 theta range of black phosphorus doped carbon was subtracted to achieve an accurate refinement.)

Detailed results on the refinement are displayed in the table below.

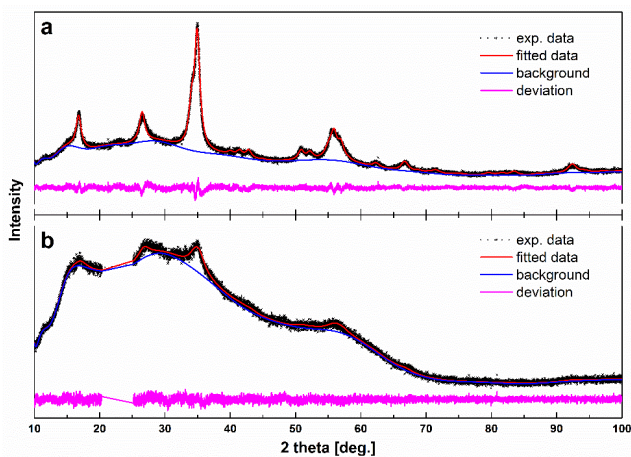| samples	Space group	Lattice parameters [Å]	Atom coordinates	U_{iso}	Avg. domain size [nm]
black phosphorus	*Cmce*	$a = 3.327$, $b = 10.490$, $c = 4.352$	8f (0, 0.1018, 0.06772)	0.01785	8.5
BP-C composite	*Cmce*	$a = 3.364$, $b = 10.472$, $c = 4.326$	8f (0, 0.1119, 0.08827)	0.04437	4.0

Table S5.1.1 Detailed Rietveld refinement results on the black phosphorus phase in the as-synthesized BP and in the BP-C composite. Note the reduced crystalline domain size and the increased atomic displacement factor U_{iso} in the composite (indicative of somewhat increased disorder in the position of the phosphorus atoms).

S5.1.4 Electrochemical performance of the BP-C composite anode for Na ion batteries
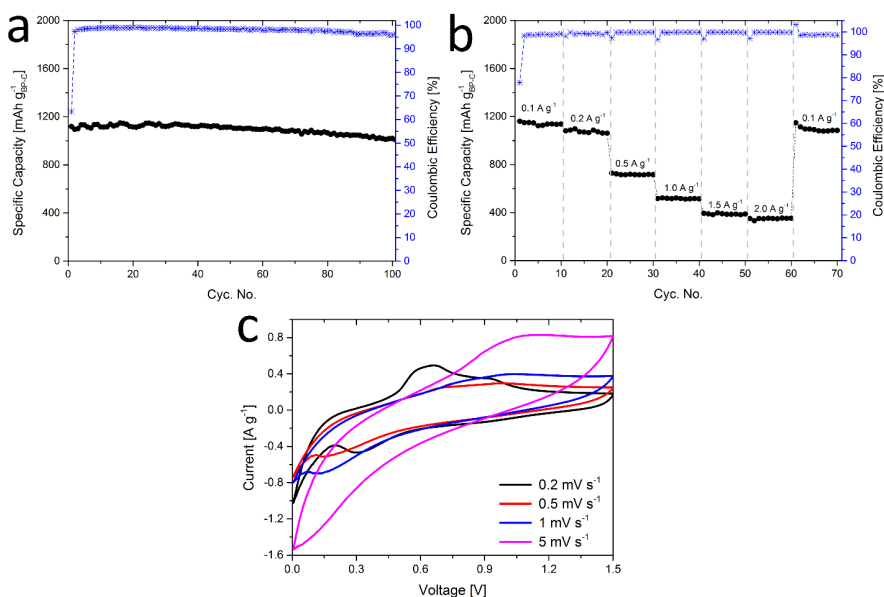
Figure S5.1.5 Electrochemical performance. (a), Capacity retention and Coulombic efficiency at 0.1 A g^{-1} and (b), Rate capability of the BP-C composite based electrodes for sodium ion batteries with respect to the total mass of the BP-C composite. (c), Cyclic voltammetry of the BP-C electrode at different scan rates.

S5.1.5 A comparison between BP with and without carbon based Na ion battery anodes
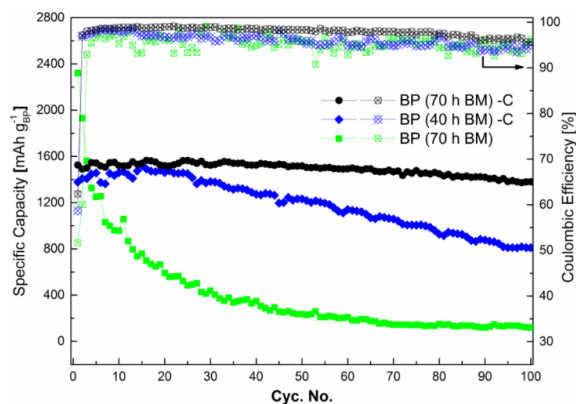
Figure S5.1.6 Electrochemical performance of sodium ion anodes based on black phosphorus with and without carbon. (The BP electrode was prepared with the same procedure that was applied in the BP-C electrode fabrication and the dis-/charge rate was 0.1 A g^{-1}.)

S5.1.6 Micro-morphologies of the phosphorus sample at different stages
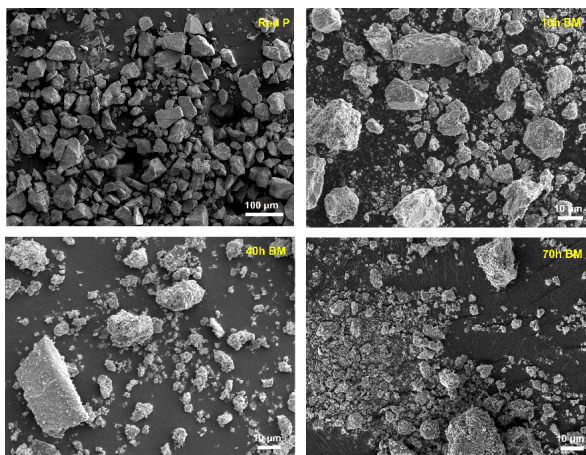
Figure S5.1.7 SEM images of phosphorus at different ball-milling stages: (a), pristine red phosphorus; (b), after 10 h milling; (c), after 40 h milling; (c), after 70 h milling.

References

[S1] A.C. Larson, R.B. Von Dreele, Los Alamos National Laboratory Report LAUR (2000) 86-748.

Chapter 5.2

A High-Rate and Ultrastable Na Ion Anode Based on a Novel Sn$_4$P$_3$-P@Graphene Nanocomposite

This chapter is based on:

Y. Xu, B. Peng, F.M. Mulder, *A High-Rate and Ultrastable Na Ion Anode Based on a Novel Sn$_4$P$_3$-P@Graphene Nanocomposite*, ***Adv. Energy Mater.* 8 (2018) 1701847.**

Abstract
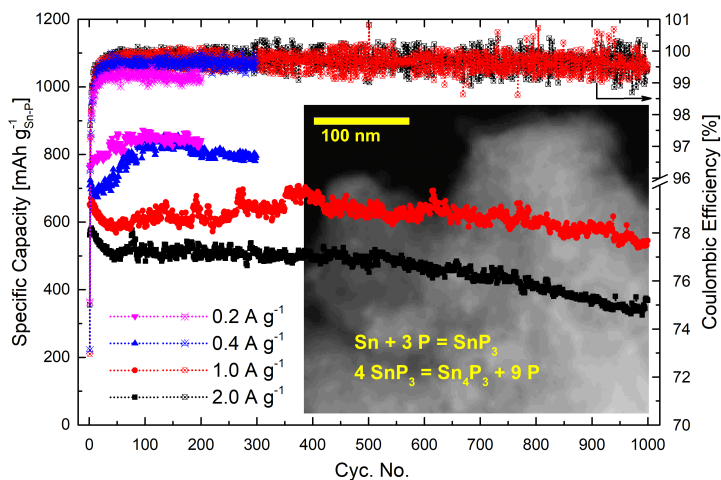
Phosphorus and tin phosphide based materials that have been extensively researched as the anode for Na ion batteries mostly involve complexly synthesized and sophisticated nanocomposites limiting their commercial viability. This work reports a Sn$_4$P$_3$-P (Sn:P = 1:3) @graphene nanocomposite synthesized with a novel and facile mechanochemical method, which exhibits unrivalled high-rate capacity retentions of >550 and 371 mAh g^{-1} at 1 and 2 A g^{-1}, respectively, over 1000 cycles and achieves excellent rate capability (>815, ~585 and ~315 mAh g^{-1} at 0.1, 2 and 10 A g^{-1}, respectively).

5.2.1 Introduction

Na ion batteries recently have received increasing research attention as an alternative to Li ion batteries due to the higher abundance and thus much lower cost of Na resources compared to Li [1-5], Phosphorus [6-14] and tin [15-23] have been intensively investigated as the anode materials for Na ion batteries due to their high capacities upon alloying with Na (Na_3P: 2596 mAh g^{-1}, $Na_{15}Sn_4$: 847 mAh g^{-1}). However, the electronic conductivity of phosphorus is low (10^{-14} S cm^{-1} for red P); and these alloying reactions are inevitably accompanied with substantial volume expansions (volume change of 490 % from P to Na_3P [12], and 525 % from Sn to $Na_{15}Sn_4$ [17]), and with drastic structural collapse when Na ions are extracted. As a result, upon repetitive dis-/charge, it undergoes irreversible and adverse pulverization of active materials and loss of electrical conduction and eventually the battery failure. To address these issues, various designs of nanostructured Sn/P-C composites have been reported [7-14, 18-23], but the manufacturing cost is still to be reduced and the achieved reversible sodiation capacity is still to be improved. Very recently, Li *et al.* [14] demonstrated a red P@MOF derived N-doped microporous carbon exhibiting a capacity of 450 mAh g^{-1} at 1 A g^{-1} after 1000 cycles. Sha *et al.* [23] fabricated Sn nanoparticles@N-doped carbon nanofiber which achieved a capacity of 390 mAh g^{-1} at 0.847 A g^{-1} over 1000 cycles.

Metal phosphides (MP_x, M = Ni [24], Cu [25, 26], Ge [27, 28], Fe [29, 30], Sn [31-41], etc.) have also shown high reversible capacities for Na ion storage and much improved cycling stability and rate capability, which originates from the enhancement of electrical conductivity upon the presence of metal atoms as electronic pathways for phosphorus atoms. Among all these metal phosphides, SnP_x received the most research attention. Fan *et al.* [31] reported a SnP_3/C nanocomposite Na ion anode delivering a capacity of ~810 mAh g^{-1} at 0.15 A g^{-1} in 150 cycles. Usui *et al.* [32] showed that Sn_4P_3 exhibits a much enhanced electrochemical cycling performance of reversible Na ion storage compared to SnP_3 due to its superior electronic conductivity and more uniform Sn dispersion in the P matrix. Liu *et al.* [36] synthesized yolk–shell Sn_4P_3@C nanospheres which achieved a reversible capacity retention of 360 mAh g^{-1} for Na ion storage at 1.5 A g^{-1} after 400 cycles. However, long-term cycling of more than 500 cycles with a high stability and high reversible capacity for Na ion storage has not been reported.

In this work, a nanocomposite of Sn_4P_3 and phosphorus (Sn:P = 1:3) embedded in a graphene matrix has been synthesized via a novel mechanochemical transformation method. This

composite exhibits an ultra-stable and much improved capacity retention at a high current rate (>550 mAh g^{-1} in 1000 cycles at 1A g^{-1}) and unrivalled rate capability (>815 mAh g^{-1} at 0.1 A g^{-1}, ~585 mAh g^{-1} at 2 A g^{-1} and ~315 mAh g^{-1} at 10 A g^{-1}). This is, to the best of our knowledge, superior to any other Sn-P compounds and other metal phosphides based materials reported as the anode for Na ion batteries and it provides substantial promise to its practical applications in Na ion batteries that typically require at least 1000 cycles.

5.2.2 Experimental details

Sample synthesis: To synthesize SnP₃, tin (Aldrich, <45 μm, 99.8%) and red phosphorus (Alfa Aesar, -325 mesh, 98.9%) powders were mixed with an atomic ratio of 1:3, then the mixture was mechanically milled for 30 hours at 400 rpm with a ball to powder ratio of 100:1 under Ar atmosphere. Subsequently, the as-synthesized SnP₃ was mixed with graphene stacks (Cabot, ~700 m² g^{-1}) with a mass ratio of 7:3 and then mechanically milled at the same conditions for 10 hours to obtain the SPG sample or 50 hours to get the SPPG nanocomposite.

Sample characterization: X-ray diffraction (XRD) patterns were obtained with a PANalytical X'Pert Pro PW3040/60 diffractometer with a Cu K$_α$ source. The operating voltage and current were 45 kV and 40 mA, respectively. Scanning electron microscope (SEM) images of the SPPG sample were obtained with a JEOL JSM 6010F scanning electron microscope working at an accelerating voltage of 5 kV. SEM based Energy Dispersive X-Ray Spectroscopy (EDX) element mapping was carried out at an accelerating voltage of 20 kV. The Transmission electron microscope (TEM) images and scanning transmission electron microscope (STEM) based EDX analysis were taken using a FEI-Tecnai with a field emission gun (FEG) source working at 200 kV. X-ray photoelectron spectroscopy (XPS) measurement was performed with a K-alpha Thermo Fisher Scientific spectrometer using a monochromatic Al K$_α$ source, and the spectra were analysed with a Thermo Avantage software.

Electrode preparation: The SPPG, SPG and SnP₃ based electrodes were prepared using a conventional slurry based method. Specifically, the active materials, sodium carboxymethyl cellulose (NaCMC) and super P carbon black are mixed with a mass ratio of 7:1:2 in deionized water until a homogeneous slurry was obtained; then the slurry was casted onto a piece of Cu foil (Goodfellow, 12.5 μm) and dried in a vacuum oven working at 70 °C for 12 hours. Finally, the electrode was mechanically compacted with a roller compressor before it

was cut into circular pieces for the final battery assembly. The mass loading of active materials is ~0.5 mg cm^{-2}.

Electrochemistry: Na ion half-cells were assembled in an Ar atmosphere glove box (O_2/ H_2O: <0.1 ppm). A sodium metal foil was employed as the counter electrode and a borosilicate micro glass fibre (Whatman) was used as the separator. The working electrolyte is 1 M $NaClO_4$ dissolved in ethylene carbonate (EC) and propylene carbonate (PC) (v/v =1:1) with 10 % fluoroethylene carbonate (FEC). The galvanostatic electrochemical performance was characterized with a MACCOR 4600 battery cycler. The cut-off voltages for sodiation and desodiation were 0.005 V and 2 V *vs.* Na/Na$^+$, respectively. Cyclic voltammetry (CV) was carried out with a PGSTAT302N Autolab potentiostat within the same voltage range.

5.2.3   Results and discussions

As described in Figure 5.2.1a, the Sn_4P_3-P@graphene nanocomposite (indicated as SPPG) is synthesized via mechanochemical transformation from the SnP_3@graphene composite (indicated as SPG) (Reaction (5.2.1)),

$$4 SnP_3 = Sn_4P_3 + 9 P \qquad\qquad (5.2.1)$$

where SnP_3 is initially mechanochemically synthesized from Sn and red P (Reaction (5.2.2)).

$$Sn + 3 P = SnP_3 \qquad\qquad (5.2.2)$$

The initial formation of SnP_3 is evidenced by XRD (Figure 5.2.1b & Figure S5.2.1 in the Supporting Information (SI)) as all the peaks can be indexed to the SnP_3 phase (Pearson's Crystal Data (PCD) #1250771, space group: *R-3mh*). It is retained after a short-term mechanical milling with graphene, and is mechanochemically converted to Sn_4P_3 (PCD#1910451, space group: *R-3mh*) when further milling is performed as is observed by XRD (Figure 5.2.1b). Rietveld refinement on the XRD patterns (Figure S5.2.2 & Table S5.2.1) shows that the average crystalline domain size of SnP_3 amounts to 15.0 nm, while that of Sn_4P_3 is much reduced to 9.4 nm due to the refinement effect of high energy mechanical milling.

The conversion from SnP_3 to Sn_4P_3 is also evident in the XPS investigation (Figure 5.2.1c & S5.2.3). In the analysis of Sn 3d XPS spectra of Sn-P compounds, multiple valence contributions (Sn^{2+}, Sn^{4+}, etc.) are generally considered [34, 39, 40, 42]. SnP_3 has a single Sn site surrounded by six P atoms in the crystal structure and a ^{119}Sn Mössbauer Isomer shift

indicates an oxidation state of +3 in bulk crystals [43], the main Sn $3d_{5/2}$ XPS peak of SnP$_3$ at 485.5 eV may therefore be assigned to Sn^{3+}. The higher binding energy peak at 487.2 eV results from oxidized Sn^{4+} on the surface of nanoparticles. Such high oxidation occurs likely because of the P surface termination leading to a higher Sn oxidation state. It should also be noted that some unavoidable surface oxidation by oxygen may be present, which is consistent with the peaks of P-O bonds in the P 2p spectra, and also in line with other XPS studies on Sn-P compounds [31, 34, 42]. However, since the P terminated surface already leads to the oxidation of Sn to +4, the oxidizing effect of oxygen on Sn may be limited. The strong peak of SPPG at 487.6 eV has a line width and shape similar to the spectrum of Sn$_4$P$_3$ in ref. [34, 39, 40], and the weak peak at 485.5 eV may indicate a small fraction of remaining SnP$_3$. The valence of Sn is suggested by the Mössbauer study [43] to be lower in Sn$_4$P$_3$ compared to SnP$_3$, and may be +2.25 on average assuming a chemical state of P^{3-}. The XPS binding energies depend on local coordination as well as valence, and 1-2 eV deviations are usually observed in binding energies for the same valence depending on the coordination in the compounds [44]. In Sn$_4$P$_3$, the Sn-1 atoms are octahedrally coordinated by six P atoms resembling SnP$_3$, whereas Sn-2 atoms have a [3+3] coordination consisting of three P and three Sn-2 atoms. Thus the binding energy will deviate from that in SnP$_3$ and shift to higher binding energies. Meanwhile, a Sn^{4+} contribution cannot be excluded for the same reason of surface termination by P.

In the SPPG sample, phosphorus is formed and embedded in the graphene matrix and it appears as black phosphorus (PCD#1214640, space group: *Cmce*) but is poorly crystalline; weak but distinguishable peaks at 27.0° and ~35.0° can be observed in the XRD pattern of SPPG corresponding to the Bragg diffraction on the lattice planes (021) and (040)/(111) of black phosphorus, respectively. SEM images (Figure 5.2.1d – f) show that the SPPG nanocomposite appears as agglomerations of nanoparticles and SEM-EDX element mapping on the agglomeration (Figure S5.2.4) reports a homogeneous distribution of P and Sn in the composite. TEM images (Figure 5.2.1g & Figure S5.2.5) and the annular dark field (ADF) STEM image (Figure 5.2.1h) show the nanosized crystalline domains of active materials embedded in the graphene matrix and distributed evenly; and the STEM-EDX based element mapping of Sn (Figure 5.2.1i) shows a consistent distribution with the distribution of active materials in the ADF-STEM image. P appears not only where Sn is concentrated but uniformly throughout the sample, and so do C and O (Figure 5.2.1j – l), which reveals that

elemental phosphorus formed in Reaction (5.2.1) distributes homogeneously within the graphene network. Therefore, taking into account the poor crystallinity of black phosphorus and small crystalline domain size of Sn_4P_3, black phosphorus and Sn_4P_3 would appear as nano-crystallites next to each other, well dispersed in the graphene matrix, thanks to the presence of graphene which alleviates the aggregation issues upon their formation during the mechanical milling. Moreover, strong interactions between the active materials and graphene can be present in the sample. For instance, the presence of P-O-C bond in the sample is evident (Figure S5.2.3) induced by the strong mechanical milling, which are also evidenced in many other phosphorus/metal phosphides - carbon systems [25, 28, 45-47].

The transformation in Reaction (5.2.1) upon the presence of graphene is interesting since neither C-P nor C-Sn binary compounds exist in bulk [48]. However, carbon - phosphorus composites can be formed in which element carbon and phosphorus are intermixed on a nanoscale [7, 49], apparently stabilized by abundant interface reactions. The presence of carbon (graphene) in the Sn-P-C composite apparently likewise enables the formation of a relatively stable C-black P composite during the high energy ball milling, which enables the transformation from SnP_3 to Sn_4P_3 with the stabilization of P in the composite being the main factor.
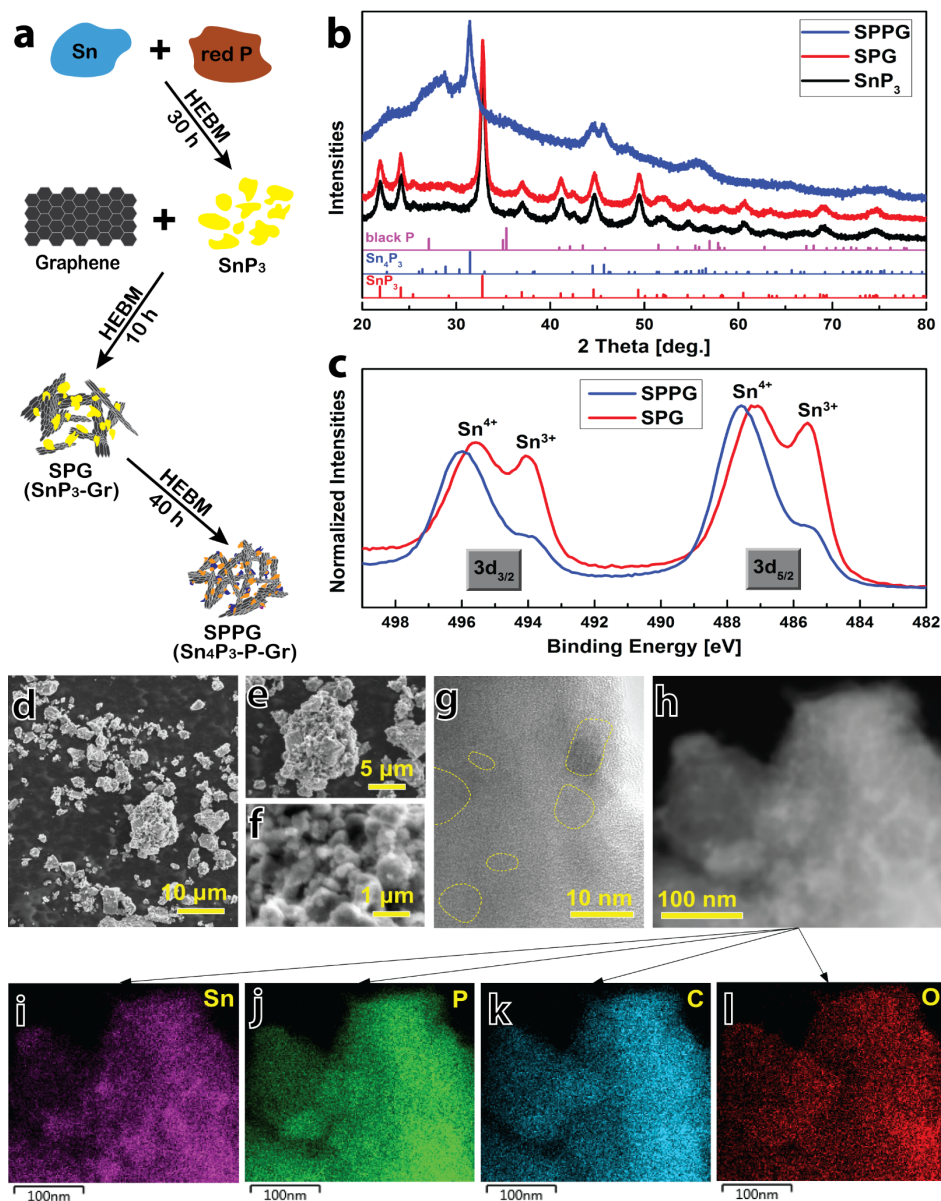
Figure 5.2.1 Sample synthesis and characterization. (a), A schematic of the mechanochemical synthesis process (HEBM: high energy ball milling). (b), XRD patterns of the samples. (reference patterns from Pearson's Crystal Data (PCD) database: SnP$_3$: PCD#1250771, space group: *R-3mh*; Sn$_4$P$_3$: PCD#1910451, space group: *R-3mh*; black P: PCD#1214640, space group: *Cmce*.) (c), XPS spectra of the SPPG and SPG samples. (d) – (f), SEM images of the SPPG sample at different magnifications. (g), High resolution TEM image of the SPPG sample. (h), ADF-STEM image of the SPPG sample and the STEM-EDX element mapping of (i), Sn and (j), P, (k), C and (l), O, respectively.

The electrochemical performance of the samples for Na ion storage has been characterized in half-cell Na ion batteries and the capacity is calculated based on the mass of Sn and P (*excl.* graphene) considering the lower mass ratio of graphene in the composites and its negligible capacity for Na ion uptake (Figure S5.2.6).

Figure 5.2.2a demonstrates that SPPG exhibits an initial desodiation capacity of 708 mAh g^{-1} at 0.4 A g^{-1}, which gradually grows to 855 mAh g^{-1} in 100 cycles and then drops to ~ 800 mAh g^{-1} in 200 cycles and keeps stable after that. A capacity of 796 mAh g^{-1} can be achieved after 300 cycles. The Coulombic efficiency is 73.1 % at the 1st cycle and jumps to 96.2 % at the 2nd cycle, and it reaches >99.5 % within 20 cycles and keeps stable afterwards. In comparison, SPG also undergoes an initial capacity growth for Na ion uptake and achieves 714 mAh g^{-1} after 70 cycles and then stays stable; the Coulombic efficiency increases to 98.9% within 20 cycles and is stabilized afterwards. However, the capacity drops gradually after 130 cycles and a capacity of only 546 mAh g^{-1} is retained in 300 cycles. In addition, the SnP$_3$ (without graphene) based electrode obtains an initial desodiation capacity of 671 mAh g^{-1} which is comparable with SPPG and SPG, but deteriorates rapidly along cycling. The capacity retention drops to <90 mAh g^{-1} in 100 cycles. Figure 5.2.2b shows that the desodiation capacity of SPPG reaches >815 mAh g^{-1} at 0.1 A g^{-1} and a capacity of ~705, ~585 and ~315 mAh g^{-1} can be achieved when the current rate increases to 0.2, 2 and 10 A g^{-1}, respectively. A capacity of >810 mAh g^{-1} can be restored when the current rate is reset at 0.1 A g^{-1} indicating its excellent rate capability. The rate performance of SPG for Na ion uptake follows a similar trend as SPPG but exhibits relatively lower capacities for Na ion storage.

It can be concluded, from the results in Figure 5.2.2a & b and Figure S5.2.7, that the capacity retention and cycling performance upgrade in the order of SnP$_3$ < SPG < SPPG, which can be associated with (i), more refined particle sizes induced by higher energy mechanical milling enabling faster kinetics for Na ion transport; (ii), better electrical conduction and alleviated volume expansion with the graphene matrix host and (iii), stronger interactions between the active materials and graphene which maintains the electrical conduction throughout the electrode along cycling; (iv), the higher intrinsic electronic conductivity of Sn$_4$P$_3$ than SnP$_3$ [32].

The electrochemical performance of the SPPG based Na ion anode (Figure 5.2.2c) reports that cycling at a relatively lower current rate (0.2 & 0.4 A g^{-1}) a gradual improvement on the

capacity is evidenced during the initial tens of cycles indicating an initial activation process, which is also observed in other reports [32, 33, 35]. The desodiation capacity at 0.2 A g^{-1} increases from 762 mAh g^{-1} to 866 mAh g^{-1} within 100 cycles and stays stable afterwards, the retained capacity reaches 842 mAh g^{-1} in 200 cycles. The Coulombic efficiency is 75.1% and 96.3 % for the 1st and 2nd cycle, respectively, and is stabilized at ~99.2 % from 30th cycle. In comparison, the activation process is not observed when the electrodes are dis-/charged at high current rates (1 and 2 A g^{-1}). Cycling at 1 A g^{-1}, the capacity of the SPPG based Na ion anode reaches 652 mAh g^{-1} for the 1st cycle with a Coulombic efficiency of 73.0% which has increased to 97.3 % in the 2nd cycle. The capacity retention deteriorates slightly in the initial 20 cycles and then stays extremely stable at ~610 mAh g^{-1} with a Coulombic efficiency >99.5 %. A reversible capacity of 607 mAh g^{-1} is achieved in 800 cycles after which a gentle degradation occurs but the retained capacity is still >550 mAh g^{-1} after 1000 cycles. The initial reversible capacity at 2 A g^{-1} is 561 mAh g^{-1} and it undergoes a similar decreasing-stable-decreasing trend as observed at 1 A g^{-1}. The Coulombic efficiency reaches >99.5 % within 15 cycles, and the retained capacity amounts to 512, 496 and 371mAh g^{-1} at 200th, 500th and 1000th cycles, respectively. The minor capacity fluctuations during the long term cycling may result from the ambient temperature variations during cycling and have also been observed in other studies [31, 33-36, 39, 40]. To the best of our knowledge, the capacity retentions at such high current rates and the cycling stability that SPPG has achieved are unparalleled among all the Sn-P compounds based anode materials for Na ion batteries.

The relatively lower initial Coulombic efficiency (73–75 %) is due to the formation of irreversible solid electrolyte interphase (SEI) layers on the surface of the active materials, which mainly takes place in the 1st cycle and is negligible in the following cycles. This irreversible process occurs at a relatively higher voltage range as can be observed in the initial sodiation voltage profile (voltage plateau at ~0.95 V in Figure 5.2.2d), which is also evidenced in the differential capacity (dQ/dV) curve (voltage peak at 0.95 V in Figure 5.2.2e) [25] and the cyclic voltammogram (broad peak at ~0.95 V in Figure 5.2.2f) [11, 12, 32-34] of the SPPG based electrode during the 1st sodiation process.

The initial Na ion insertion in SPPG undergoes several stages (at 0.78, 0.65, 0.44, 0.31, 0.18, 0.08 and 0.02 V) as illustrated in the voltage profile (Figure 5.2.2d) and differential capacity curve (Figure 5.2.2e), which originates from the stepwise Na ion insertion in phosphorus and

Sn_4P_3, and the voltage decreases with the increasing Na content in the electrode. Based on the previous reports on the Na ion storage in SnP_3 [31], Sn_4P_3 [32-41], Sn [50-54], and P [55] and it is possible that the relatively higher sodiation voltage peaks (at 0.78, 0.31 and 0.08 V) originate from the step-by-step Na ion insertion in phosphorus with the formation of Na_3P_7, NaP, Na_3P, etc., and the relatively lower voltage peaks (at 0.65, 0.44, 0.18 and 0.02 V) correspond to the reduction of Sn_4P_3 with the formation of Sn (together with Na_xP), Na_4Sn_4, Na_9Sn_4 and $Na_{15}Sn_4$, etc.. The complete sodiation reaction can be depicted as Reaction (5.2.3).

$$24\ Na + Sn_4P_3 = 3\ Na_3P + Na_{15}Sn_4 \tag{5.2.3}$$

During the desodiation process, two broad voltage peaks at 0.33 V and 0.6 V can be observed which can be assigned to the Na ion extraction from the Na-Sn alloys and Na_3P, respectively (Reaction (5.2.4) & (5.2.5)) [31-35, 38-40].

$$Na_{15}Sn_4 = 4\ Sn + 15\ Na \tag{5.2.4}$$

$$3\ Na_3P + 4\ Sn = Sn_4P_3 + 9\ Na \tag{5.2.5}$$

This is similar to the reaction mechanism proposed by Usui *et al.* [32] that, after initial sodiation forming $Na_{15}Sn_4$ and Na_3P, elemental Sn and P react individually with Na ions at different potential regions in the following cycles.
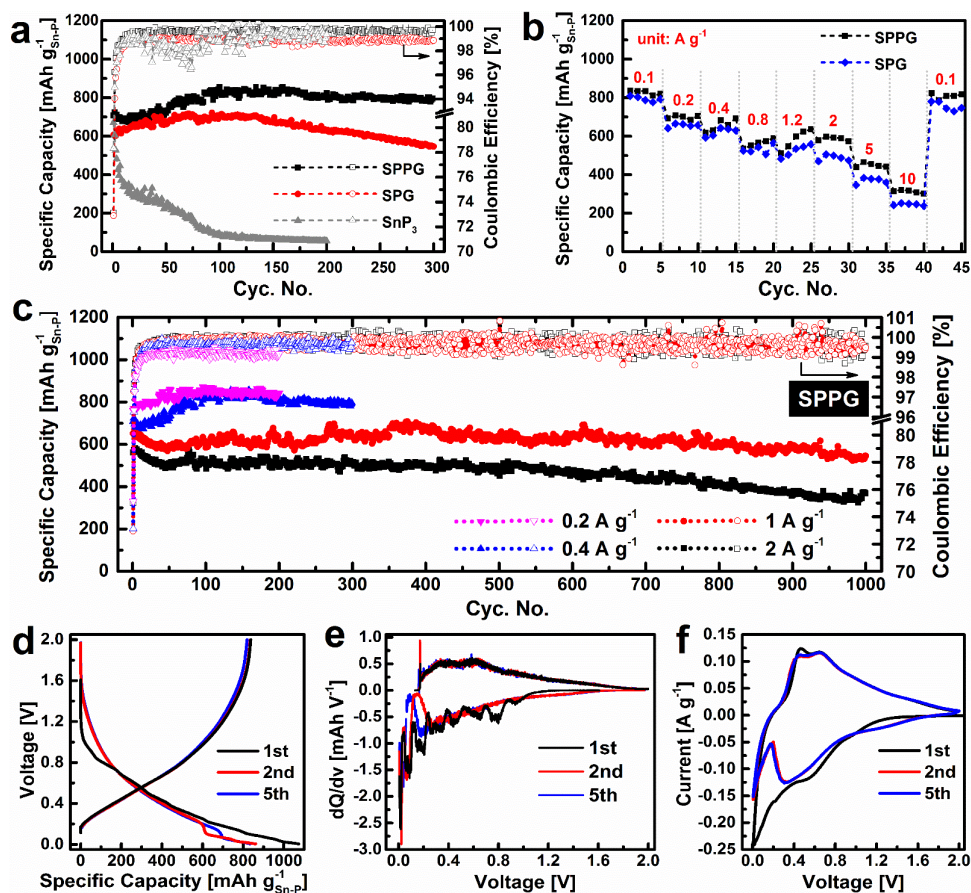
Figure 5.2.2 Electrochemical performance for Na ion uptake. (a), Capacity retentions and Coulombic efficiencies of SPPG, SPG and SnP₃ for Na ion uptake at 0.4 A g⁻¹. (b), Rate capabilities of SPPG and SPG based Na ion anodes. (c), Capacity retentions and Coulombic efficiencies for Na ion uptake in SPPG at different current rates: 0.2, 0.4, 1 and 2 A g⁻¹, respectively. (d), Voltage profiles of the SPPG based Na ion anode at 0.2 A g⁻¹. (e), Differential capacity (dQ/dV) plots for the SPPG anode reproduced from the voltage profiles shown in Figure (d). (f), Cyclic voltammograms of the SPPG anode (Scan rate: 0.5 mV s⁻¹).

Ex-situ XRD patterns (Figure 5.2.3a) of the sodiated electrode shows that the active materials have been amorphized when it is initially sodiated due to the substantial structural change upon a large amount of Na ion insertion. The active materials stay amorphous (or extremely small crystallites) when the Na ion are extracted as the phosphorus and Sn₄P₃ particles stay refined attributed to their presence within the graphene matrix, which is also consistent with the other studies [27, 35, 39, 56]. Meanwhile, the Sn 3d XPS spectrum of the desodiated

SPPG electrode is similar to that of the pristine SPPG (Figure 5.2.3b), which indicates that Sn$_4$P$_3$ is re-formed. (A detailed XPS analysis on the cycled SPPG electrode is in Figure S5.2.8.) Based on the discussions above, a proposal on the sodiation mechanism in SPPG is illustrated in Figure 5.2.3c.
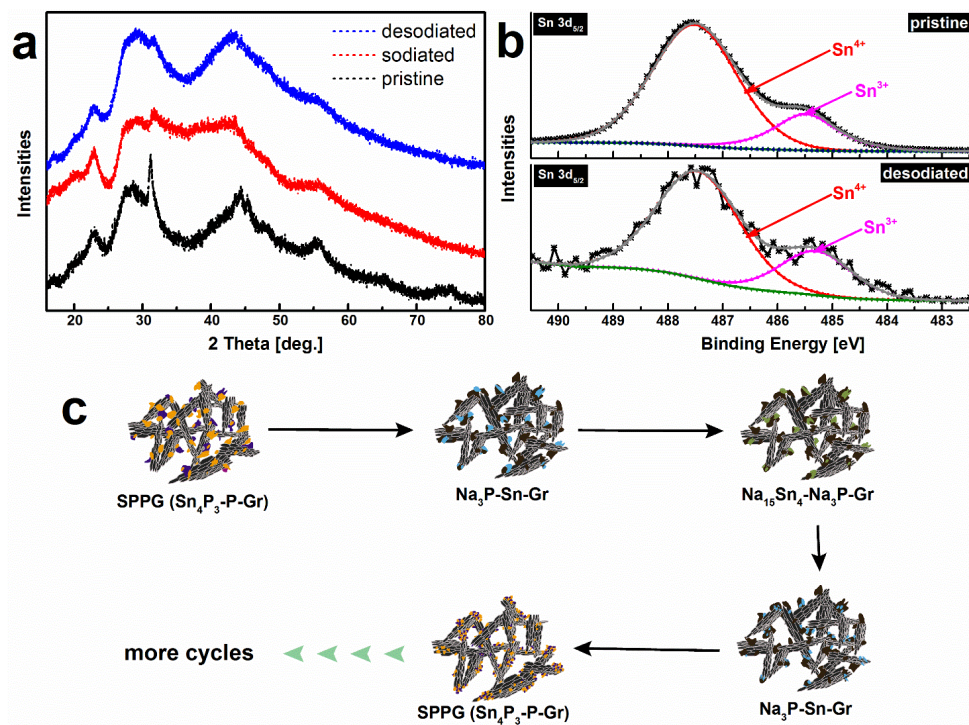

Figure 5.2.3 Mechanism of Na ion uptake in SPPG. (a), *Ex-situ* XRD spectra of the SPPG electrode at different stages. To avoid any unwanted peaks from the metal current collector, here the electrode is a thick self-supporting SPPG electrode (SPPG : PVDF: Super P carbon black = 7: 1.5: 1.5, ~500 μm in thickness; details in the SI). (b), XPS spectra of the pristine and desodiated SPPG electrode after dis-/charge for 20 cycles. (c), A schematic illustration on the de-/sodiation mechanism in SPPG.

The ultrahigh cycling stability of the SPPG composite can be contributed from several factors: (1), Nanosized phosphorus and Sn$_4$P$_3$ are embedded in the conductive graphene matrix which prevents the segregation issues and keeps the active materials nano-refined, which allows for rapid kinetics for Na ion uptake. Meanwhile, the graphene matrix also works as a host to accommodate the large volume change upon Na ion uptake. As a result, the structural integrity is retained over repetitive dis-/charge. (2), Upon the sodiation of P, less-conductive Na$_3$P is formed, which works as a shielding matrix for Sn atoms and prevents the aggregation

issues; metallic Sn provides an electrical conduction pathway for Na_3P for reversible Na ion uptake. The complementary beneficial effects of Sn and Na_3P ultimately enhance the cycling performance [32, 33, 35, 39, 56]. The high mobility of Na^+ in Na_3P [57] warrants an expedite expressway for Na ion transport throughout the active materials. (3), The strong interactions between the active materials and graphene (e.g. P-O-C bond) will maintain the electrical conduction between graphene and the active materials during cycling and thus enable a high cycling stability for Na ion storage. (4), A high Coulombic efficiency (>96%) in the 2nd cycle and growingly higher efficiencies in the following cycles (>99% within 10 cycles) have been observed indicating that the SEI formation almost stops after the 1st cycle as the initial compact NaF-dominant SEI layer protects the active materials from pulverization and further SEI formation [31, 34, 37-39] and thus a stable cycling performance is achieved. In short, the structural integrity and electronic conduction of the electrode have been maintained along cycling and thus a high cycling stability has been achieved, which is also suggested by the SEM images (Figure S5.2.9) and the Electrochemical impedance spectroscopy (EIS) measurement (Figure S5.2.10) of the cycled SPPG electrodes.

5.2.4   Conclusions

In summary, this work presents a novel Sn_4P_3-P (Sn:P = 1:3) @graphene nanocomposite mechanochemically transformed from SnP_3@graphene. This composite exhibits a remarkably high and ultra-stable capacity retention of >550 mAh g^{-1} over 1000 cycle at 1 A g^{-1} and unrivalled rate capability (>815 mAh g^{-1} at 0.1 A g^{-1}, ~585 mAh g^{-1} at 2 A g^{-1} and ~315 mAh g^{-1} at 10 A g^{-1}). This is, to the best of our knowledge, the best cycling stability and cycle life among all the reported Na ion anode materials based on Sn-P compounds, and it shows great promise for its practical applications in high energy density Na ion batteries.

References

[1] B. L. Ellis, L. F. Nazar, Curr. Opin. Solid State Mater. Sci. 6 (2012) 168-177.

[2] H. Kim, H. Kim, Z. Ding, M. H. Lee, K. Lim, G. Yoon, K. Kang, Adv. Energy Mater. 6 (2016) 1600943.

[3] W. Luo, F. Shen, C. Bommier, H. Zhu, X. Ji, L. Hu, Acc. Chem. Res. 49 (2016) 231-240.

[4] X. Xiang, K. Zhang, J. Chen, Adv. Mater. 27 (2015) 5343-5364.

[5] K. Kubota, S. Komaba, J. Electrochem. Soc. 162 (2015) A2538-A2550.

[6] W. L. H. X. Li Jiaoyang, Prog. Chem. 28 (2016) 193-203.

[7] B. Peng, Y. Xu, K. Liu, X. Wang, F. M. Mulder, ChemelectroChem 4 (2017) 2140-2144.

[8] G. L. Xu, Z. Chen, G. M. Zhong, Y. Liu, Y. Yang, T. Ma, Y. Ren, X. Zuo, X. H. Wu, X. Zhang, K. Amine, Nano Lett. 16 (2016) 3955-3965.

[9] C. Zhang, X. Wang, Q. Liang, X. Liu, Q. Weng, J. Liu, Y. Yang, Z. Dai, K. Ding, Y. Bando, J. Tang, D. Golberg, Nano Lett. 16 (2016) 2054-2060.

[10] Y. Zhu, Y. Wen, X. Fan, T. Gao, F. Han, C. Luo, S.-C. Liou, C. Wang, ACS Nano 9 (2015) 3254-3264.

[11] S. Liu, J. Feng, X. Bian, J. Liu, H. Xu, Y. An, Energy Environ. Sci. 10 (2017) 1222-1233.

[12] J. Qian, X. Wu, Y. Cao, X. Ai, H. Yang, Angew. Chem. 125 (2013) 4731-4734.

[13] J. Zhou, X. Liu, W. Cai, Y. Zhu, J. Liang, K. Zhang, Y. Lan, Z. Jiang, G. Wang, Y. Qian, Adv. Mater. 125 (2017) 1700214.

[14] W. Li, S. Hu, X. Luo, Z. Li, X. Sun, M. Li, F. Liu, Y. Yu, Adv. Mater. 29 (2017) 1605820.

[15] Z. Li, J. Ding, D. Mitlin, Acc. Chem. Res. 48 (2015) 1657-1665.

[16] M. Zhao, Q. Zhao, J. Qiu, H. Xue, H. Pang, RSC Adv. 6 (2016) 95449-95468.

[17] J. W. Wang, X. H. Liu, S. X. Mao, J. Y. Huang, Nano Lett. 12 (2012) 5897-5902.

[18] C. Kim, K.-Y. Lee, I. Kim, J. Park, G. Cho, K.-W. Kim, J.-H. Ahn, H.-J. Ahn, J. Power Sources 317 (2016) 153-158.

[19] Y. Xu, Y. Zhu, Y. Liu, C. Wang, Adv. Energy Mater. 3 (2013) 128-133.

[20] Y. Liu, N. Zhang, L. Jiao, Z. Tao, J. Chen, Adv. Funct. Mater. 25 (2015) 214-220.

[21] Y. Liu, N. Zhang, L. Jiao, J. Chen, Adv. Mater. 27 (2015) 6702-6707.

[22] Y. Guo, X. Zeng, Y. Zhang, Z. Dai, H. Fan, Y. Huang, W. Zhang, H. Zhang, J. Lu, F. Huo, Q. Yan, ACS Appl. Mater. Interfaces 9 (2017) 17172-17177.

[23] M. Sha, H. Zhang, Y. Nie, K. Nie, X. Lv, N. Sun, X. Xie, Y. Ma, X. Sun, J. Mater. Chem. A 5 (2017) 6277-6283.

[24] C. Wu, P. Kopold, P. A. van Aken, J. Maier, Y. Yu, Adv. Mater. 29 (2017) 1604015.

[25] S.-O. Kim, A. Manthiram, Chem. Commun. 52 (2016) 4337-4340.

[26] M. Fan, Y. Chen, Y. Xie, T. Yang, X. Shen, N. Xu, H. Yu , C. Yan, Adv. Funct. Mater. 26 (2016) 5019-5027.

[27] W. Li, L. Ke, Y. Wei, S. Guo, L. Gan, H. Li, T. Zhai, H. Zhou, J. Mater. Chem. A 5 (2017) 4413-4420.

[28] W. Qi, H. Zhao, Y. Wu, H. Zeng, T. Tao, C. Chen, C. Kuang, S. Zhou, Y. Huang, Sci. Rep. 7 (2017) 43582.

[29] W.-J. Li, S.-L. Chou, J.-Z. Wang, H.-K. Liu, S.-X. Dou, Chem. Commun. 51 (2015) 3682-3385.

[30] Z. Li, L. Zhang, X. Ge, C. Li, S. Dong, C. Wang, L. Yin, Nano Energy 32 (2017) 494-502.

[31] X. Fan, J. Mao, Y. Zhu, C. Luo, L. Suo, T. Gao, F. Han, S.-C. Liou, C. Wang, Adv. Energy Mater. 5 (2015) 1500174.

[32] H. Usui, Y. Domi, K. Fujiwara, M. Shimizu, T. Yamamoto, T. Nohira, R. Hagiwara, H. Sakaguch, ACS Energy Lett. 2 (2017) 1139-1143.

[33] D. Lan, W. Wang, L. Shi, Y. Huang, L. Hu, Q. Li, J. Mater. Chem. A 5 (2017) 5791-5796.

[34] W. Li, S.-L. Chou, J.-Z. Wang, J. H. Kim, H.-K. Liu, S.-X. Dou, Adv. Mater. 26 (2014) 4037-4042.

[35] J. Qian, Y. Xiong, Y. Cao, X. Ai, H. Yang, Nano Lett. 14 (2014) 1865-1869.

[36] J. Liu, P. Kopold, C. Wu, P. A. van Aken, J. Maier, Y. Yu, Energy Environ. Sci. 8 (2015) 3531-3538.

[37] Y. Kim, Y. Kim, A. Choi, S. Woo, D. Mok, N.-S. Choi, Y. S. Jung, J. H. Ryu, S. M. Oh, K. T. Lee, Adv. Mater. 26 (2014) 4139-4144.

[38] J. Y. Jang, Y. Lee, Y. Kim, J. Lee, S.-M. Lee, K. T. Lee, N.-S. Choi, J. Mater. Chem. A 3 (2015) 8332-8338.

[39] H.-S. Shin, K.-N. Jung, Y. N. Jo, M.-S. Park, H. Kim, J.-W. Lee, Sci. Rep. 6 (2016) 26195.

[40] L. Ma, P. Yan, S. Wu, G. Zhu, Y. Shen, J. Mater. Chem. A 5 (2017) 16994-17000.

[41] L. Zheng, R. A. Dunlap, M. N. Obrovac, J. Electrochem. Soc. 163 (2016) A1188-A1191.

[42] V. Tallapally, R. J. A. Esteves, L. Nahar, I. U. Arachchige, Chem. Mater. 28 (2016) 5406-5414.

[43] L. Häggström, J. Gullman, T. Ericsson, R. Wäppling, J. Solid State Chem. 13 (1975) 204-207.

[44] A. V. Naumkin, A. Kraut-Vass, S. W. Gaarenstroom, C. J. Powell, NIST X-ray Photoelectron Spectroscopy Database, 2012.

[45] J. Sun, H.-W. Lee, M. Pasta, Y. Sun, W. Liu, Y. Li, H. R. Lee, N. Liu, Y. Cui, Energy Storage Mater. 4 (2016) 130-136.

[46] J. Song, Z. Yu, M. L. Gordin, X. Li, H. Peng, D. Wang, ACS Nano 9 (2015) 11933-11941.

[47] Z. Yu, J. Song, M. L. Gordin, R. Yi, D. Tang, D. Wang, Adv. Sci. 2 (2015) 1400020.

[48] G. Peters, I. Thede, V. Vill, R. Zenczykowski, Landolt-Börnstein Substance/Property Index, LCI Publisher GmbH, 2009.

[49] J. Sun, G. Zheng, H.-W. Lee, N. Liu, H. Wang, H. Yao, W. Yang, Y. Cui, Nano Lett. 2014, 14, 4573.

[50] J. Sangster, C. W. Bale, J. Phase Equilib. Diffus. 19 (1998) 76-81.

[51] L. Baggetto, P. Ganesh, R. P. Meisner, R. R. Unocic, J.-C. Jumas, C. A. Bridges, G. M. Veith, J. Power Sources 234 (2013) 48-59.

[52] L. D. Ellis, T. D. Hatchard, M. N. Obrovac, J. Electrochem. Soc. 159 (2012) A1801-A1805.

[53] Z. Du, R. A. Dunlap, M. N. Obrovac, J. Alloys Compd. 617 (2014) 271-276.

[54] M. K. Datta, R. Epur, P. Saha, K. Kadakia, S. K. Park, P. N. Kumta, J. Power Sources 225 (2013) 316-322.

[55] M. Dahbi, N. Yabuuchi, M. Fukunishi, K. Kubota, K. Chihara, K. Tokiwa, X.-f. Yu, H. Ushiyama, K. Yamashita, J.-Y. Son, Y.-T. Cui, H. Oji, S. Komaba, Chem. Mater. 28 (2016) 1625-1635.

[56] Y.-U. Kim, C. K. Lee, H.-J. Sohn, T. Kang, J. Electrochem. Soc. 151 (2004) A933-A937.

[57] H. Lu, B. Xu, J. Shi, M. Wu, Y. Hu, C. Ouyang, Mod. Phys. Lett. B 30 (2016) 1650385.

Supporting Information for Chapter 5.2

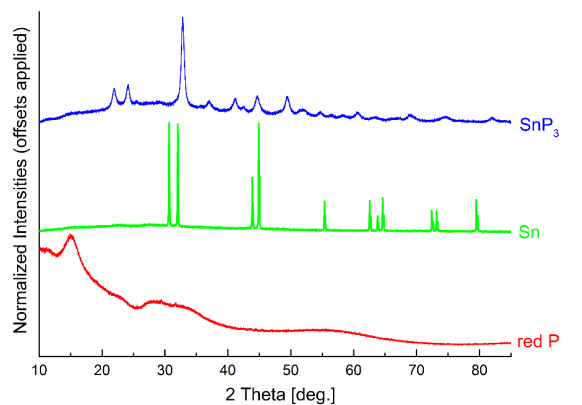## S5.2.1 XRD patterns of the SnP₃ related samples

Figure S5.2.1 XRD patterns of the samples: Red P, Sn and as-synthesized SnP₃.

S5.2.2 Rietveld refinement on the samples

Rietveld refinement on the XRD patterns was performed within the General Structure Analysis System (GSAS) software suite [S1].
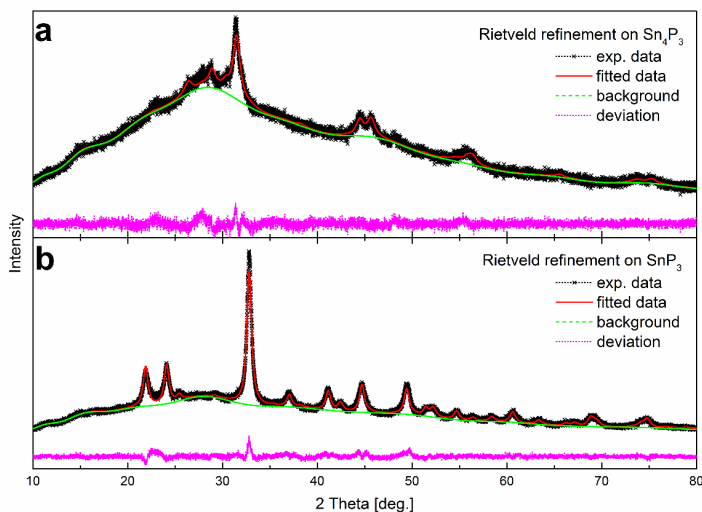

Figure S5.2.2 Rietveld Refinement on (a), Sn₄P₃ and (b), SnP₃ peaks in the XRD patterns of SPPG and SPG, respectively.

Detailed results on the refinement are displayed in the table below.

Samples	Space group	Lattice parameters [Å]	Atom coordinates	U$_{iso}$	Avg. domain size [nm]
Sn₄P₃ (in SPPG)	R-3mh	a = b = 3.985, c = 35.479	P1: 3a (0, 0, 0) P2: 6c (0, 0, 0.4258) Sn1: 6c (0, 0, 0.1358) Sn2: 6c (0, 0, 0.2889)	0.04602	9.4
SnP₃ (in SPG)	R-3mh	a = b = 7.378, c = 10.493	P: 18h (0.4894, 0.5106, 0.2283) Sn: 6c (0, 0, 0.2366)	0.01126	15.0

Table S5.2.1 Detailed Rietveld refinement results. Note the reduced crystalline domain size and the increased atomic displacement factor U$_{iso}$ in the Sn₄P₃ based composite (indicative of somewhat increased disorder in the position of the atoms).

S5.2.3 XPS analysis

The XPS specimen of pristine samples were exposed to air before the XPS measurement as the samples were treated in air and water during the electrode preparation.
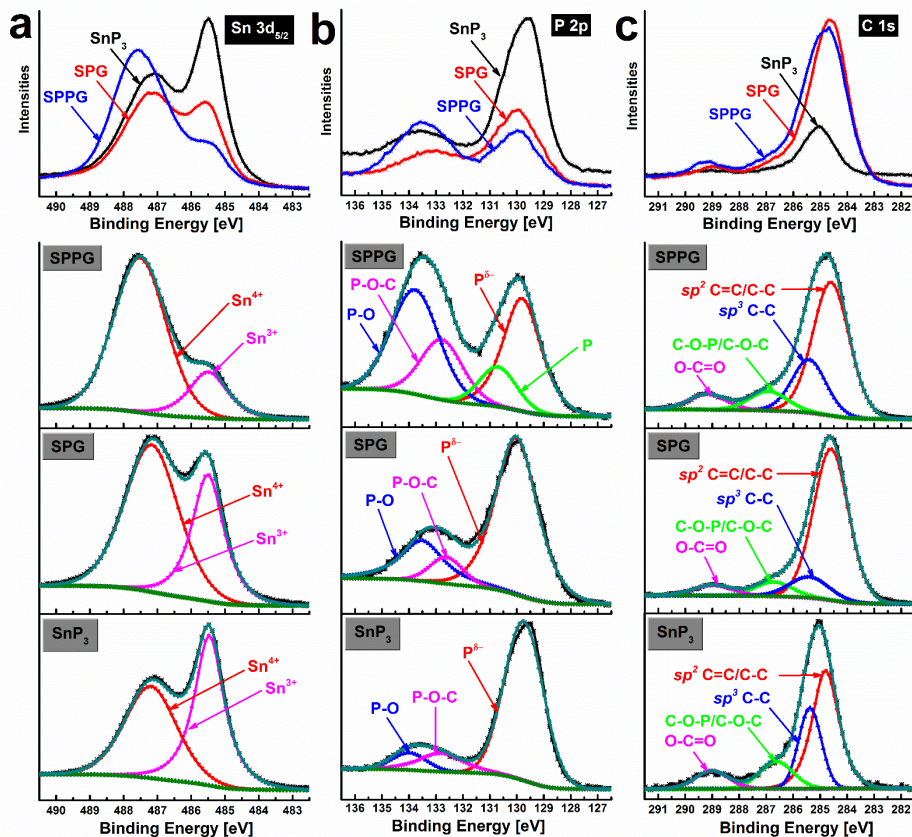

Figure S5.2.3 XPS spectra of the pristine samples. (a), SPPG, (b), SPG and (c), SnP₃. It should be noted that the low-intensity C 1s spectrum observed in the SnP₃ sample results from the adventitious carbon upon exposure to air.

S5.2.4 SEM-EDX mapping
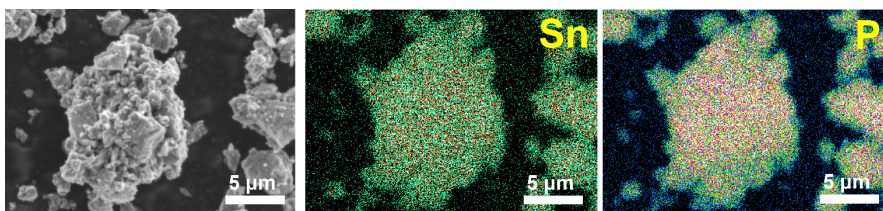
Figure S5.2.4 A SEM image of the SPPG sample and the SEM-EDX element mapping of Sn and P, respectively.

S5.2.5 TEM analysis

Figure S5.2.5 TEM images of the SPPG sample and FFT (Fast Fourier Transform) spectra of the HRTEM image. The crystalline ring with a diameter of 3.52 1/nm corresponds to the main diffraction at the lattice plane (107) of Sn$_4$P$_3$, and the indistinct but visible ring with a diameter of 5.20 1/nm is allocated to the lattice plane (110) of Sn$_4$P$_3$.

S5.2.6 Electrochemical performance

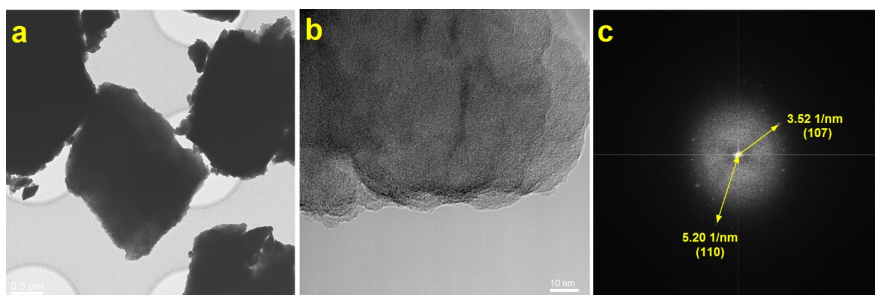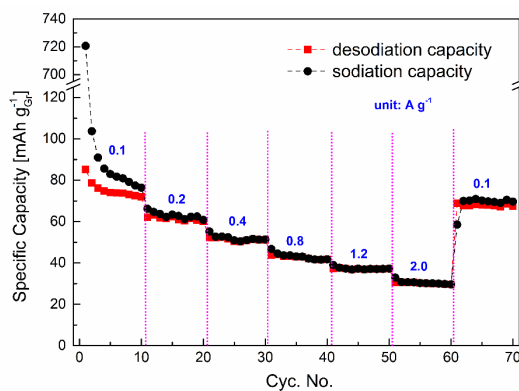Figure S5.2.6 Electrochemical performance of graphene for Na ion uptake. Here the graphene electrode (graphene : NaCMC = 90 : 10 in mass) was measured under the same conditions that were applied for the Sn-P based electrodes.
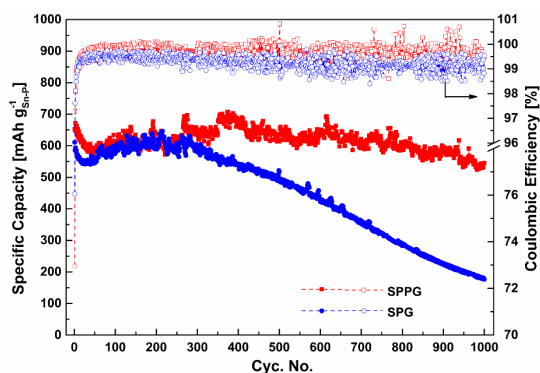

Figure S5.2.7 A comparison between the electrochemical performance of SPPG and SPG based anodes for Na ion batteries cycling at 1 A g⁻¹.

S5.2.7 XRD on the SPPG electrode at different stages

Ex-situ XRD spectra of a SPPG electrode were obtained at different stages: pristine, sodiated to 0.005V and desodiated to 2 V. To avoid any unwanted peaks from the metal current collector, here the electrode is a thick self-supporting SPPG electrode (SPPG : PVDF: Super P carbon black = 7 : 1.5 : 1.5, ~500 μm in thickness). The cycled electrode, after it was collected from the disassembled battery cell, was washed with dimethyl carbonate (DMC) to remove any electrolyte residues and dried in the Ar environment glove box before the XRD measurement was performed.

S5.2.8 XPS spectra of the cycled SPPG electrode

The cycled SPPG electrode, after full desodiation, was washed 3 times with DMC to remove the electrolyte residues and was dried in the Ar environment glove box before the XPS measurement. The specimen was transferred into the XPS analysis chamber with a Vacuum Transfer Module (VTM) to protect the electrode from air and moisture.

Comparing the spectra of the desodiated SPPG (Figure S5.2.8) and the pristine SPPG (Figure S5.2.3), it is observed that the Sn 3d XPS spectrum of the desodiated SPPG electrode is similar to that of the pristine SPPG, revealing that Sn_4P_3 is re-formed. The P-O-C bonds are maintained during cycling in both P 2p and C 1s spectra. In the C 1s spectrum, the peaks of C-F and C-H emerges and the relative intensities of C-O and C=O increase, originating from the SEI layer. In addition, it is noted that the noise ratio of the Sn 3d and P 2p spectra of the cycled electrode is high due to the coverage of the SEI layer as XPS is a surface analysis technique which typically probes the specimen surface for <10 nm.
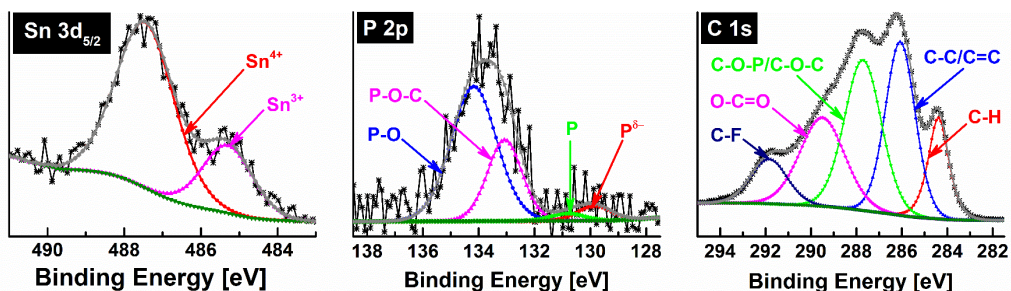

Figure S5.2.8 XPS spectra of the desodiated SPPG electrode after dis-/charge for 20 cycles.

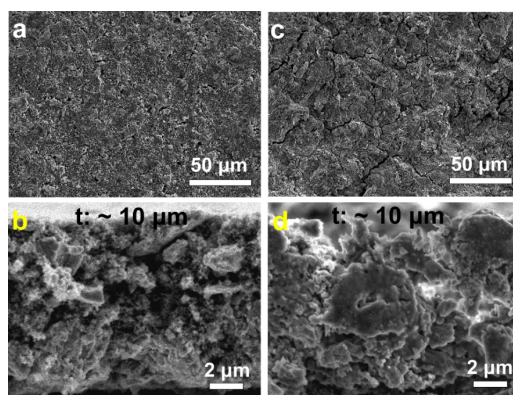**S5.2.9 SEM images of the SPPG based electrodes**

Figure S5.2.9 SEM images of the SPPG electrodes. (a), top and (b), cross-sectional view of the pristine electrode. (c), top and (d), cross-sectional view the electrode after 1000 cycles at 1 A g^{-1}.

S5.2.10 Nyquist plots of the SPPG electrode at different stages

Electrochemical impedance spectroscopy (EIS) was carried out with a PGSTAT302N Autolab potentiostat within a frequency range of 1 MHz to 1 Hz. The cycled electrode was measured at a fully desodiated state.

The Nyquist plots of the SPPG electrode illustrate a semicircle showing the charge transfer resistance of the electrode in the high frequency range. The depressed semicircle reduced drastically after the initial de-/sodiation as the electrochemical reactions improves the penetration of the electrolyte into the active materials, resulting in a reduced interfacial impedance between the electrolyte and electrode. The semicircle increased from the 1st cycle to the 20th cycle originating from the SEI layer on the surface of the electrode during the initial cycles. Then the semicircle was gradually reduced within 500 cycles indicating the drop of contact and charge transfer resistance which indicates an improved inter-particle contact and improved electronic contact which results from the combined effects of the continuously refined particles upon Na ion insertion/extraction, the confinement of the SEI layer and the compact interactions between the active materials and the graphene matrix, and therefore facilitates the activation process. Moreover, it suggests that the electrode retains its structure and morphology along high-rate dis-/charge enabling a high cycling stability during long-term cycling. The charge transfer resistance after 1000 cycles is slightly higher than that after 500 cycles due to the structural deformation during long-term cycling.
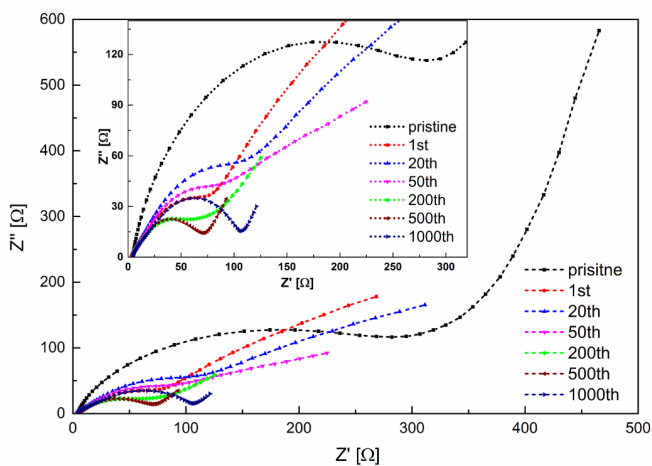
Figure S5.2.10 Nyquist plots of the SPPG electrode at different stages: before cycling and after 1, 20, 50, 200, 500 and 1000 cycles at 1 A g^{-1}.

References

[S1] A.C. Larson, R.B. Von Dreele, Los Alamos National Laboratory Report LAUR (2000) 86-748.

Summary

Modern life is moving towards a mobile and sustainable energy economy with the development of portable electronics, electrical vehicles and renewable energy technologies, in which rechargeable batteries play an essential role as a power supply. The current battery of choice is Li ion battery that is dominating the market but faces great challenges for future use mainly due to the demand for higher capacities and target for cost reduction. Next-generation rechargeable batteries such as Li-O_2, Li-S and Na ion batteries, which offers higher capacities and cost-effectiveness, are being intensively researched as potential solutions to meet the future energy storage demand. The use of Na is attractive in view of the more globally abundant Na resource compared with Li. However, the progress remains slow due to the lack of suitable electrode materials, in particular, anode materials with low-cost, high capacity, long cycle life and safety.

This thesis focuses on the search of high-performance anode materials for both Li and Na ion batteries, including metallic Li and Na, Si, MgH_2, and black P and Sn_4P_3 based composites. Various methods are involved to synthesize the active materials and electrodes in a cost-effective manner. High specific and areal capacities and stable cycling performance have been achieved for Li and Na ion storage, and comprehensive characterization on the structural, morphological and electrochemical properties has been performed to provide insights into the reaction mechanisms.

Li/Na metal is regarded as the "Holy Grail" anode of choice, however its application has been plagued by the problematic dendrite formation during Li/Na deposition and the unstable solid electrolyte interphase (SEI). This work utilizes a facile and rapid hydrogen bubble dynamic template (HBDT) electrodeposition method to produce porous 3D Ni@Cu current collectors to suppress the dendritic Li and Na deposition. It has been evidenced that Li and Na deposition occurs uniformly within the porous host thanks to the delocalized charge distribution with the presence of numerous conductive nickel tips on the current collector. The Li/Na nucleation and growth mechanism has been revealed through studying the morphological evolution of the Li/Na deposition. Moreover, it is observed with multiple characterization methods that a small amount (1 wt. %) of $LiNO_3$ additive in the electrolyte

effectively limits the SEI formation. In short, the electrodeposition fabricated porous current collector shows much promise for the practical application of Li and Na metal anodes.

High energy density alloy and conversion reaction-based anode materials such as Si, MgH_2, P and Sn_4P_3 undergo severe volume changes upon Li/Na ion absorption and unstable SEI formation, which leads to the pulverization of active materials, continuous growth of SEI and gradual electrode structural deformation upon repetitive dis-/charge. These issues result in the loss of active materials and deterioration of the electrical conduction throughout the electrodes, and the retained capacity and cycling stability are poor. Apart from that, the slow ionic transport kinetics, in particular for the relatively larger Na ions, also imposes prominent challenges for the high reversibility and rate capability of Li/Na uptake.

To overcome the problems related to the volume change, this thesis investigates Li and Na ion battery anode using nanosized active materials. The pure Si nanoparticle deposition based Li ion battery anode and the ultra-small Si nanoparticles for Na ion storage are produced via plasma enhanced chemical vapor deposition (PECVD) from silane; and the size reduction of MgH_2, black P and Sn_4P_3 is achieved with high energy ball milling (HEBM). The nanoscaling allows for a better tolerance to the volume change and thus avoids the pulverization and continuous SEI formation on the new surfaces. Moreover, these active materials are embedded within nanostructured carbon frameworks which integrates the electrical conduction throughout the electrode and confines the structural deformation of active materials. In this work, nanocomposites of MgH_2-TiF_3@carbon nanotube (CNT), black P-super P carbon black and Sn_4P_3-P@graphene have been synthesized through mechanical milling with nanocrystalline MgH_2, Sn_4P_3 and black P, respectively, uniformly embedded within the carbon matrix. In these composites, the carbon network serves as a scaffold to confine the volume expansion upon Li/Na ion uptake, and the strong interactions between the active materials and carbon maintain the electrical conduction over cycling. These synergistically beneficial effects improve the retained capacity for Li/Na ion storage and enhance the cycling stability. On the other hand, in the Si nanoparticle deposition based Li ion battery anode, the SEI layer formed in the first cycle is that stable that it even works positively as a host that allows the volume changes without undesirable pulverization by accommodating the volume change in the space between the particles and their local SEI.

Apart from controlling the volume change of the electrode, the unstable SEI growth has also been addressed with the addition of fluoroethylene carbonate (FEC) in the electrolyte, which

induces the formation of a thin and compact SEI layer that prevents the further SEI formation. In this work, a possible effect of the FEC addition has also been evidenced in the Si nanoparticle deposition based Li ion battery anode, which leads to the formation of a one-off and locally protective SEI layer mainly consisting of LiF, Li_2CO_3, Li_xSiO_y and ROCOOLi. This SEI layer exhibits excellent elasticity and mechanical strength, which protects the electrode and prevents the further SEI formation.

The kinetic limitations have been dealt with multiple methods in this thesis. Firstly, porous electrodes are applied to enable the easy access of the liquid electrolyte to the active materials, providing an express pathway for Li and Na ion diffusion throughout the electrode. In this work, a slurry-based method using anhydrous tetrahydrofuran (THF) as a solvent has been introduced, which enables the fabrication of MgH_2 based porous and thin-film electrodes allowing for a facile infiltration of the electrolyte throughout the electrode. The slurry-based manufacturing method is also applied for the Si nanoparticles, and black P-C and Sn_4P_3-P@graphene composites based electrodes. In the Si nanoparticle deposition based Li ion anode, interconnected porosities also exist that facilitates the Li ion diffusion. Secondly, nanosizing works as an effective way to accelerate the Li/Na ion transport due to the reduced diffusion distance in active material solids. The size reduction has been realized using PECVD and HEBM as mentioned above. Moreover, the addition of catalytic TiF_3 in MgH_2 based electrodes improves the Li/Na ion uptake by enhancing the hydrogen sorption kinetics in MgH_2 through the grain refinement effects of MgF_2. Additionally, in the Sn_4P_3-P@graphene composite based Na ion battery anode, the presence of electrically insulating but Na-ion conductive Na_3P works as a stabilizing matrix that eliminates the aggregation of Sn and facilitates the Na ion diffusion.

In summary, this work studies novel, low-cost, long-lifespan and safe anode materials with high capacities for Li and Na ion storage, ranging from the ultimate anode – metallic Li/Na to Si and P that exhibit the highest theoretical capacities for Li and Na ion storage, respectively. The cycling stability and rate capability of MgH_2 based Li ion battery anodes are improved with the catalysis of TiF_3. The first realization of Na ion uptake in Si and MgH_2 has also been achieved in experiments. The results presented in this thesis show great promise towards the commercial introduction of these anodes in next-generation high energy density Li and Na ion batteries.

Samenvatting

Het moderne leven beweegt in de richting van een economie van mobiliteit en duurzaamheid met de ontwikkeling van draagbare elektronica, elektrische voertuigen en duurzame energie technologieën, waarin oplaadbare batterijen en accu's een essentiële rol spelen als spanningsbron. De huidige voorkeursbatterij is de Li ionenbatterij, die de markt domineert, maar in de toekomst grote uitdagingen tegemoet ziet hoofdzakelijk door de vraag naar hogere capaciteit en rendabiliteit. De oplaadbare batterijen van de volgende generatie zoals Li-O_2, Li-S en Na ionenbatterijen, die hogere capaciteiten bij lagere kosten bieden, worden intensief bestudeerd als potentiele oplossingen om aan de toekomstige vraag naar energie tegemoet te komen. Het gebruik van Na is aantrekkelijk gezien de grotere wereldwijde beschikbaarheid vergeleken met Li. De voortgang blijft echter traag door het gebrek aan geschikte elektrode materialen, in het bijzonder anodematerialen met lage kosten, hoge capaciteit, lange levensduur en hoge veiligheid.

Dit proefschrift richt zich op het speuren naar hoge-prestatie anodematerialen voor zowel Li als Na ionenbatterijen, gebruikmakend van composieten met als basismateriaal metallisch Li en Na, Si, MgH_2, zwarte P en Sn_4P_3. Verschillende methoden zijn betrokken bij de synthese van de actieve materialen en elektroden op een kostenefficiënte manier. Hoge soortelijke en oppervlakte capaciteiten en stabiele prestaties onder ladingscycli zijn bereikt voor Li en Na ionenopslag, en omvattende karakterisering van de structurele, morfologische en elektrochemische eigenschappen is uitgevoerd om inzicht te verschaffen in de reactiemechanismen.

Li/Na metaal wordt beschouwd als de "Heilige Graal" voorkeursanode; de toepassing daarvan wordt evenwel geplaagd door problematische dendrietvorming gedurende Li/Na depositie en de instabiele vaste-stof elektrolyt interfase (SEI). Dit werk gebruikt een eenvoudige en snelle hydrogen bubble dynamic template (HBDT) elektrodepositie methode om poreuze 3D Ni@Cu stroomcollectoren te produceren en de dendritische Li en Na afzetting te onderdrukken. Het is bewezen dat Li en Na depositie uniform in het poreuze gastmateriaal plaats vindt dankzij de gedelokaliseerde ladingsverdeling door de aanwezigheid van talrijke geleidende nikkel tips op de stroomcollector. Het Li/Na nucleatie

en groei mechanisme is onthuld door de morfologische ontwikkeling van de Li/Na depositie te bestuderen. Bovendien is met verschillende karakterisatiemethoden waargenomen, dat een kleine hoeveelheid (1 gewichts %) $LiNO_3$ als elektrolytadditief de SEI vorming doeltreffend beperkt. Om kort te gaan de door elektrodepositie gefabriceerde poreuze stroomcollector is veelbelovend voor praktische toepassing van Li en Na metaalanodes.

Op legeringen en conversiereactie gebaseerde anodematerialen met hoge energiedichtheid zoals Si, MgH_2, P en Sn_4P_3 ondergaan sterke volumeveranderingen onder Li/Na ionenabsorptie en instabiele SEI vorming, die leidt tot verpulvering van actieve materialen, continue groei van SEI en geleidelijke structurele vervorming van de elektrode onder herhaalde ont-/lading. Deze punten resulteren in verlies van actief materiaal en verslechtering van de elektrische geleiding door de elektrodes heen en de overblijvende capaciteit en stabiliteit onder cycli zijn gebrekkig. Bovendien is de trage ionentransportkinetiek, in het bijzonder voor de relatief grotere Na ionen, ook een prominente uitdaging voor hoge reversibiliteit en potentiele snelheid van de Li/Na opname.

Om de problemen te overwinnen, die verband houden met de volumeverandering, onderzoekt dit proefschrift Li en Na ionenbatterijanodes met actieve materialen op nanogrootte. De op zuivere Si nanodeeltjesdepositie gebaseerde Li ionenbatterijanode en de ultrakleine Si nanodeeltjes voor Na ionenopslag worden geproduceerd via plasma enhanced chemical vapor deposition (PECVD) uit silaan; en de verkleining van de grootte van MgH_2, zwarte P en Sn_4P_3 wordt bereikt door high energy ball milling (HEBM). De nanoschaal laat een grotere tolerantie toe voor de volumeverandering en vermijdt zo de verpulvering en continue SEI vorming op nieuwe oppervlakken. Bovendien zijn deze actieve materialen ingebed in koolstofnanostructuren wat de elektrische geleiding door de elektrode heen integreert en de structurele vervorming van actieve materialen beperkt. In dit werk zijn nanocomposieten van MgH_2-TiF_3@carbon nanotube (CNT), zwarte P-super P carbon black en Sn_4P_3-P@grafeen gesynthetiseerd door mechanisch malen met nanokristallijn MgH_2, Sn_4P_3 en zwarte P, respectievelijk, uniform in de koolstof matrix ingebed. In deze composieten dient het koolstofnetwerk als substraat om de volumeuitzetting onder Li/Na ionenopname te beperken en de sterke wisselwerking tussen de actieve materialen en koolstof bewaart de elektrische geleiding over cycli. Deze synergetisch voordelige effecten verbeteren de behouden capaciteit voor Li/Na ionenopslag en verhogen de stabiliteit onder cycli. Anderzijds is in de op Si nanodeeltjesdepositie gebaseerde Li ionenbatterijanode de SEI laag gevormd in de

eerste cyclus zo stabiel dat deze zelfs positief werkt als een gastheer, die volumeveranderingen toelaat zonder onwenselijke verpulvering door de volumeverandering in de ruimte tussen de deeltjes en hun lokale SEI onder te brengen.

Buiten het beheersen van de volumeverandering van de elektrode is de instabiele SEI groei ook aangepakt met de toevoeging van fluoroethyleencarbonaat (FEC) in het elektrolyt, wat de vorming induceert van een dunne en compacte SEI laag, die verdere SEI vorming voorkomt. In dit werk is ook een mogelijk effect bewezen van de FEC toevoeging in de op Si nanodeeltjesdepositie gebaseerde Li ionenbatterijanode, wat leidt tot de vorming van een eenmalige en lokaal beschermende SEI laag hoofdzakelijk bestaande uit LiF, Li_2CO_3, Li_xSiO_y en ROCOOLi. Deze SEI laag vertoont excellente elasticiteit en mechanische sterkte, wat de elektrode beschermt en verdere SEI vorming voorkomt.

De kinetische beperkingen zijn met vele methoden behandeld in dit proefschrift. Ten eerste zijn poreuze elektrodes toegepast om gemakkelijke toegang van het vloeibare elektrolyt tot het actieve materiaal mogelijk te maken door een snelle weg te bieden voor Li en Na ionendiffusie door de elektrode. In dit werk is een op slurry gebaseerde methode geïntroduceerd met watervrij tetrahydrofuraan (THF) als oplosmiddel, die de fabricage van op MgH_2 gebaseerde poreuze en dunne-laag elektrodes mogelijk maakt, die een eenvoudige infiltratie van het elektrolyt door de elektrode toelaten. De op slurry gebaseerde productiemethode wordt ook toegepast voor de Si nanodeeltjes, zwart P-C en op Sn_4P_3-P@grafeencomposieten gebaseerde elektrodes. In de op Si nanodeeltjesdepositie gebaseerde Li ionenanode bestaan ook onderling verbonden poreusheden, die de Li ionendiffusie faciliteren. Ten tweede werkt het op nanogrootte brengen als een effectieve manier om het Li/Na ionentransport te versnellen dankzij de gereduceerde diffusieafstand in vaste stoffen van actief materiaal. De reductie in grootte is gerealiseerd met gebruik van PECVD en HEBM zoals hierboven vermeld. Bovendien verbetert de toevoeging van katalytisch TiF_3 in op MgH_2 gebaseerde elektrodes de Li/Na ionenopname door de waterstofsorptiekinetiek in MgH_2 te versnellen door korrelverfijningseffecten op MgF_2. Verder werkt, in de op Sn_4P_3-P@grafeencomposiet gebaseerde Na ionenbatterijanode, de aanwezigheid van elektrisch isolerend maar Na-ionen geleidend Na_3P als een stabiliserende matrix die de aggregatie van Sn elimineert en Na ionendiffusie faciliteert.

Om samen te vatten, dit werk bestudeert nieuwe en veilige anodematerialen met lage kosten en lange levensduur met hoge capaciteit voor Li en Na ionenopslag, lopend van de ultieme

anode – metallisch Li/Na tot Si en P die de hoogste theoretische capaciteiten vertonen voor Li en Na ionenopslag, respectievelijk. De stabiliteit onder cycli en potentiele snelheid van op MgH_2 gebaseerde Li ionenbatterijanodes zijn verbeterd met de katalyse met TiF_3. De eerste realisatie van Na ionenopname in Si en MgH_2 is ook bereikt in experimenten. De resultaten die in dit proefschrift gepresenteerd worden, beloven veel voor de commerciële introductie van deze anodes in volgende-generatie Li en Na ionenbatterijen met hoge energiedichtheid.

Acknowledgement

Upon the completion of this thesis, I want to take the opportunity to express my gratitude to all the people that I had the privilege to meet, to work with and to learn from, and from whom I have received considerable inspiration, encouragement and support during my PhD journey.

First, I would like to thank Prof. Fokko Mulder, who is not only a supervisor of my PhD research (and Master thesis project) but a mentor in my career development. The constant guidance, support and freedom he has provided throughout these years has helped me to be on track of a PhD journey and to move forward in doing independent and professional research. I also greatly appreciate his kindness, friendliness and support in my daily life.

ADEM, A green Deal in Energy Materials of the Ministry of Economic Affairs of The Netherlands, is acknowledged for the financial support in my PhD research. The materials, and technical support from industrial partners (Meyer Burger, TNO Holst center, Carbot/Norit) is also an important part of my work, without which many studies in this thesis would not have been done. Some persons that have to be mentioned here are Dr. Dana Borsa, Ellie Swaans, Dr. Sandeep Unnikrishnan and Dr. Lucas Haverkate.

The work presented in this thesis has been done with the collaboration of two research groups, ChemE-MECS and RST-SEE/FAME. I want to thank Prof. Bernard Dam, Dr. Marnix Wagemaker, Dr. Erik Kelder, Prof. Hans Geerlings, Prof. Ekkes Brück, Prof. Andreas Schmidt-Ott and Dr. Wilson Smith for providing both scientific and administrative support, and bringing forward interesting questions and discussions during the group meetings. I also thank the committee members for reviewing this thesis.

Next, I must express my sincere gratitude to Michel, Frans, Herman, Joost, Anton for their strong technical support in general lab facilities, and to Kees (XRD), Bart (XPS), Swapna (ssNMR), Shiv and Duco (SEM/TEM), Lijing (Raman) and Ben (TGA) for their training and assistance in specific measurements. Jouke is acknowledged for his kind help with multiple issues (software, taxing, and Dutch translation) in my research and life. I also wish to thank the secretaries, Heleen, Ilse, Nicole, Noortje and Wil, who are always friendly to me and helpful with my administrative issues.

I warmly acknowledge my research partners (Bo, Peter-Paul and Zhaolong), co-authors and Master students (Ashok, Sibo and Yangqun) and many bachelor students, who have made valuable contribution to my research.

I am also grateful to the research fellows around, MCES-ers, SEE-ers and NPM2/FAME-ers, who are great persons to work with and also nice friends in life. There are many names I would like to mention with great pleasure, Alex, Anca, Anna, Bei, Beien, Bernhard, Bo, Bowei, Carla, Chandra, Chao, Chuang, Deepak, Fengjiao, Haixing, Jiawei, Jicheng, Kai, Kun Qian, Kun Shen, Lei, Luc, Martjin, Michael, Ming Liu, Ming Ma, Niek, Peter-Paul, Prasad, Qian, Recep, Remco, Robin, Shasha Lv, Shasha Zhang, Sanjana, Shiv, Swapna, Thang, Tiantian, Tomas, Violetta, Wenqin, Xiaoyu, Xinmin, Xuefei, Yibole, Zhaolong, Zheng, Zhiqiang, Zhou, Zhu and many more. Special thanks go to Anna for leading me into battery research, to Peter-Paul for his kind help with many research and daily-life problems, and to Bo, Xiaoyu, Zhaolong and Zhou for their trust, everlasting friendship and strong support in my life. I also owe thanks to Chandra for giving me advice in my career development.

My sincere thanks also go to my roommates (Nan, Hongde and Maolong) and friends in China, the Netherlands and elsewhere, who have made my life pleasant outside the PhD work.

Last but not least I must express my deepest gratitude to my family for their constant and unconditional love, encouragement and support on me. I am greatly indebted to my beloved parents, wife, sisters, aunt and uncle. I love you forever.

最后，感谢我的家庭对我无条件的爱和支持。我深爱的父母、妻子、姐姐、姑姑和姑父，我亏欠你们的太多，一生也无法偿还！永远爱你们！

Yaolin Xu (徐耀林)

April 2018

Delft, the Netherlands

List of Publications

Publications related to this thesis

1, Y. Xu, A.S. Menon, S. Unnikrishnan, F.M. Mulder, *Honeycomb-like Porous 3D Nickel Electrodeposition for Stable Li and Na Metal Anodes*, ***Energy Storage Mater.* 12 (2018) 69-78.**

2, **Y. Xu**, E. Swaans, S. Chen, S. Basak, P.P.R.M.L. Harks, B. Peng, H.W. Zandbergen, D.M. Borsa, F.M. Mulder, *A High-Performance Li-Ion Anode from Direct Deposition of Si Nanoparticles*, ***Nano Energy* 38 (2017) 477-485.**

3, **Y. Xu**, E. Swaans, S. Basak, H.W. Zandbergen, D.M. Borsa, F.M. Mulder, *Reversible Na-Ion Uptake in Si Nanoparticles*, ***Adv. Energy Mater.* 6 (2016) 1501436.**

4, **Y. Xu**, F.M. Mulder, *TiF$_3$ Catalyzed MgH$_2$ as a Li/Na Ion Battery Anode*, to be submitted.

5, B. Peng†, **Y. Xu**†, K. Liu, X. Wang, F.M. Mulder, *High-Performance and Low-Cost Sodium-Ion Anode Based on a Facile Black Phosphorus - Carbon Nanocomposite*, ***ChemElectroChem* 4 (2017) 2140-2144.** (inside cover) (†: co-first author)

6, **Y. Xu**, B. Peng, F.M. Mulder, *A High-Rate and Ultrastable Sodium Ion Anode Based on a Novel Sn$_4$P$_3$-P@Graphene Nanocomposite*, ***Adv. Energy Mater.* 8 (2018) 1701847.**

Other publications

7, **Y. Xu**, F.M. Mulder, *Mg Catalyzed with TiF$_3$ as an Anode Material in Ni-MH Batteries: Multiple Approaches for a Stable Cycling Performance*, to be submitted.

8, **Y. Xu**, E. Swaans, D.M. Borsa, F.M. Mulder, *Engineering Direct Deposition of Si Nanoparticles Based Anodes for High-Performance Li-Ion Batteries*, in preparation.

9, B. Peng†, **Y. Xu**†, X. Wang, X. Shi, F. M. Mulder, *The Electrochemical Performance of Super P Carbon Black in Reversible Li/Na Ion Uptake*, ***Sci. China. Phys. Mech. Astron.* 60 (2017) 064611.** (†: co-first author)

10, B. Peng, **Y. Xu**, F.M. Mulder, *Improving the Performance of Si-Based Li-Ion Battery Anodes by Utilizing Phosphorene Encapsulation*, ***Acta Phys. -Chim. Sin.*** **33 (2017) 2127-2132.**

11, Z. Li, S. Ganapathy, **Y. Xu**, Q. Zhu, W. Chen, I. Kochetkov, C. George, L.F. Nazar, M. Wagemaker, *Fe_2O_3 Nanoparticle Seed Catalysts Enhance Cyclability on Deep (Dis)charge in Aprotic $Li-O_2$ Batteries*, ***Adv. Energy Mater.*** **(2018) 1703513.**

12, Z. Li, S. Ganapathy, **Y. Xu**, J. R. Heringa, Q. Zhu, W. Chen, M. Wagemaker, *Understanding the Electrochemical Formation and Decomposition of Li_2O_2 and LiOH with Operando X-ray Diffraction*, ***Chem. Mater.*** **29 (2017) 1577-1586.**

13, S. Lv, T. Verhallen, A. Vasileiadis, F. Ooms, **Y. Xu,** Z. Li, Z. Li, M. Wagemaker, *Monitoring the Lithium Spatial Distribution in Li-Metal Anodes*, accepted in ***Nat. Commun.*** .

14, S.A. Vasudevan†, **Y. Xu**†, S. Karwal, H.G.M.E. van Ostaay, G.M.H. Meesters, M. Talebi, E.J.R. Sudhölter, J.R. van Ommen, *Controlled Release from Protein Particles Encapsulated by Molecular Layer Deposition*, ***Chem. Commun.*** **51 (2015) 12540-12543**. (†: co-first author)

Curriculum Vitae

Yaolin Xu was born on 2 October 1989 in Henan, China. He got his Bachelor of Science degree in Physics at Department of Physics, Renmin University of China by June 2011, after which he moved to the Netherlands to pursue his Master of Science degree in Sustainable Energy Technology at Delft University of Technology (TU Delft) and graduated in July 2013.

From January 2014, he has joined the group of Materials for Energy Conversion and Storage (MECS) at Department of Chemical Engineering, TU Delft, and worked as a PhD researcher under the supervision of prof. dr. Fokko M. Mulder. His PhD project was financially supported by A green Deal in innovative Energy Materials (ADEM) program funded by Dutch Ministry of Economic Affairs and ADEM industrial partners. The research results obtained during his PhD has been presented in this doctoral thesis.